MECHANISTIC EVALUATION OF HYDROGEN EVOLVING CATALYSTS THROUGH ELECTROCHEMICAL AND SPECTROSCOPIC KINETIC ANALYSIS

Eric S. Rountree

A dissertation submitted to the faculty of the University of North Carolina at Chapel Hill in partial fulfillment of the requirements for the degree of Doctor of Philosophy in the Department of Chemistry the College of Arts and Sciences.

Chapel Hill
2017

Approved by:

Jillian Dempsey

Joseph Templeton

Mark Wightman

Gerald Meyer

Matthew Lockett

ABSTRACT

Eric S. Rountree: Mechanistic Evaluation of Hydrogen Evolving Catalysts Through Electrochemical and Spectroscopic Kinetic Analysis
(Under the direction of Jillian L. Dempsey)

The desire to generate carbon neutral fuels from renewable energy sources prompted researchers to turn their attention to biological systems several decades ago in hopes of being able to emulate the processes that allow nature to so effectively perform these fuel generating chemical reactions. Because of its energy density and chemical simplicity, hydrogen, and thus, the hydrogenase enzymes have been the focus of many of these studies. The process began by attempting to synthesize mimics of the enzyme active sites, however, after countless *structural* mimics were prepared, it became clear that the surrounding enzyme was crucial to the activity. The failure of the structural mimics to perform has more recently led to the search for *functional* mimics; molecules that, while not similar in appearance, are designed to function as the hydrogenase active site would in the midst of the surrounding enzyme.

With the focus on functional mimicry, two families of hydrogen evolution catalysts have risen to prominence; the cobaloximes, and the $Ni(P_2^R N_2^{R'})_2$ catalysts (where $P_2^R N_2^{R'}$ represents 1,5-R'-3,7-R-1,5-diaza-3,7-diphosphacyclooctane). Within this dissertation, examples of each of these catalysts are thoroughly analyzed for mechanistic understanding. In addition, study of the $Ni(P_2^{Ph} N_2^{Ph})_2$ catalyst revealed that the hydride intermediate could be isolated and reacted with proton sources independently. This allowed for a unique study of what role the proton source plays in catalytic turnover and thoroughly demonstrated that the carboxylic acid

based proton sources can react with the catalyst while in their dimerized state. This was shown to artificially suggest second order reactivity and significantly increase the acidity of the proton source.

The intense scrutiny of these catalytic mechanisms had the natural consequence of a focus on proton-coupled electron transfers, which have the potential to eliminate the need for high energy intermediates if the proton and electron can be transferred in a single step, and can open the door to catalysts that operate at a fixed overpotential, regardless of solution pH. This work carried the mechanistic study forward to a catalyst that has electron and proton transfers sufficiently coupled to generate a catalytic Pourbaix diagram. The diagram prepared in this study has shown that under catalytic conditions, the experimental Pourbaix diagram does not necessarily depict the most thermodynamically stable species, but rather only those capable of reaching equilibrium on the electrochemical timescale. These mechanistic insights will be useful to researchers designing functional mimics of the hydrogenase enzymes.

ACKNOWLEDGEMENTS

My life has changed in many ways since arriving in Chapel Hill, thank you to every person who has been a part of that. Thank you for the friendship, the advice, and the endless encouragement that I have received. Thank you to my two church families here in Chapel Hill, the Bible church and Grace.

Jillian and Joe: My decision to attend this university was based off my interactions with the two of you during my visitation. Thank you both for being wonderful encouragers during that time and through my whole five years here. Joe, thank you for allowing me space in your lab when I started out and for continuing to lobby for me over the years. Jillian, you have been an amazingly supportive advisor. I am truly grateful for your mentorship and don't imagine I will have another person as pleasant as you that I get to call boss.

Robin, Thomas and Brian: I formed a unique friendship with each of you and will not forget you. Robin, sharing an office with you was a lot of fun and showed me just how great of a person you are. Thomas, you were always like an older brother; I appreciate all the encouragement you gave me over the years and the numerous wise words. Brian, our friendship has been built on mutual respect. I have no doubt that you are going to go on to do great things. I have always admired your work ethic, commitment to values, and your perspective on scientific, philosophical, and political matters.

Other members of the Dempsey Lab (especially Noémie, Dan and Chris): You guys have been excellent workmates and friends. I have learned so much through group meetings and conversations with you. This dissertation never would have been without your help.

Mom, Dad, Travis, Tyler, Juliea, Trever, Taylor, and Logan: You guys have always been there for me, no matter what. Thank you for supporting me through school and making sure I always had everything that I needed to be successful. Thank you for being a breath of fresh air when I made trips home. I love you; thank you for loving me so well.

Kelley: Sometimes, doing the work in this thesis could feel overwhelming, but you have been there, helping me carry that burden. Any time I have had a bad day, you have considered it your mission to make sure that it didn't end that way, and when I had good days, you were still there to make sure it stayed that way. I look forward to a long, happy and prosperous life with you. You're the best. I love you.

TABLE OF CONTENTS

LIST OF SCHEMES

LIST OF TABLES

LIST OF FIGURES

LIST OF ABBREVIATIONS AND SYMBOLS

Abs	Absorbance
Å	Angstrom
cm	centimeter
CV	Cyclic voltammogram or cyclic voltammetry
E	Redox Potential
Eq.	Equation
Equiv.	Equivalent
Fc	Ferrocene
g	gram
K_x	equilibrium constant for reaction x
k_x	rate constant for process x
k_{obs}	observed reaction rate
L	Liter
mL	Milliliter
mM	Millimolar
mV	Millivolts
M	Molar
nm	Nanometer
NMR	Nuclear magnetic resonance
O	Ohm
H^+	Proton
s	Second
T	Temperature

t	Time
UV-vis	Ultraviolet-visible
V	Volt
A	Amps
CPET	Concerted proton and electron transfer
F	Faraday constant
k_f	Forward rate constant
R	Gas constant
μA	Microamps
ppm	Parts per million; chemical shift
PCET	Proton-coupled electron transfer
ν	Scan rate
FOWA	Foot-of-the-wave analysis

CHAPTER 1. Introduction

1.1 Importance of Developing Renewable Fuels

Following the onset of the energy crisis in the 1970's, President Jimmy Carter addressed the nation with a description of the nation's energy history and the two major shifts in our predominate energy source: from wood to coal and coal to oil. He then stated, "We must prepare quickly for a third change, to strict conservation [of energy] and to the use of coal and permanent renewable energy sources, like solar power.[1]" Regardless of President Carter's dream and his initiation of the Department of Energy, a tumultuous political climate and constantly fluxional oil price has dampened the efforts to make this third change. Even more, over the years, politicians and the general public have had an increased awareness of the impending dangers associated with climate change, exponentially rising greenhouse gas levels, and eye opening moments regarding the need for national energy autonomy, and yet a relatively insignificant amount of progress toward stymying these problems has occurred.[2–4] The only long-term solution to deal with these issues collectively is to shift global reliance to renewable energy, whether that be wind, hydroelectric, geothermal, or solar energy.

Though significant progress has been made in the field of energy harvesting, energy storage and transport have posed a persistent barrier to progress;[5,6] several forms of renewable

energy, including wind and solar, are intermittent, requiring that they be harvested as available, rather than as needed.[7,8] Further, our current infrastructure is weighted heavily toward liquid fuels and consequently, changing our infrastructure to accommodate another form of energy would be quite a demanding and expensive endeavor (it is highly unlikely in the near term).[9] In summary, it is not solely the development of renewable energy collection that proves to be important, but also the development of cost-effective methods to store and transport energy. With this in mind, electrocatalytic fuel producing reactions have come to the forefront of many research programs.

Electrocatalysis is currently poised to provide a solution to the renewable energy storage problem. Coupling the conversion of energy poor feedstocks—such as water and carbon dioxide—to energy rich fuels, particularly liquid fuels, would allow for a carbon neutral energy economy. As a result, our infrastructure could be maintained, the advance of the human component in climate change would be halted, and a complete national energy autonomy would be allowed. Unfortunately, though electrocatalytic complexes have been actively sought over the last several decades, very few catalysts are esteemed within the literature.[10] Understanding how these catalysts proceed, specifically with regard to proton-coupled electron transfers (PCET), is the focus of this compendium.

1.2 Homogeneous Electrocatalysis and the Proton-Coupled Electron Transfer

Throughout the electrochemical literature there are two categories of electrocatalysis: *heterogeneous,* whereby the electrode surface acts as the catalytic platform, and *homogeneous*, where the catalyst freely diffuses within the solution, receiving its reducing or oxidizing equivalents from an inert electrode.[11–13] Both categories have their own advantages and disadvantages, but the molecular research community is primarily concerned with the ability

to perform in depth mechanistic analysis, a characteristic that is uniquely afforded to homogeneous systems where individual intermediates can be isolated and studied independently, and electronic structure can be tuned through functionalization.[14,15] In general, the molecular research community is motivated to study reaction mechanisms because of the promise to gain insight into what could improve the efficiency of the reaction. When examining fuel producing electrocatalytic reactions, this mechanistic insight usually surrounds PCET reactions, as they are ubiquitous in all forms of fuel producing catalysis.[16] PCET is traditionally viewed in terms of a square scheme (Scheme 1.1) where concerted and stepwise routes are possible. Reactions that proceed via the stepwise routes, though often kinetically favorable, necessarily proceed through high energy intermediates. Consequently, PCET reaction mechanisms are often studied with an eye tuned toward determining favorable conditions for the concerted pathway.

Scheme 1.1. Square scheme representation of a homogeneous PCET reaction where species M receives one electron and one proton to form MH. H-A represents an acid molecule, and ET, PT, and CPET indicate electron transfer, proton transfer, and concerted proton-electron transfer, respectively.

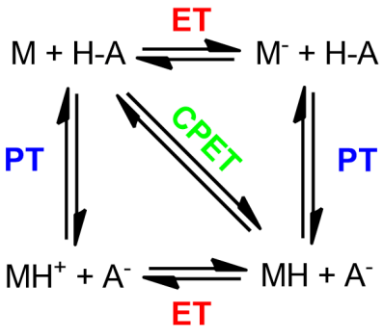

1.3 Electrochemical Methodology

1.3.1. Cyclic Voltammetry

Cyclic voltammetry (CV) is the most common electroanalytical technique employed to study molecular electrocatalysts. Illustrated in Figure 1.1 is a typical cyclic voltammogram for a solution phase species P undergoing a reversible one electron reduction to species Q. Starting at an initial potential at which the complex exists nominally in a single redox state, P, the potential is scanned in the negative direction. When the potential is sufficiently negative to reduce P, cathodic current begins to flow as P is reduced to Q. The current response is defined by the relationship of two parameters — the electron transfer rate constant between the electrode and the analyte ($k°$, cm s^{-1}), and the transport (via diffusion) of the electroactive material to the electrode surface (described by the mass transport coefficient, m_T).[17,18] When electron transfer to the analyte is rapid in relation to the mass transport of the analyte ($k° >> m_T$, electrochemical reversibility) and the electrogenerated product is stable on the timescale of the experiment (chemical reversibility),[19] the rising cathodic current observed can be explained by the Nernst Equation, shown below for the reaction $P + e^- \rightleftharpoons Q$, where C_P and C_Q are the concentrations of P and Q at the surface of the electrode, respectively, and $E^{\circ\prime}$ is the formal potential of the reduction process.[20]

$$E = E^{\circ\prime} + \frac{RT}{nF} ln \frac{C_P}{C_Q} \qquad (Eq. 1.1)$$

When the applied potential is altered, the ratio of C_P and C_Q will adjust in accordance with the Nernst Equation. In the limit of fast electrode kinetics, a dramatic increase in cathodic current is observed at potentials in the region of $E^{\circ\prime}$ as P is reduced.

One might assume that the current should increase exponentially at even more negative potentials, as predicted by Butler-Volmer theory.[21] However, at sufficiently negative applied potentials, any oxidized species at the electrode surface is reduced, causing the concentration of the oxidized species (C_P) near the electrode to be diminished, as illustrated by the concentration-distance profiles shown in Figure 1.1. This effect manifests itself in the voltammogram as a peak in current (i_p) followed by a decrease in current flow as the potential is scanned further negative. A concentration gradient is formed and the oxidized species from solution must be transported from the bulk solution to the electrode surface in order for additional current to flow. The rate of diffusion through this depleted diffusion zone dictates the observed current if high concentrations of electrolyte and unstirred solutions are employed in the cyclic voltammetry experiment; under these conditions, diffusion is well approximated as the sole mode of mass transport for the analyte. The thickness of the diffusion layer (δ) depends on the timescale (t) of the voltammogram scan ($\delta \sim \sqrt{Dt}$, where D is the diffusion coefficient of P, cm^2/s), and t is inversely proportional to the scan rate υ ($t \sim \frac{RT}{F\upsilon}$).[21] As such, the diffusion layer expands over the course of one scan, with the relative thickness decreasing with increasing scan rate.

At the switching potential, the scan direction is reversed, but current continues to flow because the applied potential is still sufficiently negative to reduce P (although the concentration of this species at the electrode has been significantly diminished by this point and diffusion layer thickness has increased). Importantly, the depletion of P is matched by the accumulation of Q. As the applied potential becomes increasingly positive, Q is oxidized (such that the ratio of C_P/C_Q at the electrode surface satisfies the Nernst Equation) and an anodic current flows following the same principles as described for the cathodic current.

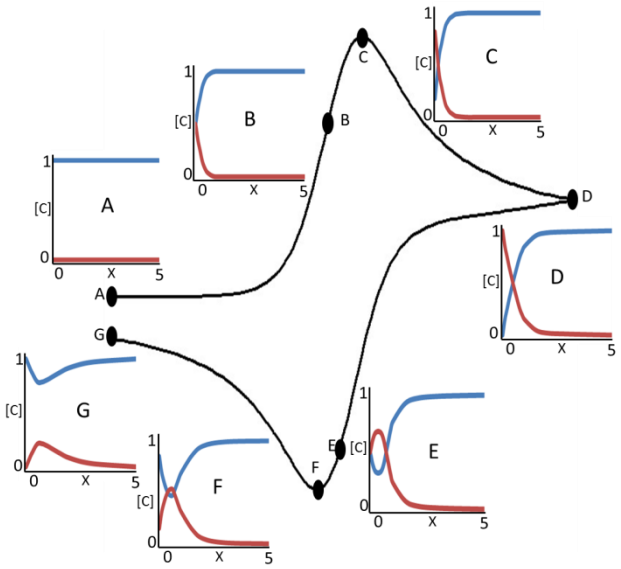

Figure 1.1 Concentration profiles (concentration (mM) vs. distance from the electrode (cm x 10^{-2})) at various points during a reversible cyclic voltammetric wave. Scan rate = 100 mV s^{-1}, C_P (Blue), C_Q (Red). Adapted from Reference [17]. Copyright © 2011, Imperial College Press.

1.3.2. Idealized Catalytic Responses

Electrocatalytic processes can occur via many mechanisms with numerous possible CV responses. These responses may be dependent on multiple variables including scan rate, catalyst and substrate concentrations, and the rate constants of the catalytic mechanism. Savéant and coworkers have rigorously mapped out the CV responses for the one electron reduction of substrate A to B by a redox catalyst P, where the rate limiting step is homogeneous electron transfer (the E_rC_i' mechanism).[22,23]

$$P + e^- \rightleftharpoons Q$$

$$Q + A \xrightarrow{k_e} P + B$$

The CV responses for this process depend on the dimensionless parameters[23]

$$\lambda = \left(\frac{RT}{F}\right)\left(\frac{k_e C_P^0}{\upsilon}\right)$$

$$\gamma = \frac{C_A^0}{C_P^0}$$

where λ is the kinetic parameter, γ the excess factor, k_e is the rate constant of the outer sphere electron transfer from the reduced catalyst Q to the substrate A, C_P^0 the bulk concentration of redox catalyst P, and C_A^0 the bulk concentration of substrate A. A two dimensional plot of λ versus γ has been created with the various limiting CV responses divided into zones (Figure 1.2).[23,24] The various zones and CV responses from Figure 1.2 are discussed here.

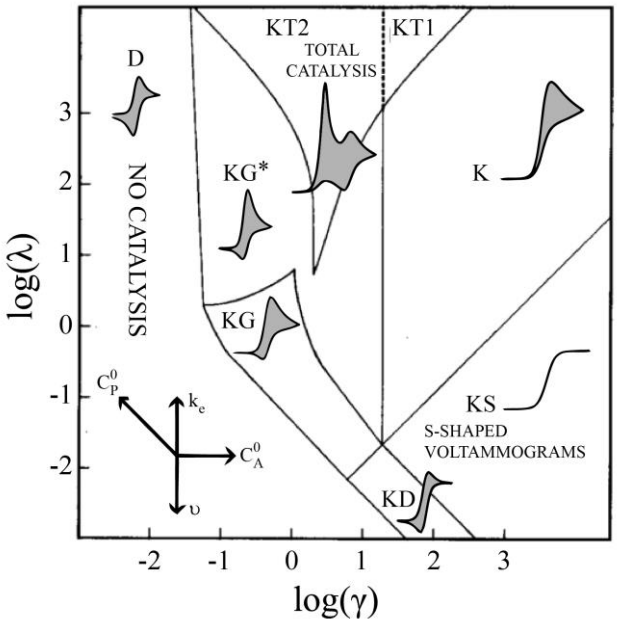

Figure 1.2. Kinetic zone diagram and simulated CV waveforms for the one electron reduction of substrate A via a redox catalyst mediator P where λ is the kinetic parameter and γ is the excess factor (see text). The compass rose visually depicts how catalysis may move between zones (C_P^0 is initial concentration of catalyst, C_A^0 is initial concentration of substrate, υ is the scan rate, and k_e is the rate constant for homogeneous electron transfer from reduced catalyst to substrate). The CV waveforms follow the convention of negative potentials to the right and cathodic current upward. Scans are started from positive potentials. Waveforms adapted with permission from reference [24]. Copyright 2008, American Chemical Society. Zone diagram reprinted (with minor modifications) from reference [23], Copyright 1984, with permission from Elsevier.

Zone D *(no catalysis)* The CV observed is that of the reversible redox couple P/Q.

Zone KS *(S-shaped, pure kinetic conditions*[23] *— no substrate consumption)* In Zone KS, an S-shaped response is observed where the forward and reverse scans trace each other exactly. This region is characterized by the situation where substrate concentration at the electrode surface is equal to the bulk concentration.[25]

Zone K *(pure kinetic conditions, substrate consumption)* In Zone K, competition between consumption of substrate by the rate determining step, with diffusion of new substrate to the electrode, results in a peaked CV and a reverse scan which does not lie on top of the forward scan. Despite depletion of substrate, no reverse redox wave is seen as any reduced catalyst is oxidized through catalytic turnover.

Zone KT2 and KT1 *(total catalysis, pure kinetic conditions, substrate consumption)* Total catalysis is observed when the catalyst immediately consumes all of the accessible substrate within the timescale of the forward scan, resulting in a CV with two peaks. A catalytic current is initially observed but substrate is quickly totally consumed, resulting in a peak. As the potential is scanned more negative, the reversible redox wave of the catalyst is seen in the same position without substrate present.

Zone KD *(no substrate consumption)* The waveform depicted in Zone KD describes catalysts that are operating under the conditions of no substrate consumption (large γ), similar to that of Zone KS. However, in this scenario the waveform is not a perfect 'S' shape due a reduced value of the kinetic parameter, λ.

Zones KG and KG* *(substrate consumption)* Waveforms depicted in Zones KG and KG* arise from conditions described by a small γ and small λ.[23] Similar to Zone KT2, where total catalysis occurs, Zones KG and KG* are limited by substrate diffusion to the electrode from the bulk.

The theory behind the cyclic voltammetry of catalytic E_rC_i' reactions was formulated by Delahay & Stiehl,[26] Nicholson & Shain,[27,28] and Savéant & coworkers.[23,29–32] Several assumptions are made in the treatment: electron transfer between the electrode and redox active couple P/Q is fast and Nernstian; by corollary, the homogeneous electron transfer (chemical) step (Q + A) that reforms P is rate limiting; $C_A^0 \gg C_P^0$ (large γ); the diffusion coefficients of species P and Q are approximately equal; E_i (initial potential of the scan) is sufficiently positive such that the resulting measurement is independent of this value; the substrate A exhibits no redox behavior at the electrode in the window of interest. The observed (or apparent) pseudo-first order rate constant, k_{obs}, is defined by Eq. 1.2 (for the E_rC_i' mechanism) and is intrinsic to the homogeneous chemical reaction Q + A, and hence not potential dependent. Simply stated, k_{obs} represents the rate at which P is formed from Q through a homogeneous process.

$$k_{obs} = k_e C_A^0 \qquad (Eq.\,1.2)$$

Under the conditions for Zone KS the resulting wave can be described by Eq. 1.3, where *n* is the number of electrons transferred in the redox event, *A* the electrode surface area in cm^2 (usually treated as the geometric surface area, though the electrochemical surface area is preferred), *D* the diffusion coefficient of the redox species P in cm^2/s, and C_P^0 the bulk concentration of redox species P in mol cm^{-3}.

$$i = \frac{nFAC_P^0\sqrt{Dk_{obs}}}{1 + exp\left[\frac{nF}{RT}\left(E - E_{P/Q}^o\right)\right]} \qquad (Eq.\,1.3)$$

Importantly, Eq. 1.3 indicates that no peak is observed. At potentials significantly negative of $E_{P/Q}^0$ (≈100 mV), Eq. 1.3 is simplified and the catalytic plateau current i_c can be described by Eq. 1.4. i_c is independent of scan rate, as current is controlled only by regeneration of P through the chemical reaction Q + A.[31]

$$i_c = nFAC_P^0\sqrt{Dk_{obs}} \qquad (Eq.\,1.4)$$

k_{obs} can be deduced from i_c. Frequently, the i_c–k_{obs} relationship is divided by the Randles-Sevcik Equation, which describes the dependence of the peak current i_p (amperes) on scan rate υ (V s^{-1}) (Eq. 1.5) for a reversible redox process.

$$i_p = 0.4463\, nFAC_{\mathrm{P}}^0\left(\frac{nF\upsilon D}{RT}\right)^{1/2} \qquad (Eq.\,1.5)$$

This yields the relationship shown in Eq. 1.6,

$$\frac{i_c}{i_p} = \frac{1}{.446}\sqrt{\left(\frac{RT}{nF\upsilon}\right)k_{obs}} \qquad (Eq.\,1.6)$$

Eq. 1.6 is often desirable as it does not require an independent measurement of D, A or C_P^0 to determine k_{obs}. It must be noted that *n* in Eq. 1.4 represents the number of electrons transferred to P from the electrode, and thus is only different than *n* in **Error! Reference source not ound.** in the case i_p is determined from a separate redox event (this may at times be necessary due to some interference at the event of interest[25]) or when successive electron transfers occur at the electrode following chemical steps. This is discussed further in Section 3.3.2.3, but it should be noted that as written, Eq. 1.6 assumes the values of *n* in **Error! Reference source ot found.** 1.4 is one.

It is worth reiterating that the use of Eq. 1.4 and Eq. 1.6 is restricted to the S-shaped curves obtained in Zones KS and KD (where the plateau current is used).[22] Access to Zone KS (and KD) necessitates that i_c is not limited by substrate diffusion — substrate consumption is always negligible and the assumption $C_A = C_A^0$ holds true. Experimentally, the S-shaped CV response of Zone KS can be obtained by increasing the substrate concentration (increasing γ) or increasing scan rate to limit substrate consumption. Additionally, access to the pure kinetic

zones requires the chemical reaction be fast in comparison to the timescale of the voltammogram — thus in the case of slow catalysis (small k_e), υ may be decreased to increase the value of λ. However, caution must be exercised as slow scan rates (and very large λ) may lead to substrate consumption within the diffusion layer. To ensure an appropriate scan rate is being utilized, the scan rate independence of i_c should be confirmed.[33] Further, at very slow scan rates, a 'false' plateau shape may be achieved as a result of natural convection.[13,31] Lastly, in many cases the S-shaped response wave may not be accessible. Side-phenomena, such as catalyst deactivation, inhibition of current by product adsorption to the electrode, and background H_2 evolution are known to perturb catalytic responses.[34]

While the discussed equations and zone diagram specifically model one electron redox catalysis with homogeneous electron transfer as the rate determining step, the various regions and CV responses have become general reference points for more complicated mechanisms.[35] This is crucial as all relevant reactions require multiple electrons, multiple substrate molecules, or commonly both.

1.3.3. Potential Shifting: Kinetic and Thermodynamic

During the investigation of homogeneous PCET reactions, potential shifts of a redox couple ($E_{1/2}$ in reversible systems, peak potential (E_P) in irreversible systems, and wave half-heights ($E_{cat/2}$) in catalytic systems) are commonly observed when changes to the solution occur (generally changes are applied to the proton source or concentration).[36–39] We describe these shifts as either *kinetic* or *thermodynamic*. Despite the difference in our assigned nomenclature, both cases represent the solution reestablishing equilibrium following an electron transfer.

When the potential shift is identified as thermodynamic, it implies that electron transfer between the solution species and the electrode is rate limiting, and that all proton transfers occur either in concert with electron transfer or at a rate such that the solution is at equilibrium at the electrode surface.[40] Under these conditions, the redox potential for the reaction of interest depends upon the solution free energy and can be represented using a Pourbaix diagram; a Pourbaix diagram defines the boundaries between the most thermodynamically stable species as a function of solution free energy and potential.[41] Because the electron transfers are assumed rate limiting, no experimental parameters aside from solution free energy can alter the position of the redox couple.

If the shift in potential is described as kinetic, the proton transfers are rate limiting instead of the electron transfers and, as a result, the solution is not at equilibrium at the electrode surface. Reversibility is thereby prohibited, confining the analysis to E_P and $E_{cat/2}$. Because the proton transfer is rate limiting, it is possible for the measured potential to be affected by the parameters used to make the measurement, *e.g.*, the scan rate or the absolute concentration of the proton source. In addition, as is described in Chapter 2, the observed rate constant for the proton transfer can be obtained from the magnitude of the shift.[42]

1.3.4. Foot-of-the-Wave Analysis

Oftentimes, it is difficult to achieve the S-shaped catalytic response currents of Zone KS. Competing side phenomena, such as substrate consumption, catalyst deactivation, and product inhibition cannot always be eliminated through experimental parameters. A method termed foot-of-the-wave analysis (FOWA) has been presented and applied by Savéant and Costentin to estimate kinetic information for electrochemical catalytic processes whose

corresponding voltammograms do not meet the rigid requirements to be characterized as Zone KS, yet have an accessible "foot" to the catalytic wave (i.e., there are no redox events distorting the foot of the wave).[13,34,43,44]

The foot-of-the-wave analysis (FOWA) begins with Eq. 1.7, which describes a catalytic response current for a multi-electron, multi-step reaction as a function of potential obtained under the conditions of Zone KS and the case in which the first chemical step is rate determining and $E_{cat/2} = E_{redox}$.

$$i = \frac{nFAC_P^0\sqrt{Dn'k_{obs}}}{1 + exp\left[\frac{nF}{RT}(E - E_{redox})\right]} \qquad (Eq.\,1.7)$$

Normalization of **Error! Reference source not found.** by i_p, the peak current in the bsence of substrate, as defined by the Randles-Sevcik equation (Eq. 1.5), yields Eq. 1.8.

$$\frac{i}{i_p} = \frac{2.24\sqrt{\frac{RT}{nFv}}\sqrt{n'k_{obs}}}{1 + exp\left[\frac{nF}{RT}(E - E_{redox})\right]} \qquad (Eq.\,1.8)$$

Figure 5a presents data in the format of i/i_p vs. $E - E_{redox}$. Under purely kinetic conditions with no substrate consumption, and the classic sigmoidal current response is obtained as predicted by Eq. 1.7; however, side-phenomena cause the response current to deviate from the predicted S-shape. In the example shown in Figure 5a, the influence of substrate consumption increases as the bulk substrate concentration decreases. FOWA assumes that catalysis is occurring under purely kinetic conditions at the foot of the wave and this can be used to analyze voltammograms that deviate from the S-shaped wave of Zone KS as a result of these undesired side phenomena.

Re-plotting i/i_p versus $1/\{1 + exp\left[\frac{nF}{RT}(E - E_{redox})\right]\}$ results in a straight line for response currents obtained under Zone KS conditions (Figure 1.3B). Side phenomena result in deviation from the predicted linear relationship, but at the foot of the wave, the plot holds to the linear expectation. Thus a linear extrapolation can be performed to retrieve the expected linear relationship had no side-phenomena occurred. From Eq. 1.8 we see that k_{obs} can be determined from the slope of this line ($m = 2.24\sqrt{RT/nF\upsilon}\sqrt{n'k_{obs}}$).[34] It is key to note that this method of FOWA can only be applied to the scenarios described above—the first chemical step is rate limiting and $E_{cat/2} = E_{redox}$. The value for k_{obs} extracted from this analysis describes the reactivity of the catalyst *in the hypothetical absence of side phenomena*.

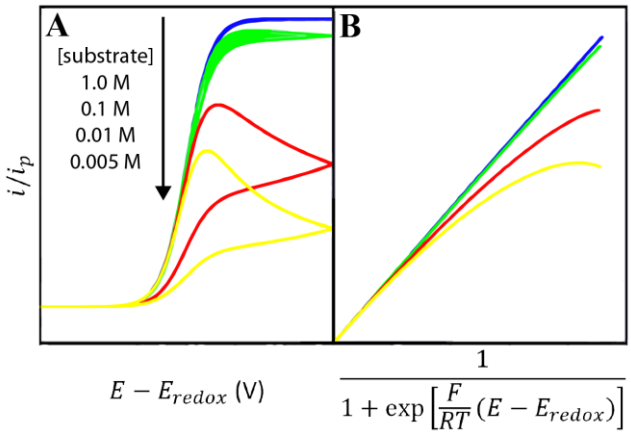

Figure 1.3. A) Simulated CV responses for catalytic conversion of substrate to product with various concentrations of substrate (shown decreasing from blue to yellow), with υ = 0.1 V/s, DP = 10-5 cm2 s-1, C_P^0 = 1 mM, T = 298 K, n′ = 2 and kC_A^0 = 50 s-1. B) FOWA linear plots for the same CV responses showing the linear fits obtained. Adapted with permission from Reference 34. Copyright (2012) American Chemical Society.

FOWA expressions have also been presented for more general scenarios which do not satisfy the conditions put forth above, including heterolytic pathways in which the second chemical step is rate limiting, intermediate cases in which the first and second chemical steps have comparable rates, and the homolytic reaction pathway.[44] Unlike the derivation presented

above, these expressions do not require that $E_{cat/2} = E_{redox}$, which is important because $E_{cat/2}$ cannot always be accurately or directly determined from a CV if side phenomena are active. While detailed derivations of these FOWA expressions are beyond the scope of this work, the current–potential responses for most of the scenarios take the form of Eq. 1.9, where the expressions for i_c and $E_{cat/2}$ are unique to each specific scenario.

$$i = \frac{i_c}{1 + exp\left[\frac{F}{RT}\left(E - E_{cat/2}\right)\right]} \qquad (Eq. 1.9)$$

At the foot of the wave, $E \gg E_{cat/2}$, and thus $exp\left[\frac{F}{RT}\left(E - E_{cat/2}\right)\right] \gg 1$. This approximation yields the current–potential approximation presented in Eq. 1.10.

$$i \approx i_c exp\left[-\frac{F}{RT}\left(E - E_{\frac{cat}{2}}\right)\right] \qquad (Eq. 1.10)$$

By plotting current versus $exp\left[-\frac{F}{RT}(E - E_{redox})\right]$, rate information can be gleaned from the slope of the resulting linear region at the foot of the wave. It is key to note that application of FOWA can generally only provide rate information for the chemical step immediately following electron transfer. This is demonstrated for the *EECC* case with all electron transfers occurring at the electrode in Figure 1.4.

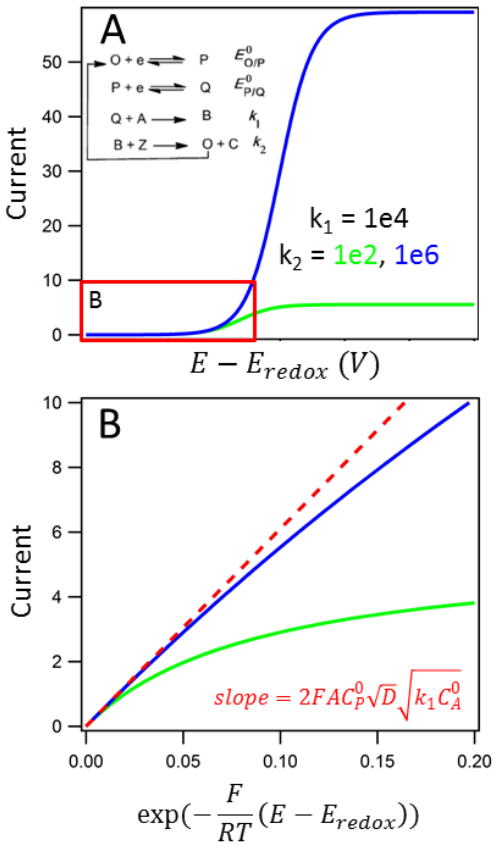

Figure 1.4. A) CV response for the *EECC* case with no substrate depletion in the case that k_2 is rate limiting (green) and the case that k_1 is rate limiting (blue). B) FOWA analysis reveals that the linear region corresponds to k_1 regardless of the rate determining step.

1.4 Stopped-Flow Rapid Mixing Coupled with Optical Spectroscopy

Stopped-flow spectroscopy is a powerful tool for extracting kinetic information and has been used to examine PCET in various systems.[45–48] Stopped-flow has been applied to the study of both catalytic cycles and elementary reaction steps where the reaction is accompanied by clear spectral changes. In a typical stopped-flow experiment, the contents of two syringes are rapidly mixed and the absorbance of the system recorded over time, either as full spectra at designated time delays or as single-wavelength kinetics traces (absorbance vs. time). A general-purpose UV-vis absorption spectrometer may be used in cases where reaction kinetics are sufficiently slow such that adequate mixing can occur using simple stirring.[49]

Stopped-flow methods are amenable to monitoring the reaction between many reagent types or even combinations of reagents. For PCET studies these may be chemical reductants, oxidants, hydride donors, acid, or base, for example. Once the two solutions have been rapidly mixed, the absorbance is recorded as a function of time. When monitoring a single elementary step, pseudo-first order conditions are often employed, enabling the reaction kinetics to be fit to a single exponential to extract an observed rate constant k_{obs}. For complex reactions, the kinetics traces can be fit using a kinetics model based on a series of differential equations describing the concentrations of each reactant, intermediate and product as a function of time. Obtaining rate constants through stopped-flow measurements has been shown to corroborate electrochemically derived rate constants.[42,45,46]

CHAPTER 2. Potential-Dependent Electrocatalytic Pathways: Controlling Reactivity with pK_a for Mechanistic Investigations of a Nickel-Based Hydrogen Evolution Catalyst

2.1. Introduction

With the search for sustainable energy becoming increasingly imperative, many researchers have turned their focus to molecular electrocatalysis to evaluate methods by which fuel production can be driven by renewable energy sources. Several reactions have been targeted in this effort, including water oxidation, hydrogen evolution, oxygen reduction and carbon dioxide reduction.[13,50–53] The simplest of these reactions is hydrogen formation, as it is just a two proton–two electron process (Eq. 2.1), but even this has proven difficult to mediate efficiently with transition metal-based catalysts.

The $[Ni(P_2^R N_2^{R'})_2]^{2+}$ class of molecules, which can mediate both proton reduction and hydrogen oxidation, have played an important role in advancing the field of molecular hydrogen evolution catalysts thus far.[5,33,50,54–60] In these complexes, $P_2^R N_2^{R'}$ refers to a generic ligand set of the form 1,5-R'-3,7-R-1,5-diaza-3,7-diphosphacyclooctane which contains two coordinating phosphines and two non-coordinating amines that are postulated to promote proton shuttling to and from the metal center. Studies of the role of the pendant amines and ligand electronics for these molecules has given meaningful insight into structure-activity

relationships and the role of the secondary coordination sphere.[55,61–64] This understanding has already guided the design of increasingly efficient and fast hydrogen evolving catalysts.[25,33,55,57]

$$2H^+ + 2e^- \rightleftharpoons H_2 \qquad (Eq.2.1)$$

In addition to the synthetic preparation of these catalysts and the quantification of their catalytic activity, it is of significant interest to understand the mechanisms by which hydrogen is evolved and to quantify the rate constants associated with the elementary steps. The catalytic reduction of protons to dihydrogen by a transition metal complex can occur through various mechanisms that differ by the sequence of the electron transfer steps (reduction of the catalyst or intermediates, denoted *E*) and the homogeneous chemical steps (protonation steps, denoted *C*). Several possible pathways for hydrogen evolution and their corresponding electrochemical analyses have been recently outlined by Costentin and Savéant.[44] By considering the individual elementary steps, one can envision perturbing the pathway of hydrogen evolution by varying parameters such as the strength of the acid employed and the applied potential. The $[Ni(P_2^R N_2^{R'})_2]^{2+}$class of molecules is an excellent example of this tunable reactivity. The $Ni^{II/I}$ and $Ni^{I/0}$ redox couples are generally both reversible and tend to be spaced relatively close together (10-500 mV) depending upon the R and R′ substituents.[56] As such, more than one mechanism is viable, including an *ECEC* pathway, whereby the first protonation follows reduction of the Ni^{II} complex to Ni^{I}, as well as an *EECC* process where the first protonation follows reduction of the catalyst to Ni^0 (Scheme 2.1).[60] The dominant pathway will depend on the relative rates of protonation for Ni^{I} vs. Ni^0 and the separation of the $Ni^{II/I}$ and $Ni^{I/0}$ redox couples. A recent study of a $[Ni(P_2^R N_2^{R'})_2]^{2+}$ successor, $[Ni(P_2^{Ph} N^{C_6H_4Br})_2]^{2+}$($P_2^{Ph} N^{C_6H_4Br}$

= 1-*para*-bromophenyl-3,7-triphenyl-1-aza-3,7-diphosphacycloheptane), utilizing [(DMF)H][OTf] as the proton source suggested that indeed these pathways operate in parallel.[65] Further, Raugei and coworkers recently revealed that for $[Ni(P_2^{Ph}N_2^{Ph})_2(CH_3CN)][BF_4]_2$ (Figure 2.1), the *ECEC* and *EECC* pathways also operate in parallel.[60] In this report, it was predicted that if a proton source with the appropriate pK_a is used, the *EECC* pathway can be selectively promoted as the dominant operating pathway. In this work, we report that through judicious choice of acid, reactivity can indeed be tuned to promote the *EECC* pathway, allowing us to examine the reaction mechanism in the absence of competing phenomenon. Through a combination of electrochemical analysis and spectroscopy, rate constants for the elementary steps of this reaction pathway were determined and an off-cycle intermediate was shown to limit the overall rate of catalytic turnover.

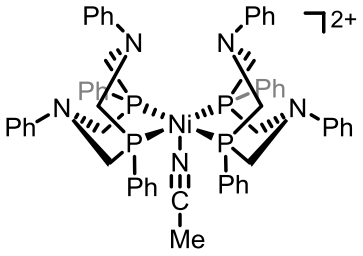

Figure 2.1. Structure of $[Ni(P_2^{Ph}N_2^{Ph})_2(CH_3CN)]^{2+}$.

Scheme 2.1. Proposed catalytic cycle highlighting both the *ECEC* and *EECC* pathways. The *EECC* pathway—the focus of this work—is highlighted. Specific elementary steps of interest are marked with their corresponding rate constants. Some steps expected to be of importance to the overall catalytic cycle, including those regarding exo protonation of Ni^{I} species, have been removed for clarity.[66]

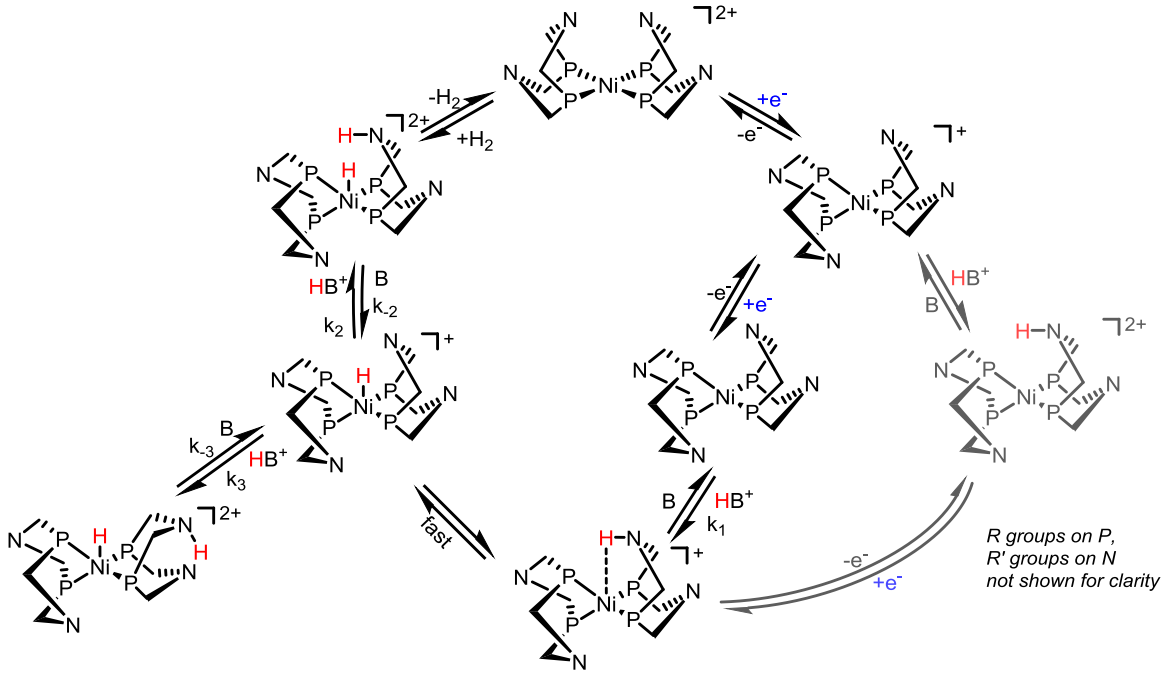

2.2. Results

2.2.1. Electrocatalytic Response with Anilinium.

The cyclic voltammogram (CV) of the $[Ni(P_2^{Ph}N_2^{Ph})_2]^{2+}$ complex exhibits two reversible, one-electron reduction waves, corresponding to the $Ni^{II/I}$ and $Ni^{I/0}$ couples, separated by 200 mV in acetonitrile (–0.83 V and –1.03 V, all values reported versus $Fc^{+/0}$ couple, Appendix A.1).[61] In a 1:1 dimethylformamidium:dimethylformamide (pK_a = 6.1)[67] acetonitrile solution, a large, yet non-ideal (non-sigmoidal) catalytic response corresponding to the catalytic production of hydrogen is obtained (Figure 2.2).[60]

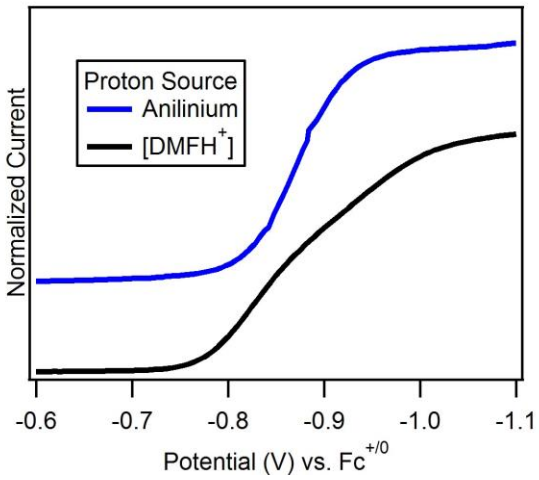

Figure 2.2. Electrocatalytic response obtained for $[Ni(P_2^{Ph}N_2^{Ph})_2]^{2+}$ (1 mM) with 1:1 [(DMF)H][BF_4]:[DMF] (70 mM, black) and with anilinium tetrafluoroborate (0.5 M, blue). The catalytic response with anilinium is a classical catalytic sigmoid while with $(DMF)H^+$, the catalytic response has initial sigmoidal character and then changes slope ca. 150 mV prior to reaching a plateau. Voltammograms recorded at 100 mV/s in 0.2 M [NBu_4][PF_6] CH_3CN solutions.

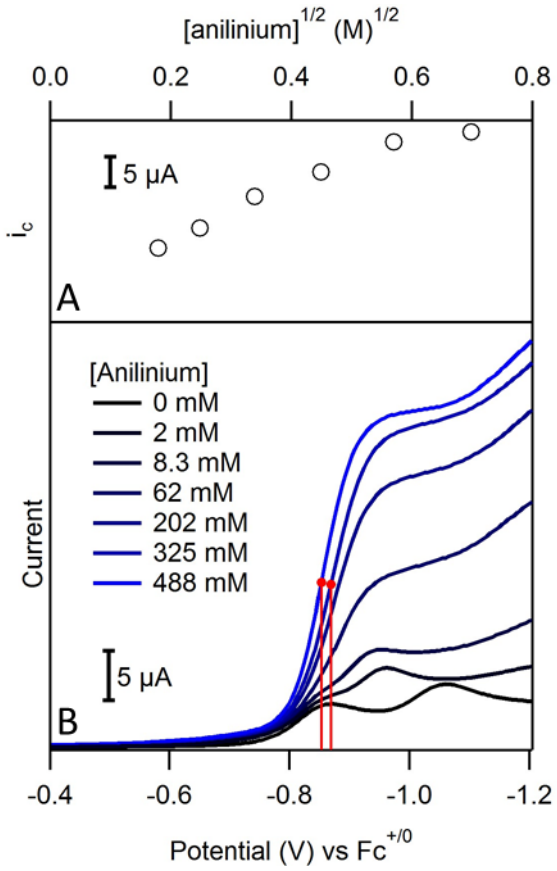

Figure 2.3. Anilinium concentration dependence for electrocatalysis. A) The plateau current (i_c) plotted against the square root of the anilinium concentration, exhibits the linear dependence anticipated for a reaction that is first order in acid up to ca. 360 mM anilinium. At higher concentrations, the current levels off. B) Linear sweep voltammograms of 0.9 mM $[Ni(P_2^{Ph}N_2^{Ph})_2]^{2+}$ with varied concentrations of anilinium tetrafluoroborate. For the two most concentrated solutions, $E_{cat/2}$ is marked to highlight the shift in potential. Voltammograms recorded at 100 mV/s in 0.2 M $[NBu_4][PF_6]$ CH_3CN solutions.

By contrast, a more ideal sigmoidal catalytic response is obtained with anilinium ($pK_a = 10.6$)[67] as the proton source. When examining the voltammetric wave over a range of anilinium concentrations (Figure 2.3), three key observations are made.

(1) At low acid concentrations, (2 mM and 4.1 mM) the $Ni^{II/I}$ wave remains unaltered, but a significant shift (ca. 100 mV) in the peak corresponding to the $Ni^{I/0}$ couple is observed. This peak continues to shift as the concentration of acid is increased. (2) As the concentration of acid is increased, the catalytic current deviates from an initial first-order response in acid[68] and

approaches a zone where the catalytic plateau current is acid-independent. (3) Even after the current plateau becomes zero-order in acid, the half-wave potential for the catalytic sigmoid ($E_{cat/2}$) continues to shift positive with acid concentration.[68] Analysis of these three features provides key details of the mechanism and kinetics associated with catalytic hydrogen production.

2.2.2. Protonation of a Ni^0 species to form Ni^{II}-H.

Upon the addition of 1 equiv. anilinium tetrafluoroborate to a solution of $[Ni(P_2^{Ph}N_2^{Ph})_2]^{2+}$, a new oxidation feature is observed via CV at approximately –0.4 V (Figure 2.4). This stoichiometric acid addition does not lead to catalytic turnover, but was anticipated to promote formation of the Ni^{II}-H species, $[HNi(P_2^{Ph}N_2^{Ph})_2]^{+}$, upon protonation of the Ni^0 species formed electrochemically. To determine if the new peak observed corresponds to the oxidation of the Ni^{II}-H, the hydride complex was synthesized and evaluated independently.

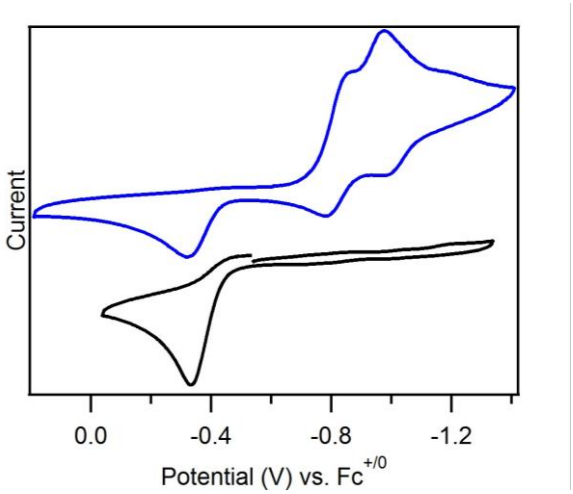

Figure 2.4. Cyclic voltammograms of 1.5 mM $[Ni(P_2^{Ph}N_2^{Ph})_2]^{2+}$ and approximately 1 equivalent of anilinium (blue) compared with the cyclic voltammogram of 0.6 mM of the independently synthesized Ni^{II}-hydride (black) in CH_3CN. The new oxidation observed at –

0.4 V for $[Ni(P_2^{Ph}N_2^{Ph})_2]^{2+}$ in the presence of acid matches that of the isolated hydride. Voltammograms recorded at 100 mV/s in 0.2 M $[NBu_4][PF_6]$ CH_3CN solutions.

$[HNi(P_2^{Ph}N_2^{Ph})_2]^{+}$ was prepared by addition of 1 equiv. of sodium borohydride to $[Ni(P_2^{Ph}N_2^{Ph})_2]^{2+}$ in acetonitrile and is stable over a period of several days, provided it is kept under an inert atmosphere. The hydride peak in the ^{1}H NMR is observed as a quintet ($^2J_{PH}$ = 30.5 Hz) at –8.1 ppm,[61] consistent with related nickel(II)-hydride complexes, and the $^{31}P\{^1H\}$ singlet shifts from 6.6 to 17.4 ppm.[69–71] The CV of the synthesized hydride shows no redox activity at the $Ni^{II/I}$ and $Ni^{I/0}$ redox potentials of $[Ni(P_2^{Ph}N_2^{Ph})_2]^{2+}$, but instead an irreversible oxidation is observed at approximately –0.4 V, confirming the assignment of the new oxidation wave observed in the CV of $[Ni(P_2^{Ph}N_2^{Ph})_2]^{2+}$ and 1 equiv. acid (Figure 2.4). Increasing the scan rate did not produce any noticeable increase in reversibility up to 25 V/s.

Peak Shift Analysis. The rate constant for the protonation of the Ni^0 species $[Ni(P_2^{Ph}N_2^{Ph})_2]$ was first determined by analyzing the peak shift of the $Ni^{I/0}$ redox wave as a function of acid concentration. While the $Ni^{I/0}$ wave quickly becomes buried under the catalytic wave as the acid concentration is increased, catalytic turnover is thwarted upon the addition of excess aniline (1 M), allowing the kinetics of protonation to be isolated. The peak shift ($E_P - E_{1/2}$) of the $Ni^{I/0}$ peak was recorded as a function of aniline concentration (0–306 mM) (Figure 2.5). While the ratio of aniline base to anilinium changes dramatically over the course of this titration, the peak location was shown to be unaffected by base concentration (Appendix A.2).

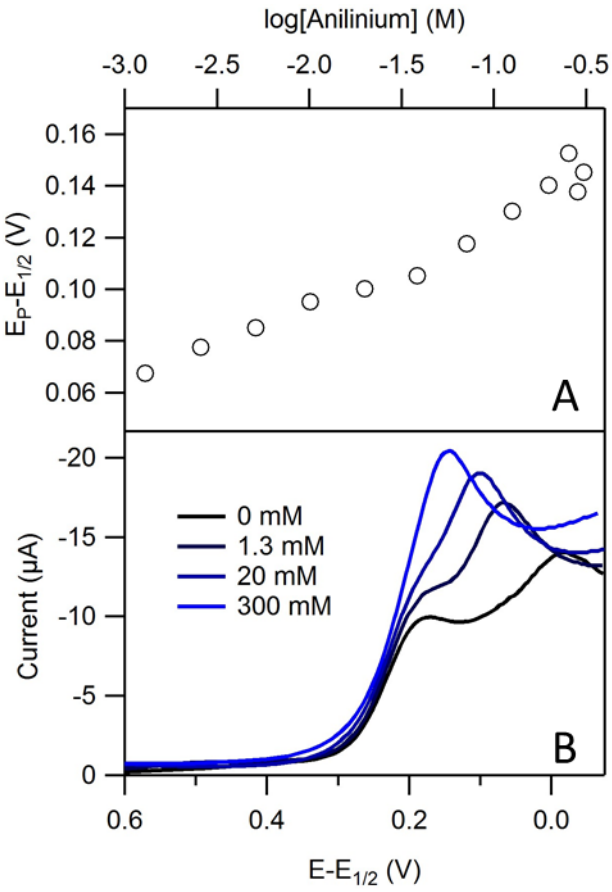

Figure 2.5. EC rate analysis of $[Ni(P_2^{Ph}N_2^{Ph})_2]^{2+}$. As a solution of 1 mM $[Ni(P_2^{Ph}N_2^{Ph})_2]^{2+}$ containing 1 M aniline is titrated with anilinium tetrafluoroborate, the peak location of the $Ni^{I/0}$ reduction shifts positively with concentration. A) Peak location at different concentrations of anilinium; the peak shifts 33 mV per decade indicating an EC mechanism and giving a rate constant for hydride formation of 1.2×10^6 M^{-1} s^{-1}. B) Linear sweep voltammograms at several concentrations of anilinium. Current is plotted versus ($E - E_{1/2}$), where $E_{1/2}$ corresponds to the reversible $Ni^{I/0}$ wave. Voltammograms recorded at 100 mV/s in 0.2 M $[NBu_4][PF_6]$ CH_3CN solutions.

For an electrochemical *EC* mechanism, in which a Nernstian electron transfer is followed by an irreversible chemical step, the magnitude of the peak shift can be related to the rate constant for protonation under pseudo-first-order conditions per Eq. 2.2, where F is Faraday's constant, $[BH^+]$ is the concentration of anilinium, k_1 is the second order rate constant for protonation, υ is the scan rate, T is temperature, and R is the ideal gas constant.[28,72]

$$E_P = E_{1/2} - \frac{RT}{F}(.78) + \frac{RT}{2F}\ln\left(\frac{k_1[BH^+]RT}{F\upsilon}\right) \qquad (Eq.2.2)$$

The relationship observed between peak shift and acid concentration (Figure 2.5) is consistent with Eq. 2.2, which predicts a slope of 30 mV/decade (observed slope is 33 mV/decade) and provides a rate constant for protonation of 1.2 x 10^6 $M^{-1}s^{-1}$.

Foot-of-the-Wave Analysis. As was mentioned previously, in Figure 2.3, we observe that even after the current plateau loses its first order dependence on anilinium concentration, the value of $E_{cat/2}$ continues to shift positively. This behavior is anticipated for *EECC* scenarios in which the first step of the catalytic cycle is not rate limiting; evaluation of the rate constant for this first step is possible through foot-of-the-wave analysis (FOWA).[44] This analysis offers many advantages over other methods to extract rate data; for instance, the kinetics can be analyzed at the earliest time-points in the experiment when only a small fraction of the catalyst is active so that inhibiting factors such as substrate depletion or product inhibition will have a minimal effect on the measurement.[34,44,46,68,73] Use of FOWA requires that several assumptions be made; the reaction must not be limited by heterogeneous electron transfer steps, substrate must be present in sufficient excess such that its depletion is not a factor at the foot of the wave, the catalyst does not degrade significantly on the timescale of the experiment, and in the case of a multi-step reaction, the mechanism should be established prior to analysis.[34,44,46] For multi-step catalytic reactions following an *EECC*-type mechanism, application of FOWA provides the pseudo-first order rate constant for the first chemical step ($k_{FOWA} = k_1[BH^+]$) in the catalytic cycle via Eq. 2.3, where i_c refers to the current at potential E in the catalytic wave, D_{cat} is the

diffusion coefficient of the catalyst, C_{cat} is the concentration of the catalyst, and A is the area of the working electrode.[44,68]

$$i_c = 2FAC_{cat}\sqrt{k_{FOWA}D_{cat}}\exp\left[-\frac{F}{RT}(E - E^0)\right] \qquad (Eq.\,2.3)$$

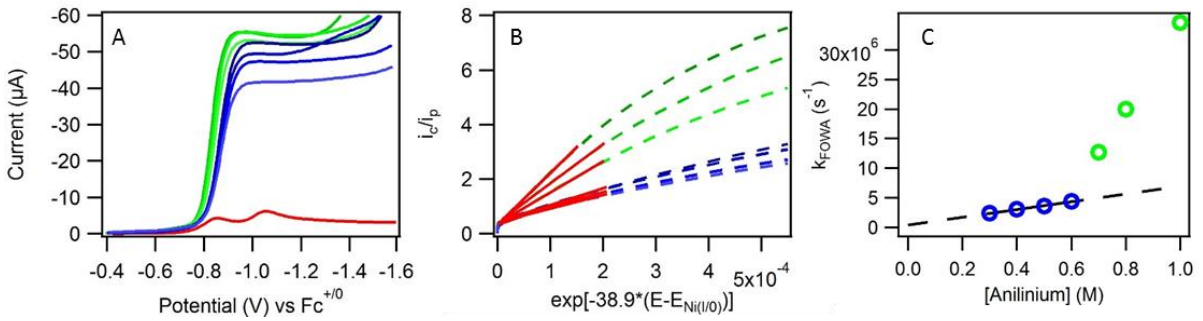

Figure 2.6. FOWA of $[Ni(P_2^{Ph}N_2^{Ph})_2]^{2+}$. A) Cathodic sweeps of catalytic cyclic voltammograms with 1 mM $[Ni(P_2^{Ph}N_2^{Ph})_2]^{2+}$ and 0–1 M anilinium tetrafluoroborate. B) For FOWA, the ratio of catalytic current to the non-catalytic peak current of the $Ni^{II/I}$ reduction is plotted vs. $e^{-\frac{F}{RT}*(E-E_{Ni^{I/0}})}$ (F/RT = 38.9). The linear portion of the FOW plots were fit (red lines). C) The pseudo-first order rate constants obtained from the FOWA analysis. Rate constants for the 0.3 – 0.6 M anilinium datasets are shown as the blue data points and are fit to a line with a slope of 6.5 x 10^6, while those at higher concentrations (green) fit to a line with a much steeper slope that does not intercept the origin, signifying a change in mechanism, likely a shift from an EECC to ECEC. Voltammograms recorded at 50 mV/s in 0.2 M $[NBu_4][PF_6]$ CH_3CN solutions.

As the catalytic wave that originates for the $Ni^{I/0}$ couple overtakes the $Ni^{II/I}$ potential, the anticipated accuracy of FOWA analysis with an underlying redox wave was first investigated. It was shown to cause tolerable error in the calculation (Appendix A.3). After validating the extension of FOWA to our data, analysis of a series of voltammograms recorded with anilinium concentrations between 0.3 and 1 M (Figure 2.6A) was carried out to determine the rate constant for protonation of the Ni^0 species. The resulting voltammograms were then converted to the FOWA plot according to Eq. 2.4 (Eq. 2.3 divided by the Randles-Sevcik Equation), where *n* represents the number of electrons in the wave corresponding to i_p (the peak current

of the $Ni^{II/I}$ reduction wave in the absence of catalyst). The slope of the initial linear region (m) was then determined (Figure 2.6B) and the observed rate constant (k_{FOWA}) was calculated using Eq. 2.5.

$$\frac{i_c}{i_p} = \frac{0.7179}{n}\sqrt{\frac{k_{FOWA}}{n\upsilon}}\exp\left[-\frac{F}{RT}\left(E - E^0_{I/0}\right)\right] \qquad (Eq.\,2.4)$$

$$k_{FOWA} = \left(\frac{m}{3.212}\right)^2 \qquad (Eq\ 2.5)$$

A plot of k_{FOWA} vs. concentration of anilinium (Figure 2.6C) reveals two distinct regions. At low concentrations of anilinium (0.3–0.6 M), linear regression provides a value for k_1 of 6.5 x 10^6 M^{-1} s^{-1}, while at higher acid concentrations, a steeper dependence is observed and the linear fit does not pass through the origin. This change in slope suggests a change in mechanism, likely from *EECC* at lower concentrations to *ECEC* at higher concentrations (see below). In this scenario, FOWA can be performed using the reduction potential for $Ni^{II/I}$, which results in a rate constant of 10 M^{-1} s^{-1} (Figure 2.7).

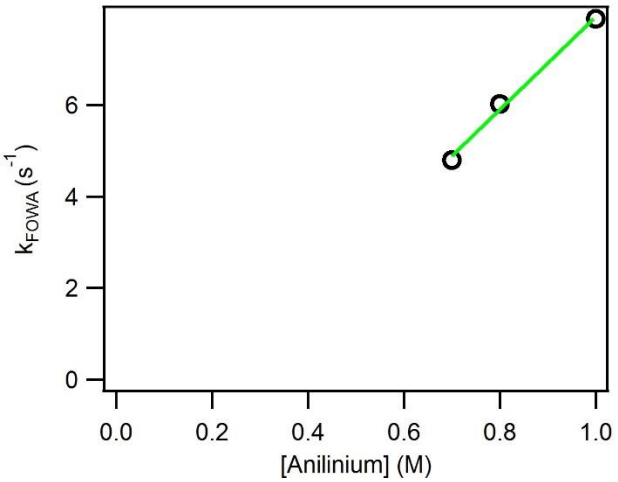

Figure 2.7. Rate constant determined from FOWA vs. $Ni^{II/I}$. The data suggest that the first step in the catalytic cycle at the foot of the wave is actually protonation of Ni^I at high acid concentrations (0.7–1 M anilinium). Using the $Ni^{II/I}$ redox potential instead of the $Ni^{I/0}$ results in the k_{FOWA} values shown here. Fitting a line to this data gives a rate constant of 10 $M^{-1}s^{-1}$ for protonation of Ni^I by anilinium.

2.2.3. Reactivity of Ni^{II}-H

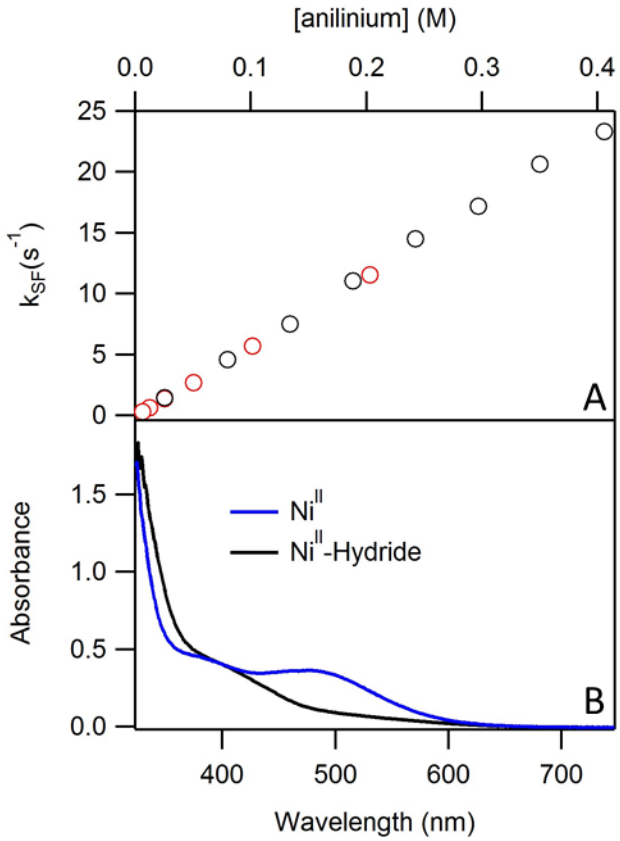

Figure 2.8. Stopped-flow results for $[HNi(P_2^{Ph}N_2^{Ph})_2]^+$. A) Observed pseudo-first order rate constant k_{SF} determined from stopped-flow kinetics studies vs. anilinium concentration. The linear relationship provides a first order rate constant of 58 $M^{-1}s^{-1}$. Red and black markers indicate data obtained from separate experiments. Experimental conditions: 0.2 mM $[HNi(P_2^{Ph}N_2^{Ph})_2]^+$ B) Absorbance spectra of 0.36 mM $[Ni(P_2^{Ph}N_2^{Ph})_2]^{2+}$ and $[HNi(P_2^{Ph}N_2^{Ph})_2]^+$ in CH_3CN.

Stopped-flow kinetics analysis. Reaction of the isolated Ni^{II}-H complex with anilinium to generate $[Ni(P_2^{Ph}N_2^{Ph})_2]^{2+}$ was monitored using stopped-flow spectroscopy. As the bright yellow Ni^{II}-H has substantially distinct optical properties from the dark red $[Ni(P_2^{Ph}N_2^{Ph})_2]^{2+}$ complex (Figure 2.8B), reaction kinetics were evaluated by optically monitoring the appearance of $[Ni(P_2^{Ph}N_2^{Ph})_2]^{2+}$ (λ_{obs} = 500 nm) as a function of time (ms–s). The kinetics traces recorded as a function of anilinium concentration (Appendix A.4) under

pseudo-first order conditions ([anilinum]>>[Ni^{II}-H]) were fit with single exponential kinetics. The first-order rate constant k_{SF} is linearly dependent on anilinium concentration (Figure 2.8, top) giving a second order rate constant of 58 M^{-1} s^{-1} for the conversion of $[HNi(P_2^{Ph}N_2^{Ph})_2]^+$ to $[Ni(P_2^{Ph}N_2^{Ph})_2]^{2+}$. On longer timescales (ca. 1–150 s), continued growth of $[Ni(P_2^{Ph}N_2^{Ph})_2]^{2+}$ absorption was observed, suggesting a second process was necessery for full conversion. This second process could not be fit to single exponential kinetics, suggesting the involvement of an intermediate species generated during the reaction (Appendix A.4). At all concentrations of anilinium, the short timescale kinetics accounted for conversion of ca. 88% of $[HNi(P_2^{Ph}N_2^{Ph})_2]^+$ to $[Ni(P_2^{Ph}N_2^{Ph})_2]^{2+}$ (Appendix A.4). In contrast to the protonation of the Ni^0 species, addition of aniline to the reaction solution causes the observed rate of the fast timescale reaction to slow significantly. Additionally, the slow kinetics regime is substantially elongated with base; after the initial fast kinetics regime, the absorption reaches a plateau and then a slow conversion (~25 minutes) to $[Ni(P_2^{Ph}N_2^{Ph})_2]^{2+}$proceeds (Figure 2.9). We attribute this to the reversibility of hydrogen formation in the presence of excess base (see below).

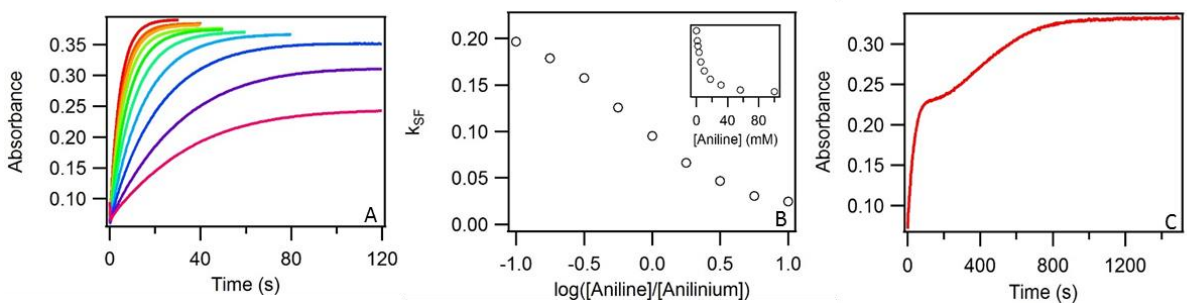

Figure 2.9. Influence of Added Base on Stopped-Flow Reaction Kinetics. A) Stopped-flow kinetics with 0.2 mM $[HNi(P_2^{Ph}N_2^{Ph})_2]^+$, 5 mM anilinium and 0.5 (red) to 50 mM (magenta) aniline recorded at 500 nm. B) The pseudo-first order rate constant k_{SF} vs. the log of the aniline:anilinium ratio. Inset: Pseudo-first order rate constant k_{SF} plotted vs. the aniline concentration. C) In the presence of 50 mM base, the slow kinetics regime proceeds over a significantly longer period of time (25 min) than in the absence of base (< 2 min).

Kinetics details obtained from electrocatalytic plateau currents. Catalytic voltammograms were recorded over a range of concentrations of anilinium. The overall rate constant for catalysis under steady-state electrocatalytic conditions was determined from the current plateau. For an *EECC* reaction, the plateau current (i_{pl}) is a function of the overall rate constant for catalysis (k_{pl}) as defined by Eq. 2.6.[44] The rate constant k_{pl} reflects the rate limiting chemical step, or a composite of elementary steps, for electrocatalysis (see below). Dividing i_{pl} by i_p (peak current of the $Ni^{II/I}$ wave in the absence of catalysis) gives Eq. 2.7. Rearrangement of Eq. 2.7 provides an expression for k_{pl} (n = 1 and υ = 0.05 V/s, Eq. 2.8, Appendix A.5). The overall rate constant plotted versus the anilinium concentration (Figure 2.10) reveals a first-order dependence on acid at low acid concentrations, but k_{pl} approaches an acid-independent region as the concentration is increased, consistent with previous reports.[61,62,74,75]

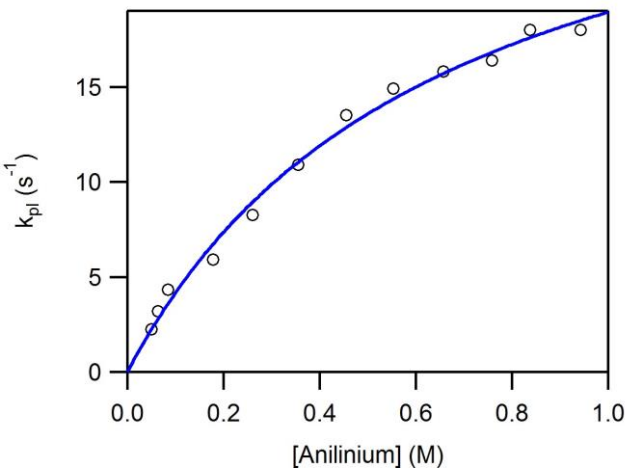

Figure 2.10. The observed rate constants obtained from the current plateau of catalytic voltammograms of 0.4 mM (calculated using Eq. 2.4), vs. anilinium concentration. Data points are fit with $k_{pl} = \frac{k_2 k_{obs,-3}[BH]}{k_3[BH]+k_{obs,-3}}$ with k_2 = 48 M^{-1} s^{-1}, k_3 = 12 $M^{-1}s^{-1}$ and $k_{obs,-3}$ = 8 s^{-1} (rate constants defined in Scheme 2.1 and discussed below, derivation of Eq. 2.8 can be found in Appendix A.5). Voltammograms recorded at 50 mV/s in 0.2 M $[NBu_4][PF_6]$ CH_3CN solutions.

$$i_{pl} = 2FAC_{cat}\sqrt{k_{pl}D_{cat}} \qquad (Eq.\,2.6)$$

$$\frac{i_{pl}}{i_p} = \frac{4.48}{n}\sqrt{\frac{RTk_{pl}}{nFv}} \qquad (Eq.\,2.7)$$

$$k_{pl} = \left(\frac{i_{pl}/i_p}{3.212}\right)^2 \qquad (Eq.\,2.8)$$

Ni^{II}-H reactivity in the presence of excess aniline examined via NMR. The long timescale reactivity of Ni^{II}-H observed in the stopped-flow experiments suggests the presence of a reaction intermediate; to probe this hypothesis, the reaction of Ni^{II}-H with 1 equiv. anilinium and 10 equiv. of aniline was monitored by $^{31}P\{^{1}H\}$ NMR spectroscopy. With this large excess of base employed for these experiments, we obtained an equilibrium between the reactants, intermediates and products as hydrogen formation is reversible in the presence of excess base (Figure 2.11).[61]

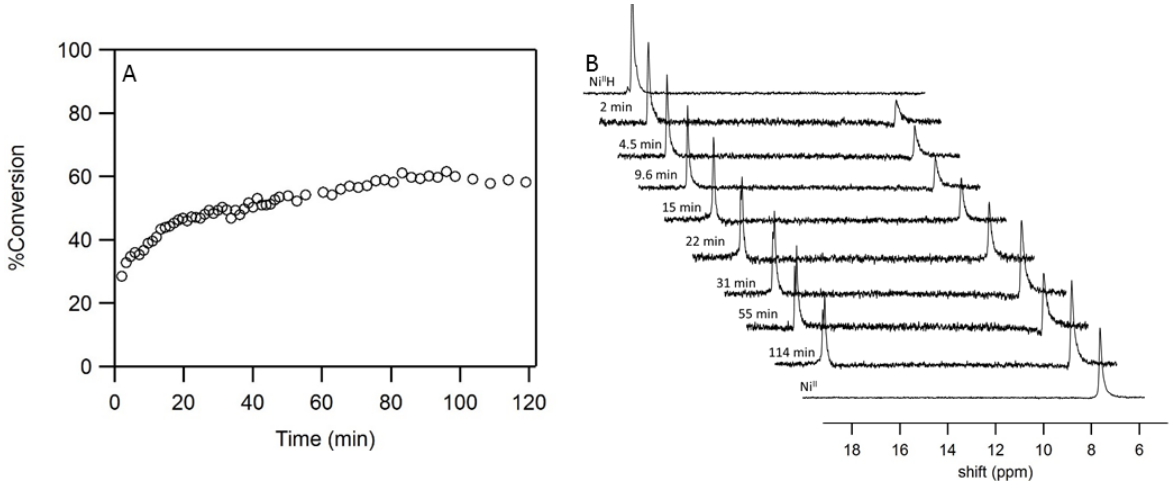

Figure 2.11. Equilibrium of Ni^{II}-H and Ni^{II} in the Presence of Excess Base, Monitored by NMR. A solution of 2.5 mM $[HNi(P_2^{Ph}N_2^{Ph})_2]^{1+}$, 2.5 mM anilinium tetrafluoroborate and 25 mM aniline was prepared and immediately examined by ^{31}P NMR. A) The estimated conversion of $[HNi(P_2^{Ph}N_2^{Ph})_2]^{+}$to $[Ni(P_2^{Ph}N_2^{Ph})_2]^{2+}$ based on the relative integrations of the peak at 17.4 ppm. B) ^{31}P NMR spectra showing the equilibration of the two species. The top spectra is of $[HNi(P_2^{Ph}N_2^{Ph})_2]^{+}$ alone and the bottom spectra is $[Ni(P_2^{Ph}N_2^{Ph})_2]^{2+}$ alone. The hydride peak appears to split into a doublet, but this is attributed to poor decoupling of the hydride.

Upon mixing, the singlet at 17.4 ppm corresponding to Ni^{II}-H decreases in intensity and a new resonance appears at 6.6 corresponding to $[Ni(P_2^{Ph}N_2^{Ph})_2]^{2+}$. Assuming no degradation, integration of the peaks after equilibrium is established (6 hours) shows that $[Ni(P_2^{Ph}N_2^{Ph})_2]^{2+}$ accounts for 63% of the total nickel concentration. No additional species were identified by NMR, suggesting that the differences observed in the stopped-flow experiments (discussed above) upon the addition of excess base does not result from the creation of more of the anticipated intermediate.

2.3. Discussion

2.3.1. Isolation of the *EECC* Mechanism.

Work by Raugei and coworkers has shown that with relatively strong acids like $(DMF)H^+$, the Ni^I species formed upon reduction of $[Ni(P_2^{Ph}N_2^{Ph})_2]^{2+}$ is protonated, promoting catalysis via an *ECEC* pathway at potentials near the $Ni^{II/I}$ reduction potential. As the potential approaches the $Ni^{I/0}$ wave, rapid electron transfer to generate Ni^0 outcompetes protonation of the Ni^I species and the *EECC* mechanism becomes competitive.[60,65] Computational studies suggest that the pK_a values of $[Ni(P_2^{Ph}N_2^{Ph})_2H]^{2+}$ and $[Ni(P_2^{Ph}N_2^{Ph})_2H]^{+}$ differ by approximately 8 pK_a units, indicating that stronger acids are necessary to protonate the Ni^I species than the Ni^0 complex.[33] As such, it was reasoned that protonation of the Ni^I species could be averted by raising the pK_a of the acid employed for catalysis, allowing the more potential-intensive *EECC* mechanism to be isolated. Indeed, dramatic differences in catalytic response are observed for anilinium vs. $(DMF)H^+$, indicating that the reaction pathway for hydrogen generation can be controlled by choice of proton source (Fig. 2). The catalytic current response observed upon the addition of low concentrations of

anilinium further support the assertion that catalysis proceeds via an *EECC* mechanism with weak acids, as the catalytic wave grows off the $Ni^{I/0}$ reduction wave (Fig. 3).

2.3.2. Kinetic Analysis of Protonation.

In the *EECC* reaction pathway presented in Scheme 2.1, the $[Ni(P_2^{Ph}N_2^{Ph})_2]^0$ complex formed upon two sequential electrochemical reductions of the Ni^{II} species is protonated to produce the Ni^{II}-H species $[HNi(P_2^{Ph}N_2^{Ph})_2]^+$. Identification of this reaction intermediate is supported by comparison of the voltammetric features observed for $[Ni(P_2^{Ph}N_2^{Ph})_2]^{2+}$ with substoichiometric acid to those of the independently synthesized hydride complex (Fig. 4). Two methods were utilized to obtain the rate constant for protonation of the Ni^0 species—*EC* peak shift analysis and FOWA. The former afforded a rate constant of 1.2 x 10^6 M^{-1} s^{-1}, similar to the rate constant of 6.5 x 10^6 M^{-1} s^{-1} determined via FOWA at low acid concentration (0.3–0.6 M). We anticipate the small difference in rate constants may be due differing effects of electron transfer kinetics on the two analyses. Notably, at higher acid concentrations (> 0.6 M), the observed first order rate constants calculated via FOWA are substantially higher than those determined at low acid concentrations. This observation is consistent with the assertion that two parallel mechanisms are operating. While protonation of the Ni^I species is not kinetically competitive at low anilinium concentrations, these data suggest that protonation of the singly reduced catalyst can compete at high concentration of this weak acid. When FOWA is performed at these higher acid concentrations assuming an *ECEC* pathway, a rate constant of 10 $M^{-1}s^{-1}$ is estimated for the protonation of Ni^I by anilinium (Figure 2.7). While protonation of the Ni^0 species by anilinium is five orders of magnitude faster than the protonation of Ni^I, the concentration of Ni^I is much higher than Ni^0 at the potentials near the foot of the wave and thus protonation of the former can compete at these potentials. For comparison, Wiedner *et al.*

measured a rate constant of 3 x 10^5 M^{-1} s^{-1} for protonation of Ni^I with the much stronger proton source $(DMF)H^+$ by analyzing the current-potential relationship of the catalytic waves.[76] Artero and Savéant have previously estimated a similar value of k_1 for protonation by $(DMF)H^+$ (7.5 x 10^4 M^{-1} s^{-1}) via analysis of the plateau current and the $E_{1/2}$ value.[77]

2.3.3. Formation of an Off-Cycle Intermediate.

Because protonation of the Ni^0 species occurs at a sufficiently rapid rate, we expected that a subsequent elementary step, such as protonation of Ni^{II}-H or H_2 release would be rate limiting for catalytic turnover. As such, we anticipated that stopped-flow kinetics—which monitored the reformation of Ni^{II} upon protonation of Ni^{II}-H—and the electrochemical current plateau studies should yield the same observed rate constants because they both measure the conversion of $[HNi(P_2^{Ph}N_2^{Ph})_2]^+$ to $[Ni(P_2^{Ph}N_2^{Ph})_2]^{2+}$, provided the same mechanism is followed in each experiment. As is readily observed in Figures 2.8 and 2.10, the kinetics of the two experiments differ dramatically. For the cyclic voltammetry experiments, the observed rate constant is first order in acid at low acid concentrations, but saturates at higher acid concentrations with an overall rate constant of approximately 20 s^{-1}. By contrast, the stopped-flow kinetics remain first order in acid at all concentrations tested, even when observed rate constants exceed 20 s^{-1}. These differences can be interpreted by considering the various accessible protonation modes of $[HNi(P_2^RN_2^{R'})_2]^{2+}$ complexes which have been revealed through extensive experimental and computational study.[33,66,74,78–82] Protonation of Ni^{II}-H can occur in an endo or an exo mode (Figure 2.12). In the endo isomer, the pendant amine is protonated proximal to the metal center, while for the exo species the proton is 'pinched' between two amines.[66] Studies have suggested that exo isomer ($H_{exo}Ni^{II}H$) is catalytically inactive and the species must be deprotonated and reprotonated to form the endo isomer to re-

enter the catalytic cycle (Scheme 2.1).[40,80,83] The endo isomer ($H_{endo}Ni^{II}H$) is required for H_2 formation and catalytic turnover.

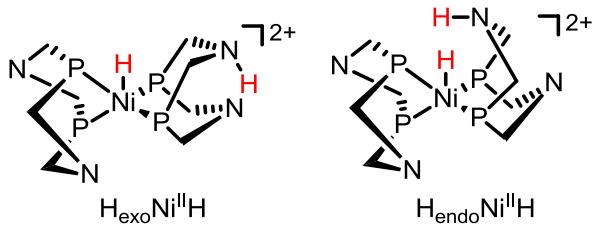

Figure 2.12. Endo versus exo protonation of $HNi\left(P_2^{Ph}N_2^{Ph}\right)_2$. Phenyl substituents on the phosphines and amines omitted for clarity.

With this in mind, we examined how the formation of the catalytically inactive $H_{exo}Ni^{II}H$ species—an off-cycle intermediate—would influence the observed kinetics in both the stopped-flow and cyclic voltammetry data in the proposed reaction cycle (Scheme 2.1). As detailed below, the production of Ni^{II} and H_2 upon reaction of the isolated Ni^{II}-H species with excess acid will follow pseudo-first-order kinetics in the fast kinetic regime—the observed rate constant (k_{SF}) varying linearly with acid concentration. By contrast, the observed rate constant obtained from the plateau current of catalytic cyclic voltammograms ($k_{overall}$) will initially be first order in acid but become acid-independent at larger concentrations of acid. This major difference arises because Ni^{II}-H and $H_{exo}Ni^{II}H$ reach an equilibrium under catalytic conditions (as experienced in the reaction layer of the voltammetry experiment), and their concentrations are at steady state (the observation of a well-defined current plateau in the catalytic voltammograms is indicative of steady-state conditions), while this is not the case when monitoring the direct reaction of the isolated $Ni^{II}H$ ($[HNi\left(P_2^{Ph}N_2^{Ph}\right)_2]^+$) with acid (as in the fast kinetic regime of the stopped-flow experiments).

The stopped-flow experiments carried out monitor the appearance of $[Ni(P_2^{Ph}N_2^{Ph})_2]^{2+}$ as a function of time. As proposed above, the Ni^{II} species is generated upon rapid release of H_2 from the $H_{endo}Ni^{II}H$, the latter formed by protonation of the $Ni^{II}H$.

$$Ni^{II}H + BH^+ \xrightarrow{k_2} H_{endo}Ni^{II}H + B$$

$$H_{endo}Ni^{II}H \xrightarrow{fast} Ni^{II} + H_2$$

Assuming release of H_2 from $H_{endo}Ni^{II}H$ is rapid,[64] the formation of Ni^{II} from $Ni^{II}H$ is governed by the protonation step, which is first order in both acid and $Ni^{II}H$. The change in concentration of the Ni^{II} species as a function of time can be described per Eq. 2.9.

$$\frac{d[Ni^{II}]}{dt} = k_2[Ni^{II}H][BH^+] \qquad (Eq. 2.9)$$

However, the reversible protonation of $Ni^{II}H$ to form $H_{exo}Ni^{II}H$ must also be accounted for, which affects the concentration of $Ni^{II}H$.

$$Ni^{II}H + BH^+ \xrightarrow{k_3} H_{exo}Ni^{II}H + B$$

$$H_{exo}Ni^{II}H + B \xrightarrow{k_{-3}} Ni^{II}H + BH^+$$

Consideration of the off-cycle intermediate in the kinetics analysis yields an observed rate constant under pseudo first order conditions ($[BH^+]>>[NiH]$) for the fast regime that is the sum of the rate constants for endo protonation (k_2) and exo protonation (k_3) times the acid concentration (Eq. 2.10).

$$k_{SF} = (k_2 + k_3)[BH^+] \qquad (Eq. 2.10)$$

Kinetics analysis of the catalytic voltammograms, by contrast, accounts for the steady-state concentrations of reaction intermediates generated under catalytic conditions. In this analysis, it is assumed that reduction of Ni^{II} to Ni^0 and subsequent protonation are both rapid; formation of Ni^{II} immediately results in the formation of $Ni^{II}H$.

$Ni^{II} + 2e^- + BH^+ \xrightarrow{fast} Ni^{II}H + B$

$Ni^{II}H + BH^+ \xrightarrow{k_2} H_{endo}Ni^{II}H + B$

$Ni^{II}H + BH^+ \xrightarrow{k_3} H_{exo}Ni^{II}H + B$

$H_{exo}Ni^{II}H + B \xrightarrow{k_{-3}} Ni^{II}H + BH^+$

$H_{endo}Ni^{II}H \xrightarrow{fast} Ni^{II} + H_2$

A series of differential equations can be derived to describe the change in concentrations of $Ni^{II}H$, $H_{exo}Ni^{II}H$ and H_2 as a function of time. Evaluating for the production of H_2 over time reveals an overall rate constant for catalysis that is dependent upon the rate constants for endo and exo protonation (k_2 and k_3) and the rate constant for deprotonation of $H_{exo}Ni^{II}H$ (k_{-3}). We thus determine that the rate constant k_{pl} determined from the catalytic CVs does not reflect a single rate-limiting step, rather reflects the composite of rate constants describing the reactivity of the Ni^{II}-H. Stated otherwise, the second *C* in the *EECC* reaction does not reflect a single elementary step, but is a composite of the kinetics of the second protonation, release of hydrogen, and formation/deprotonation of exo species. It must be noted that in order to

simplify the electrochemical analysis, the base dependence for deprotonation of $H_{exo}NiH$ was not included and is therefore represented in the equation as a first-order rate constant $k_{obs,-3}$. At low acid concentrations, k_{pl} is dependent on [BH^+], while at high acid concentration, $k_3[BH^+] >> k_{obs,-3}$ and the observed rate becomes acid independent.

$$k_{pl} = \frac{k_2 k_{obs,-3}[BH^+]}{k_3[BH^+] + k_{obs,-3}} \qquad (Eq. 2.11)$$

Equations 2.10 and 2.11 were applied to the stopped-flow and plateau current data, respectively, to determine rate constants k_2 and k_3. The relative values were obtained from stopped-flow by considering the total rate constant for protonation ($k_2 + k_3$, 58 M^{-1} s^{-1}, Figure 2.8) and the extent of conversion to Ni^{II} in the fast kinetics (Appendix A.4). The observed 88% conversion to Ni^{II} in the fast kinetics predicts that k_2 is 7.3 times faster than k_3, giving a value for k_2 of 51 M^{-1} s^{-1} and a value for k_3 of 7 M^{-1} s^{-1}. Fitting the electrocatalytic plateau current (k_{pl} vs. [anilinium], Figure 2.10) to Eq. 2.11 provided values of 48 M^{-1} s^{-1} for k_2 and 12 M^{-1} s^{-1} for k_3, similar to those obtained from stopped-flow analysis. The electrochemical data also gives a value for $k_{obs,-3}$ of 8 s^{-1}, but as noted above, this value holds little meaning as it should have a dependence on base concentration.

The second kinetic regime observed in the stopped-flow experiments (in the absence of excess base, see below), which leads to the complete conversion of $[HNi(P_2^{Ph}N_2^{Ph})_2]^{1+}$ to $[Ni(P_2^{Ph}N_2^{Ph})_2]^{2+}$, is congruent with the idea that the $H_{exo}Ni^{II}H$ intermediate must be converted back to an on-cycle intermediate before turnover. Attempts to spectroscopically detect this intermediate were not successful; both manual inspection and singular value decomposition (Appendix A.7) of spectral traces at various timepoints after mixing revealed

only a linear combination of $[Ni(P_2^{Ph}N_2^{Ph})_2]^{2+}$ and $[HNi(P_2^{Ph}N_2^{Ph})_2]^{1+}$ absorbance spectra, indicating that the $H_{exo}Ni^{II}H$ absorbance may be spectroscopically indistinguishable from these species. The reaction was also investigated by $^{31}P\{^1H\}$ NMR (Figure 2.11 and Appendix A.9) in search of the third species, yet no reaction intermediate was detected.

A value for k_{-3} (100 $M^{-1}s^{-1}$, Appendix A.8) was estimated by kinetics simulations of the stopped-flow traces, however the values obtained were fairly inconsistent from dataset to dataset, suggesting the process is more complex than the simple deprotonation depicted in Scheme 2.1. For instance, it has been suggested that initial protonation in the exo position is followed by boat-to-chair isomerization in order to form the stabilizing 'pinched' N-H-N hydrogen bond of the off-cycle intermediate.[64] The pK_a values of these two species are expected to differ substantially; competing deprotonation of the two exo-protonated species, along with the kinetics of chair-boat isomerization, likely complicate the determination of rate constant k_{-3}.

Inspection of the mechanism presented in Scheme 2.1 suggests that addition of excess base to the reaction should accelerate catalysis by facilitating deprotonation of $H_{exo}Ni^{II}H$ and this should be reflected in the reaction kinetics observed via cyclic voltammetry. However, addition of aniline (conjugate base of anilinium) reduces the catalytic current. Further, the addition of aniline in stopped-flow experiments results in a significant decrease of the observed rate constant k_{SF} and a decrease in the percent conversion to $[Ni(P_2^{Ph}N_2^{Ph})_2]^{2+}$ in the fast kinetic regime. We posit that aniline rapidly deprotonates the $H_{endo}Ni^{II}H$ species before H_2 can be released. Excess of aniline also causes the long timescale kinetics to slow, rather than speed up as would be predicted if base facilitates deprotonation of the off-cycle intermediate $H_{exo}Ni^{II}H$. To probe the effects of base further, the reactivity of the Ni^{II}-H with anilinium in

the presence of excess base was examined via $^{31}P\{^{1}H\}$ NMR. With 1 equiv. anilinium and 10 equiv. of aniline, the reaction approached an equilibrium between the Ni^{II} species and the Ni^{II}-H. The $H_{exo}Ni^{II}H$ species was not detected.

Together, these data, suggest that the production of hydrogen in the presence of excess aniline inhibits the reaction of the Ni^{II}-H with acid to produce H_2 from reaching completion. Based on the propensity of these nickel species to heterolytically cleave H_2 in the presence of base, we conclude that the equilibrium established between the Ni^{II} species and the Ni^{II}-H in the presence of excess base results from this process. Under this equilibrium, effusion of hydrogen from the solution would be required for the reaction to proceed to completion. By contrast, when no base is added to the reaction solution, the evidence suggests that the longer timescale kinetics do not reflect the reversibility of hydrogen release and cleavage, as the concentration of anilinium, which should influence this equilibrium, has no effect on the extent of reaction. At all anilinium concentrations, the fast timescale kinetics account for 88% of the conversion, as would be expected if two species (Ni^{II} and $H_{exo}Ni^{II}H$) were formed simultaneously in processes that are first order in anilinium. Rather, the long timescale kinetics likely reflect the deprotonation of the $H_{exo}NiH$ species to reform $Ni^{II}H$ which can lead to productive H_2 evolution. Exploring the details of these elementary reaction steps is the focus of our ongoing investigations.

The equilibrium reached between $[Ni(P_2^{Ph}N_2^{Ph})_2]^{2+}$ and $[HNi(P_2^{Ph}N_2^{Ph})_2]^{+}$ in the presence of excess aniline provides an opportunity to estimate the rate constant k_{-2}. Using the value of k_{-3} determined from analysis of the long timescale stopped-flow kinetics, the equilibrium between $H_{exo}Ni^{II}H$, $Ni^{II}H$, and Ni^{II} was examined. With this value of k_{-3}, no $H_{exo}Ni^{II}H$ species should be spectroscopically detectable as the equilibrium between Ni^{II}-H and

$H_{exo}Ni^{II}$-H should afford approximately 300 times the concentration of the former over the latter under the given conditions, consistent with experimental observations. A value of k_{-2} (1.5 x 10^4 M^{-2} s^{-1}) was also estimated from the equilibrium established (Appendix A.9). The value is provided as a third order rate constant, but the conversion from $[Ni(P_2^{Ph}N_2^{Ph})_2]^{2+}$ to $[HNi(P_2^{Ph}N_2^{Ph})_2]^{+}$ likely occurs in two elementary steps (Scheme 2.1)—hydrogen binding followed by proton abstraction.[61] As such, the third order rate constant is not a true rate constant for an elementary step, but rather reflects the rate of proton abstraction from the hydrogen bound $H_{endo}Ni^{II}H$ species which is in equilibrium with the Ni^{II} complex.

Table 2.1. Rate constants determined for elementary reaction steps of hydrogen production catalyzed by $[\boldsymbol{Ni(P_2^{Ph}N_2^{Ph})_2}]^{2+}$.

	k_1 (M^{-1} s^{-1})	k_2 (M^{-1} s^{-1})	k_{-2} (M^{-2} s^{-1})	k_3 (M^{-1} s^{-1})	k_{-3} (M^{-1} s^{-1})
EC	$1.2x10^6$				
FOWA	$6.5x10^6$				
Stopped-Flow		51		7	100
Current Plateau		48		12	
NMR			$1.5x10^4$		

2.4. Conclusions

The $[Ni(P_2^RN_2^{R'})_2]^{2+}$ class of molecules and their successors[33,65] are some the most renowned hydrogen evolution catalysts to date. A great deal of effort has gone into the study of what makes them so efficient and fast, including thermodynamic,[66] kinetic,[61] structural,[55] and environmental[78] aspects. This has opened the door for researchers to make use of these complexes as tools for both technique development and application based research.[84] In this work, investigations of $[Ni(P_2^{Ph}N_2^{Ph})_2]^{2+}$ illustrate the ability to control the reaction mechanism by judicious choice of proton source pK_a. The elementary steps of catalysis were

then examined. Electrochemical methodology, specifically peak shift analysis and foot-of-the-wave analysis, provided the rate constant for protonation of the Ni^0 species. Electrochemistry, stopped-flow spectroscopy and NMR spectroscopy were all used in concert to interpret the rest of the catalytic pathway beyond hydride formation. The mechanism, as we have postulated and consistent with past proposals,[66] is shown in Scheme 2.1. Rate constants for elementary steps determined from these analyses are presented in Table 2.1. Good agreement was found across techniques for the values of k_1, k_2 and k_3. Due to experimental limitations, the values for k_{-2} and k_{-3} were determined by a single technique each.

This work contributes to our understanding of the $[Ni(P_2^R N_2^{R'})_2]^{2+}$ catalysts, especially by confirming that catalysis is initiated by hydride formation and that the zero-order acid dependence observed in catalytic voltammograms at high acid concentrations is a result of biasing the formation of an off-cycle intermediate $H_{exo}Ni^{II}H$. Perhaps more importantly, this work illustrates the importance of extending beyond electrochemical methods for examining catalytic reaction pathways and evaluating reaction kinetics. The in-depth study of the Ni^{II}-H reactivity by stopped-flow kinetic analysis has presented a platform for detailed analysis of the effect of proton source on hydrogen evolution catalysis; work that is currently underway in our laboratory. The agreement we have found between the stopped-flow and electrochemical measurements, along with other studies of its kind,[46] should instill confidence for use of both methods in future studies of electrocatalysts.

2.5. Experimental

2.5.1. General Materials and Methods

Molecular synthesis was performed under N_2 either on a Schlenk line or in an inert-atmosphere glovebox. Acetonitrile (Fisher Scientific, HPLC grade, >99.9%) and diethyl ether (Fisher Scientific, >99%) were degassed with argon and dried using a Pure Process Technology solvent system. Aniline (Sigma-Aldrich) was degassed using a freeze-pump-thaw technique and stored in the inert-atmosphere glovebox. Dimethylformamide was degassed with N_2 and stored in the inert-atmosphere glovebox. Tetrabutylammonium hexafluorophosphate (TCI, >98%) was recrystallized from hot ethanol, filtered, washed with cold ethanol, and dried at room temperature under vacuum overnight. Nickel powder (Sigma-Aldrich) and phenylphosphine (Alfa Aesar) were used as received. Dimethylfomamidium triflate,[40] anilinium tetrafluoroborate,[67] and $[Ni(P_2^{Ph}N_2^{Ph})_2(MeCN)][BF_4]_2$ [61] were prepared by literature methods. NMR spectra were recorded on either a Bruker 400 MHz spectrometer (characterization) or a Bruker 600 MHz spectrometer (kinetics). ^{1}H NMR were referenced to proteo solvent impurities and ^{31}P and ^{31}P{^{1}H} were referenced to a standard of phosphoric acid. Simulations for mechanistic interpretation were performed in MATLAB (MathWorks) using differential equation solver ode45 or ode23s. UV-Vis absorption measurements were taken on an Agilent Cary 60 UV-vis spectrophotometer using 1 cm path length quartz cuvettes.

2.5.2. Preparation of Ni^{II}-H ($[HNi(P_2^{Ph}N_2^{Ph})_2]^+$).

To a stirred acetonitrile solution (~1 mL) of $[Ni(P_2^{Ph}N_2^{Ph})_2]^{2+}$ (5.5 mg, 4.7 μmol), 76 μL of a 60.8 mM solution of sodium borohydride (1 equivalent) was added. Subsequently, the solvent and residual BH_3 were removed under vacuum. The resulting yellow solid was then dissolved into ~0.5 mL of deuterated acetonitrile. NMR suggested 100% conversion. ^{1}H NMR

(CD_3CN, 400 MHz): δ -8.1 (quintet, $^2J_{PH}$ = 30.5 Hz, NiH). $^{31}P\{^1H\}$ NMR (CD_3CN, 160 MHz): δ 17.4 (s).

2.5.3. Electrochemistry.

Electrochemical experiments were performed under a nitrogen atmosphere in an inert atmosphere glovebox using dry acetonitrile with 0.2 M $[Bu_4N][PF_6]$ electrolyte on a Pine Instruments WaveDriver potentiostat with a silver wire pseudo-reference separated from the main solution by a glass frit, a glassy carbon counter electrode and a 3mm disk glassy carbon working electrode. A freshly polished working electrode was used for every voltammogram recorded. Electrodes were polished before experiments with 0.05 μm alumina powder (CH Instruments, contained no agglomerating agents) Milli-Q water slurries. They were then rinsed and sonicated to remove residual alumina. Before measurements were taken, electrodes were pretreated by scanning two cycles from 1 V to -2 V (vs. Ag wire) at 400 mV/s in electrolyte solution.[67] In a generic catalysis experiment, a stock solution of $[Ni(P_2^{Ph}N_2^{Ph})_2(MeCN)][BF_4]_2$and ferrocene (internal reference) was prepared (both ~1 mM) and then two separate, equal volume, solutions were prepared using the stock solution; one that only contained $[Ni(P_2^{Ph}N_2^{Ph})_2(MeCN)][BF_4]_2$ and another that contained the same concentration of catalyst and an acid. The cyclic voltammetric response of the catalyst only was measured and then the solution containing the acid was titrated in over ~10 additions. A similar procedure was performed for the peak shift experiments, the stock solutions also contained 1 M in aniline. All scans were referenced to the ferrocene/ferrocenium couple post data collection. The direct reduction of anilinium is sufficiently negative on glassy carbon such that it should not interfere in the analyzed region.[67]

2.5.4. Stopped-Flow Experiments.

Stopped-Flow experiments were performed on a Hi-Tech Scientific SF-61 DX2 double mixing stopped-flow in single mixing mode with Kinetic Studio data acquisition software (v2.33). Single wavelength kinetics measurements were taken using a dual reference/main PMT set-up with a tungsten lamp. Spectra measurements were taken using a photo-diode array with a xenon lamp. Stopped-flow measurements were all performed under an N_2 atmosphere. This was accomplished by preparing solutions inside an inert-atmosphere glovebox in septum-sealed bottles. A solution of $[HNi(P_2^{Ph}N_2^{Ph})_2]^+$ (0.2 – 0.5 mM) was prepared by dissolving $[Ni(P_2^{Ph}N_2^{Ph})_2]^{2+}$ in approximately 10 ml of acetonitrile, then a 1 equiv. of sodium borohydride was added and the solution was diluted to 25 ml. Stock solutions anilinium were also prepared. PEEK tubing was used to transfer solutions directly from sealed bottles to the stopped flow syringes to avoid exposure to air. To ensure purity, the syringe was purged three times with each solution prior to each measurement. In a typical experiment, one syringe was loaded with the $[HNi(P_2^{Ph}N_2^{Ph})_2]^+$ solution and the other was loaded with the anilinium solution of the desired concentration. Upon injection, absorbance vs. time was monitored at 500 nm. Fitting of the resulting traces was performed using a single exponential in Igor Pro 6.34A Software. The residual borane was shown through control reactions to not affect the stopped-flow kinetics.

2.5.5. NMR equilibrium.

9 mg of $[Ni(P_2^{Ph}N_2^{Ph})_2(MeCN)][BF_4]_2$ was dissolved in 1 mL of deuterated acetonitrile (5 mM). A 0.5 ml aliquot was removed and a $^{31}P\{^1H\}$ NMR was taken. 1 equiv. $NaBH_4$ was then added to generate the hydride in situ in the remaining 1 mL. Separately, 1 mg of anilinium BF_4 (5 mM) and 5 µL of aniline (50 mM) were dissolved in 25 mL acetonitrile.

0.5 mL of the hydride solution and 0.5 mL of the anilinium:aniline solution were placed in a J. Young air-free NMR tube. $^{31}P\{^{1}H\}$ NMR spectra were obtained for each of the three solutions after allowing equilibrium to be established (equilibrium is established in approximately 2 h, appendix A.13, however spectra were recorded at 6 h).

CHAPTER 3. Reactivity of Proton Sources with a Nickel Hydride Complex in Acetonitrile: Implications for the Study of Fuel Forming Catalysts

3.1. Introduction

In hopes of one day mitigating our looming energy crisis, many researchers have dedicated research efforts to the fundamental study and development of solar energy conversion technologies.[5,16,86–89] The major challenge with solar energy utilization is the intermittency of the sun; energy storage is essential in order to meet the economic demands for energy transport and timely use. One solution to this challenge is the production of solar fuels, whereby the energy from the sun is used to convert energy poor molecules such as water and/or carbon dioxide into oxygen and either hydrogen or a carbon based fuel.[13,90] The proposed methodologies for these transformations are numerous, but our research has focused on production of fuels using homogeneous catalysts, an approach that has garnered tremendous attention over the past decade.[13,68,91,92]

In spite of the fact that the preferred medium for future solar fuel production schemes is water, the study of homogeneous catalysts has predominantly been explored in acetonitrile and other non-aqueous solvents.[25,93–95] Acetonitrile offers advantages when the goal is to elucidate the reaction mechanisms of a fuel production catalyst: it is a highly polar solvent, offering solubility properties close to that of water (relative to other organic solvents);[96] despite

high resistivity, it is electrochemistry friendly, with a large potential window and the ability to dissolve established inert electrolytes;[97] and it has a large optical window making it amenable to spectroscopic study. Further, while acetonitrile is aprotic, a self-consistent pK_a scale for acids is available.[98–101] This provides researchers studying molecular catalysts with an opportunity to control both the proton source concentration and strength. However, there are limited examples in which this has been utilized effectively as a tool to explore reaction mechanisms. Most often, proton sources are selected purely on the basis of pK_a with little regard for other important characteristics of acids in acetonitrile, such as their tendency to homoconjugate, heteroconjugate, or dimerize. This may be, in part, a result of limited reports describing the proton source's impact on catalysis. Towards this end, we have recently reported the study of direct reduction of Brønsted acids on glassy carbon electrode surfaces in acetonitrile in which we parameterized current-potential responses as a function of various acid features.[67]

With a deeper understanding of the properties of acids and their reactivity at glassy carbon electrodes, we sought to next examine the influence of these various acid parameters on the reactivity of molecular catalysts. In this work, we report the reaction kinetics of a host of acids with a well-known hydrogen evolution catalyst, $[Ni(P_2^{Ph}N_2^{Ph})_2(CH_3CN)][BF_4]_2$ ($P_2^{Ph}N_2^{Ph}$ = 1,3,5,7-tetraphenyl-1,5-diaza-3,7-diphosphacyclooctane).[61,62,102–104] In a recent study, we demonstrated that a nickel(II)-hydride intermediate in the catalytic cycle, $[HNi(P_2^{Ph}N_2^{Ph})_2]^+$ ($Ni^{II}H$), can be prepared and isolated.[42] The significant spectroscopic differences between $[Ni(P_2^{Ph}N_2^{Ph})_2]^{2+}$ and $Ni^{II}H$ enable spectroscopic monitoring of the reaction of $Ni^{II}H$ with acid to form $[Ni(P_2^{Ph}N_2^{Ph})_2]^{2+}$ and H_2, and the kinetics of this elementary step are readily determined via stopped-flow spectroscopy. The rate constant

obtained from this time resolved data was consistent with that from analysis of electrocatalysis data, signifying that the observed rate of catalysis is governed by elementary steps post-hydride formation. As such, the reaction of $Ni^{II}H$ with acid provides a convenient platform to study the role of the proton source, as the kinetics of a single elementary reaction step can be directly determined and the added complexity of the electron transfers and the hydride formation step are eliminated. In this work, we use the acids in Table 3.1 to evaluate the effect of pK_a, conjugate base presence, water addition/impurities, homoconjugation and dimerization on the overall reactivity of the proton source for hydrogen evolution in acetonitrile. These data reveal a linear free energy relationship between rate constant and pK_a, show that multiple forms of molecular association significantly impact catalysis, and indicate that water contributes as a proton source itself after hydronium formation.

Table 3.1. Acids evaluated in this work with corresponding pK_a values (acetonitrile).

Acid	pK_a	Reference
4-methoxyanilinium	11.86	[105]
4-methylanilinium	11.4	[106]
4-tertbutylanilinium	11.1	[67]
anilinium	10.62	[105]
4-chloroanilinium	9.7	[67]
4-bromoanilinium	9.43	[67]
4-trifluoromethoxyanilinium	9.28	[38]
4-iodoanilinium	9.27	[106]
4-(methylbenzoate)anilinium	8.62	[38]
4-trifluoromethylanilinium	8.03	[105]
4-cyanoanilinium	7.0	[67]
dimethylformamidium	6.1	[107]
trifluoroacetic Acid	12.65	[108]
trichloroacetic acid	10.75	[108]
p-toluenesulfonic acid	8.6	[100]
hydronium	2.2	[109]

.

3.2. Results

3.2.1. Effects of acid pK_a

The effect of proton source pK_a on reaction kinetics was first considered. This parameter is one of the most commonly considered factors for experimentalists when selecting acids for electrocatalysis studies. We used a series of para-substituted aniliniums for this study. Aniliniums are touted for their low homoconjugation constants, and provide a fairly large range of accessible pK_a values through para-substitution (~6 units). The reaction of these acids with $Ni^{II}H$ to produce H_2 and Ni^{II} was monitored by stopped-flow spectroscopy (Scheme 3.1).

Scheme 3.1. Reaction of $Ni^{II}H$ to form H_2 and Ni^{II}.

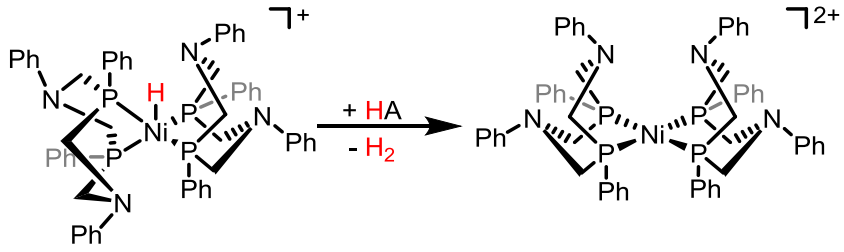

Upon rapid mixing of a solution of $Ni^{II}H$ and acid, the appearance of the Ni^{II} product was monitored as a function of time (λ_{obs} = 500 nm) and a first order observed rate constant was obtained by fitting the single wavelength kinetics trace, following previously reported procedures.[42] Second order rate constants were determined from the relationship of the observed rate constant and acid concentration. A linear free energy relationship was observed between the log(k) and pK_a (Figure 3.1) for acids with pK_a values in the range of 12 to 8.6. For acids with pK_a values in the range of 8.6 to 7, the rate constant becomes pK_a independent. The slope of a linear regression in the range of pK_a values 12 to 8.6 is 0.7.

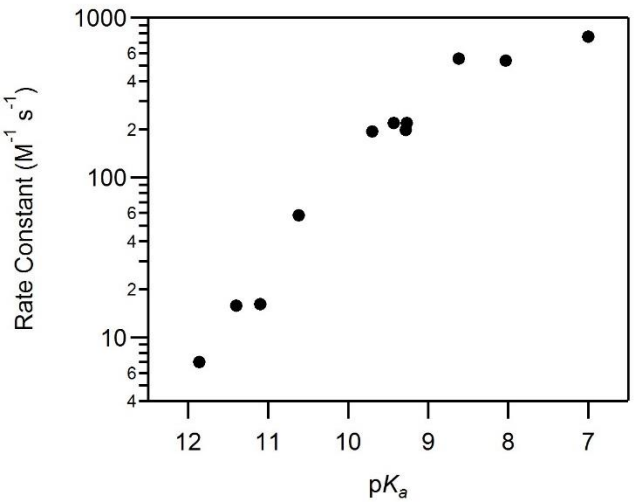

Figure 3.1. Second order rate constants vs. acid pK_a for the reaction of $Ni^{II}H$ with para-substituted aniliniums (Table 3.1). The linear region between pK_a 12 to 8.6 has a slope of 0.7.

3.3.2. Effect of Conjugate Base Addition

In studies of molecular catalysts for hydrogen production or CO_2 reduction, the conjugate base of an acid is often added to solution.[110,111] The advantages are two-fold; 1) it allows for a more accurate determination of the overpotential for the reaction (see below), and 2) when performing electrochemical measurements, it creates a more stable environment near the electrode surface by preventing rapid fluctuations of the relative conjugate base concentration as acid equivalents are consumed.[112,113]

To investigate how the addition of conjugate base affects the rate of reaction between $Ni^{II}H$ and an acid, the observed first order rate constant was determined as a function of the base:acid ratio for several of the para-substituted aniliniums described above, as well as trifluoroacetic acid and dimethylformamidium (Figure 3.2). Datasets were collected under conditions in which the acid concentration was held constant and the base concentration was varied.

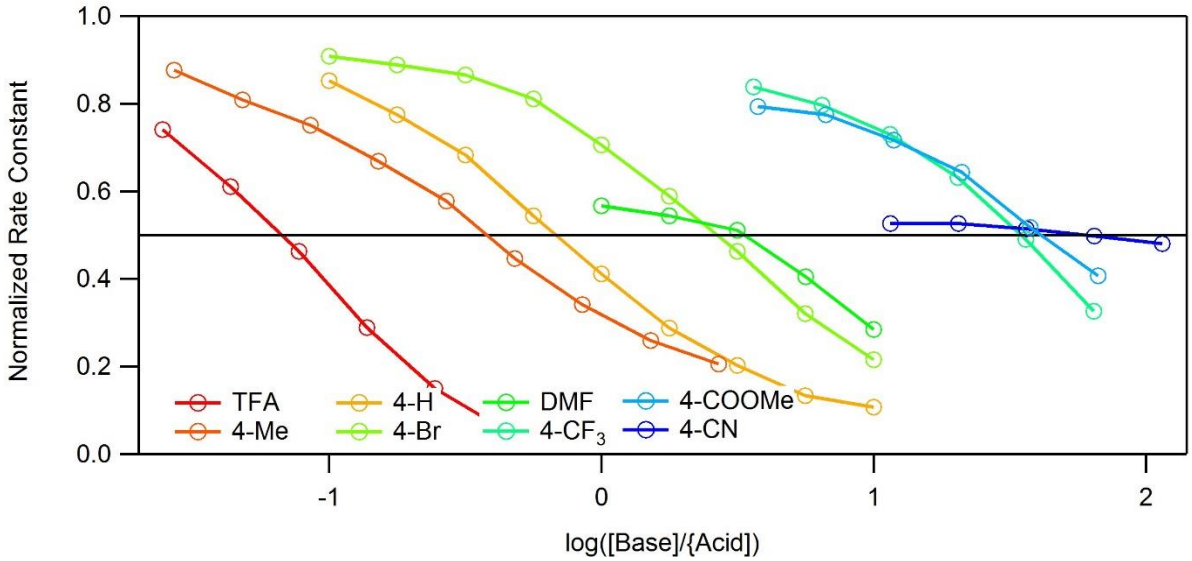

Figure 3.2. Normalized rate constant plotted vs. base:acid ratio. Observed first order rate constants determined in the presence of base were normalized to the observed first order rate constant in the absence of base. In each case, the acid concentration was held constant and the base concentration was varied. Trifluoroacetic acid (TFA, pK_a = 12.65, 9.5 mM), 4-methylanilinium (4-Me, pK_a = 11.4, 3.4 mM), anilinium (4-H, pK_a = 10.62, 5 mM), and 4-bromoanilinium (4-Br, pK_a = 9.43, 5 mM), dimethylformamidium (DMF, pK_a =6.1, 1 mM), 4-trifluoromethylanilinium (4-CF_3, pK_a = 8.03, 3.1 mM),, 4-(methylbenzoate)anilinium (4-COOMe, pK_a = 8.6, 1.6 mM),, and 4-cyanoanilinium (4-CN, pK_a = 7, 1 mM), are represented here. The acids with a pK_a values lower than 9 did not follow any trend, in keeping the pK_a independence shown for this range in Figure 3.1. Markers represent actual data points; lines in between are a guide for the eye.

For acids of pK_a > 9, reactions slowed as the base concentration was increased. These acids exhibit a pK_a-dependent rate constant (see above). At lower pK_a values, a larger ratio of base to acid is necessary to affect change of the observed rate constant. For acids with pK_a < 9, no predictable behavior was observed (i.e. the point at which the observed rate constant begins to decrease has no correlation to pK_a). Notably, no decrease in observed rate constant is seen with added base concentration for p-cyanoanilinium beyond the first addition. In both regions (pK_a > 9 and pK_a < 9), data was collected for an acid that is not a para-substituted anilinium (trifluoroacetic acid, pK_a = 12.65, and dimethylformamidium, pK_a = 6.1). The rate constant for trifluoroacetic acid (pK_a = 12.65) decreases with increasing base concentration and trends with

other high pK_a acids. While added base affects the rate constant of dimethylformamidium (pK_a = 6.1), the effect is *more* pronounced than other low pK_a acids, consistent with the lack of a trend for acids of pK_a <9. Notably, neither trifluoroacetic acid nor dimethylformamidium follow the rate constant-pK_a correlation observed for para-substituted aniliniums (Figure 3.1, see below).

3.3.3. Effect of Molecular Association

Unlike in water, where acids are easily stabilized by the polar, protic solvent, proton sources in acetonitrile are prone to self-association reactions to promote stability, significantly altering their characteristics (Table 3.2). Unfortunately, reported equilibrium constants for homoconjugation and dimerization of acids in acetonitrile are limited, making the methodical study of these parameters difficult. For homoconjugation, very few acids with reported equilibrium constants (K_{HC}) above 10 M^{-1} are in the working range of our platform catalyst; for this study we analyze p-cyanoanilinium (K_{HC} = 1.2 M^{-1}), dimethylformamidium ($DMFH^+$, K_{HC} = 49 M^{-1}) and p-toluenesulfonic acid (tosic acid, K_{HC} = 1000 M^{-1}). For acid dimerization, there are no reported equilibrium values in acetonitrile, to the best of our knowledge, for acids in our pK_a working range. However, literature precedent,[108] as well as our results (see below), suggest that carboxylic acids, including trifluoroacetic acid (TFA), and trichloroacetic acid (TCA), are prone to dimerization in acetonitrile.

Table 3.2. Forms of molecular association in acetonitrile. *AH* represents neutral acids, BH^+ represents cationic acids. [a]Heteroconjugation can occur in multiple ways, only one example is shown here.

Homoconjugation	$BH^+ + B \rightleftharpoons BHB^+$ or $AH + A^- \rightleftharpoons AHA^-$
Dimerization	$2AH \rightleftharpoons (AH)_2$
Heteroconjugation[a]	$AH + B \rightleftharpoons AHB$
Aggregation	$xB + BH^+ \rightleftharpoons B_{x+1}H^+$

Homoconjugation. Rate constants for the reaction of $Ni^{II}H$ with $DMFH^+$ and tosic acid were measured as a function of acid concentration. For $DMFH^+$, k_{obs} is linear with acid concentration for 0–5 mM $DMFH^+$, but the observed rate constant becomes acid concentration independent at higher concentration. Across three separate experiments, the value at which the observed rate constant becomes concentration independent varies from 80 s^{-1} to 120 s^{-1} (Appendix B.2). We speculate that this is due to slight variations in the concentrations of trace water in the solutions. A second order rate constant of 12,750 M^{-1} s^{-1} is extracted from the acid-independent region (Table 3.3). We were unable to accurately measure a rate constant for tosic acid as the reaction kinetics were too fast to establish reliable observed rate constant vs. concentration data. A k > 130,000 $M^{-1}s^{-1}$ is estimated from a sample containing 5 mM tosic acid (k_{obs} = 640 s^{-1}). For comparison, the rate constant for the strongest anilinium (p-cyanoanilinium, pK_a = 7.0) is 760 $M^{-1}s^{-1}$. The observed rate constants for these three acids show a clear trend with K_{HC}; faster rate constants correlate to larger K_{HC} values.

Table 3.3. pK_a, homoconjugation constant, and rate constants for three acids with substantially different homoconjugation constants.

	PK_A	K_{HC} (M^{-1})	K ($M^{-1}S^{-1}$)
P-CYANOANILINIUM	7	1.2	760
DIMETHYLFORMAMIDIUM	6.1	49[112]	12,750
TOSIC ACID	8.6	1000[100]	>130,000

Dimerization. Equilibrium constants for dimerization of TFA or TCA in acetonitrile are not available (one previous study even noted no dimerization was observed via infrared spectroscopy).[114] However, there is literature precedent for dimerization of carboxylic acids in acetonitrile.[115] Measurement of the observed rate constant for the reaction of $Ni^{II}H$ with TFA and TCA reveals second order reactivity for both species, suggesting dimerization of the trihaloacetic acid species (Figure 3.3). While this is the first time second order reactivity has been shown for the delivery of a single proton, second order reactivity has been observed for TFA in several other reports of molecular electrocatalysts for H_2 production.[116–122]

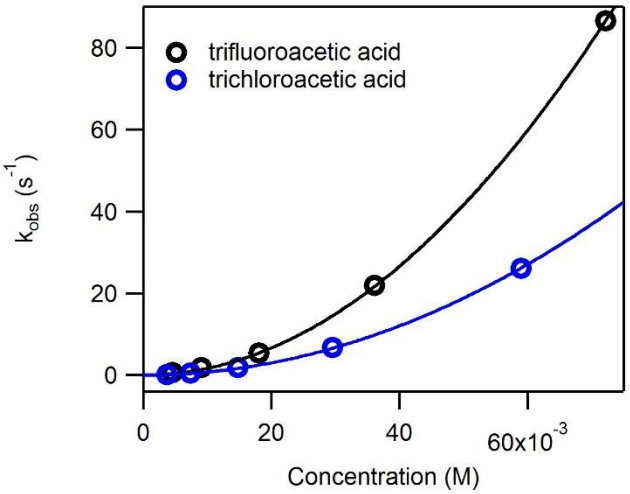

Figure 3.3. Observed rate constant versus acid concentration for trifluoroacetic acid and trichloroacetic acid. Both acids exhibit second order reactivity. The overlaid lines represent the equation $k_{obs} = A[Acid]^2$. For trifluoroacetic acid A = 16,600 $M^{-2}s^{-1}$, and for trichloroacetic acid A = 7500 $M^{-2}s^{-1}$.

Both TFA and TCA are relatively weak acids, yet they both have surprisingly high rate constants as compared to the aniliniums. Further, TFA is the weaker acid of the two, yet its rate constant is over a factor of two larger than that for TCA (16,600 versus 7,500 $M^{-2}s^{-1}$), suggesting reactivity likely has more to do with its equilibrium constant for dimerization than its pK_a value. Dimerization constants are not available, but homoconjugation constants for the two acids are reported to be 8000 M^{-1} for TFA and 320 M^{-1} for TCA.[108] Under the assumption that relative dimerization constants scale with homoconjugation constants, the higher apparent second order rate constant of TFA is consistent with a higher concentration of active (dimerized) species.

3.3.4. Effect of Water.

Given that (1) water is the desired feedstock for future applications of fuel-producing reactions and (2) that water is both a common impurity in organic solvents, particularly acetonitrile, and intentionally added in many electrocatalytic hydrogen evolution studies, we sought to understand its reactivity and influence on elementary steps related to hydrogen evolution by molecular catalysts. As is discussed below, we find that in acetonitrile, water can both act as the acid/base and interact with proton sources to stabilize them.

Water as a Proton Source. To examine the effect of water on proton source reactivity, we systematically added water to solutions of four different acids (triflic acid, $DMFH^+$, 4-cyanoanilinium, and anilinium) and monitored the change in observed rate constant as a function of water concentration. The results for triflic acid, $DMFH^+$, and p-cyanoanilinium are shown in Figure 3.4. As water concentration is increased, the observed rate constant initially increases. These results suggest the protonation of water by the parent acid occurs as the

concentration of water is increased, and the hydronium (or hydronium hydrate) reacts with $Ni^{II}H$ to form H_2 with a larger rate constant, in comparison to the parent acid. For acids with lower pK_a values, an increase in rate is observed at lower concentrations of water, consistent with the equilibrium expected for hydronium formation based on the difference between the expected effective pK_a values for hydronium and the parent acids. For anilinium (pK_a = 10.6), the addition of water has no effect on the observed rate constant (Appendix B.3). After an initial increase in rate constant with added water, the observed rate constant begins to decrease as the concentration of water is increased further for the three stronger acids studied. This observation is reminiscent of Figure 3.2, where increases in base concentration are shown to lead to a decrease in the observed rate constant, suggesting water also plays the role of a base. Notably, the observed rate constants for the three acids converge at these higher acid concentrations.

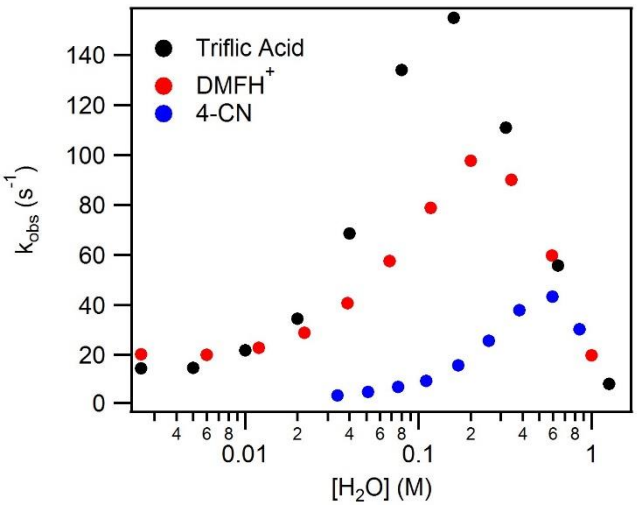

Figure 3.4. Water's effect on rate. Concentration of water versus observed rate constant for 1.25 mM triflic acid (pK_a = 2.6), 1.3 mM dimethylformamidium ($DMFH^+$, pK_a= 6.1), and 2.5 mM 4-cyanoanilinium (4-CN, pK_a = 7). Observed rate constants obtained from reaction with $Ni^{II}H$ to form hydrogen.

Heteroconjugation. Water can stabilize hydrogen bonding species through heteroconjugation. Upon the addition of water to solutions of TFA, a decrease in the observed rate constant is observed (Figure 3.5). The reactivity of TFA is influenced by the extent of dimerization; the introduction of water to the solution increasingly disfavors dimerization as water forms heteroconjugates with TFA. We expect any acid that is prone to homoconjugation will heteroconjugate with water.

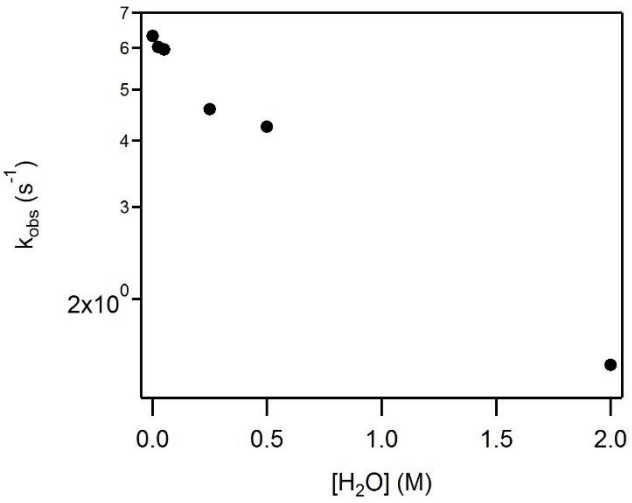

Figure 3.5 Observed rate constant for reaction between 25 mM solutions of trifluoroacetic acid and 0.2 mM solutions of $Ni^{II}H$ in the presence of water. The concentration of water was varied from 0 to 2 M.

3.3. Discussion

3.3.1. Acids in Acetonitrile

The behavior of acids in acetonitrile differs substantially from their behavior in water.[67] Catalysis involving acids in acetonitrile can be likened to general-acid catalysis, whereby proton transfer occurs directly from the molecular acid to a proton acceptor (as opposed to specific acid catalysis where the reactive proton source is the protonated form of the solvent formed upon dissociation of the acid).[123] A pK_a scale in acetonitrile is available but it has, in

large part, been formed through self-consistent measurements.[100] However, no acids are known to fully dissociate in acetonitrile[113] and those in which dissociation can be observed result in degradation of the solvent.[124] Therefore, it is still a matter of debate as to whether the concept of pH (which is defined by the extent of acid dissociation, and thus solvated protons) can be directly extended to acetonitrile. As such, protons in acetonitrile are only available locally, unlike in water, where proton transfer is mediated by hydrogen-bonded water chains via Grotthus-type transport processes.[125] Consequently, catalysts must generally interact directly with the supplied proton source—a molecular acid—ensuring that the physical properties of the proton source will affect the proton transfer reaction. In addition, acetonitrile is not prone to hydrogen bonding. As a result, acids in acetonitrile tend to associate with each other and with other species in solution to promote stability. Known forms of molecular association are homoconjugation,[126] dimerization,[115] heteroconjugation[127] and aggregation,[112] each of which is discussed in detail below.

3.3.2 pK_a

The thermodynamic potential for acid reduction to hydrogen (Eq. 3.1) is related to the acid pK_a as described by Eq. 3.2.[34,77,112,113,128]

$$2\,AH + 2\,e^- \overset{E_{AH/H_2}}{\rightleftharpoons} 2\,A^- + H_2 \qquad (Eq.\,3.1)$$

$$E_{AH/H_2} = E^0_{H^+/H_2} - \frac{2.303RT}{F}\left[\mathrm{p}K_a(\mathrm{AH}) + \log\left(\frac{\alpha_{H_2}^{\frac{1}{2}}\alpha_{A^-}}{\alpha_{AH}}\right)\right] \qquad (Eq.\,3.2)$$

The equilibrium potential for this reaction (E_{AH/H_2}) can be calculated using Eq. 3.2 where R is the gas constant, T is the temperature, F is Faraday's constant, α is the activity of the

subscripted species , and $E^0_{H^+/H_2}$ is the standard potential for the hydrogen electrode (reported as -0.028 V vs $Fc^{+/0}$ by Roberts and Bullock[112]).[67] E_{AH/H_2} is typically used to determine the overpotential for catalytic reactions. However, direct use of the reaction quotient does not afford an accurate value for E_{AH/H_2} due to complications from molecular association (to determine the exact value for E_{AH/H_2}, experimental methodology has been developed).[112,126] It is intuitive to suggest that a larger difference between the catalysis initiating redox event for the catalyst and E_{AH/H_2} (the overpotential by some definitions) should result in a higher rate of turnover for catalysis. Stated otherwise, stronger acids should result in faster turnover frequencies as the operating potential for molecular species rarely[111] changes substantially from one proton source to another. Even so, such correlations between catalytic rate constants for H_2-evolving catalysts and acid strength have not been studied thoroughly.[38] However, as illustrated by the observed rate constants for the reaction of $Ni^{II}H$ with para-substituted anilniums, $DMFH^+$, tosic acid, TFA, and TCA (Figure 3.1, Table 3.3, Figure 3.3, and Appendix B.1), the anticipated trend between reaction rate and driving force does not fully hold; the trend cannot be generalized across different classes of acids. Factors such as molecular association, transition state, and acid independent catalytic steps must all be considered.

In Figure 3.1, log(*k*) for para-substituted aniliniums above a pK_a of 9 are linear with pK_a with a slope of –0.7. Similar relationships were observed for both the first and second protonation of a cobaloxime catalyst with para-substituted aniliniums.[38] Below a pK_a of 9, the reaction becomes pK_a independent. In an attempt to rationalize these results, we first recognized the similarity of Figure 3.1 to plots of log(k_{obs}) vs. pH for general acid catalysis in water which exhibits a pH independent and pH dependent regime.[123] However, for general acid catalysis these two regimes arise from differences in the extent of acid dissociation (and thus

concentration of HA) as a function of solution pH and the acid pK_a, thus this rationale cannot be readily extended to acetonitrile. To extend this concept, we must consider the catalyst as the species that is protonated to some extent based upon the difference between pK_a values of the protonated catalyst and the acid. The observed rate constant could reflect an acid-independent step post-protonation, and thus the concentration of the protonated catalyst, as defined by the equilibrium based on the ΔpK_a values, influences the observed rate constant. However, acid concentration independence would be expected in the same region that pK_a independence is observed, inconsistent with the data here.

Second, we considered the relationship between the rate constants and the pK_a. Examining Figure 3.1 under these pretenses, we see two distinct regions, one with a slope of –0.7 and another with a slope close to 0. Two scenarios could give rise to these relationships. First, two distinct mechanisms for protonation could be operating, one for low pK_a acids and another for high pK_a acids. For instance, changing acid strength may change preferred protonation sites due to the differing thermodynamics for proton transfer.[66] We next considered the possibility that the transition state for the proton transfer reaction differs across the series of the aniliniums. If, in the transition state, the proton rested more on the acid than on the $Ni^{II}H$, a pK_a dependent response would be expected. Likewise, if proton transfer to $Ni^{II}H$ were more complete (a more product-like transition state), a pK_a-independent response could be explained. This analysis is limited to $[Ni(P_2^{Ph}N_2^{Ph})_2]^{2+}$ as in the case of the aforementioned cobaloxime catalysts, the pK_a dependence held across all acids studied and no pK_a-independent region was observed.[38]

3.3.3 Base Addition

Upon the addition of conjugate base to the solution, proton sources with a pK_a > 9 show a pK_a dependent trend (the lower the pK_a, the more base required to slow the reaction rate). With pK_a < 9, no recognizable trend was observed. Unlike the data in Figure 3.1, this trend holds across various acid structures, as is witnessed by the evaluation of trifluoroacetic acid and dimethylformamidium. The break in the trend for acids with pK_a < 9 may be due to homoconjugation. *p*-cyanoaniline has the smallest homoconjugation constant, 1.2 M^{-1}, and is the least affected by base addition; dimethylformamidium has the highest homoconjugation constant 49 M^{-1}, and is affected most by base addition. At these high concentrations of base, even relatively small homoconjugation constants can have a large impact on the concentration of available protons (under the assumption that homoconjugated species are less reactive). These data suggest that the influence of base:acid ratio on rate constant is likely a purely thermodynamic phenomenon, and does not correlate with acid structure.

While not evaluated in this study, recent work has shown that the addition of base can actually increase the observed reaction rate through other interactions with the catalyst molecule. For $[Ni(P_2^{Ph}N_2^{Ph})_2]^{2+}$, addition of the conjugate base to the reaction positively influences the global reaction rate by inhibiting the formation of a prominent off-cycle intermediate.[42,104]

3.3.4 Molecular Association

Molecular association of acids in acetonitrile is discussed throughout the hydrogen evolution literature, and is invoked to explain both rate enhancing[116] and inhibiting[111] effects. However, very little work has been devoted to this topic since seminal work by Kolthoff and Chantooni over 40 years ago.[108] In this work we have examined three specific types of molecular association — homoconjugation, heteroconjugation, and dimerization. Of note,

recent work by Jackson and Surendranath illustrates that the *sterics* of the proton source can also significantly impact reactivity, a parameter we are not able to address with our acid selection in this work.[129] In addition, Elgrishi, *et. al.* recently observed significantly slowed reactivity for the formation of a cobalt hydride when providing steric bulk around the proton.[39]

Homoconjugation is the most commonly discussed form of molecular association in the literature, often for its ability to alter the effective pH of the solution from the traditional titration curve.[112,116,126,130–132]. Because acetonitrile is not prone to hydrogen bonding and has relatively weak ion solvating ability as compared to water,[96] acids and bases often find ways to stabilize themselves through the formation of hydrogen bonds with their conjugate (Table 3.2). When little or no conjugate base is present, homoconjugation causes the acid dissociation equilibrium to shift towards protonated solvent as the conjugate base formed can stabilize the parent acid through a hydrogen bonded complex, yielding higher effective acidity. Likewise, a more basic solution is created when excess conjugate base is present as the free parent acid is then removed through stabilizing interactions with the base.

The depletion of the active proton source in the presence of excess base,[104] and the increase of acidity in excess acid-containing solutions,[116] each originating from homoconjugation, have been used to explain unexpected rate constants in the fuel forming catalysis literature. The correlation we observe between dramatically different rate constants for acids with starkly different homoconjugation constants (Table 3.3) suggests that reaction kinetics can be significantly affected by this parameter beyond influencing effective acidity; it appears that the value of K_{HC} may be just as valuable in anticipating reactivity as acid pK_a. It has previously been suggested that increased reaction rates could be accessed through improved hydrogen bonding abilities.[133,134] As homoconjugation reflects the formation of

hydrogen bonds for proton sources, it is easy to imagine that a conjugate base present in solution can act as a transition state stabilizer through hydrogen bonding, facilitating catalysis. The same could be said for heteroconjugating species (the most commonly considered being water); while this has yet to be explicitly shown, such reasoning has been invoked to explain the acceleration of catalysis with added water.[103,135] However, the molecular association process can also have the counter effect as well; we observe that rate constants for TFA decrease upon the addition of water, suggesting that heteroconjugation between water and TFA inhibits dimerization of TFA, thereby lowering the observed rate constant (see below).

Acid dimerization has not, to our knowledge, been discussed in the electrocatalysis literature. Carboxylic acids are known to dimerize in acetonitrile, however, the carboxylic acids with reported dimerization constants (mostly benzoic acid derivatives)[108] have high pK_a values and are rarely employed in the analysis of fuel-producing electrocatalysts. However, the reaction of $Ni^{II}H$ with TFA and TCA shows a second order dependence on acid concentration (Figure 3.3), suggesting that dimerization does occur with a small dimerization constant (<1 M^{-1}, Appendix B.4). Alternatively, 2 equivalents of TFA or TCA could interact with the catalyst in a termolecular reaction, though the clean and well-defined reaction to release H_2 with all other acids does not support this hypothesis. Further, based on the rate constant–pK_a correlations of Figure 3.1, and the high pK_a values of TFA (12.7) and TCA (10.8), slow reactivity with $Ni^{II}H$ is predicted. However, dimerized carboxylic acids consistently show decreases in pK_a values from the parent acid between 3.3 and 4 units, which would suggest the active dimerized species of TFA to have a pK_a of ca. 9 and that of TCA of approximately ca. 7.[108] Based simply on the pK_a values of these two acids, a higher rate constant would be expected for reactivity of $Ni^{II}H$ with TCA than with TFA, contrary to

observations. Yet, as stated earlier, the homoconjugation constant of TFA is an order of magnitude higher than that for TCA; if the dimerization constants follow the same trend, the apparent higher rate constant for TFA would simply be a result of a higher concentration of the active, dimerized species. In several reported studies, second order reactivity is seen with these acids in acetonitrile, but given the complexity of electrocatalysis, it has not been attributed to the reactivity of the acid itself.[116–122] This confirmation of a second order response for an elementary reaction step involving a single proton will be vital to future studies utilizing these acids.

3.3.4 Water in Acetonitrile

Water, and some alcohols, are unique bases in acetonitrile; the favorability of their aggregation results in an effective pK_a for the hydronium ion that is concentration dependent. Di-, tri-, and tetrahydrates of the hydronium ion have been shown to exist in acetonitrile; the increased stability of the larger aggregates results in an increase in basicity to the fourth order as the concentration of water is increased.[109]

The most obvious consideration for water is the use of hydronium as a proton source. Water itself is unlikely to act as a proton source in acetonitrile as its pK_a is above the autoprotolysis constant for acetonitrile.[67] Hydronium, the monohydrate of a single proton, has a reported pK_a of 2.2,[109] making it a very strong acid in acetonitrile. However, under most circumstances, the hydrated forms of hydronium ($[H(H_2O)_2]^+$, $[H(H_2O)_3]^+$, $[H(H_2O)_4]^+$), which have higher effective pK_a values, are more likely to be present ($K_{dihydrate}$ = 7.9 x 10^3 M^{-2}, $K_{trihydrate}$ = 5.0 x 10^4 M^{-3}, $K_{tetrahydrate}$ = 2.0 x 10^5 M^{-4})[109]. Because of this, water can establish a non-trivial protonation equilibrium with acids that have pK_a values as high as 7 or more.

In our experiments, a fixed concentration of acid was added to the solution using three different sources with pK_a values ranging from 2.6 to 7. Water was titrated in and the rate of reactivity between $Ni^{II}H$ and the acid/water mixture was recorded as a function of water concentration (Figure 3.4). We find that water influences the reaction kinetics in two ways. First, at very low water concentrations (<10 mM), the rate constant is unaffected (at low concentration where water aggregate formation is still unfavorable, no effect is seen), but as the concentration is increased, we observe an exponential increase in the observed rate constant. We anticipate that this spike in reactivity is due to the formation of hydronium hydrates at higher water concentrations; it has also been suggested that there may be a specific hydronium hydrate that is most favorable for reaction with a catalyst based on sterics and energetics.[136] We attempted to determine if a specific hydrate is favored for reactivity with $Ni^{II}H$ by modeling our data using the known aggregation constants and pK_a values of water and our acids. However, the vast number of parameters, along with an incomplete understanding of how bases slow the reaction mechanistically (see above), prevented this analysis.

While added water initially leads to an increase in the observed rate constant, a sharp decline is observed as the concentration is further increased. At high acid concentrations, the observed rate constants for the three acids converge. We initially considered this could be due to the favored formation of the tetrahydrate under these concentration; slower reactivity of the tetrahydrate as opposed to the other hydrates could give rise to this inflection. However, data could not be fit to this model. By contrast, we suggest that the decline in the observed rate constant results from water's role as a base. As shown in Figure 3.2, the addition of base lowers the observed reaction rate for a given acid.

3.3.5 Reactivity Intrinsic to the Catalyst

This work has focused on the impact of the proton source on reactivity in hydrogen evolution catalysis. However, it is important to recognize that some reactivity is acid independent and intrinsic to the catalyst itself. These steps are generally ascribed to intramolecular rearrangements or the release of product.[38,62] Within this study, we see evidence of acid independence when using two acids, p-cyanoanilinium, and dimethylformamidium. The reaction of $Ni^{II}H$ with both becomes acid concentration- and pK_a-independent when observed rate constants exceed 80 s^{-1}, suggesting formation of the Ni^{II} species upon release of H_2 is governed by an elementary step subsequent to proton transfer. However, tosic acid reacts with $Ni^{II}H$ with pseudo-first order rate constants that far exceed 80 s^{-1}. Similarly, while reactivity with TFA was only recorded up k_{obs} = 80 s^{-1}, no immediate plateau is anticipated based on the upward curvature and the second-order dependence on acid. One major difference between these acids and dimethylformamidium and p-cyanoanilinium is the charge; tosic acid and TFA are neutral acids, while p-cyanoanilinium and dimethylformamidium are cationic species. We speculate that this difference could lead to a change in the site of protonation of the catalyst (pendant amine vs. direct protonation of the hydride), leading to different kinetic profiles.

3.4. Conclusion

The reactivity of a $Ni^{II}H$ with a series of acids in acetonitrile was evaluated with respect to a variety of acid parameters, including pK_a, acid:base mixtures, homoconjugation, heteroconjugation, dimerization, and water presence. Keeping similar structures for the acids and changing the driving force (through a series of para-substituted aniliniums) led to a linear free energy relationship between the rate constant for this elementary step and the acid pK_a.

When comparing structurally dissimilar acids, rate constants were shown to increase with the magnitude of the homoconjugation constant. Second order kinetics were observed for reactivity with trifluoroacetic and trichloroacetic acid, suggesting acid dimerization can play a previously unexpected role in reactivity. For several acids, the observed rate constant was shown to increase with water concentration based on the pK_a of the parent acid, suggesting hydronium hydrate formation. By contrast, water caused the observed rate constant for trifluoroacetic acid to decrease, suggesting water inhibits acid dimerization through heteroconjugation. These data reveal that the selection of proton sources for study of molecular electrocatalysts must account for more than simply acid strength. It is critical to understand how each individual acid behaves and how this might be manifested in experimental results.

3.5. Experimental

3.5.1. General Materials and Methods

Synthesis of all compounds was performed under a nitrogen atmosphere, either on a Schlenk line or in an inert-atmosphere glovebox. Acetonitrile (Fisher Scientific, HPLC grade, > 99%) and diethyl ether (Fisher Scientific, >99%) were degassed with argon and dried using a Pure Process Technology solvent system. Aniline (Sigma-Aldrich), and Trifluoroacetic acid (Sigma-Aldrich, 99%) were degassed using a freeze-pump-thaw technique and stored in the inert-atmosphere glovebox and dimethylformamide (Fisher Scientific) was degassed by purging with nitrogen for 30 minutes and stored in the inert atmosphere glovebox. 4-methylaniline (Sigma-Aldrich), 4-bromoaniline (Acros Organics, 96%), 4-(methylbenzoate)aniline (Sigma-Aldrich), 4-cyanoaniline (Matrix Scientific), trichloroacetic acid (TCI America, >99%), trifluoromethansulfonic acid (Acros Organics, 99%), 3-nitroaniline (TCI, >98%), methyl orange (Aldrich), tetrabutylammonium iodide (Sigma),

silver trifluoracetate (Aldrich), and tetrafluoroboric acid diethyl ether complex (Aldrich) were used as received. The tetrafluoroborate salts of 4-methoxyaniliinium, 4-tertbutylanilinium, anilinium, 4-chloroanilinium, 4-bromoanilinium, 4-trifluoromethoxyaniilinium, 4-(methylbenzoate)anilinium, 4-trifluoromethylanilinium, and 4-cyanoanilinium, were prepared as reported.[38,67] Dimethylformamidium triflate,[85] and $[Ni(P_2^{Ph}N_2^{Ph})_2(MeCN)][BF_4]_2$[61] were prepared as reported. Tetrabutylammonium hexafluorophosphate (TCI, >98%) was recrystallized from hot ethanol, filtered, washed with cold ethanol, and dried under vacuum overnight. NMR spectra were taken on a Bruker 400 MHz spectrometer and reference to proteo solvent impurities.[137] Spectrophotometric titrations were performed on an Agilent Cary 60 UV-vis spectrophotometer as previously described.[67]

3.5.2. 4-methylanilinium and 4-iodoanilinium preparation

4-methylanilinium tetrafluoroborate, and 4-iodoanilinium tetrafluoroborate were prepared by the same procedure presented for the other aniliniums in the literature, however, starting weights for each were 4-methylaniline, 2.4 g, and 4-iodoaniline, 3.2 g. 4-methylanilinium: Yield 0.7 g, 16%. ^{1}H NMR (400 MHz, CD_3CN) δ (ppm): 8.1 (broad singlet, 3H, -NH_3), 7.36 (d, 2H, -C_6H_4-), 7.11 (d, 2H, -C_6H_4-), 2.41 (s, 3H, -CH_3). Anal. Calcd.: C, 43.12; H, 5.17; N, 7.18. Found: C, 43.36; H, 5.07; N, 7.24. 4-iodoanilinium: Yield 2.2 g, 49%. ^{1}H NMR (400 MHz, CD_3CN) δ (ppm): 7.85 (d, 2H, -C_6H_4-), 7.2 (d, 2H, -C_6H_4-). Anal. Calcd.: C, 23.49; H, 2.30; N, 4.56. Found: C, 23.63; H, 2.16; N, 4.53. Full ^{1}H NMR spectra provided in the SI.

3.5.3. Tetrabutylammonium trifluoroacetate preparation

1 g of silver trifluoroacetate and 1.65 g of tetrabutylammonium iodide were dissolved separately in 10 mL of acetone. The solution of tetrabutylammonium iodide was added

dropwise to the silver trifluoroacetate solution. Upon addition, silver iodide (a yellow solid) precipitated out of solution. The solvent was pulled off the supernatant under vacuum, leaving behind the tetrabutylammonium trifluoroacetate (a white solid). Anal. Calcd.: C, 60.82; H, 10.21; N, 3.94. Found: C, 59.88; H, 10.08; N, 3.85.

3.5.4. Stopped-Flow Experiments

Stopped-Flow experiments were performed on a Hi-Tech Scientific SF-61 DX2 double mixing stopped-flow in single mixing mode with Kinetic Studio data acquisition software (v2.33). Single wavelength kinetics measurements were taken using a dual reference/main PMT set-up with a tungsten lamp. Stopped-flow measurements were all performed under an N_2 atmosphere. This was accomplished by preparing solutions inside an inert-atmosphere glovebox in septum-sealed bottles. A solution of $[HNi(P_2^{Ph}N_2^{Ph})_2]^+$ (0.1 – 0.5 mM) was prepared by dissolving $[Ni(P_2^{Ph}N_2^{Ph})_2]^{2+}$ in approximately 10 ml of acetonitrile, then a 1 equiv. of sodium borohydride was added and the solution was diluted to 25 ml. Acid solutions were prepared from a fresh stock solution (along with a stock solution of base for the acid:base ratio studies). PEEK tubing was used to transfer solutions directly from sealed bottles to the stopped flow syringes to avoid exposure to air. To ensure purity, the syringe was purged three times with each solution prior to each measurement. In a typical experiment, one syringe was loaded with the $[HNi(P_2^{Ph}N_2^{Ph})_2]^+$ solution and the other was loaded with the acid solution (a fresh solution was prepared for each measurement). Upon injection, absorbance vs. time was monitored at 500 nm. Fitting of the resulting traces was performed using a single exponential in Igor Pro 6.34A Software. The residual borane was previously shown to not affect the stopped-flow kinetics.[42]

CHAPTER 4. Linear Free Energy Relationships in the Hydrogen Evolution Reaction: Kinetic Analysis of a Cobaloxime Catalyst

4.1. Introduction

Among the many homogeneous complexes that have recently been pursued as catalysts for hydrogen production,[10,51,138] cobaloxime derivatives have garnered tremendous attention for their versatility in hydrogen-evolving systems.[51,139] Specifically, cobaloximes (Scheme 4.1) have been reported to mediate H_2 production[139,140] under both aqueous and non-aqueous conditions as both electrocatalysts[51,93,94,141–147] and as components of photocatalysis schemes.[51,148–166] Significant experimental and theoretical work has been conducted to explore their primary operative catalytic mechanism(s).[51,94,139,141,142,167–170]

Scheme 4.1 $Co(dmgBF_2)_2(L)_2$.

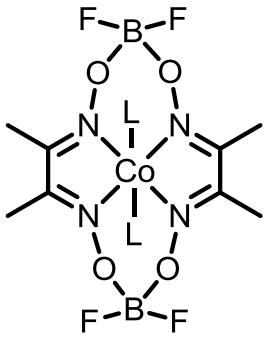

Two reaction mechanisms (Scheme 4.2) have been previously identified as viable pathways for H_2 production by $Co(dmgBF_2)_2(CH_3CN)_2$ (**1**):[167,168,170]

1) an *ECEC'* pathway in which H_2 is produced upon protonation of a Co^{II}–H species (**1^{2-}(H$^+$)**)

and

2) a bimetallic route by which two Co^{III}–H complexes (**1^-(H$^+$)**) react homolytically to release H_2, and reform two equivalents of **1**

In both pathways the reaction is initiated by reduction of **1** to **1^-** (E_1) followed by protonation to generate **1^-(H$^+$)** (C_1 in Scheme 4.2).[167,169,170] **1^-(H$^+$)** has been ascribed as a Co^{III}–H species,[51,94,155,167,168,170] though recent work from the groups of Peters[171] and Norton[172,173] have suggested that the metal hydride may tautomerize to a Co^I species with a protonated ligand. In contrast, spectral monitoring has revealed that protonation is accompanied by a substantial bleaching of the Co^I signal, data which support the initial assignment of **1^-(H$^+$)** as a Co^{III}–H.[168]

Scheme 4.2. Pathways of H_2 evolution.

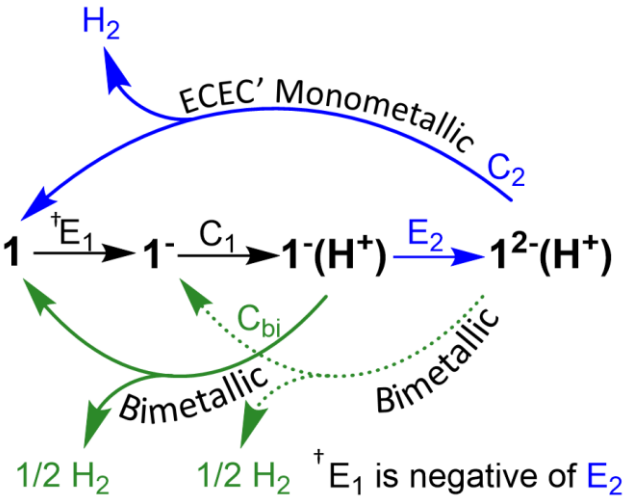

In the *ECEC'* monometallic pathway, reduction of $\mathbf{1}^{-}\mathbf{(H^{+})}$ (E_2) is expected to occur readily at applied potentials capable of reducing **1**; the reduction potential of $\mathbf{1}^{-}\mathbf{(H^{+})}$ has been computationally estimated to be *ca.* 20–100 mV more positive than that of $\mathbf{1}^{0/-}$.[167,170] $\mathbf{1}^{-}\mathbf{(H^{+})}$ and $\mathbf{1}^{-}$ can also undergo solution electron transfer to form $\mathbf{1}^{2-}\mathbf{(H^{+})}$ and **1** (k = 9.2 x 10^6 M^{-1} s^{-1}), as observed via transient absorption spectroscopy.[168] Subsequent protonation of the putative Co^{II}-H species $\mathbf{1}^{2-}\mathbf{(H^{+})}$ is followed by H_2 release and regeneration of the Co^{II} species (C_2). As previously mentioned, the $\mathbf{1}^{-}\mathbf{(H^{+})}$ species can also react via a bimetallic (homolytic) pathway in which two hydride species react to release H_2 (C_{bi}). This pathway involving $\mathbf{1}^{-}\mathbf{(H^{+})}$ was initially proposed based on the digital simulation of catalytic cyclic voltammograms for **1** with tosic acid and p-cyanoanilinium.[94] Computational work has also suggested that this pathway is viable,[167,169] and, more recently, evidence for the microscopic reverse of this reaction—homolytic cleavage of H_2 by **1**—has been presented using high H_2 pressures.[172–174] An analogous reaction could occur via the $\mathbf{1}^{2-}\mathbf{(H^{+})}$ species.

While these spectroscopic, electrochemical, and computational characterizations have provided critical insight to the catalytic pathways leading to H_2 production, these prior studies

have focused on H_2-evolving mechanisms with a limited set of structurally unrelated acids (i.e., tosic acid,[94] hydrochloric acid,[141,143] tetrafluoroboric acid,[141] trifluoroacetic acid,[141,143] *p*-cyanoanilinium,[143] triethylammonium,[142] and photoacids[168]). Additionally, no correlations between reaction kinetics and acid strength have been made. Finally, two factors have made reexamining the electrochemical analysis of **1** attractive:

1) the last decade has witnessed the development of powerful methods for analyzing catalytic cyclic voltammograms[34,44,68,175,176]

and

2) it has been recognized that the nuances of acid behavior in non-aqueous solvents (e.g., homoconjugation) can have profound impacts on electrocatalytic responses.[67,112,126,128]

Thus, we revisited the electrocatalytic activity of **1** in acetonitrile to obtain improved mechanistic information and to determine if the elementary step kinetics can be clearly correlated with proton source strength.

In this work, we utilize cyclic voltammetry to evaluate **1** as a H_2-evolution catalyst with *para*-substituted anilinium derivatives spanning a five pK_a(CH_3CN) unit range (ca. 7–12). Experiments were performed to assess the stability of **1** in the presence of these acids and care was taken to minimize catalyst decomposition during measurement.[94,141–143] This careful methodology enabled the catalytic order in **1** to be reassigned as one, rather than less than first order as initially reported.[94]

Additionally, systematic analyses of catalytic voltammograms indicate that an *ECEC'* reaction mechanism is primarily operative under the conditions used. Rate constants for two acid-dependent elementary steps and one acid independent step of the catalytic cycle were determined through evaluation of catalytic currents, foot-of-the-wave analysis, and, for systems exhibiting waveforms conforming to the total catalysis zones of Savéant's *EC'* zone diagram,[22] assessment of current-potential responses. Both the first and second proton transfers to the catalyst are governed by similar linear free energy relationships, while an acid-independent rate constant describes the kinetics after the second proton transfer. Additionally, we demonstrate for the first time that kinetic information can be determined from current-potential analysis of total catalysis waveforms for two-electron, two-proton processes and that these kinetic data are consistent with those obtained via foot-of-the-wave analysis. Together, these studies provide new insight to the pathways of cobaloxime-mediated H_2 production and illustrate the extensive kinetic and mechanistic detail that can be gleaned from catalytic cyclic voltammograms.

4.2. Results and Discussion

4.2.1. Electrochemistry of $Co(dmgBF_2)_2(CH_3CN)_2$

A $Co(dmgBF_2)_2(CH_3CN)_2$ (**1**), formed upon dissolution of $Co(dmgBF_2)_2(H_2O)_2$ in acetonitrile,[141] was analyzed by cyclic voltammetry (CV). In the absence of acid, a reversible one-electron wave, assigned to the $Co^{II/I}$ ($\mathbf{1^{0/-}}$) couple, is observed with $E°' = –0.914$ V (all values reported vs. Fc^+/Fc couple), in agreement with prior reports (Figure 4.1).[141] An irreversible, one-electron wave, assigned to the $Co^{III/II}$ couple ($\mathbf{1^{+/0}}$), is observed with $E_{1/2} = +0.125$ V. The voltammetric responses were then recorded for **1** in the presence of acid across a series of *para*-substituted anilinium derivatives. Anilinium has a small homoconjugation

formation constant of ca. 4,[108] and substituted anilinium derivatives are expected to have similarly small homoconjugation constants.[67,112] The acids utilized spanned five pK_a units (pK_a values (CH_3CN): 4-methoxyanilinium, pK_a = 11.86;[105] 4-*t*-butylanilinium, pK_a = 11.1;[67] anilinium, pK_a = 10.62;[105] 4-chloroanilinium, pK_a = 9.7;[67] 4-trifluoromethoxyanilinium, pK_a = 9.28 (see SI–1, Supporting Information); 4-(methylbenzoate)anilinium, pK_a = 8.62;[38] 4-trifluoromethylanilinium, pK_a = 8.03;[105] 4-cyanoanilinium, pK_a = 7.0).[177] For all acids, an increase in cathodic current and loss of reversibility was observed at the $\mathbf{1}^{0/-}$ couple, indicating catalytic acid reduction.

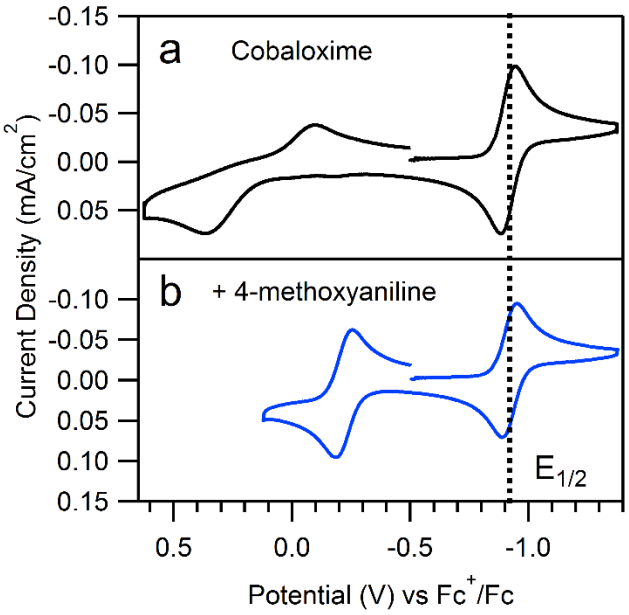

Figure 4.1. Effect of aniline bases on electrochemistry of 1. Cyclic voltammograms of a) 0.38 mM **1**, alone; and b) in the presence of 2 mM 4-methoxyaniline. Addition of 4-methoxyaniline alters the electrochemical reversibility and potential of the $\mathbf{1}^{+/0}$ ($Co^{III/II}$) wave, but does not affect the $\mathbf{1}^{0/-}$ ($Co^{II/I}$) wave. Voltammograms recorded at 100 mV/s in 0.25 M $[Bu_4N][PF_6]$.

In addition to the catalytic response currents observed near $E°'(\mathbf{1}^{0/-})$ upon the addition of anilinium acids, a new reversible wave appears in the voltammogram during catalytic measurements and the irreversible $\mathbf{1}^{+/0}$ wave vanishes. This wave was found to vary in location

depending upon acid strength with the weakest acid (4-methoxyanilinium pK_a = 11.86) resulting in a reversible wave at approximately $E_{1/2}$ = –0.22 V; stronger acids result in a positive shift of the wave. Addition of aniline bases to solutions of **1** (without acid) gives rise to an identical feature (Figure 4.1b), suggesting that this new wave results from the oxidation of a cobalt complex in which aniline (formed during catalysis) has coordinated the metal center, likely displacing the axial acetonitrile ligands. Although the position of the $\mathbf{1}^{+/0}$ ($Co^{III/II}$) wave is affected by dissolved aniline, the $\mathbf{1}^{0/-}$ ($Co^{II/I}$) wave is not (Figure 4.1). This suggests that a rapid equilibrium between the aniline-bound and unbound species gives rise to this behavior and that the oxidized $\mathbf{1}^{+}$ (Co^{III}) species is stabilized by aniline base. The kinetic data herein indicate that the same acetonitrile-coordinated species is active for catalysis with all acids used. UV-vis titrations of **1** with aniline suggest that **1** can reversibly bind two equivalents of aniline in a stepwise fashion (Appendix C.2).

Across the series of anilinium acids studied, the catalytic response currents differ substantially in their shape and position.[178] For acids of pK_a > ca. 9.5, the onset of the catalytic wave occurs at potentials more positive than $\mathbf{1}^{0/-}$ and a broad oxidation wave is observed on the anodic scan, a feature that is most pronounced at low acid concentration, suggesting oxidation of a singly protonated species that has yet to turn over (see Appendix C.6). The catalytic waves are peaked at the lowest acid concentrations recorded (ca. 1 – 8 mM) and approach a plateau shape at higher concentrations (Figure 4.2a). The catalytic current density approaches a scan rate independent regime. Stronger acids shift the catalytic wave to even more positive potentials and reduce the current magnitude of the broad oxidation wave. For the strongest acids explored, pK_a < ca. 9.5, a double-peaked waveform is observed at low acid concentrations, which, as the acid concentration is increased, transforms into a sharp, single

peaked waveform (Figure 4.2b). For these stronger acids, a plateau shape is not reached until concentrations of ca. 30 mM acid; however, at these concentrations the current response becomes independent of acid concentration (zero order in acid) and reaches a limiting current value (see below).

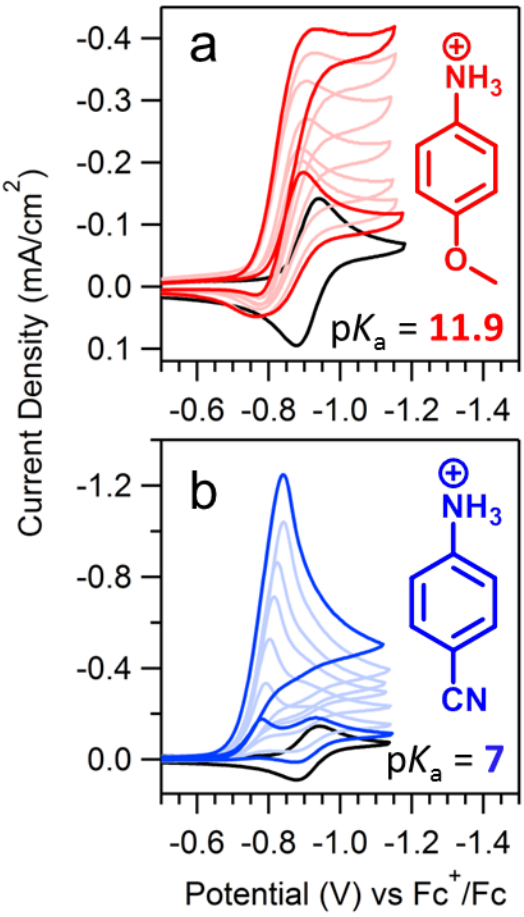

Figure 4.2. Catalytic cyclic voltammograms of 0.5 mM 1. a) Cyclic voltammograms of 0.5 mM **1** with additions of 4-methoxyanilinium (0, 1, 2, 4, 8, 12, 20, and 28 mM, respectively). b) Cyclic voltammograms of 0.5 mM **1** with additions of 4-cyanoanilinium (0, 0.5, 1.0, 1.5, 2.0, 2.5, 3.0, and 4.0 mM, respectively). Voltammograms recorded at 100 mV/s in 0.25 M $[Bu_4N][PF_6]$.

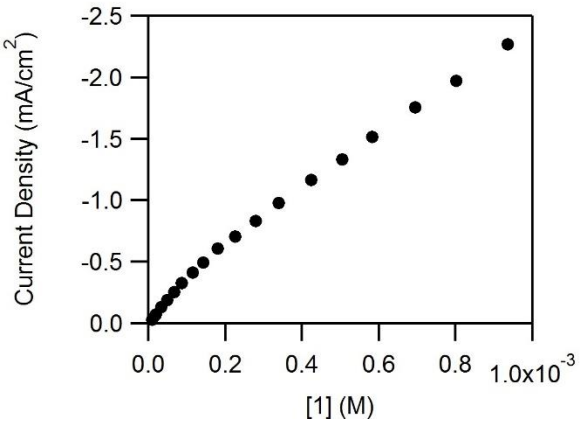

Figure 4.3. Plateau currents for cyclic voltammograms of varying concentrations of **1** with 75 mM anilinium. Voltammograms recorded at 100 mV/s in 0.2 M $[Bu_4N][PF_6]$. See SI–3 for voltammograms.

4.2.2. Identifying the Dominant Reaction Mechanism

Previously, catalysis by **1** with *para*-toluenesulfonic acid (tosic acid) was found to be less than first order in catalyst (**1**).[94] In this work, catalytic voltammograms were recorded for an extended range of catalyst concentrations (0–1 mM) in the presence of 75 mM anilinium (Fig. 3). These data, like those reported in reference[94], reveal catalytic currents that have a less than first order dependence on the concentration of **1**. Another dataset was obtained with 4-trifluoromethylanilinium; the same behavior was observed (Appendix C.2). Two possible scenarios were postulated. First, inhibition of catalysis by the formation of a dimerized cobalt species in solution was considered. This was ruled out by overlaying the anilinium and 4-trifluoromethylanilinium datasets (Appendix C.2). Inhibition would affect both datasets in the same manner and therefore the two datasets should have identical curvature, yet they display unique dependencies on catalyst concentration. Second, inhibition of catalysis by aniline base formed within the reaction layer (as a product of catalytic H_2 production) was considered. As discussed above, aniline bases are capable of ligating **1**, and the aniline-bound species should have a more negative reduction potential than the corresponding acetonitrile bound species. As

the catalyst concentration is increased, more aniline is formed in the reaction layer. Digital simulation confirmed that under steady state catalytic conditions, the coordination of aniline will inhibit catalysis as the aniline must dissociate prior to reduction at the catalytic potentials considered in this work (Appendix C.2). These data and simulations indicate that catalysis is indeed first order in catalyst concentration, but the plateau current vs. catalyst concentration plot deviates from linearity as catalyst concentration is increased due to the effects of catalyst inhibition by aniline coordination.

While the coordination of aniline explains the deviation from linearity in the plateau current vs. catalyst concentration plot recorded in this work, reference 7 used tosic acid in the study of **1**. It seemed unlikely that tosylate readily binds **1** and UV-vis titrations in our lab suggest that it does not under the conditions explored. In order to understand the less than first order dependence in reference 7, catalytic voltammograms were collected with tosic acid as the proton source (Fig. 4). Under the conditions explored in reference 7, the catalytic voltammograms transition from a plateau to a peaked shape as the catalyst concentration is increased, suggesting substrate depletion at high concentrations of **1**. This was confirmed by comparing a plot of catalytic peak height current vs. [**1**] to the plot of current at a specific applied potential early in the catalytic wave (prior to substantial substrate depletion) vs. [**1**]. Current values recorded at the peak of the voltammogram exhibit a less than first order appearance on catalyst, while the current obtained early in the catalytic wave is linear with respect to catalyst concentration.

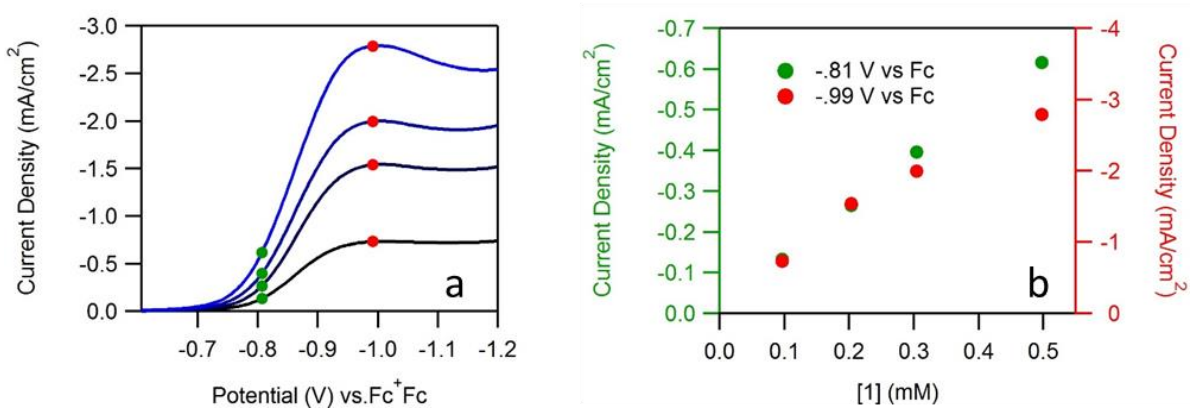

Figure 4.4. Voltammograms of varied concentrations of **1** in the presence of 37 mM tosic acid. a) As the concentration of **1** is increased, the voltammograms become peaked, likely due to substrate depletion. b) Green data points represent the current passed near the foot of the wave, prior to substrate depletion and show a response consistent with first order kinetics with respect to [**1**]. Red data points represent the peak current and demonstrate the effect of substrate depletion on the apparent order. Voltammograms recorded at 100 mV/s in 0.2 M $[Bu_4N][PF_6]$.

Next, the catalytic response currents were recorded as a function of acid concentration. For weaker acids (pK_a > ca. 9.5), plots of the catalytic plateau current i_{pl} (for samples at low acid concentrations, where no plateau is observed, the peak current was used) versus $[acid]^{1/2}$ are linear (see below), indicating that the observed rate constant for catalysis is first order in acid, consistent with prior results.[94,143] It should be noted that **1** decomposes slowly in the presence of both tosic acid and 4-trifluoromethylanilinium, as observed by UV-Vis absorption measurements (for example, for a 0.2 mM solution of **1**, ca. 10% of the absorbance at 425 nm is lost over one hour in presence of 60 mM 4-trifluoromethylanilinium). Consequently, care was taken during measurements to minimize acid-catalyst encounter time (see Section 4.4.3 and Appendix C.4).

Together, these observations can be used to assign the dominant operative mechanism as a heterolytic *ECEC'* pathway. Catalysis that is first order in both catalyst and acid indicates either 1) a monometallic *ECEC'* pathway or 2) a homolytic pathway in which the first protonation step is rate limiting. For this system, the observation that $E_{cat/2}$ (the half-wave

potential for the catalytic sigmoid) shifts to values positive of $E°'(\mathbf{1}^{0/-})$ indicates that the first chemical step (protonation of $\mathbf{1}^-$) is rapid relative to subsequent chemical steps.[44] With rapid protonation of $\mathbf{1}^-$, the first order dependence of the plateau current on both catalyst concentration and acid concentration thus diagnose the reactivity as heterolytic, in contrast to the $[\text{acid}]^0$ and $[\text{catalyst}]^{3/2}$ dependences expected for the homolytic pathways.[176] Of note, given that the inhibition from aniline binding appears to be minor at the concentrations of **1** we have chosen to work with (~0.5 mM), we have chosen to simplify the analysis of kinetics by proceeding without explicit consideration for this phenomena.

4.2.3. Determination of Global Rate Constants from Plateau Currents

With an *ECEC'* assignment, an observed rate constant (k_{pl}) for catalysis can be directly determined from Eq. 4.1. This equation describes the plateau current, i_{pl}, for an *ECEC'* reaction in which the second electron transfer is easier than the first. In Eq. 4.1, D_P is the diffusion coefficient of the catalyst, F is Faraday's constant, A is the geometric electrode surface area, and C_P^0 is the concentration of the catalyst, [**1**].[12–14] D_P was determined from the scan rate dependence of the peak current of the reversible $\mathbf{1}^{0/-}$ wave and the Randles-Sevcik equation (see Appendix C.1). In most cases, k_{pl} was found to be first order with respect to acid concentration (see below), allowing the second order rate constant k_{global} ($k_{pl} = k_{global} C_A^0$, where C_A^0 is the acid concentration) to be determined for each of the acids.

As noted above, the positive potential shift observed for catalytic waves indicates that the initial protonation of $\mathbf{1}^-$ (described by k_1) is rapid. From this, it is assumed that k_{global} does not equal k_1, but instead reflects the rate constant describing the second protonation step, k_2. This is later confirmed by direct determination of k_1 (see below). A linear correlation is

observed between log(k_2) and acid pK_a (slope = –0.77), indicating overall acceleration of catalysis with stronger acids (Figure 4.5).

$$i_{pl} = 2FAC_P^0\sqrt{D_P k_{pl}} \quad \text{(Eq. 4.1)}$$

Of note, Eq. 4.1 assumes that the two electrons required to complete catalytic turnover are transferred to the catalyst at the electrode.[44] It is possible that the second reduction occurs via a homogeneous electron transfer from **1**$^-$ (a disproportionation mechanism, DISP[22]); however, the rate of homogeneous electron transfer from **1**$^-$ to **1**$^-$**(H**$^+$**)** is relatively slow (k = 9.2 x 10^6 M^{-1} s^{-1}).[168] Further, by cyclic voltammetry no definitive evidence to distinguish electron transfer at the electrode vs. DISP, such as curve crossing,[22] was observed. If DISP facilitates the second electron transfer, the application of Eq. 4.1 will introduce a small margin of error for this system (rates underestimated by a factor of 2 or less[68]).

For stronger acids (pK_a < ca. 9.5), no plateau currents are observed and plots of the *peak* current vs. [acid]$^{1/2}$ are *not* linear. By contrast, linearity is observed for *peak* current vs. [acid], with identical slopes (ca. –300 μA cm^{-2} M^{-1}) for all acids in the regime. This, along with the observation of sharply peaked voltammograms, indicates that the catalytic current response is governed by diffusion of substrate into the reaction layer (see appendix C.4).[22] Under these conditions, Eq. 4.1 cannot be applied. Instead, the linear relationship established between log(k_2) and pK_a for acids of pK_a > ca. 9, was extrapolated into the lower pK_a regime to estimate k_2 for acids in the pK_a-independent region (Figure 4.5).

4.2.4. Evaluating k_1 via Foot-of-the-Wave Analysis

A Foot-of-the-wave analysis (FOWA) was used to estimate the rate constant for the *first* chemical step (k_1) of hydrogen evolution. FOWA can be used to extract kinetic information from the onset, or 'foot,' of the catalytic wave, a region where the current-potential

response exhibits 'idealized' behavior and few side phenomena (e.g., catalyst degradation and substrate consumption) impact the voltammogram.[13,34,44,179] For *EECC'*, *ECEC'*, and *ECCE'* reaction pathways in which all of the electron transfers occur at the electrode, the current-potential response at $E >> E^{\circ\prime}(\mathbf{1}^{\mathbf{0}/-})$ can be approximated by Eq. 4.2, where T is temperature and R is the gas constant.[44] Eq. 4.2 can be divided by the Randles-Sevcik equation, which describes the peak current (i_p) of a homogeneous, diffusion controlled one-electron transfer reaction, to produce Eq. 4.3, where $E-E^{0\prime}$ is the difference between the applied potential (E) and the formal potential of the redox couple ($E^{0\prime}$) in the absence of substrate (e.g., the $\mathbf{1}^{\mathbf{0/-1}}$ redox couple that triggers catalysis), υ is scan rate, and n is the number of electrons transferred in the homogeneous process.

$$i_c \approx 2FAC_{\mathrm{P}}^{0}\sqrt{D_{\mathrm{P}}k_{FOWA}}\exp\left[-\frac{F}{RT}\left(E-E^{0\prime}(\mathbf{1}^{\mathbf{0}/-})\right)\right] \qquad \text{(Eq. 4.2)}$$

$$\frac{i_c}{i_p} \approx \frac{4.48}{n}\sqrt{\frac{RTk_{FOWA}}{nF\upsilon}}\exp\left[-\frac{F}{RT}\left(E-E^{0\prime}(\mathbf{1}^{\mathbf{0}/-})\right)\right] \qquad \text{(Eq. 4.3)}$$

Plots of i_c/i_p vs. $\exp\left[-\frac{F}{RT}\left(E-E^{0\prime}(\mathbf{1}^{\mathbf{0}/-})\right)\right]$ are linear near the foot of the wave, and an observed rate constant (k_{FOWA}) can be determined from the slope of this region (see Appendix C.5). As FOWA has not previously been applied to voltammograms exhibiting total catalysis (total consumption of substrate at the electrode surface followed by the reversible wave of catalyst reduction[22,23]), we carried out a series of digital simulations to evaluate whether or not FOWA can be reliably extended to these voltammograms. Our simulations indicate that FOWA provides an accurate value for the simulated rate constant, even under total catalysis conditions (see appendix C.5).

Values for k_{FOWA} were found to correlate linearly with acid concentration, allowing a second order rate constant, k_1 ($k_{FOWA} = k_1 C_{\mathrm{A}}^{0}$), to be calculated for each acid (obtaining k_{FOWA}

required careful consideration of the formation of aniline bound species, as such binding interfered with precise referencing of voltammograms, see appendix C.5). Values for k_1 spanned 3.06 x 10^4 – 2.73 x 10^8 M^{-1} s^{-1} (Figure 4.5). As was the case for k_2, a linear correlation is observed between log(k_1) and pK_a (for the acids with pK_a > 8.5) with a slope of –0.97 (Table 4.1, Figure 4.5). The rate constants for the two strongest acids deviate from this linear correlation, likely because the values are approaching the diffusion limit or are reaching a limiting value with respect to the electron transfer rate considering the significant kinetic shifts of the voltammetric response. Values for k_1 are three orders of magnitude greater than those of k_2 (k_{global}). This further supports the assignment that the protonation step described by k_1 is not the rate limiting step and that k_{global} reflects k_2, the protonation of $\mathbf{1^{2-}(H^+)}$ (see above).

Table 4.1. Table of calculated rate constants as determined by FOWA (k_1), plateau analysis (k_2), and the maximum plateau current (k_Ω). *Indicates k_2 values extrapolated from data points in the higher pK_a regime.

Acid Identity	***pK$_a$ (CH$_3$CN)***	***k_1 (M^{-1} s^{-1})***	***k_2 (M^{-1} s^{-1})***	***k_Ω (s^{-1})***
4-methoxyanilinium	11.86	3.06×10^4	33.9	-
4-tert-*butylanilinium*	11.1	1.45×10^5	151	-
anilinium	10.62	4.66×10^5	328	-
4-chloroanilinium	9.7	3.70×10^6	1760	-
4-trifluoromethoxyanilinium	9.28	9.91×10^6	3340	~125
4-(methylbenzoate)anilinium	8.62	3.80×10^7	11500*	-
4-trifluoromethylanilinium	8.03	7.97×10^7	32700*	~125
4-cyanoanilinium	7.0	2.73×10^8	204000*	~125

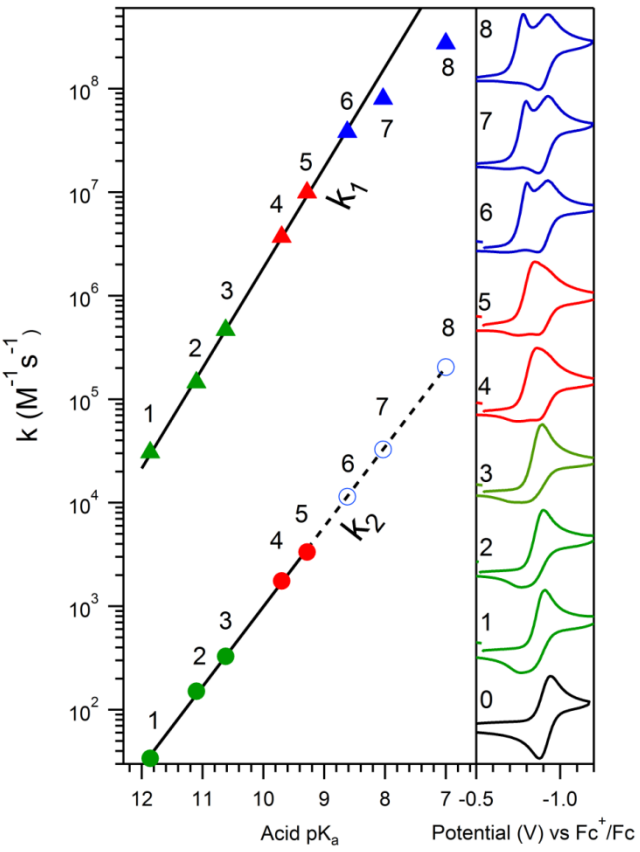

Figure 4.5. All rate constants as a function of pKa. *Left:* Rate constants calculated in this work. k_2 (k_{global}) values (solid circles) were calculated from acid concentration-dependent catalytic plateau currents using Eq. 4.1. Extrapolated values for k_2 (empty circles) were estimated using the linear relationship established at higher pK_a values. k_1 values were calculated by applying FOWA to the acid titration experiments. *Right:* cyclic voltammograms of solutions containing 1 and 1 equivalent of an anilinium derivative. Anilinium identities: 0) no acid, 1) 4-methoxyanilinium, 2) 4-*t*-butylanilinium, 3) anilinium, 4) 4-chloroanilinium, 5) 4-trifluoromethoxyanilinium, 6) 4-(methylbenzoate)anilinium, 7) 4-trifluoromethylanilinium, and 8) 4-cyanoanilinium. Voltammograms recorded at 100 mV/s in 0.25 M [Bu_4N][PF_6].

4.2.5. Acid-independent Catalytic Currents at High Substrate Concentrations

As acid concentration is increased, i_c reaches a limiting value (i_c^{MAX}) that is constant across all acids explored (Figure 4.6). The concentration of acid required to reach this concentration- and pK_a-independent current decreases as acid strength increases. These data indicate that under such conditions, a slow, acid-independent step governs catalytic turnover. We describe this acid-independent step by a first-order rate constant (k_Ω) and speculate that it may reflect formation of the H–H bond or release of H_2 from the **1(H$_2$)** species. From the

average value for i_c^{MAX} (obtained from solutions containing **1** and acids of pK_a ca. 7-9), k_Ω was determined from Eq. 4.1 to be ca. 125 s^{-1}. In order to determine if this acid-independent step affects the accurate determination of k_1 from FOWA and k_2 from plateau current analysis, a series of digital simulations were carried out.[38] We found that incorporation of this step into a kinetic model does not impact FOWA and minimally impacts the plateau analysis for moderate strength acids, and not at all for weak acids.

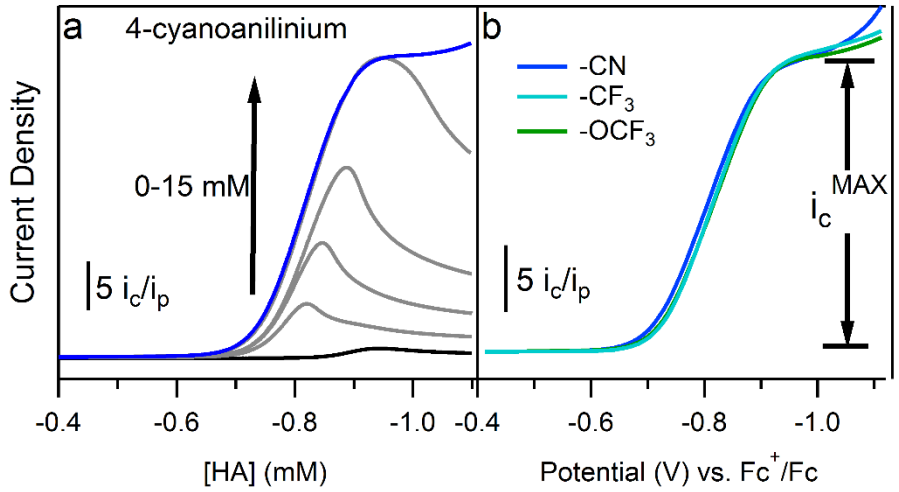

Figure 4.6. a) Cyclic voltammograms of 0.5 mM 1 in the presence of 0–15 mM 4-cyanoanilinium. b) Cyclic voltammograms of 0.5 mM 1 in the presence of para-substituted anilinium derivatives: 60 mM 4-cyanoanilinium (–CN, dark blue), 60 mM 4-trifluoromethylanilinium (–CF_3, light blue), and 180 mM 4-trifluoromethoxyanilinium (–OCF_3, green). Voltammograms recorded at 100 mV/s in 0.25 M [Bu_4N][PF_6].

4.2.6. Extracting Kinetic Information from Voltammograms Exhibiting Total Catalysis

A The catalytic voltammograms generated for **1** with the strongest employed anilinium acids (pK_a < ca. 9) exhibit both a catalytic wave and the reversible catalyst-only $\mathbf{1}^{0/-}$ redox wave at low acid concentrations, features that merge into a single, sharply peaked wave at higher acid concentrations (Figure 4.2). This behavior is notable and is indicative of total catalysis (zones KT2 and KT1 in Savéant's EC' zone diagram).[23,68] Further consistent with the

assignment of total catalysis is the linear relationship between the catalytic peak current and C_A^0 (see above). This linear relationship indicates that substrate diffusion governs the catalytic response.[22] At applied potentials ca. 100 mV positive of $E°'$(**1**$^{0/-}$), only a small fraction of **1** has been reduced to **1**$^-$, as governed by the Nernst equation. However, in the presence of strong acids (pK_a < ca. 9) the catalytic rate is sufficiently fast to ensure that even small amounts of activated catalyst (**1**$^-$) consume all substrate at the surface of the electrode. Consequently, catalytic current quickly peaks as the reaction layer is depleted of acid, leaving only **1**, H_2, and the conjugate base at the electrode surface. As the potential is scanned further cathodically, more **1** is reduced (per the Nernst Equation), but the **1**$^-$ formed has no substrate to reduce, and is thus re-oxidized during the anodic scan, giving rise to a reversible wave after the initial catalytic response (zone KT2).[22,23,68] Concentration profiles generated from simulated datasets further illustrate this concept (appendix G). As the substrate concentration is increased (increasing the excess factor, $\gamma = C_A^0/C_P^0$), the reversible wave becomes obscured by the catalytic wave, indicating the catalyst is now operating in zone KT1.[22,23,68]

To the best of our knowledge, there are only four experimental examples of total catalysis that have been published in the literature,[142,180–182] with a few accompanying discussions.[23,183–185] These examples identify the experimentally-produced zone KT2 waveform shapes; however, none evaluate the voltammetric responses to determine kinetic information, despite clear relationships between peak potential E_p and experimental parameters that have been thoroughly characterized by Savéant and coworkers (Eq. 4.4).[22]

$$E_p = E^{0\prime} - \frac{RT}{F}(0.409) + \frac{RT}{2F} ln\left(\frac{RTk_1 D_P (C_P^0)^2}{F\upsilon D_A C_A^0}\right) \qquad \text{(Eq. 4.4)}$$

To obtain kinetic information, the total catalysis waveforms were examined for solutions that contained the three strongest acids (4-cyanoanilinium, 4-

trifluoromethylanilinium, and 4-(methylbenzoate)anilinium), and were evaluated with respect to the three variables known to affect total catalysis waveforms from Eq. 4.4, C_A^0, υ, and C_P^0 (Figure 4.7).

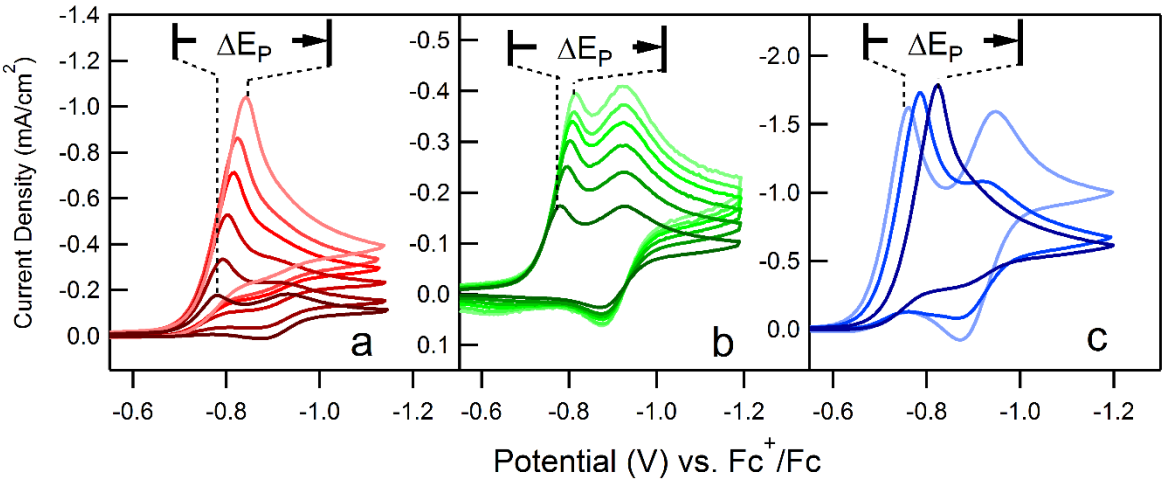

Figure 4.7. Sets of voltammograms in which each of the variables in Eq. 4.5 were varied. a) Titrations of 4-cyanoanilinium (0.5, 1.0, 1.5, 2.0, 2.5, 3.0 mM) into a 0.5 mM solution of 1 at 100 mV/s. b) Voltammograms of 0.5 mM 4-cyanoanilinium and 0.5 mM 1 at 100, 200, 300, 400, 500, and 600 mV/s. c) Solutions of 5 mM 4-cyanoanilinium and 1.25, 2.5, and 5.0 mM 1 at 100 mV/s. Voltammograms recorded in a 0.25 M [Bu_4N][PF_6].

The absence of kinetic analysis for previous experimental systems is likely because Eq. 4.4 was derived for a one-electron, one-substrate *EC'* reaction. The limited scope of Eq. 4.4 restricts analysis of multi-electron, multi-step reactions, such as the one explored in this work. Eager to extract additional kinetic and mechanistic information from the waveforms conformed to zones KT2 and KT1, we empirically determined, through rigorous simulations, an analogue to Eq. 4.4 that accommodate a two-electron, two-substrate reaction.

Peak shift analysis of KT2 voltammograms measures the kinetic shift of the voltammogram in much the same way as FOWA. With this in mind, it must first be recognized that analyzing the peak shift for an *ECEC'* mechanism will primarily reveal information about k_1, the first chemical step, as it is responsible for the kinetic shift. Simulations were performed to determine the overall contributions of k_1 and k_2 to the peak location during total catalysis

(see appendix G). We initially hoped that we might be able to determine k_1 using FOWA and then use the nuances of the KT2 peak location to determine k_2, however, we found that the effect of k_2 on the peak was minimal and could only serve to induce error in the measurement (see appendix G). In order to identify an expression correlating peak position for total catalysis waveforms and k_1 for *ECEC'* reaction mechanisms, we initially made two assumptions: 1) that the second electron transfer is much easier than the first, and 2) k_2 is much faster than k_1. From these assumptions, we empirically generated a new expression, Eq. 4.5, to describe the effect of k_1 on the catalytic peak location (E_P).

$$E_p = E^{0\prime} - \frac{RT}{F}(0.409) + \frac{RT}{2F} ln\left(\frac{RTk_1 D_P (2C_P^0)^2}{Fv D_A C_A^0}\right) \qquad \text{(Eq. 4.5)}$$

Eq. 4.5 differs from Equation 4.4 by the concentration of catalyst; in Eq. 4.5 the catalyst concentration is multiplied by two. Under the assumptions defined, we have generated a scenario in which the moment the catalyst is reduced it consumes two equivalents of substrate, thus acting as if the concentration of catalyst had been doubled.

Realizing that the assumptions made to empirically determine Eq. 4.5 limit the application of this expression to analyze total catalysis waveforms, rigorous simulation was performed to determine the conditions under which Eq. 4.5 is practical. From these simulations, we sought to determine the relative formal potentials of the two electron transfer processes ($E_2 - E_1$) and the relative values of k_1 and k_2. For *complete* accuracy, two conditions must be satisfied, 1) both k_1 and k_2 must be greater than 1 x 10^7 M^{-1} s^{-1}, but k_2 does *not* need to be faster than k_1, and 2) $\log(k_2/k_1) + 32(E_2 - E_1) > 2.7$ (full details of the conditions along with measures of the accuracy outside of these bounds can be found in appendix G). While these boundaries are not formulated in terms of dimensional parameters, they provide a general description of the limitations of Eq. 4.5. Use of Eq. 4.5 outside of the specified conditions will

always result in an *underestimation* of k_1. Unfortunately, it is difficult to know if these conditions have been met. In this work, we considered the three strongest acids and determined that they most closely match the conditions required to apply Eq. 4.5. It was found that the results obtained are consistent with the FOWA results, despite failure to fully conform to the conditions necessary for complete accuracy (Table 4.2, Figure 4.8).

Table 4.2. k_1 rate constants calculated using the Eq. 4.5 and FOWA.

Variable Changed	*4-cyanoanilinium* $k_1\ (M^{-1}s^{-1})$	*4-trifluoromethylanilinium* $k_1\ (M^{-1}s^{-1})$	*4-(methylbenzoate)anilinium* $k_1\ (M^{-1}s^{-1})$
C_A	$2.32\text{x}10^8$	$7.06\text{x}10^7$	$2.95\text{x}10^7$
v	$1.31\text{x}10^8$	$6.10\text{x}10^7$	$3.39\text{x}10^7$
C_P^0	$9.57\text{x}10^7$	-	-
Average	$1.53\text{x}10^8$	$6.58\text{x}10^7$	$3.17\text{x}10^7$
FOWA ***value:***	$2.73\text{x}10^8$	$7.97\text{x}10^7$	$3.80\text{x}10^7$

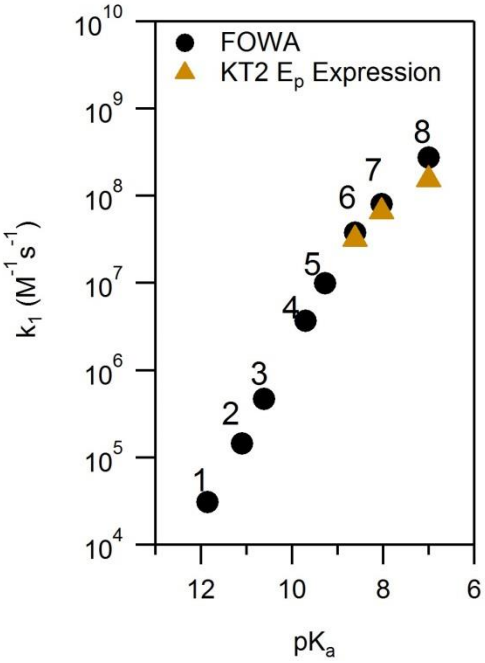

Figure 4.8. Black points: k_1 values as produced by FOWA of acid titrations into solutions of 0.5 mM 1 at 100 mV/s. Gold points: k_1 values as determined from Eq. 4.5. For points 6 and 7, the average k_1 was calculated from acid titration and scan rate variation data. For 8, k_1 was calculated from the average of acid titration, scan rate, and catalyst concentration data.

In summary, we found that analysis of KT2 peak locations can be accomplished for multi-electron, multi-substrate systems under certain conditions. Given the limitations of the

empirically determined Eq. 4.5, researchers may find more general application of FOWA to determine reaction kinetics from voltammograms exhibiting total catalysis. Ultimately, derivation of equations to describe peak shifts of KT2 voltammograms for the various multi-electron, multi-substrate reactions will provide more comprehensive insight to reaction kinetics from total catalysis waveforms.

4.2.7. Mechanistic Insight into Cobaloxime-Catalyzed Hydrogen Production

Collectively, these data provide new insight to cobaloxime-catalyzed hydrogen production. The kinetics analysis for this series of aniliniums is consistent with an *ECEC'* mechanism, as illustrated in Figure 4.9. The rate constants for protonation of $\mathbf{1}^{-}$ (k_1), determined via FOWA and current-potential analysis of voltammograms exhibiting total catalysis behavior, are not rate-limiting and increase with decreasing pK_a.

The reaction intermediate formed upon protonation, $\mathbf{1^{-}(H^{+})}$, a putative Co^{III}-H that may tautomerize, is readily reduced to $\mathbf{1^{2-}(H^{+})}$. Subsequent protonation of this Co^{II}-H (or tautomer), $\mathbf{1^{2-}(H^{+})}$, occurs with a rate constant (k_2) that is acid pK_a dependent and approximately 3 orders of magnitude slower than the respective k_1 value, as determined from analysis of acid-dependent plateau currents which reflect the rate-limiting step. Identification of two starkly different second-order rate constants supports the assignment of an *ECEC'* reaction pathway. The resulting $\mathbf{1^{2-}(H^{+})_2}$ (Co^{II}–H_2) species then undergoes an acid-independent step with a first-order rate constant (k_Ω) of 125 s^{-1}, likely H–H bond formation or H_2 release. k_Ω was determined from catalytic voltammograms recorded at high acid concentrations in which the voltammetric responses were acid concentration- and pK_a-independent.

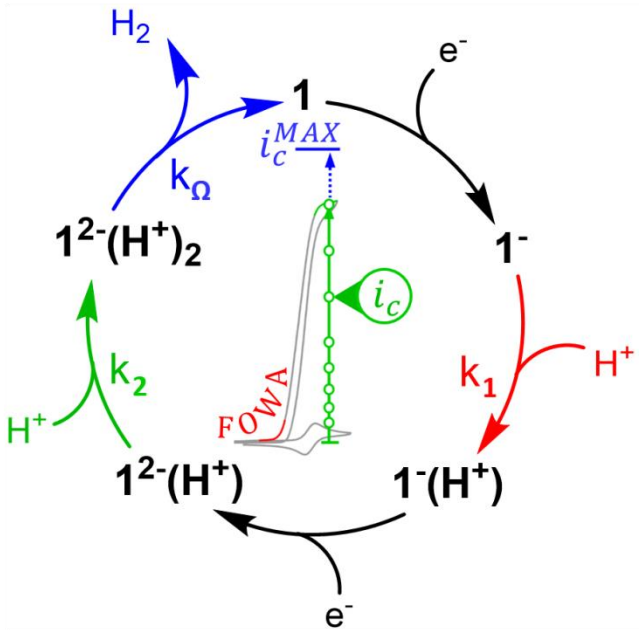

Figure 4.9. The proposed hydrogen evolving mechanism of 1. Rate constants were determined by FOWA (k_1), Eq. 4.1 (k_2), and via interpretation of $\boldsymbol{i_c^{MAX}}$ (k_Ω).

The *ECEC′* mechanism supported by our data is not consistent with the conclusions of two earlier mechanistic analyses of voltammetric data, which, based on digital simulations of catalytic voltammograms, concluded that either *ECCE′*[143] or *ECC′* (homolytic)[94] pathways were operative. However, neither study considered a pathway involving the reduction of **1**$^{-}$**(H**$^{+}$**)** in the analysis. Not until experimental evidence of **1**$^{-}$**(H**$^{+}$**)** (Co^{III}–H) reduction by excess Co^{I} in solution[168] and a pair of concurrent theoretical reports was it established that the $Co^{III/II}$–H reduction potential was positive of $E°'(Co^{II/I})$ (it had previously been thought that $E°'(Co^{III/II}$–H) occurred at ca. –1.38 V).[94,167,170]

While our data do *not* indicate that a bimetallic (homolytic) mechanism dominates under the conditions explored in this work, this route could be a minor but concurrent pathway and/or could be accessed under alternative conditions.[176] Recent experimental and theoretical work has suggested that such a pathway is viable.[167,169,172–174] The pursuit of experimental conditions

to promote this pathway and examine the reaction kinetics is of significant interest to our group and others.[176]

4.3. Conclusion

The electrocatalytic behavior of $Co(dmgBF_2)_2(CH_3CN)_2$ was studied in the presence of *para*-substituted anilinium derivatives in order to investigate the reaction kinetics as a function of pK_a and further probe the H_2 production mechanism. For *para*-substituted aniliniums with pK_a > 9.5, the observed rate of catalysis is first order in acid at low to moderate concentrations of acid. At higher concentrations, the catalytic plateau current reaches a limiting value, i_c^{MAX}. Acid-dependent catalytic currents were also observed for stronger acids, but the voltammograms remained peaked and governed by the rate of substrate diffusion. However, at high substrate concentrations, acid concentration-independent plateau currents were reached with the same limiting i_c^{MAX} observed for weaker acids. This concentration- and pK_a-independent limiting current suggests a rate-limiting, acid-independent elementary step (k_Ω = 125 s^{-1}), likely hydrogen release or H–H bond formation. From the acid-dependent region, a global rate constant for catalysis is obtained which reflects a rate-limiting step that is first order in acid. The rate constant of the first proton transfer reaction, k_1, was determined from FOWA (all acids) and Eq. 4.5 (for voltammograms exhibiting total catalysis, KT2, behavior). As k_1 values are three orders of magnitude greater than k_{global}, and a kinetic shift is observed for the catalytic waves, it can be concluded that this rate constant reflects k_2, the protonation of **1^{2-} (H^+)**. Linear free energy relationships were observed between the rate constants for both elementary proton transfer steps with respect to acid pK_a; the log(k_1)–pK_a relationships have a slope of –0.97, and the log(k_2)–pK_a relationship have a slope of –0.77. The difference between

these linear free energy relationships likely reflects the differences between the nucleophilic species undergoing reaction with the *para*-substituted aniliniums in these two chemical steps.

Together these data support the assignment of an *ECEC'* mechanism for cobaloxime-catalyzed hydrogen evolution under the studied conditions. The kinetics of the elementary steps of the catalytic cycle are dictated by the pK_a of the proton source; the acid pK_a similarly influences both k_1 and k_2. Kilgore and coworkers previously demonstrated that for a series of $[Ni(P_2^RN_2^{Ph})_2(CH_3CN)][BF_4]_2$ ($P_2^RN_2^{Ph}$ = 1,5-diaza-3,7-diphosphacyclooctane) hydrogen evolution catalysts, the catalytic wave shifts to more positive potentials with more electron-withdrawing phosphine substituents, but electrocatalytic activity decreases.[56] In this work, we show similar trends when the overpotential is modulated through the strength of the acid.[68,112,113] This relationship further highlights that catalytic activity and overpotential are intimately coupled.

4.4. Experimental

4.4.1. General Considerations

All reactions were performed using either a high-vacuum manifold with standard Schlenk techniques or in a nitrogen-filled glovebox. Solvents were degassed with argon, passed through an alumina column using a Pure Process Technology Solvent System, and stored over molecular sieves in the glovebox. Water for polishing was obtained from a Milli-Q system. Tetrabutylammonium hexafluorophosphate (TCI, >98%) was recrystallized from hot EtOH, washed with cold ethanol, and dried under vacuum for 8 hours at 80 °C.

$Co(dmgBF_2)_2(H_2O)_2$ (**1**) was synthesized and recrystallized according to literature methods.[186] Anilinium tetrafluoroborate, 4-chloroanilinium tetrafluoroborate, 4-*tert*-

buytlanilinium tetrafluoroborate, 4-methoxyanilinium tetrafluoroborate, and 4-cyanoanilinium tetrafluoroborate were prepared as reported.[67]

Absorbance measurements were taken using an Agilent Cary 60 UV-vis spectrophotometer. ^{1}H NMR spectra were collected with a Bruker 400 MHz spectrometer and referenced to proteo solvent impurities.[137] Atlantic Microlabs, Inc., performed all elemental analysis.

4.4.2. Acid Synthesis

The anilinium acids 4-trifluoromethoxyanilinium tetrafluoroborate, 4-(methylbenzoate)anilinium (tetrafluoroborate salt), and 4-trifluoromethylanilinium tetrafluoroborate were prepared by the same procedure presented for the others in the literature, however, starting weights for each were 4-trifluormethoxyaniline, 0.5 g, methyl 4-aminobenzoate, 1.2 g, and 4-trifluoromethylaniline, 4.9 g.[67] 4-trifluoromethoxyanilinium: Yield 0.48 g, 64%. ^{1}H NMR (400 MHz, CD_3CN) δ (ppm): 7.42-7.53 (multiple peaks, 5H, C_6H_5-), 8.14 (s, 3H, -NH_3). Anal. Calcd.: C, 31.73; H, 2.66; N, 5.29. Found: C, 31.58; H, 2.53; N, 5.27. 4-(methylbenzoate)anilinium: Yield 1.3 g, 68%. ^{1}H NMR (400 MHz, CD_3CN) δ (ppm): 3.86 (s, 3H, -CH_3), 7.24 (d, -C_6H_4-), 8.05 (d, -C_6H_4-). Anal. Calcd.: C, 40.21; H, 4.22; N, 5.86. Found: C, 41.24; H, 4.07; N, 5.91. 4-trifluoromethylanilinium: Yield 3.9 g, 52%. ^{1}H NMR (400 MHz, CD_3CN) δ (ppm): 7.42-7.53 (multiple peaks, 5H, C_6H_5-), 8.14 (s, 3H, -NH_3). Anal. Calcd.: C, 33.77; H, 2.83; N, 5.63. Found: C, 33.92; H, 2.71; N, 5.60. Full ^{1}H NMR spectra provided in the SI.

4.4.3. Electrochemical Methods

All electrochemical measurements were performed in a nitrogen-filled glovebox, using electrode leads that were fed through a custom port and connected to a Pine Instruments WaveDriver potentiostat. A three-electrode cell was used for all experiments, utilizing glassy carbon working and counter electrodes (CH Instruments, 3 mm diameter) and a silver wire pseudo-reference that had been immersed in a glass tube fitted with a porous Vycor tip and filled with a 0.25 M $[Bu_4N][PF_6]$ acetonitrile solution. The glassy carbon electrodes were polished using a Milli-Q water slurry of 0.05 micron polishing powder (CH instruments, containing no agglomerating agents), rinsed and sonicated in Milli-Q water, and rinsed with acetone. Working electrodes were electrochemically pretreated with two cyclic scans between 0.7 and -2.8 V (approximately) at 300 mV/s in 0.25 mM $[Bu_4N][PF_6]$ solution. Background voltammograms of electrolyte-only solutions were collected for every electrode at the appropriate scan rate. All voltammograms were recorded in 0.25 M $[Bu_4N][PF_6]$ acetonitrile solutions and internally referenced to ferrocene. Each scan was collected using a clean, pretreated working electrode, and the solution was stirred between scans. As **1** was observed to degrade by UV-vis in the presence of stronger acids (see SI), the data collection procedure was modified for 4-trifluoromethylanilinium and 4-cyanoanilinium. For solutions containing these acids, fresh solutions of **1** were used for *each* electrochemical measurement in which solutions contained more than 8 mM acid. Under such circumstances, data collection began immediately after addition of acid to the fresh solutions of **1**.

Electrochemical simulations were performed using Gamry's DigiElch software. Generation of peak potential grids to evaluate the total catalysis equation working boundaries was performed in MATLAB (The Mathworks). Simulations were performed using in-house

prepared scripts utilizing a higher order Crank-Nicolson implicit finite differences method on a non-uniform grid.[187,188] Scripts provided as supplementary information.

CHAPTER 5. Experimental Access to Non-Aqueous Potential-pKa Diagrams of Catalytic Systems

5.1. Introduction

Shifting global energy consumption away from fossil fuels to more sustainable resources remains a pressing concern. While efficiencies of devices that harvest energy from renewable sources, particularly solar energy,[189] continue to improve, we are still behind the mark in our capacity to store this energy.[5] Energy storage is a crucial requirement for efficacy of renewable energy given the intermittency of these sources.[86,87] As a result, fuel producing electrocatalytic reactions are an attractive approach to generating a transportable and carbon neutral energy source.[9] All viable fuel producing reactions are underpinned by proton-coupled electron transfer (PCET) processes.[13] PCET is pervasive in biological systems and it is the careful execution of this process that allows enzyme reactions to proceed with high efficiencies.[190,191] It is anticipated that careful tuning of PCET processes in artificial fuel production schemes will allow similar efficiencies. Consequently, advancing the fundamental understanding of PCET is of great importance to the renewable energy community.[192]

Historically, Pourbaix diagrams have been important for understanding electrochemical PCET reactions. Pourbaix diagrams are plots that map thermodynamically stable species at any applied potential as a function of the solution free energy (most generally the pH).[41] However, these studies have overwhelmingly been performed in water, where the molecule or material of interest has immediate access to the required protons. While fuel

production in and from water is considered the ultimate goal,[193] acetonitrile is often used by researchers studying electrocatalytic fuel production, as it offers many advantages in fundamental studies of catalyst activity and mechanism (large electrochemical potential window, established inert electrolytes, the ability to evaluate the catalyst in the absence of the proton source, etc.).[106] However, with only a few exceptions,[194] experimental Pourbaix diagrams of fuel-producing catalysts in acetonitrile have not been experimentally generated. For most catalysts, the potential of the catalytic wave is independent of the solution free energy (as often defined by the pK_a of the proton source). This is primarily due to kinetic limitations on the proton transfer steps. While concerted transfer of the proton and electron is possible, few examples have been reported in aprotic solvents.[48] For a stepwise reaction where the proton and electron are transferred sequentially, the driving force of the electron transfer reaction is fixed at a specific potential. Therefore, to shift the redox potential the proton transfer steps must be sufficiently fast such that a minute concentration of reduced catalyst at the electrode surface will allow Le Chatelier's principle to shift the equilibrium to the protonated species.[37] In most systems, these kinetic limitations restrict access to information about the most thermodynamically stable species as a function of applied potentials.

Recently, an intentional effort has extended Pourbaix analysis to non-aqueous, aprotic solvents, and thus potential-pK_a diagrams for select molecular PCET reactions are now reported under these conditions.[194] Importantly, this work identified that Nernstian behavior for a PCET processes $\mathrm{M}/\mathrm{MH}_m^{-(n-m)}$ (where M is a transition metal coordination complex and $\mathrm{MH}_m^{-(n-m)}$ is its reduced and protonated form) in aprotic solvents can be described by Eq. 5.1, where $E_{1/2}$ represents the observed potential of the reversible redox wave, $E^{0'}\left(\mathrm{M}^{0/-\mathrm{n}}\right)$ the potential in the absence of a proton source, HA the molecular acid involved in the PCET

reaction, m the number of protons, n the number of electrons, $[A^-]$ the concentration of base, and [HA] the concentration of acid.

$$E_{1/2} = -E^{0'}\left(M^{\frac{0}{-n}}\right) + 2.303\frac{mRT}{nF}\left(pK_a\left(MH_m^{-(n-m)}\right) - pK_a(HA) - \log\left[\frac{[A^-]}{[HA]}\right]\right) \quad (Eq.\,5.1)$$

Extension of non-aqueous potential-pK_a diagrams from single electron, single proton reactions, such as those described in reference [194], to catalytic systems is crucial in order to exploit the insight provided to PCET processes in the development of efficient and versatile catalysts.[195] For select hydrogen evolution catalysts (including the focus of this work, below), catalysis is initiated by a PCET process that accesses a Nernstian equilibrium on the electrochemical time scale, resulting in a clear relationship between $E_{cat/2}$, (the potential at half-height of the catalytic wave) and the pK_a of the proton source. As highlighted above, the potential-pK_a diagram cannot be mapped unless $E_{cat/2}$ is thermodynamically controlled. Beyond the ability to produce a potential-pK_a diagram, such pK_a-dependent reactivity is valued because it results in a fixed catalytic overpotential (defined here as the difference between the thermodynamic potential of hydrogen formation, $E^0_{1/2(HA/H_2)}$,[67,113] and $E_{cat/2}$) regardless of proton source, as the potential of $E_{cat/2}$ moves in sync with $E^0_{1/2(HA/H_2)}$.[111] As discussed above, this is generally not the case for systems studied in acetonitrile as $E_{cat/2}$ is fixed at the location of the catalysis initiating redox event,[68] such that the overpotential varies as a function of the acid source used. Having a fixed overpotential, rather than a fixed $E_{cat/2}$, is advantageous in the design of fuel producing devices as a much wider range of effective pH values would be amenable to the same catalyst. In addition, considering Eq. 5.1, it becomes

feasible to tune a catalyst to a desired overpotential through modifications to the pK_a of the protonation site and redox potential, even down to the point of zero overpotential.

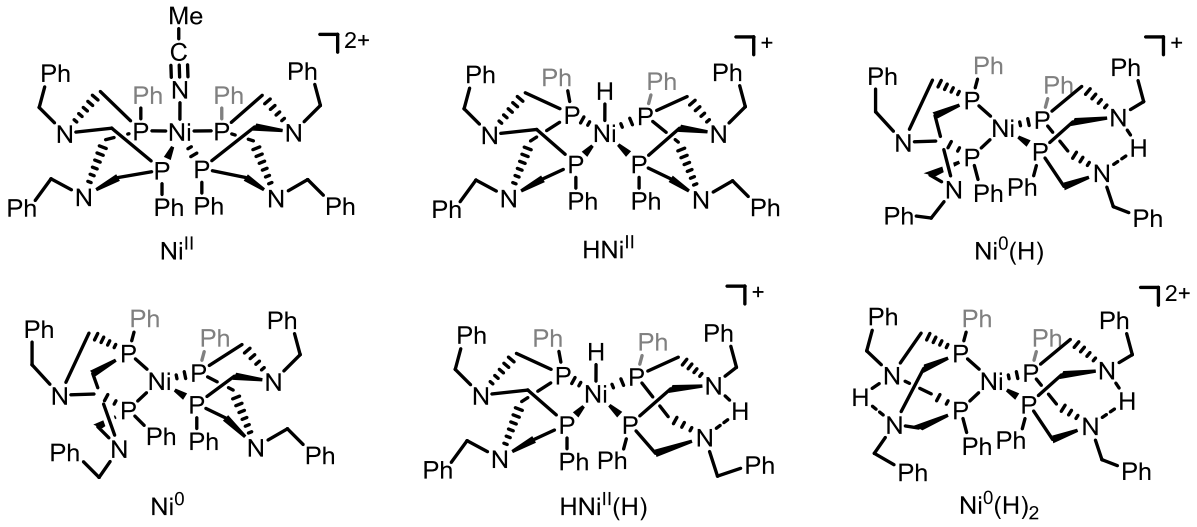

Figure 5.1. Structure of $[Ni(P_2^{Ph}N_2^{Bz})_2(CH_3CN)]^{2+}$ (top left) and the various protonation and redox states discussed herein. In abbreviations, an 'H' located to the left of Ni in a label indicates the hydrogen is a hydride while a 'H' located to the right of Ni in a label indicates it is bound to the ligand. Complex charges are omitted from abbreviations for clarity.

To our knowledge there has only been one reported catalyst that experimentally exhibits a clear pK_a-dependent $E_{cat/2}$ in acetonitrile, the hydrogen evolution catalyst $[Ni^{II}(P_2^{Ph}N_2^{Bz})_2]^{2+}$ (Figure 5.1, $P_2^{Ph}N_2^{Bz}$ = 1,5-dibenzyl-3,7-diphenyl-1,5-diaza-3,7-diphosphacyclooctane).[111] When catalytic voltammograms were recorded in acetonitrile as a function of the pK_a of the proton source, Appel *et al.* found $E_{cat/2}$ varied as a function of acid pK_a with a slope of 57 mV per pK_a unit in the pK_a range 6 – 12. This is approximately the slope predicted by Eq. 5.1 for a PCET reaction with an equal addition of protons and electrons. In this same report, several relevant intermediates, including the Ni^{II} -hydride $[HNi^{II}(P_2^{Ph}N_2^{Bz})_2]^+$ (HNi^{II}), and the doubly ligand protonated Ni^{II} and Ni^0 species ($Ni^{II}(H)_2$ and $Ni^0(H)_2$, Figure 5.1), were observed by ^{1}H and ^{31}P NMR spectroscopy.[102,111] In order to better understand the pK_a-dependent reactivity displayed by $Ni(P_2^{Ph}N_2^{Bz})_2$,

Hammes-Schiffer and coworkers carried out complementary computational studies and identified the thermochemically stable species as a function of acid pK_a and applied potential.[40] From these data, a theoretical Pourbaix diagram (reprinted here as Figure 5.2) was generated and the authors concluded that the experimentally observed potential-pH relationship resulted from a two-electron, two-proton PCET process.[40] Tantalizingly, it was proposed that other regimes may be experimentally observable as well, including a one-proton, two-electron regime from effective pH 11.8 to 15.2 and a one-proton, one-electron regime from effective pH 15.2 to 19.4.

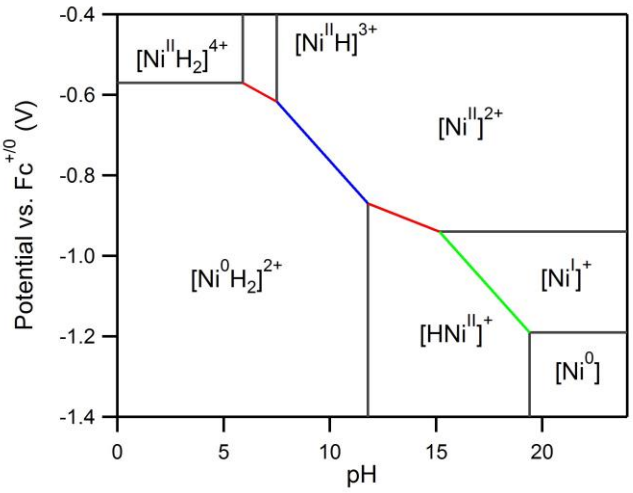

Figure 5.2. Theoretical Pourbaix diagram for $[Ni^{II}(P_2^{Ph}N_2^{Bz})_2]^{2+}$. H before Ni represents a hydride while H after Ni represents ligand protonation. Red lines represent one proton, two electron transitions and have a slope of ~29.5 mV/pH unit. The blue line represents a two electron, two proton transition and the green line represents a one proton, one electron transition, both have slopes of ~59 mV/pH unit.. Copyright (2013) American Chemical Society.[40]

Given the need for a better fundamental understanding of PCET processes leading to thermodynamic relationships between E_(cat/2) and proton source pKa, we have revisited the electrochemical reactivity of Ni(P_2^Ph N_2^Bz)_2 using the computational study as a guiding framework in an attempt to answer or further clarify the following questions:

(1) Can the entire Pourbaix (potential-pKa) diagram be experimentally mapped by cyclic voltammetry by changing the solution free energy? Namely, will the other predicted regimes also be evident by cyclic voltammetry, or is the pH/pKa dependence limited to the stronger acids where it is possible to protonate the complex prior to electron transfer?

(2) Why does this catalyst exhibit a pH/pKa dependent Ecat/2 in an aprotic solvent while so many others exhibit prohibitive kinetics and are unable to establish the Nernstian equilibrium on the electrochemical timescale?

and

(3) Do the boundaries defined using experimental E_(cat/2) values represent the boundaries between thermodynamic sinks at a given pH/pKa and potential, or do they represent kinetically accessible species that do not necessarily represent the thermodynamic sink?

5.2. Results

5.2.1. pH and pK_a

Pourbaix diagrams are generally plotted with the electrochemical potential and pH of the solution as the x and y axes, respectively. This is problematic when working in aprotic solvents. In water, pH is represented as the activity of solvated protons, which are able to directly interact with other species in solution; pK_a is then defined by the relationship between a given acid and the solvent (water). In aprotic solvents, as protons are not solvated (indeed,

protonated acetonitrile decomposes[67]), pK_a values are defined relative to a reference compound and so all non-aqueous pK_a values are relative.[100,105] Our current understanding of acid reactivity in acetonitrile is that all reactions occur as *general acid* reactions, where the proton is transferred directly to and from the acid (as opposed to *specific acid* reactions where the proton transfers occur through the solvated intermediate).[194] Given this distinction, we intentionally try to distance ourselves from the term "pH" due to its insinuation of *specific acid* reactivity. Thus, we report all of our findings in reference to the pK_a of the acid being utilized. Throughout this work, we have primarily used 1:1 acid:base conditions with overall excess acid/base such that concentration terms for acid and base in Eq. 5.1 can be omitted, allowing the results to be reported with respect to acid pK_a. However, it became necessary in some cases to vary the ratio between acid and base; for these cases we report the "effective pH" of the buffered solution using the Henderson-Hasselbalch expression $pH = pK_a + \log([Base]/[Acid])$. In these cases, precise language and clear experimental details are used for clarity.

5.2.2. Optical Signatures of Isolated Species

Reaction equilibria and kinetics are optically monitored throughout this work using UV-visible absorbance spectroscopy. As such, we made every effort to assign reaction species to their corresponding UV-visible absorbance profile. Four of these intermediates were isolated and evaluated independently: $[Ni^{II}(P_2^{Ph}N_2^{Bz})_2]^{2+}$ (Ni^{II}), $[Ni^0(P_2^{Ph}N_2^{Bz})_2]$ (Ni^0), $[Ni^{II}(P_2^{Ph}N_2^{Bz}H)_2]^{4+}$ ($Ni^{II}(H)_2$), and $[HNi^{II}(P_2^{Ph}N_2^{Bz})_2]^{+}$ (HNi^{II}). Their corresponding spectra are presented in Figure 5.3. Ni^{II} has a characteristic peak with λ_{max} = 485 nm that is that is typical for $Ni^{II}(P_2^RN_2^{R\prime})_2$ species.[42] Protonation to form $Ni^{II}(H)_2$ changes little about the overall appearance of the spectrum, blue-shifting λ_{max} to 470 nm and increasing the

extinction coefficients below 500 nm. The hydride (HNi^{II}) absorbs primarily in the UV region, with a tailing feature in the visible and no distinct absorbance peaks. Reduction to Ni^0 results in a more strongly absorbing species with λ_{max} = 405 nm.

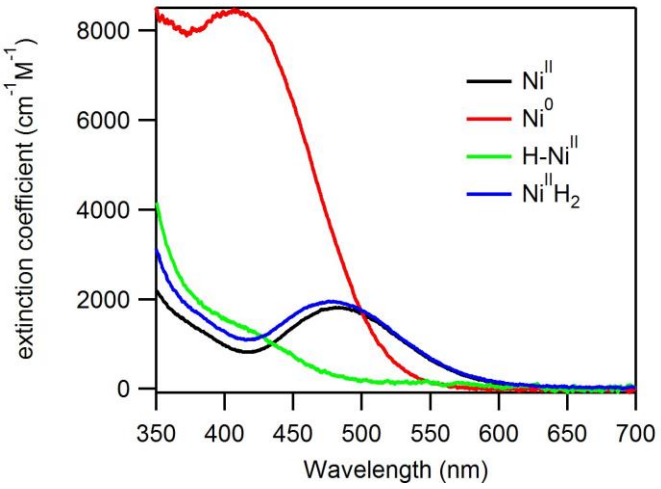

Figure 5.3. Absorbance spectra for the isolated complexes $[Ni^{II}(P_2^{Ph}N_2^{Bz})_2]^{2+}$ (Ni^{II}), $[Ni^0(P_2^{Ph}N_2^{Bz})_2]$ (Ni^0), $[HNi^{II}(P_2^{Ph}N_2^{Bz})_2]^+$ (HNi^{II}), and $[Ni^{II}(P_2^{Ph}N_2^{Bz})H_2]^{4+}$ ($Ni^{II}(H)_2$) in CH_3CN.

5.2.3. Experimental Determination of Thermochemical Properties

As a first step towards investigating the complete potential-pK_a diagram for $[Ni^{II}(P_2^{Ph}N_2^{Bz})_2]^{2+}$ (Ni^{II}), we sought to establish the pK_a values and the redox potentials for the species that could independently be prepared and isolated. In previous reports, the $Ni^{II/I}$ and $Ni^{I/0}$ reduction potentials were established by cyclic voltammetry as -0.94 and -1.19 V vs. $Fc^{+/0}$, respectively. The free energy for addition of H_2 to Ni^{II} ($H_2 + Ni^{II} \rightleftharpoons Ni^0H_2$) was measured as 2.7 ± 0.2 kcal/mol, the free energy for addition of a hydride ($H_2 + Ni^{II} + B \rightleftharpoons HNi^{II} + BH$, B represents a base) was measured as 57.1 ± 0.3 kcal/mol, and the average pK_a for the addition of two protons to Ni^{II} ($2BH + Ni^{II} \rightleftharpoons Ni^{II}(H)_2$) was measured to be 6.7 ±

0.4 kcal/mol with NMR spectroscopy.[102,111] A singly protonated Ni^{II} species was not observed.

5.2.3.1. pK_a of $[Ni^{II}(P_2^{Ph}N_2^{Bz})(H)_2]^{4+}$. In work by Appel *et al.*,[111] ^{31}P and ^{1}H NMR spectra recorded as a function of acid concentration showed only the appearance of the doubly protonated species ($Ni^{II}(H)_2$), not the singly protonated species ($Ni^{II}(H)$). Specifically, upon addition of acid to Ni^{II}, only one new phosphorous peak was observed and integration of the ^{1}H NMR peaks for the new species formed and the conjugate base suggested a net two proton transfer to the Ni^{II} species. This is in contrast with computational work suggesting the doubly protonated species is 1.6 pK_a units more acidic than the singly protonated species (though the difference between these computed pK_a values of 5.9 and 7.5 was within error).[40] This discrepancy and the large error bars of ±0.4 pK_a units for the NMR measurements encouraged us to revisit this thermochemical value. Spectrophotometric titrations of $[Ni^{II}(P_2^{Ph}N_2^{Bz})_2]^{2+}$ were performed using three separate acids: 4-cyanoanilinium (pK_a = 7),[67] 4-trilfuoromethylanilinium (pK_a = 8.03),[105] and 4-(methylbenzoate)anilinium (pK_a = 8.62).[38] Experimentally, it was difficult to spectroscopically distinguish the unprotonated species ($[Ni^{II}(P_2^{Ph}N_2^{Bz})_2]^{2+}$, Ni^{II}) and the doubly protonated species ($[Ni^{II}(P_2^{Ph}N_2^{Bz}H)_2]^{4+}$, $Ni^{II}(H)_2$) (Figure 5.3). In addition, the doubly protonated species, $Ni^{II}(H)_2$, was found to slowly degrade, consistent with previous reports (Appendix D.1). To counter this, absorbance was only monitored at one wavelength (λ_{abs} = 415 nm) so that it could be accurately recorded while completing each of the experiments within approximately 15 minutes to limit the impact of degradation.

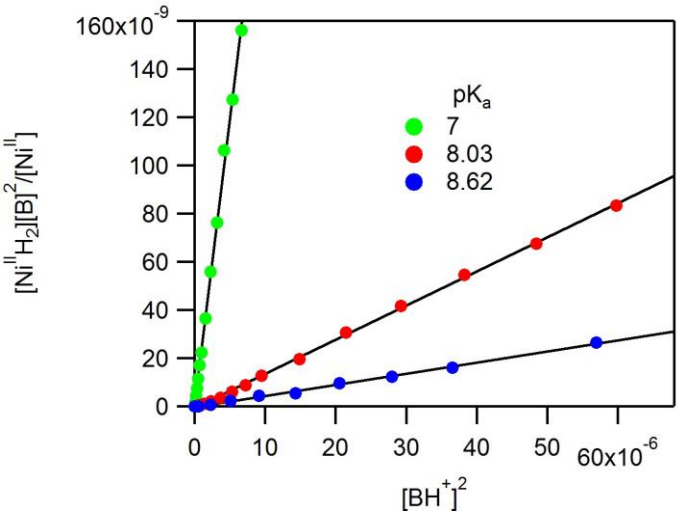

Figure 5.4. Spectrophotometric titrations of ($[Ni^{II}(P_2^{Ph}N_2^{Bz})_2]^{2+}$ with 4-cyanoanilinium (green, pK_a = 7.0), 4-trifluoromethylanilinium (red, pK_a = 8.03), and 4-(methylbenzoate)anilinium (blue, pK_a = 8.62). The vertical axis is defined by $[Ni^{II}H_2][B]^2/[Ni^{II}]$ and the horizontal axis by $[BH^+]^2$ where BH^+ and B are the acids and their conjugate bases. Concentrations of Ni^{II} and $Ni^{II}H_2$ were determined from the absorbance at 415 nm, using the extinction coefficients of the two species at 415 nm (Figure 5.3, $\varepsilon_{Ni^{II}} = 825\ cm^{-1}\ M$, $\varepsilon_{Ni^{II}} = 1100\ cm^{-1}\ M$), and concentrations of acid and base were calculated from the input concentration and the appearance of $Ni^{II}(H)_2$. Slopes of the black lines are 0.024 (green), 0.0015 (red), and 0.00045 (blue), representing $pK^{1/2}_{Ni^{II}H_2}$ values for the two proton transfers to Ni^{II} of 6.19, 6.58, and 6.92 according to Eq. 5.2 and 5.3.

From these absorbance vs. acid concentration titration data, linearity is observed when plotting $[Ni^{II}H_2][B]^2/[Ni^{II}]$ against $[BH^+]^2$ for all three acids used (Figure 5.4), indicating the addition of two protons, as opposed to one (where linearity would be observed when plotting $[Ni^{II}H][B]/[Ni^{II}]$ against $[BH^+]$; for our data this plot exhibits a curved dependence, Appendix D.2). Observation of the two-proton equilibrium is consistent with the observations of Appel *et al.*, described above.[111] The slopes of the black lines represent the equilibrium constant for each reaction (Eq. 5.2) allowing the average pK_a value ($pK^{1/2}_{Ni^{II}(H)_2}$) to be determined (Eq. 5.3).

$$[BH^+]^2K = \frac{[Ni^{II}H_2][B]^2}{[Ni^{II}]} \qquad (Eq.5.2)$$

$$avg.pK_a(Ni^{II}H_2 \,\&\, Ni^{II}H) = pK^{1/2}_{Ni^{II}H_2} = 2 * pK_a(BH^+) + \log(K) \qquad (Eq.5.3)$$

Despite the linearity observed in the data as predicated by Eq. 5.2, the three independently recorded data sets yield varying $pK^{1/2}_{Ni^{II}(H)_2}$ values—the apparent $pK^{1/2}_{Ni^{II}(H)_2}$ increases with the pK_a of the acid being used for the titration, resulting in values of 6.19, 6.58, and 6.92. The average value of these three measurements is 6.56, well within the error of the original measurements (6.7 ± 0.4). However, given the reliability of spectrophotometric titrations for measurement of pK_a values, we do not think the change in apparent $pK^{1/2}_{Ni^{II}(H)_2}$ from acid to acid is experimental error, but rather it represents a real change in the system. It seems plausible that there is an interaction between the conjugate base and Ni^{II} such as the replacement of the axial solvent ligand with the conjugate base, but we have not pursued experimental evidence to support any such interactions. We utilize the average pK_a for the potential-pK_a diagram below.

5.2.3.2. pK_a *of* $[HNi^{II}(P_2^{Ph}N_2^{Bz})_2]^+$. The pK_a of the Ni(II) hydride species ($[HNi^{II}(P_2^{Ph}N_2^{Bz})_2]^+$, HNi^{II}) was also determined by spectrophotometric titration using triethylammonium. Just as for $Ni^{II}(H)_2$, the titration was performed monitoring absorbance at a single wavelength (λ_{abs} = 430 nm) in order to complete the titration within 15 minutes as HNi^{II} was found to react to generate Ni^I and H_2 through a bimolecular pathway on the timescale of 40 minutes (Appendix D.3). The spectrophotometric titration of Ni^0 with triethylammonium was performed twice and the results were combined into a single plot of $[HNi^{II}][B]/[Ni^0]$ against $[BH^+]$ (Appendix D.4), revealing a pK_a of 20.15 for HNi^{II}, which

is within the margin of error of the thermochemical cycle previously used which found a pK_a value of 19.4.[111]

5.2.3.3. Cyclic Voltammetry of $[Ni^{II}(P_2^{Ph}N_2^{Bz}H)_2]^{4+}$. The doubly protonated Ni(II) species $Ni^{II}(H)_2$ was isolated by dissolving $[Ni^{II}(P_2^{Ph}N_2^{Bz})_2]^{2+}$ in a 1:1 mixture of acetonitrile and diethyl ether, adding two equivalents of tetrafluoroboric acid diethyletherate complex, and isolating the precipitated species, identified as the doubly protonated species by ^{31}P NMR (a single peak in the $^{31}P\{^1H\}$ NMR at -16 ppm[111] confirmed that the doubly protonated species was the only species present in the resulting precipitate). Cyclic voltammetry of $Ni^{II}(H)_2$ revealed a complex concentration dependence. At ≤ 0.1 mM, an irreversible reduction feature is observed at -0.9 V vs. $Fc^{+/0}$, consistent with the $Ni^{II/I}$ redox couple (see above). A second irreversible reduction wave is observed at -0.7 V when the concentration of $Ni^{II}(H)_2$ is increased above ca. 0.1 mM (Appendix D.5). Further increases in concentration to the mM range gives rise to a third reductive peak at ca. -0.52 V which exhibits reversibility (Figure 5.5). Despite the concentration dependence observed (discussed in detail below), this third redox feature was initially considered to correspond to the two-electron reduction of $Ni^{II}(H)_2$ predicted by the computational studies used to generate Figure 5.2, in which the second reduction of $Ni^{I}(H)_2$ to generate $Ni^{0}(H)_2$ was calculated to occur at a more positive potential than the first.[40]

A 28.5 mV separation is expected between the cathodic and anodic peaks for a two-electron couple and a 57 mV separation is expected for a one-electron couple.[72] The peak separation measured for the redox couple at -0.52 V is ca 80 mV; inconclusive as slow electron transfer kinetics can also give rise to large peak-to-peak separations. From the diffusion

coefficient for $[Ni(P_2^{Ph}N_2^{Bz})_2]^{2+}$ (6 x 10^{-6} cm^2 s^{-1}, Appendix D.6), and the assumption that the value is approximately the same for $Ni^{II}(H)_2$, the peak current recorded for the wave at -0.52 V suggests a one-electron reduction per the Randles-Sevcik equation. Despite the prediction that a two-electron reduction would be observed for $Ni^{II}(H)_2$, these data indicate that only a single electron is transferred. We attribute this discrepancy to slow electron transfer kinetics for the two-electron reduction of $Ni^{I}(H)_2$, as a second electron transfer wave consistent with the $Ni^{I}(H)_2$ reduction is not observed when scanning further cathodically. In addition, at slow scan rates, the redox wave at -0.52 V gradually loses reversibility (Appendix D.5). This is likely a result of H_2 formation, which would require either a second electron transfer from the electrode or an intermolecular electron transfer between 2 equivalents of $Ni^{I}(H)_2$ (solution electron transfer). These data support the assignment of the wave observed at -0.52 V as the two electron reduction of $Ni^{II}(H)_2$.

Further investigation of the second concentration-dependent redox feature observed at -0.7 V revealed that this reductive feature has a fixed current magnitude beyond a concentration of 1 mM $Ni^{II}(H)_2$ (Appendix D.5). Acetonitrile is notorious for basic impurities; given the location of this reductive peak and its fixed current contribution, we postulate that a <1 mM basic impurity persists in our acetonitrile with a pK_a for its conjugate acid of 8 or less. This basic impurity would completely deprotonate $Ni^{II}(H)_2$ when it is at a low concentration, consistent with the observation of the $Ni^{II/I}$ reduction wave at -0.9 V. Increasing the concentration of $Ni^{II}(H)_2$ would then create a larger concentration of protonated impurity and allow at PCET reaction between Ni^{II} and the acidic species upon scanning cathodically (the reductive feature at -0.7 V, see below, section 5.2.4.1). Only after the concentration of

$Ni^{II}(H)_2$ is higher than that of the basic impurity can its own redox chemistry be realized with the appearance of the reversible redox couple at -0.52 V.

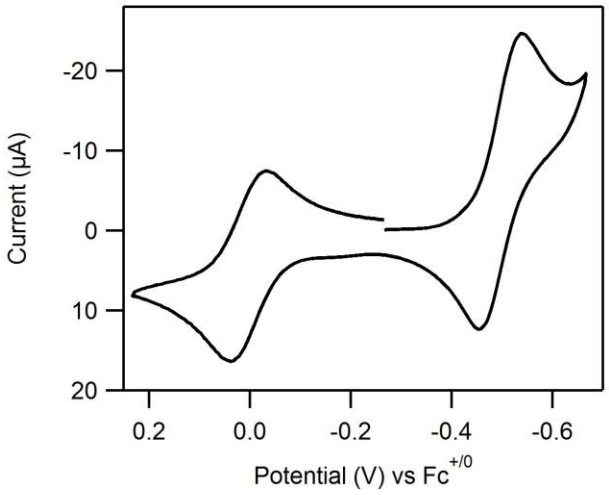

Figure 5.5. Cyclic voltammogram of $[Ni^{II}(P_2^{Ph}N_2^{Bz}H)_2]^{4+}$ at 4.7 mM. The reversible wave observed at -0.52 V is assigned to the two electron reduction of $[Ni^{II}(P_2^{Ph}N_2^{Bz}H)_2]^{4+}$. The ferrocene couple (internal standard) is observed at 0 V. Voltammogram recorded at 800 mV s^{-1} in 0.25 M $[NBu_4][PF_6]$ CH_3CN solution.

5.2.4. Electrochemistry in the Presence of Acid:Base Mixtures

The electrochemical response of $Ni(P_2^{Ph}N_2^{Bz})_2$ was evaluated with cyclic voltammetry using 50 mM 1:1 acid:base solutions containing acids with pK_a values spanning the range 5 – 20. As noted earlier, in the absence of acid, the $Ni^{II/I}$ redox couple is observed at -0.94 V, the $Ni^{I/0}$ couple at -1.19 V, and the two-electron reduction of $Ni^{II}(H)_2$ at -0.52 V. The following experiments were designed to explore the coupling of the proton transfer reactions to these electrochemical reductions. Five distinctly different responses were obtained depending on the strength of the acid employed; each region is discussed below.

5.2.4.1. Region 1, effective pH > 17. The theoretical diagram in Figure 5.2[40] predicts that the $Ni^{I/0}$ reduction can be coupled to protonation to form HNi^{II} with acids in the pK_a range 15.8

– 19.4. This is experimentally predicted to manifest itself as a 59 mV/decade slope for this redox feature corresponding to the one-electron, one-proton $Ni^{I} \rightleftharpoons HNi^{II}$ redox couple. In cyclic voltammetry measurements of Ni^{II}, the predicted 59 mV per decade shift in the potential of the reversible wave corresponding to the $Ni^{I/0}$ couple (Figure 5.6A) is observed when using 4-dimethylaminopyridinium (pK_a = 17.95),[105] triethylammonium (pK_a = 18.82)[105] and pyrrolidinium (pK_a = 19.56).[105] Examining reactivity as a function of scan rate, a flattening of the oxidation peak for this couple is observed on the anodic scan (while the reduction peak remains unperturbed). This suggests that the reverse (oxidative) PCET reaction proceeds via a slow PT-ET reaction pathway (Figure 5.7), where slow deprotonation prevents the complex from being fully oxidized on the reverse trace.[72]

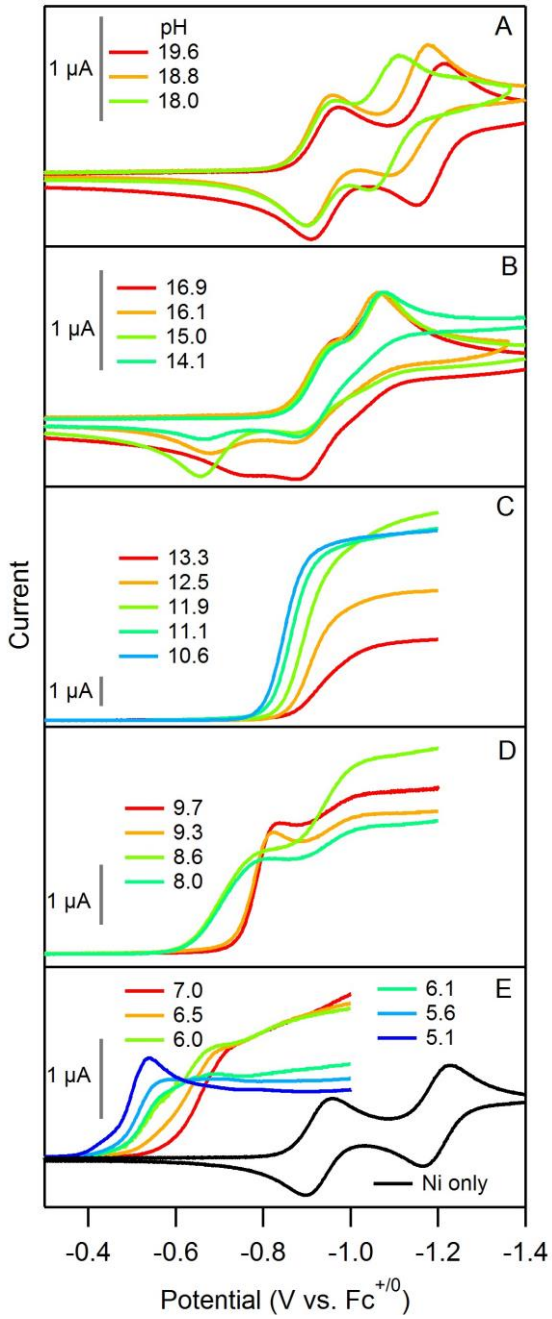

Figure 5.6. Cyclic Voltammograms of 0.6 mM $[Ni^{II}(P_2^{Ph}N_2^{Bz})_2]^{2+}$ in acid:base solutions ranging in pH from 19.6 to 5.1. All solutions are 50 mM of the respective acid and base except where otherwise noted. All voltammograms recorded at 50 mV/s in 0.25 M $[NBu_4][PF_6]$ CH_3CN solution with a 1 mm diameter glassy carbon electrode. The anodic scan trace has been removed for scans that show no oxidative features. The black trace in pane E is a cyclic voltammogram in absence of acid for reference. A) Region 1: pyrrolidinium (pK_a = 19.56), triethylammonium (pK_a= 18.82), and 4-dimethylaminopyridinium (pK_a= 17.95). B) Region 2: benzylammonium (pK_a= 16.91), 2-aminobenzimidazolium (pK_a= 16.08), 2,4,6-collidinium

(pK_a= 14.98), and 2,6-lutidinium (pK_a= 14.13). C) Region 3: 2-picolinium (pK_a= 13.32), pyridinium (pK_a= 12.53), 4-methoxyanilinium (pK_a= 11.86), 4-tertbutylanilinium (pK_a= 11.1), and anilinium (pK_a= 10.62). D) Region 4: 4-chloroanilinium (pK_a = 9.7), 4-triflouromethoxyanilinium (pK_a= 9.28), 4-(methylbenzoate)anilinium (pK_a= 8.62), and 4-trifluoromethylanilinium (pK_a= 8.03). E) Region 5: Effective pH was varied within this dataset using non-stoichiometric ratios of acid:conjugate base. Three scans were performed with 4-cyanoanilinium with an acid concentration of 50 mM and base concentrations of 50 mM (effective pH = 7), 15.8 mM (effective pH = 6.5) and 5 mM (effective pH = 6), and three scans were performed with 2,6-dichloroanilinium with an acid concentration of 50 mM, and base concentrations of 500 mM (effective pH = 6.06), 158 mM (effective pH = 5.56), and 50 mM (effective pH = 5.06).

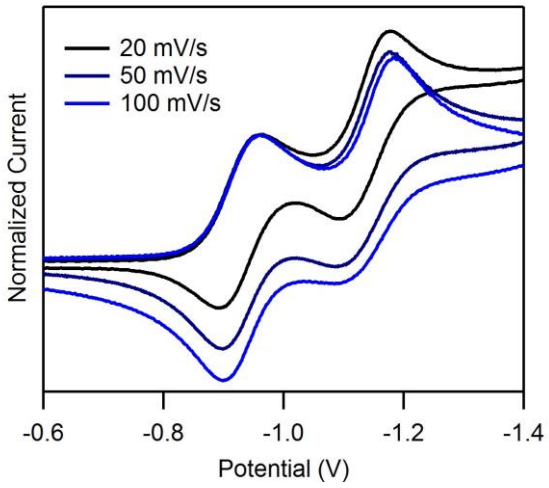

Figure 5.7. Cyclic voltammograms of 0.6 mM $[Ni^{II}(P_2^{Ph}N_2^{Bz})_2]^{2+}$ in 50 mM triethylammonium:trimethylamine recorded at 20 mV/s, 50 mV/s, and 100 mV/s in 0.25 M [NBu$_4$][PF$_6$] CH$_3$CN solution. Voltammograms normalized to unity at the peak of the $Ni^{II/I}$ cathodic wave.

5.2.4.2. Region 2, effective pH 14-17. When evaluating the electrochemical response with 2,6-lutidinium (pK_a = 14.13),[39] 2,4,6-collidinium (pK_a = 14.98),[39] 2-aminobenzimidazolium (pK_a = 16.08),[105] and benzylammonium (pK_a = 16.91),[105] the $Ni^{II/I}$ redox couple remains unperturbed. The reductive wave for the $Ni^{I/0}$ couple is shifted positive to approximately -1.05 V for all acids and a new anodic wave is observed (Figure 5.6B). This oxidative wave position varies as a function of acid pK_a; the oxidative wave occurs at more negative potentials when the conjugate base of the acid employed is stronger. This oxidative reactivity is consistent

with an EC reaction scheme (ET-PT) where the oxidation of HNi^{II} is coupled to deprotonation, the kinetics of which increase as a function of base strength.[72] The pK_a independence of this second reductive feature and the large separation (>200 mV) between it and the corresponding oxidative wave suggests that between pK_a 14 and 17, the PCET reduction ($Ni^{I} \rightleftharpoons HNi^{II}$) is kinetically limited by the proton transfers and cannot be used as a boundary for an experimental potential-pK_a diagram.

5.2.4.3. Region 3, effective pH 10-14. When voltammograms are recorded in the presence of 2- methylpyridine (pK_a = 13.32),[39] catalytic activity is observed as the driving force for reduction of acid to H_2 is increased, as evidenced by the sigmoidal shape of the voltammograms and increase in the magnitude of the current. The catalytic current increases significantly as the pH is lowered through pyridinium (pK_a = 12.53).[105] The highest recorded catalytic current is observed for 4-methoxyanilinium (pK_a = 11.86);[105] the stronger acids 4-tertbutylanilinium (pK_a = 11.1),[67] and anilinium (pK_a = 10.62)[105] give rise to catalytic currents of similar magnitude to 4-methoxyanilinium (Figure 5.6C). Despite the observation that the maximum current rises then tapers off across this pK_a range, the $E_{cat/2}$ shifts 30 mV positive per decade through this entire region ($E_{cat/2}$ was determined by fitting the catalytic wave to a sigmoid and using the potential at its half max, Appendix D.8).

In order to test for a concentration dependence on the position of $E_{cat/2}$, while keeping the acid:base ratio at 1:1, the absolute concentrations of 4-tertbutylanilinium and 4-tertbutylaniline were varied between 30 mM and 100 mM. All cyclic voltammograms recorded under these conditions resulted in $E_{cat/2}$ values between -0.864 and -0.866 V, suggesting that the reduction is thermochemically, not kinetically, controlled (Appendix D.7, Table 5.1).

5.2.4.4. Region 4, pH 8-10. After shifting to stronger proton sources than anilinium, significant changes in the observed catalytic currents are observed. Using 4-chloroanilinium (pK_a = 9.7),[67] 4-triflouromethoxyanilinium (pK_a = 9.28),[38] 4-(methylbenzoate)anilinium (pK_a = 8.62),[38] and 4-trifluoromethylanilinium (pK_a = 8.03),[105] the catalytic currents recorded are lower than those observed with anilinium and the waves are no longer sigmoidal in shape (Figure 5.6D). Instead, they appear as two overlapping sigmoids with what appears to be a second catalysis-initiated redox event occurring a few hundred millivolts more cathodic than the first. A notable shift in the width and position of the first (more positive) catalytic wave is observed between samples measured with acids of pK_a 9.28 and 8.62, insinuating a possible change in mechanism across this region (see below). To determine if the difference seen in this region is a result of solution free energy or the specific acids being used, a 10:1 ratio of anilinium:aniline (pK_a = 10.6) was utilized such that the effective pH was similar to that of a 1:1 solution of 4-chloroanilinium:4-chloroaniline (pK_a = 9.7). Under these conditions, the voltammetric response of the 10:1 anilinium:aniline sample was nearly identical to the 1:1 4-chloroanilinium:4-chloroaniline sample at the catalytic onset, suggesting that solution free energy dominates the voltammetric response, rather than specific acid-base interactions (Figure 5.8).

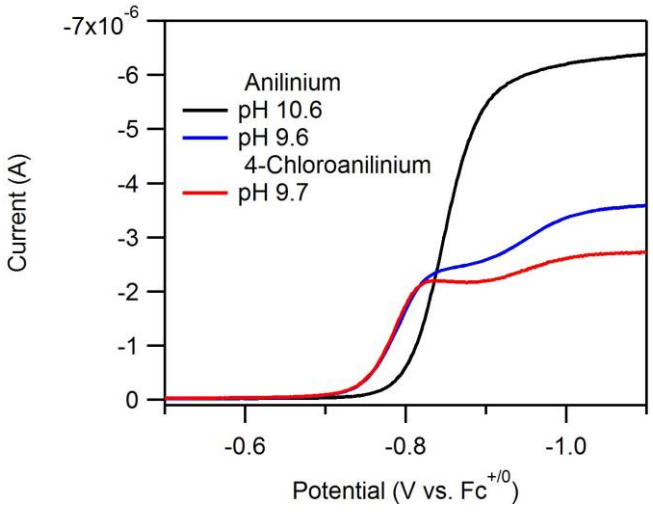

Figure 5.8. Cyclic voltammograms of 0.6 mM $[Ni^{II}(P_2^{Ph}N_2^{Bz})_2]^{2+}$ in pH 10.6 (50 mM : 50 mM anilinium:aniline), pH 9.6 (50 mM : 5 mM anilinium:aniline), and pH 9.7 (50 mM :50 mM 4-chloroanilinium:4-chloroaniline). All scans at 50 mV/s in 0.25 M $TBAPF_6$ electrolyte on 1 mm diameter glassy carbon electrodes.

5.2.4.5 Region 5, effective pH < 8. Experimentally, we were limited to two acids in the effective pH < 8 region where the Ni^{II} species is expected to be fully protonated as $Ni^{II}(H)_2$: 4-cyanoanilinium (pK_a = 7),[67] and 2,6-dichloroanilinium (pK_a = 5.06).[105] As such, data for a range of effective pH values were obtained by altering the ratios of acid to base with both acids (Figure 5.6E). At an effective pH of 6, a pre-wave, consistent with the reduction of $Ni^{II}(H)_2$ (see above), grows in at potential anodic (ca. –0.52 V) to the catalytic wave.

5.2.5. Protonation Kinetics Monitored via Stopped-Flow Rapid Mixing Techniques

In order to gain a more complete picture of the acid-base reactivity of Ni^0 and HNi^{II}, stopped-flow rapid mixing coupled with optical spectroscopy was used to monitor the reaction of these species with representative acids from each of the regions outlined in the previous section. For the reactions of HNi^{II}, the hydride was prepared directly prior to loading the stopped-flow syringe in order to limit degradation time (see experimental section for details).

5.2.5.1. Region 1, effective pH > 17: Reaction of $[Ni^0(P_2^{Ph}N_2^{Bz})_2]$ *with triethylammonium or 4-dimethylaminopyridinium.* Reaction of Ni^0 with triethylammonium (pK_a = 18.8) resulted in a relatively simple kinetic profile where only Ni^0 (λ_{max} = 405 nm) and the hydride product HNi^{II} are observed, indicating quantitative conversion via protonation per:

$$Ni^0 \xrightarrow{HA} HNi^{II}$$

The kinetics traces were single exponential, suggesting first order reactivity with respect to Ni^0. However, no clear trend between k_{obs} and concentration of triethylammonium was

observed (Appendix D.8). Analogous experiments were also performed using mixtures of 4-dimethylaminopyridium (pK_a = 18.0) and its conjugate base to generate solutions with effective pH values ranging from 17 to 19. However, under these conditions, the hydride was observed immediately upon mixing for all traces, precluding the observation of any intermediate species or resolution of protonation kinetics within the time resolution of the instrument.

5.2.5.2. Region 2, effective pH 14-17: Reaction of $[Ni^0(P_2^{Ph}N_2^{Bz})_2]$ *with 2,4,6-collidinium.* Rapid mixing of Ni^0 with mixtures of 2,4,6-collidinium (pK_a = 15.0) and 2,4,6-collidine immediately gives rise to a reaction intermediate (Int_A) characterized by an absorbance profile containing a broad absorbance shoulder between 400 and 500 nm (t = 0.015 s, Figure 5.9A). As discussed below, we tentatively assign this intermediate as a ligand-protonated Ni^0 species. Subsequent spectra (t= 0.2 s shown in Figure 5.9A) contained a weaker tailing absorbance (350-500 nm), consistent with the spectrum of isolated HNi^{II}. Spectra recorded at longer time delays were consistent with the appearance of Ni^{II} (t = 150 s shown in Figure 5.9A), presumably concomitant with the formation of H_2. Both formation of the hydride (monitored at 350 nm) and Ni^{II} (monitored at 500 nm) were first order in acid as the data is single exponential and the observed rate constant increases linearly with acid concentration. However, increases in the concentration of conjugate base led to an increase in the rate constant measured for HNi^{II} formation (monitored at 350 nm, $k = 8\,x\,10^3\,M^{-1}\,s^{-1}$ at 0.5 mM collidine and $9\,x\,10^5\,M^{-1}\,s^{-1}$ at 10 mM collidine) and a decrease in the rate constant for Ni^{II} formation ($k = 7\,M^{-1}\,s^{-1}$ at 0.5 mM collidine and $0.7\,M^{-1}\,s^{-1}$ at 10 mM collidine) (Figure 5.9B–C). These data suggest that collidine acts as a proton shuttle, mediating conversion between the putative ligand-protonated Ni^0 species (Int_A) and HNi^{II}, and hinders reaction of

HNi^{II} with collidinium to produce H_2; base has previously been demonstrated to play these roles.[42,106]

Notably, linear extrapolations of the observed rate constants vs. acid concentration for hydride formation (λ_{obs} = 350 nm) do not intercept the origin, suggesting that the hydride can be formed in both a first-order and a second-order reaction as the intercept of the plot has been shown in past studies to represent the rate of reaction in the absence of the explicit proton source.[169,196,197] We interpret this by considering the observation of an unidentified intermediate Int_A detected in initial optical spectra recorded at short timescales (0.015 s). If this intermediate is a ligand-protonated Ni^0 species (such as some isomer of the formulation $Ni^0(H)$, see below for further discussion), it could react via (1) an intramolecular reaction to form HNi^{II} (a first-order reaction), (2) an intermolecular reaction with a second equivalent of this putative protonated Ni^0 intermediate, followed by deprotonation, to form HNi^{II}, or (3) an intermolecular reaction with acid, followed by deprotonation, to form HNi^{II}. To further test the hypothesis that reactivity of Ni^0 with 2,4,6-collidinium proceeds as:

$$Ni^0 \xrightarrow{HA} Int_A \xrightarrow{?} HNi^{II} \xrightarrow{HA} Ni^{II} + H_2$$

direct reactivity of HNi^{II} with 2,4,6-collidinium was explored with stopped-flow. Rapid mixing of HNi^{II} with 2,4,6-collidinium gave rise to spectra changes consistent with direct conversion to Ni^{II} (and H_2). The single wavelength kinetics traces for this reaction yielded identical rate constants to those obtained for the observed formation of Ni^{II} from the intermediate assigned as HNi^{II} upon mixing Ni^0 with 2,4,6-collidinium (Appendix D.9), as expected.

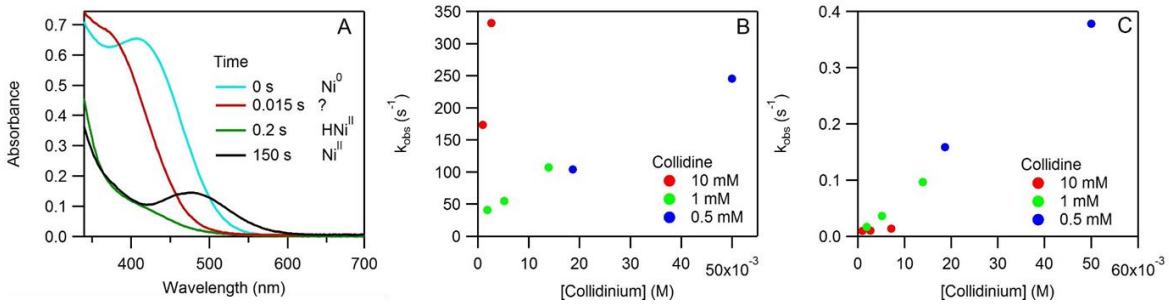

Figure 5.9. A) Representative spectra for the reaction of 0.08 mM $[Ni^0(P_2^{Ph}N_2^{Bz})_2]$ with a mixture of 1 mM 2,4,6-collidinium and 0.5 mM 2,4,6-collidine recorded at various time delays after rapid mixing via stopped-flow. B) Observed rate constants for the formation of HNi^{II} upon rapid mixing of 0.08 mM $[Ni^0(P_2^{Ph}N_2^{Bz})_2]$ with 2,4,6-collidinium (0-50 mM) in the presence of 2,4,6-collidine (0.5, 1 and 10 mM). Rate constants obtained from single exponential fits of the absorbance vs. time traces recorded at 350 nm. C) Observed rate constants for the reaction of 0.08 mM $[HNi^{II}(P_2^{Ph}N_2^{Bz})_2]^+$ with 2,4,6-collidinium (0-50 mM) in the presence of 2,4,6-collidine (0.5, 1 and 10 mM) to form to Ni^{II} and H_2, observed via the formation of Ni^{II} at 500 nm. Rate constants obtained from single exponential fits of the absorbance vs. time traces recorded at 500 nm.

5.2.5.3. Region 3 and 4, effective pH 8-14: Reaction of $[Ni^0(P_2^{Ph}N_2^{Bz})_2]$ *with pyridinium and anilinium.* At an effective pH of 13.5 (1 mM pyridinium, 10 mM pyridine), the hydride (HNi^{II}) is observed immediately upon mixing and H_2 forms relatively slowly, as detected by the growth of the Ni^{II} signal at 500 nm, with a pseudo-first order observed rate constant of 0.18 s^{-1} (Figure 5.10A).

$$Ni^0 \xrightarrow{HA} HNi^{II} \xrightarrow{HA} Ni^{II} + H_2$$

In range of effective pH values 11.5-13.5, an equilibria between HNi^{II} and a putative protonated hydride species, is observed. These observations are discussed in detail in Section 5.2.5.5. Between effective pH values of 9 and 11.5 (4-chloroanilinium (pK_a = 9.7), anilinium (pK_a = 10.6), 4-tertbutylanilnium (pK_a = 11.1), and 1 mM pyridinium:0.1 mM pyridine

(effective pH 11.5)), an unrecognized intermediate (Int_B, Appendix D.10) with absorbance features shouldering between 350 and 450 nm is observed immediately upon mixing. The absorbance features of Int_B are similar, though substantially blue shifted (ca. 50 nm) from those observed for Int_A (Appendix D.10). Under these conditions, HNi^{II} is not observed, but the formation of Ni^{II} is observed on the timescale of seconds (Figure 5.10B). More rapid formation of Ni^{II} is observed under more basic conditions (higher effective pH). Given the formation of Int_B upon acid addition but inconsistency of its optical features with those of HNi^{II}, this intermediate is likely a ligand protonated species. However, we cannot assign it as a singly or doubly protonated species ($Ni^0(H)$ or $Ni^0(H)_2$ respectively).

$$Ni^0 \overset{HA}{\rightarrow} Int_B \overset{HA}{\rightarrow} Ni^{II} + H_2$$

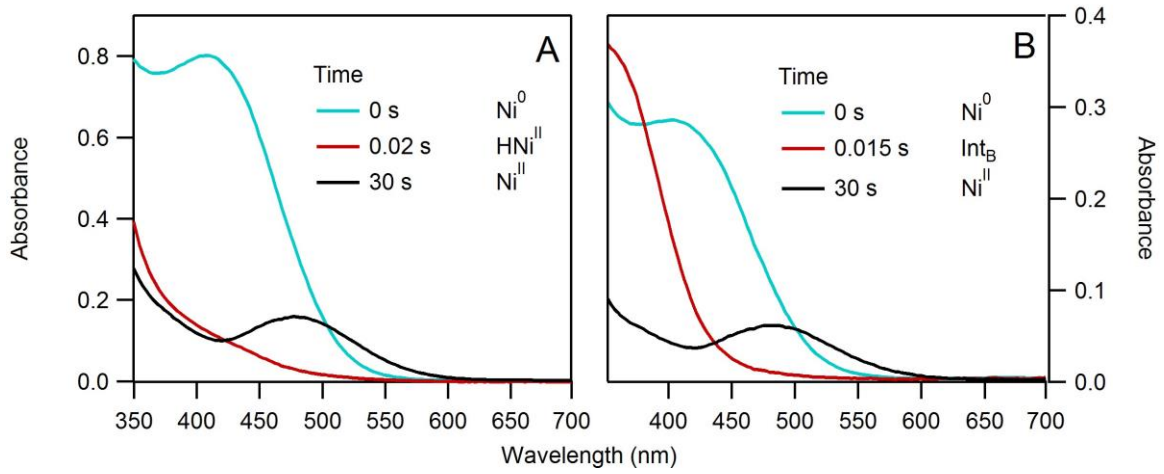

Figure 5.10. A) Representative spectra for the reaction of 0.1 mM $[Ni^0(P_2^{Ph}N_2^{Bz})_2]$ with 10 mM pyridine and 1 mM pyridinium (effective pH = 13.5) recorded at various time delays after rapid mixing via stopped-flow. Reaction is observed to proceed through the HNi^{II} intermediate. B) Representative spectra for the reaction of 0.031 mM $[Ni^0(P_2^{Ph}N_2^{Bz})_2]$ with 1.1 mM anilinium and 2.5 mM aniline (effective pH = 10.2) recorded at various time delays after rapid mixing via stopped-flow. Reaction is observed to proceed through the Int_B intermediate.

As discussed, formation of HNi^{II} was not observed upon mixing Ni^0 with acids in this range of effective pH values (9-11.5). Thus, we hypothesize that hydride formation from Int_B is the rate determining step under these conditions, followed by rapid protonation to release H_2 and form Ni^{II}. To test this hypothesis, HNi^{II} was isolated and mixed directly with anilinium. In this reaction, formation of Ni^{II} was observed (λ_{obs} = 500 nm) with a rate constant (4.2 s^{-1}) approximately two orders of magnitude larger than the observed rate constant for Ni^{II} formation from Ni^0 and the same acid (0.102 s^{-1}, Figure 5.11).

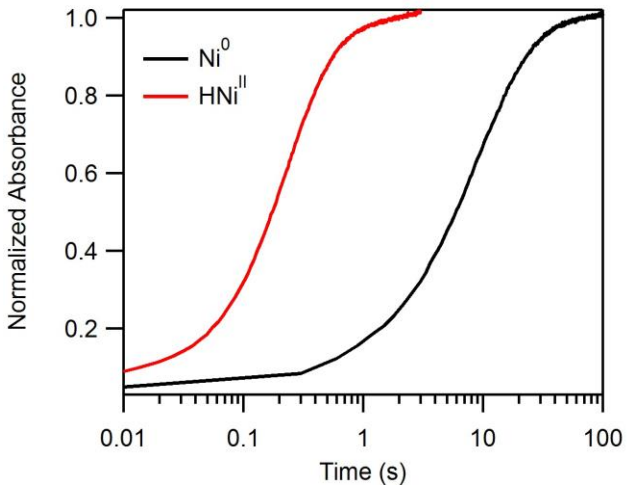

Figure 5.11. Comparison of the reaction of either 0.13 mM $[Ni^0(P_2^{Ph}N_2^{Bz})_2]$ or 0.21 mM $[HNi^{II}(P_2^{Ph}N_2^{Bz})_2]^+$ with 10 mM anilinium. Absorbance traces shown were each taken at 500 nm to monitor the appearance of $[Ni^{II}(P_2^{Ph}N_2^{Bz})_2]^{2+}$ and have been normalized for ease of comparison.

5.2.5.4. Region 5, effective pH < 8: Reaction of $[Ni^0(P_2^{Ph}N_2^{Bz})_2]$ *with 4-cyanoanilinium.* Stopped-flow rapid mixing of Ni^0 and 4-cyanoanilinium (pK_a = 7.0) gave rise to immediate formation of Int_B as detected by the signature optical profile observed at 0.015 s. On the millisecond timescale, the absorbance features for Int_B bleached and blue-shifted to give rise to a new absorbing species (Int_C). Subsequently, over the seconds timescale, formation of Ni^{II} was observed, as evidenced by the signature absorbance feature at 500 nm (Figure 5.12).

Reaction of Int_B to form Int_C was monitored at 350 nm as a function of acid concentration; kinetics traces could not be fit to single exponential fits and showed an unpronounced dependence on acid concentration (Appendix D.11). Formation of the Ni^{II} reaction product was monitored on the seconds timescale at 500 nm and could similarly not be fit to single exponential kinetics. The reaction kinetics at 500 nm qualitatively appeared to be acid-concentration independent, though the conversion appeared to decrease as acid concentration was increased, suggesting degradation (Appendix D.11).

To examine the role of a potential HNi^{II} intermediate in H_2 production, the reaction of HNi^{II} was with 4-cyanoanilinium was investigated. Upon rapid mixing, the absorbance spectrum recorded at t = 2 s was similar to the spectrum recorded at the same time point for the reaction of Ni^0 with 4-cyanoanilinium and contains a mixture of Int_C and Ni^{II} (Appendix D.9). Further, the kinetics profiles for the formation of Ni^{II} (λ_{obs} = 500 nm) observed when mixing HNi^{II} with 4-cyanoanilinium were very similar to those recorded upon mixing Ni^0 with the same acid concentration, suggesting involvement of a common intermediate, Int_C (Appendix D.9). These two observations—detection of a common intermediate (Int_C) and the similarity of these kinetics profiles for the formation of Ni^{II} (and H_2) — along with the similarity of the absorbance features for Int_C and HNi^{II} (both with trailing absorbances from the ultraviolet to 400 nm), support assignment of Int_C as a ligand-protonated hydride species, $HNi^{II}(H)$, suggesting the following reactivity:

$$Ni^0 \xrightarrow{HA} Int_B \rightarrow Int_C \rightarrow Ni^{II} + H_2$$

$$Int_C = HNi^{II}(H)$$

In this reaction scheme, the unpronounced acid dependence observed for the reaction of Int_B to Int_C could be due to an intramolecular proton transfer from a doubly-protonated Ni^0 species to a $HNi^{II}(H)$, or intermolecular protonation of a singly-protonated Ni^0 species followed by intramolecular proton shuttling to form the same product. In either scenario, Int_C—a protonated hydride species—plays a clear role in H_2 production.

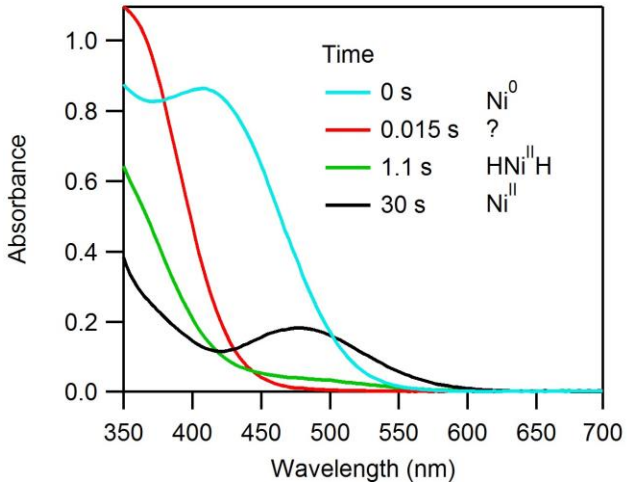

Figure 5.12. Representative spectra for the reaction of 0.1 mM $[Ni^0(P_2^{Ph}N_2^{Bz})_2]$ with 11.5 mM 4-cyanoanilinium recorded at various time delays after rapid mixing via stopped-flow.

5.2.5.5. Effective pH values 11.5-13.5: Reaction of $[Ni^0(P_2^{Ph}N_2^{Bz})_2]$ *with pyridinium/pyridine mixtures.* When examining the reactivity of Ni^0 with mixtures of pyridine and pyridinium (effective pH values between 13.5 and 11.5), the initial spectrum recorded at 0.015 s corresponds to Int_B. Rapidly, (20-50 ms, Figure 5.13) Int_B reacts to form an equilibrium between HNi^{II} and an unknown intermediate. This equilibrium mixture then reacts on the seconds timescale to form Ni^{II} and H_2. In spectra recorded at ca. 50 ms time delays (see time points indicated in Figure 5.13A), the established equilibrium optically manifests itself as an absorbance shoulder between 350 and 400 nm, the magnitude of which increases as the pH is lowered. Attempts to fit linear combinations of the HNi^{II} spectrum with the established spectra

for either Int_A or Int_B were unsuccessful. However, linear combinations of HNi^{II}, the newly assigned protonated hydride $HNi^{II}(H)$ (Int_C, see above), and a small contribution of Ni^{II} (arising from catalyst turnover) match well to the recorded spectra at the indicated time delays (Figure 5.13).

$$Ni^0 \xrightarrow{HA} Int_B \rightarrow \left[HNi^{II} \underset{A^-}{\overset{HA}{\rightleftharpoons}} HNi^{II}(H) \right] \xrightarrow{HA} Ni^{II} + H_2$$

From the deconvolution of the spectra of these equilibrium mixtures recorded at effective pH values of 12.9 and 12.1 (Figure 5.13B), the composition of the mixtures (containing HNi^{II}, $HNi^{II}(H)$ (Int_C), and Ni^{II}) were used to estimate a pK_a of 12.3 for ligand based proton on $HNi^{II}(H)$.

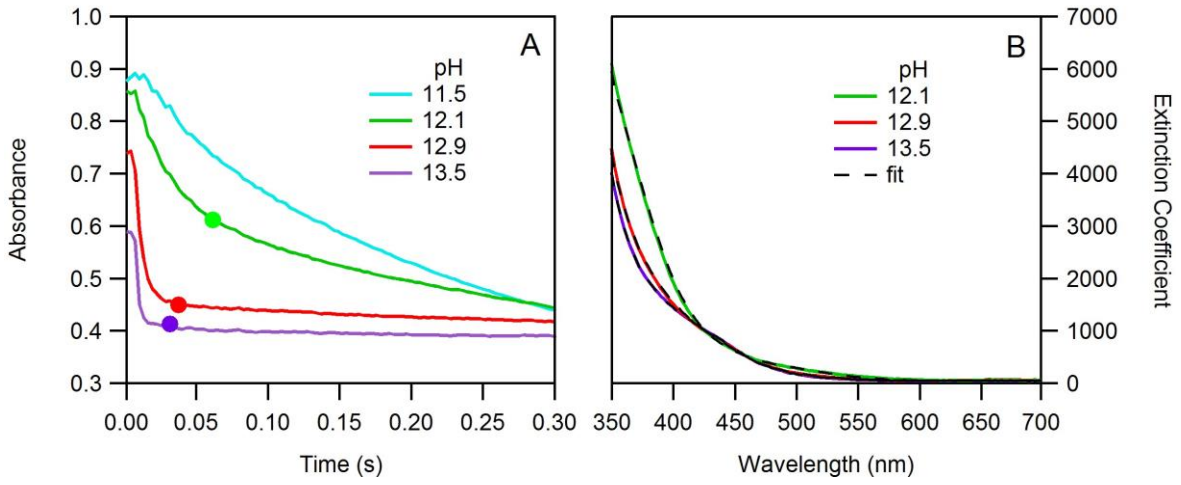

Figure 5.13. A) Kinetics traces recorded at 350 nm (corresponding to the disappearance of Int_B), for the reaction of 0.1 mM $[Ni^0(P_2^{Ph}N_2^{Bz})_2]$ with solutions of pyridinium:pyridine at effective pH values of 11.5, 12.1, 12.9, and 13.5. At early time delays, the reaction reaches an equilibrium, signified by the effective pH-dependent spectra shown in panel B, prior to the appearance of the Ni^{II} signal when the effective pH is higher than 12. The dots represent the time delays when the spectra in panel B were recorded. B) Spectra at time delays noted in panel A were fit with a linear combination of the spectra for the hydride (HNi^{II}), protonated hydride ($HNi^{II}(H)$, Int_C), and Ni^{II}. pH 13.5: 100% HNi^{II}; pH 12.9: 84% HNi^{II}, 14% $HNi^{II}(H)$, and 2% Ni^{II}; pH 12.1: 31% HNi^{II}, 60% $HNi^{II}(H)$, and 9% Ni^{II}.

5.3. Discussion

5.3.1. The Pourbaix Diagram

Pourbaix diagrams identify the most thermodynamically stable species at any given potential and (effective) pH. A true Pourbaix diagram for $[Ni(P_2^{Ph}N_2^{Bz})_2]^{2+}$ would only contain Ni^{II} (or $Ni^{II}(H)_2$) and H_2, as catalysis favors formation of these reaction products.[198] However, in the interest of gaining mechanistic insight into catalysis, it is productive to map out the most stable catalytic intermediates in a "quasi-Pourbaix Diagram;"[66] equilibria between intermediates should be represented by the potential of $E_{cat/2}$ under the conditions where Nernstian equilibria are formed on the electrochemical timescale.

We first established all accessible thermodynamic values possible via cyclic voltammetry. As discussed in Section 5.2.1, we define the x-axis as effective pH, as opposed to pK_a.[194] The redox potentials for the $Ni^{II/I}$ and $Ni^{I/0}$ couples have previously been established as -0.94 and -1.19 V vs $Fc^{+/0}$, respectively. Spectrophotometric titrations (Section 5.2.3.1-5.2.3.2) were used to determine the pK_a of HNi^{II} (20.15, previously calculated through a thermochemical cycle as 19.4) and the p$K^{1/2}_{Ni^{II}H_2}$ of $Ni^{II}(H)_2$ (6.56, previously established by NMR as 6.7).[111] Both pK_a values are within error of the previously reported values. From cyclic voltammetry measurements of $Ni^{II}(H)_2$, the one-electron reduction of was established as -0.52 V (Section 5.2.5.3). However, no subsequent reduction wave for $Ni^{I}(H)_2$ was observed. Previous computational work has suggested that the second electron transfer is thermodynamically easier than the first, which indicates a two-electron wave would be observed. We attribute our observation of a single one-electron reduction to slow electron transfer kinetics for the two-electron couple. Reduction to Ni^0 is anticipated to be

accompanied by a large structural rearrangement, but past work has shown that $Ni^{II}(H)_2$ exists in the pinched *exo* state (Figure 5.1), where *exo* denotes that the protons are held distal to the metal center on the pendant amine, and "pinched" denotes that the hydrogen is coordinated by both amines on each P_2N_2 ligand. As such, the necessary structural rearrangement is anticipated to be dramatically hindered by the "pinched" ligand geometry. As such, we assign the thermochemical potential for the two-electron $Ni^{II}(H)_2/HNi^{II}(H)$ couple as -0.52 V. These values were used to construct the anticipated potential-effective pH diagram in Figure 5.14.

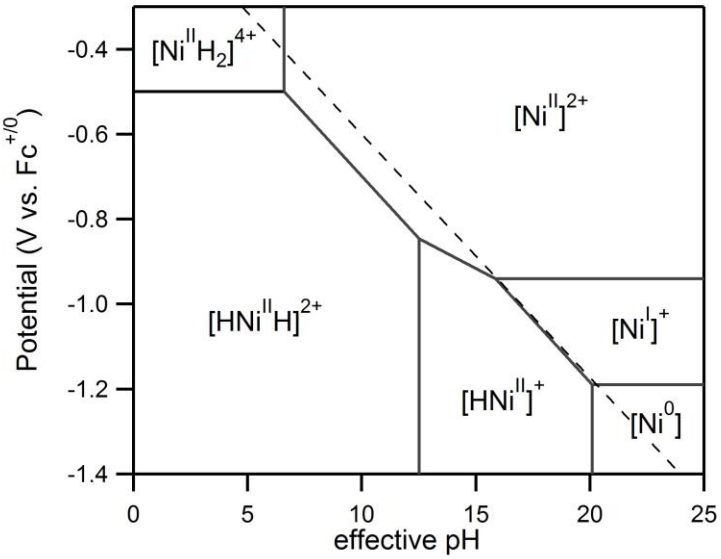

Figure 5.14. Potential-pH diagram for $Ni(P_2^{Ph}N_2^{Bz})_2$ in acetonitrile. The dashed line represents the thermodynamic potential for conversion of protons to hydrogen.[67,113]

As noted above, this diagram differs slightly from the analogous diagram reported by Hammes-Schiffer[40] (based on computational analysis and prior experiments[111]). In addition to updated experimental thermochemical values that have been revisited, we change from assignment of $Ni^0(H)_2$ as the most stable species at low effective pH values and cathodic potentials to $HNi^{II}(H)$. The assignment as $HNi^{II}(H)$ is based on our stopped-flow results showing the formation (via Int_B) of $HNi^{II}(H)$ (Int_C) upon reaction of Ni^0 and acid prior to

hydrogen formation at effective pH values below 13.5 (Section 5.2.5.4). We also optically observe this intermediate (Int_C) upon rapidly mixing both HNi^{II} and Ni^0 with 4-cyanoanilinium, supporting assignment as the ligand-protonated hydride $HNi^{II}(H)$. In the initial report of the Pourbaix Diagram for $[Ni(P_2^{Ph}N_2^{Bz})_2]^{2+}$, no experimental value was available for the pK_a for $HNi^{II}(H)$ (originally assigned as being the ligand-only protonation species $Ni^0(H)_2$),[40] though a thermochemical cycle was used to estimate a pK_a value of 12.5. In our work, reaction of Ni^0 with solutions containing pyridine:pyridinium mixtures to access a range of effective pH values between 11.5 and 13.5 (Section 5.2.5.5, Figure 5.13) revealed an equilibrium between this putative $HNi^{II}(H)$ intermediate and the isolable HNi^{II} species. From these experiments, the pK_a of the ligand-based proton of $HNi^{II}(H)$ is estimated as 12.3, in line with the pK_a of 12.5 established from the intersection of the sloped lines in Figure 5.14 defining the two-electron/two-proton $Ni^{II}/HNi^{II}(H)$ and the 2-electron/1-proton Ni^{II}/HNi^{II} couples.

5.3.2. Electrochemically Determined Redox Potentials

We next sought to populate the diagram with experimental data recorded at different effective pH values as a function of applied potential. Cyclic voltammograms of $Ni(P_2^{Ph}N_2^{Bz})_2$ recorded with acids ranging in pK_a from 5.06 to 19.56— and the reduction features observed within— were used to define redox couples observed for conditions spanning an effective pH range 4.56 – 19.56. A complete list of the assignments are presented in Table 5.1 and examples can be found in Appendix D.12. For effective pH <14 (Regions 3–5), pH-dependent catalytic responses were observed (Sections 5.2.4.3-5.2.4.5), and the $E_{cat/2}$ values were used to establish the experimental data points in Table 5.1. For experiments in which two overlapping catalytic features are observed, $E_{cat/s}$ values for the anodic features are considered. For effective pH 14–

17 (Region 2), non-Nernstian reactivity was observed and the potential of peak cathodic current was recorded in lieu of a thermodynamic value (Section 5.2.4.2). For effective pH >17 (Region 1) the $E_{1/2}$ for the reversible waves observed is used (Section 5.2.4.1).

Table 5.1. $\boldsymbol{E_{cat/2}}$ (from sigmoidal fit), peak potential and $\boldsymbol{E_{1/2}}$ determined from cyclic voltammograms of $\left[\boldsymbol{Ni(P_2^{Ph}N_2^{Bz})_2}\right]^{2+}$ recorded as a function of effective pH.

Proton Source	Acid:Base (mM)	Effective pH	Potential (V)	Type
2,6-dichloroanilinium	50:16	4.56	-0.490	$E_{cat/2}$
2,6-dichloroanilinium	50:50	5.06	-0.490	$E_{cat/2}$
2,6-dichloroanilinium	50:160	5.56	-0.510	$E_{cat/2}$
2,6-dichloroanilinium	50:500	6.06	-0.527	$E_{cat/2}$
4-cyanoanilinium	50:5	6.00	-0.531	$E_{cat/2}$
4-cyanoanilinium	50:16	6.50	-0.621	$E_{cat/2}$
4-cyanoanilinium	50:50	7.00	-0.650	$E_{cat/2}$
4-trifluoromethylanilinium	50:50	8.03	-0.695	$E_{cat/2}$
4-(methylbenzoate)anilinium	50:50	8.62	-0.702	$E_{cat/2}$
4-trifluoromethoxyanilinium	50:50	9.28	-0.782	$E_{cat/2}$
4-chloroanilinium	50:50	9.70	-0.786	$E_{cat/2}$
anilinium	50:5	9.62	-0.788	$E_{cat/2}$
anilinium	50:50	10.62	-0.849	$E_{cat/2}$
4-tertbutylanilinium	30:30	11.10	-0.866	$E_{cat/2}$
4-tertbutylanilinium	50:50	11.10	-0.866	$E_{cat/2}$
4-tertbutylanilinium	55:55	11.10	-0.866	$E_{cat/2}$
4-tertbutylanilinium	100:100	11.10	-0.864	$E_{cat/2}$
4-methoxyanilinium	50:50	11.86	-0.886	$E_{cat/2}$
pyridinium	50:50	12.53	-0.908	$E_{cat/2}$
2-picolinium	50:50	13.32	-0.930	$E_{cat/2}$
2,6-lutidinium	50:50	14.13	-0.919, -1.013	peak
2,4,6-collidinium	50:50	14.98	-0.912, -1.028	peak
2-aminobenzimidaxole	50:50	16.08	-0.915, -1.002	peak
benzylammonium	50:50	16.91	-0.920, -1.013	peak
4-dimethylaminopyridine	50:50	17.95	-0.932, -1.076	$E_{1/2}$
trethylammonium	50:50	18.82	-0.932, -1.134	$E_{1/2}$
pyrrolidinium	50:50	19.56	-0.932, -1.180	$E_{1/2}$

Overlaying the result of these assignments on the diagram presented in Figure 5.14 (Figure 5.15) reveals discrepancies between the recorded $E_{1/2}$ values and the thermochemical boundaries implied. Only at the effective pH extremes (pH < 6 and pH > 17) do the redox potentials determined from cyclic voltammetry experiments overlay the black lines of the diagram as expected. Above effective pH 17, two reversible waves are observed (Figure 5.6A). The first is fixed at -0.932 V and corresponds to the $Ni^{II/I}$ couple. The second shifts 60 mV per decade and, based on its alignment with the diagram in Figure 5.14, can be assigned as the Ni^{I}/HNi^{II} couple. Below effective pH 6, a reductive wave is observed at -0.5 V, in line with that observed for the reduction of isolated $Ni^{II}(H)_2$ (Figure 5.6E). In between pH 6 and 17, three distinct regions are observed. Each is discussed in detail below.

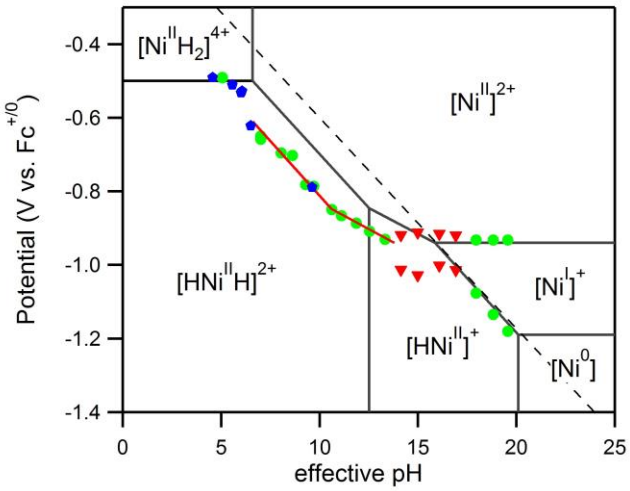

Figure 5.15. Potential-pH diagram for $[Ni(P_2^{Ph}N_2^{Bz})_2]^{2+}$ in acetonitrile (from Figure 5.14) with overlain of redox potentials determined from cyclic voltammetry (Table 5.1). Data points displayed represent the $E_{cat/2}$ and $E_{1/2}$ for solutions of 50 mM 1:1 acid:base solutions (green), $E_{cat/2}$ for varied ratio solution to obtain effective pH values (blue), and the potentials obtained from cyclic voltammograms that did not represent Nernstian equilibria (red). Red lines are a guide for the eye representing 30 (right) and 60 (left) mV per decade lines.

5.3.2.1. Non-Nernstian Reactivity. Two redox couples are observed between pH 14 and 17 (Region 2) via cyclic voltammetry; the first is fixed at -0.932 V and corresponds to the $Ni^{II/I}$ couple, while the second the second contains distinct reduction and oxidation events that are significantly separated in potential (> –400 mV, Figure 5.6B). This separation represents a system that is unable to achieve a Nernstian equilibrium on the timescale of the cyclic voltammetry experiment. As such, this data holds little value in the construction of a potential-pH diagram as the redox couple observed is under kinetic control. The peak values for the reduction events (Table 5.1) are represented in Figure 5.15 as red triangles, and as expected, do not align with any thermochemical transitions.

5.3.2.2. 30 mV per decade slope. Based on the thermochemical data presented in Figure 5.14, a shift in the observed redox couple of 30 mV per decade is expected between pH 12.5 and 16, consistent with 2-electron/1-proton transformation of the Ni^{II}/HNi^{II} couple. As noted above, we do not observe this reactivity, due to slow electron kinetics. However, we do observe a 30 mV per decade trend between pH 10.6 and 13.3 (Region 3, Appendix D.13), shifted significantly in effective pH (approximately two units) from its expected location (Figure 5.15). Given the thermodynamic values outlined previously, we remain confident in the thermochemical boundaries outlined in Figure 5.14. As such, two possible explanations exist for an observed 30 mV per decade slope:

(1) the slope represents a kinetic limitation on the first chemical step of the catalytic process that responds to the pK_a of the proton source with a one-to-one dependence between the log of the rate constant on acid pK_a (this reactivity has been observed in one other hydrogen evolution study[38]), as each order of magnitude of increase in rate constant for the first chemical step corresponds to a 30 mV shift of $E_{cat/2}$,[68]

or

(2) the slope represents a thermodynamic two electron, one proton reaction unique to the Ni^{II}/HNi^{II} couple expected at higher effective pH values.

To test the first scenario, a substrate concentration experiment was performed using a 1:1 4-tertbutylaniline:4-tertbutylanilinium at varying absolute concentrations. As an EC reaction would lead to a potential dependence on k_{obs}, where $k_{obs} = k_{PT}$[HA], a shift in observed potential would be expected for both variation of k_{PT} (as controlled by acid strength) and [HA]. These experiments (Section 5.2.4.3, Appendix D.7) revealed a fixed $E_{cat/2}$ for all concentrations above 30 mM, suggesting that the reaction is *not* under kinetic control.[72]

Towards the second explanation, we considered various two electron, one proton equilibria that could form on the electrochemical timescale, and reasoned that one could occur between Ni^{II} and $Ni^{0}(H)$. This insinuates a kinetic limitation for the formation of the hydride, favoring initial protonation of the ligand on the cyclic voltammetry timescale. Kinetic control of ligand protonation—over hydride formation—is discussed further below.

5.3.2.3. 60 mV per decade slope. Similar to the 30 mV per decade slope, a ca. 60 mV per decade slope is observed between effective pH values of 7 and 10.6, as predicted and previously observed[111] (Appendix D.13). However, the potential-pH relationship is shifted approximately two pH units from the location predicted by our thermochemical measurements (Figure 5.15). Because of this shift, we can again confidently assert that this 60 mV per decade slope does not correspond to an equilibrium between Ni^{II} and $HNi^{II}(H)$. The potential-pH redox couple observed could correspond to either:

(1) a two-electron, two-proton equilibrium between Ni^{II} and the initially ligand-protonated species $Ni^{0}(H)_2$,

or

(2) a one-electron, one-proton equilibrium between Ni^{II} and $Ni^{I}(H)$.

Currently, we have no experimental evidence to favor one of these explanations over the other, though for both explanations, the assignment of a PCET couple between Ni^{II} and a ligand protonated species ($Ni^{0}(H)_2$ or $Ni^{I}(H)$) is supported by the immediate formation of a ligand protonated species (Int_B) upon rapid mixing between Ni^{0} and acid solutions with effective pH <13.5. Under these conditions, the ligand protonated species Int_B was observed subsequently react to form HNi^{II} and/or $HNi^{I}(H)$ hydride intermediates. These data indicate that protonation at the ligand, as opposed to the metal center, is the kinetically favored product. The potential-pK_a relationship observed via cyclic voltammetry, however, indicates that the PCET couple between Ni^{II} and a ligand protonated species is under thermodynamic control.

5.3.3. The Role Ligand Protonated Species in Observed Reactivity

As discussed above, the experimentally observed regions with 30 and 60 mV per decade slopes can each be interpreted by two distinct explanations, resulting in the construction of four possible potential-pK_a diagrams (Figure 5.16). In order to distinguish the two sets of thermochemical boundaries, red and purple lines are used in Figure 5.16 to describe boundaries between the putative ligand protonated species observed in stopped-flow experiments and postulated to be involved in electrochemical equilibria detected via cyclic voltammetry. The black lines established by Hammes-Schiffer and coworkers have been retained for the more thermodynamically stable hydride species.[40]

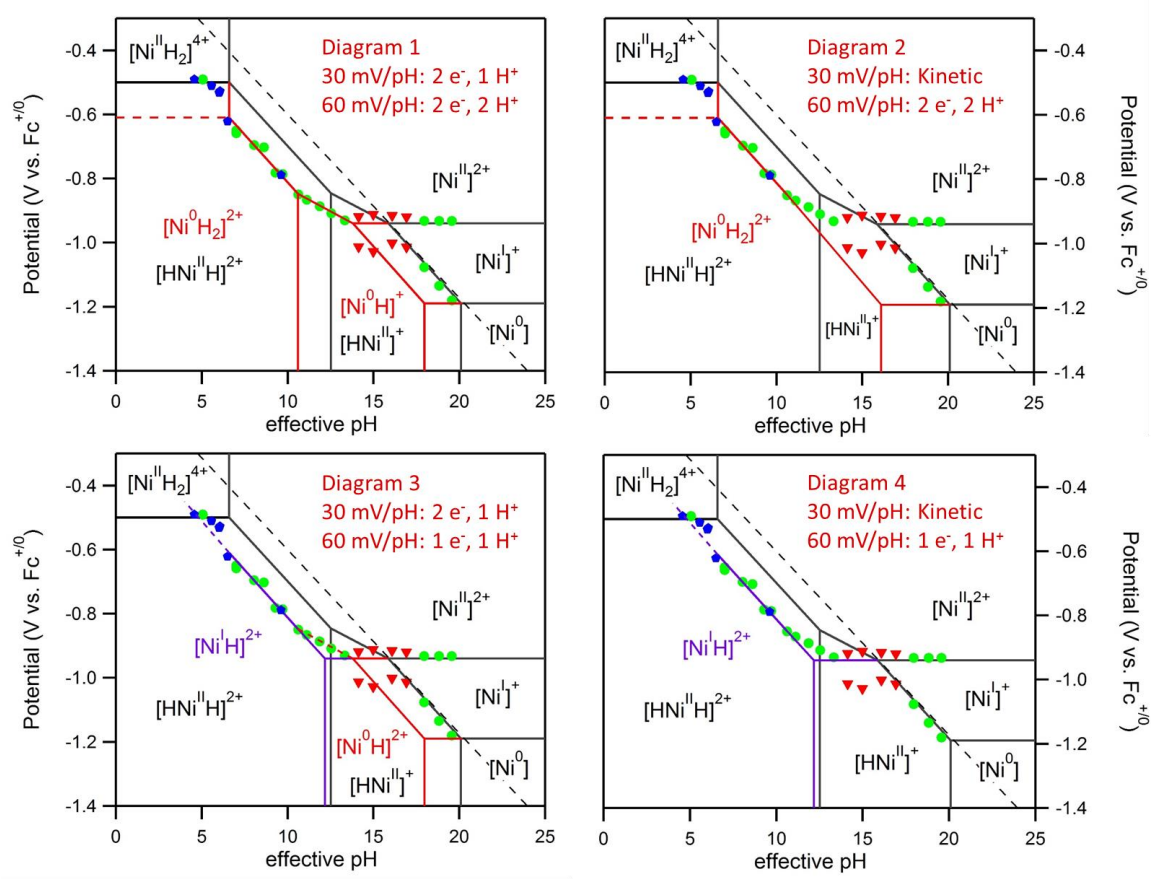

Figure 5.16. Potential-pH diagrams for $[Ni(P_2^{Ph}N_2^{Bz})_2]^{2+}$ in acetonitrile with overlay of redox potentials determined from cyclic voltammetry (Table 5.1). Diagrams 1 through 4 represent the various combinations of cases for a) the 30 mV per decade slope corresponding to either a kinetic shift or a two-electron, one-proton equilibrium and b) the 60 mV per decade slope corresponding to either a two-electron, two-proton equilibrium or a one-electron, one-proton equilibrium. Black lines on the diagram represent the expected equilibria for the more thermodynamically stable hydride species. Red and purple lines on the diagram represent the postulated equilibria for the kinetically accessible ligand protonated species.

We propose each of the four diagrams presented in Figure 5.16 is viable based on the potential-pK_a relationships observed via cyclic voltammetry, with the limitations of the current data prohibiting absolute assignment. However, we outline evidence in support and against each diagram below based upon reactivity observed in our stopped-flow rapid mixing experiments and the previous computational studies.

5.3.3.1. Diagram 1. Diagram 1 assigns the 30 mV per decade slope to a two-electron, one-proton equilibrium between Ni^{II} and $Ni^{0}(H)$ species and the 60 mV per decade slope to the a two-electron, two-proton equilibrium between Ni^{II} and $Ni^{0}(H)_2$ species. As discussed previously, a substrate concentration study using a 1:1 4-tertbutylaniline:4-tertbutylanilinium revealed a fixed $E_{cat/2}$ above 30 mM, providing support for assignment of the 30 mV per decade sloped region as a thermodynamic, rather than a kinetic, shift of the catalytic wave (Section 5.2.4.3). In addition, the catalytic current decreases significantly when traversing from the 30 mV per decade slope to the 60 mV per decade slope (Figure 5.6), which would be expected as the doubly protonated $Ni^{0}(H)_2$ formed at lower effective pH values would likely be in the pinched *exo* state and consequently, catalytic turnover would be impeded.[40,111]

Intersection of the 30 mV and 60 mV per decade lines (Figure 5.16, Diagram 1) suggests that $Ni^{0}(H)_2$ has a pK_a of 10.6. The point of intersection between the 30 mV per decade line with the horizontal line describing the $Ni^{I/0}$ couple is connected to the horizontal line describing the $Ni^{II/I}$ couple with a 60 mV per decade sloped line to describe the putative $Ni^{I}/Ni^{0}(H)$ redox couple (not observed). From this, a pK_a of 18 is predicted for $Ni^{0}(H)$. We anticipated that the formation of both $Ni^{0}(H)$ and $Ni^{0}(H)_2$, as well as an equilibrium between these species (and between Ni^{0} and $Ni^{0}(H)$) would be observed in stopped-flow experiments upon mixing Ni^{0} with the appropriate acids or acid/base mixtures. However, in experiments performed near the effective pH corresponding to the predicted $Ni^{0}(H)$ pK_a (18), the immediate formation of HNi^{II} was observed (Section 5.2.5.1). For all experiments performed at or below an effective pH of 13.5, the immediate formation of an unknown intermediate (Int_B) was observed upon mixing (Section 5.2.5.3). Int_B reacted further to form Ni^{II} (and release H_2), via hydride intermediates under some conditions. If the pK_a of $Ni^{0}(H)_2$ is indeed ca.10.6, we

hypothesized that a clear transition between the initial formation of $Ni^0(H)$ to the formation of $Ni^0(H)_2$ would be observed as the effective pH was lowered, but saw no evidence in support. It is possible that the absorbance spectra for Ni^0H_2 and Ni^0H are nearly identical in the visible region, as the unprotonated and doubly protonated Ni^{II} species (Ni^{II} and $Ni^{II}(H)_2$) have nearly identical optical spectra. If so, the species assigned Int_B could actually be either the singly or doubly protonated complexes.

5.3.3.2. Diagram 2. Diagram 2 assigns the 30 mV per decade slope to a kinetic shift and the 60 mV per decade slope to a two-electron, two-proton equilibrium between Ni^{II} and $Ni^0(H)_2$ species. In this case, the intersection between the (extended) 60 mV per decade line with the horizontal line representing the $Ni^{I/0}$ couple establishes a predicted $pK^{1/2}_{Ni^0(H)_2}$ for $Ni^0(H)_2$ of 16. This is much higher than the pK_a predicted by Diagram 1, and suggests that only the unprotonated and doubly protonated Ni^0 species will be observed. In attempt to observe an equilibrium between Ni^0 and $Ni^0(H)_2$ the reaction between Ni^0 and acids with pK_a values near 16 was examined via stopped-flow rapid mixing. However, immediate formation of HNi^{II} was observed at effective pH of 16, preventing determination of the pK_a for any ligand protonated species. In addition, computational work[40] calculated that the pK_a of $Ni^0(H)_2$ is substantially lower than that of $Ni^0(H)$ (11.8 vs. 19.4, respectively), which is inconsistent with Diagram 2 which predicts only the Ni^0 and $Ni^0(H)_2$ species are accessed in acidic conditions. However, the observation of Int_B upon rapid mixing of Ni^0 with acidic solutions of effective pH < 13.5 (Section 5.2.4.3), lends support to this diagram, as only a single ligand-protonated species ($Ni^0(H)_2$) would be accessed across a wide range of effective pH values.

5.3.3.3. Diagram 3. Diagram 3 assigns the 30 mV per decade slope to a two-electron, one-proton equilibrium between Ni^{II} and $Ni^{0}(H)$ species and the 60 mV per decade slope as a one-electron, one-proton equilibrium between Ni^{II} and $Ni^{I}(H)$ species. Assignment of the 30 mV per decade slope as a thermodynamically-controlled shift is supported by the arguments presented for Diagram 1; namely, the observation that absolute acid/base concentrations do not influence the position of $E_{1/2}$ (Section 5.2.4.3) as would be expected for a kinetic shift. In support of the 60 mV per decade assignment is the observation that $Ni^{II}(H)_2$ exhibits reversible one-electron redox chemistry (Section 5.2.3.3, Figure 5.5), not the anticipated two electron redox chemistry. As discussed above, we attributed this to slow electron transfer kinetics for the second reduction. If the two-electron PCET reduction of Ni^{II} to $HNi^{II}(H)$ is similarly slow on the electrochemical timescale, one-electron, one-proton chemistry ($Ni^{II}/Ni^{I}(H)$ couple) would be observed.

These assignments—a two-electron, one-proton equilibrium and a one-electron, one-proton equilibrium are difficult to clearly rationalize together and thus we represent these PCET couples with different colored lines in Diagram 3. The mechanism switch—from a two-electron redox couple to a one-electron redox couple, could be due to the influence of electron transfer kinetics on the observed redox couples. Specifically, under stronger acidic conditions, ligand protonation in the *exo* pinched geometry may impede electron transfer kinetics and the anticipated two-electron, two-proton reactivity expected.

Lastly, the intersection of the 60 mV per decade line with the horizontal line representing the reversible $Ni^{II/I}$ couple suggests that the pK_a of $Ni^{I}(H)$ ($Ni^{I} \rightleftharpoons Ni^{I}(H)$) is

ca. 12.2. Experimental confirmation of this expected pK_a was not sought due to difficulties in studying the Ni^I species arising from its disproportionation to Ni^{II} and Ni^0 (Appendix D.3).

5.3.3.4. Diagram 4. Diagram 4 assigns the 30 mV per decade slope to a kinetic shift and the 60 mV per decade slope to a one-electron, one-proton equilibrium between Ni^{II} and $Ni^I(H)$ species. Just as in Diagram 3, the slow electron transfer kinetics observed for $Ni^{II}(H)_2$ that give rise to observation of one-electron redox chemistry (Section 5.2.3.3, Figure 5.5) provide support for assignment of the 60 mV per decade slope as a one-electron, one-proton process. However, as for Diagram 2, observation that absolute acid/base concentrations do not influence the position of $E_{1/2}$ (Section 5.2.4.3) fail to support the assignment of the 30 mV per decade slow as a kinetic shift.

5.3.4. The Role of Kinetics in an Experimental Pourbaix Diagram

While we are unable to confidently assign the redox couples that underpin the effective pH-dependent $E_{cat/2}$ values observed, we know that the experimentally observed 30 mV and 60 mV per decade regions determined from cyclic voltammetry experiments do not correspond to Nernstian equilibria between the most thermodynamically quasi-stable reaction intermediates identified by Hammes-Schiffer,[40] Appel[111] and in this work. More generally, we recognize that potential-pH trends obtained from cyclic voltammetry under catalytic conditions do not necessarily represent borders between the most stable reaction intermediates. Instead, they represent the thermochemistry of the specific equilibria that form on the timescale of the experiment.

To exemplify this, we revisit the stopped-flow rapid mixing studies between Ni^0 and an anilinium:aniline mixture (pK_a = 10.6, Section 5.2.5.3, Figure 5.10). Upon mixing,

immediate formation of a ligand protonated species (Int_B) is observed. On longer timescales, Ni^{II} (and (H_2) is formed but no hydride intermediate (HNi^{II} or $HNi^{II}(H)$) is optically detected. However, extensive studies of $[Ni(P_2^{Ph}N_2^{Bz})_2]^{2+}$ and the $[Ni(P_2^{R}N_2^{R\prime})_2]^{2+}$ family of catalysts indicate that hydrogen production involves a nickel(II)-hydride intermediate.[40,42,56,102,111] As such, our observations of Int_B reacting to form Ni^{II}, without optical detection of a hydride intermediate, suggests that formation of the hydride is rate limiting under these conditions. If so, then an equilibrium between Ni^{II} and either of the hydride species (HNi^{II} and $HNi^{II}(H)$) will not be established as the hydride will quickly react to release H_2 and generate Ni^{II}.

Rate-limiting hydride formation from the ligand-protonated complex (Int_B) implies that an equilibrium will be formed between the unreduced Ni^{II} species and the ligand-protonated complex. As such, it is not only the pK_a values of quasi-stable nickel hydride species (HNi^{II} and $HNi^{II}(H)$) that are relevant to the construction of this potential-pH diagram, but also the pK_a values of the reaction intermediates with protonated amine ligands ($Ni^0(H)$ and $Ni^0(H)_2$).

5.4. Conclusions

In this work, we have demonstrated experimentally determined potential- pK_a relationships for molecular catalysts may not directly correspond to boundaries reflecting the most thermodynamically stable reaction intermediates, but instead can reflect other equilibria, such as between un-reduced catalysts and an intermediate that forms prior to the rate-determining step. As discussed above, we consider the shift of $E_{cat/2}$ as a function of acid pK_a to be valuable behavior for catalysts because of the opportunity to access acid pK_a-independent

overpotentials. Catalysts displaying this behavior should be versatile for applications in future devices. By examining the catalyst properties that give rise to these desired potential-pK_a relationships in this work, we have aimed to reveal design features that may more generally engender pK_a-dependent $E_{cat/2}$ in catalysis. Specifically, we have shown that for $[Ni(P_2^{Ph}N_2^{Bz})_2]^{2+}$, the potential-p$K_a$ relationships observed between effective pH 6.6 and 10.6 arise from a Nernstian equilibrium between the Ni^{II} species and a reduced, ligand-protonated product ($Ni^{I}(H)$ or $Ni^{0}(H)_2$) as opposed to the hydride species $HNi^{II}(H)$ that is the thermodynamically quasi-stable species at these applied potentials and effective pH values. Identification of this Nernstian equilibrium insinuates that the pK_a responsible for determining $E_{cat/2}$ is that of the pendant amine, not the hydride intermediate. Therefore, if the benzyl group on the pendant amine can be modified without sacrificing the pH dependent reactivity, it should be possible to lower the effective pH-independent overpotential by increasing the pendant amine basicity with an electron donating group.

It is not surprising that protonation of the pendant amine gives rise to the observed pK_a dependence of $E_{cat/2}$, as hydride formation can be more kinetically challenging than other protonation processes, often inhibiting reversible PCET electrochemistry.[39] Additional studies exploring the influence of a secondary coordination sphere proton relay sites on potential-pK_a relationships in catalysis will help realize more efficient systems for PCET transformations.

5.5. Experimental

5.5.1. General Materials and Method

Molecular synthesis was performed under N_2 either on a Schlenk line or in an inert-atmosphere glovebox. Acetonitrile (Fisher Scientific, HPLC grade, >99.9%), Tetrahydrofuran

and diethyl ether (Fisher Scientific, >99%) were degassed with argon and dried using a Pure Process Technology solvent system. All acidic species were prepared with a tetrafluoroborate counterion; the details of their preparation are provided in Appendix D.14. All bases used that are liquids at room temperature were filtered neat through silica gel and then stored over 3Å molecular sieves to remove any residual water. All bases that are solid at room temperature were sublimed to ensure purity. Tetrabutylammonium hexafluorophosphate (TCI, >98%) was recrystallized from hot ethanol, filtered, washed with cold ethanol, and dried at 80° C under vacuum overnight. Nickel powder (Sigma-Aldrich) and phenylphosphine (Alfa Aesar) were used as received. $[Ni^{II}(P_2^{Ph}N_2^{Bz})_2(MeCN)][BF_4]_2$ and $[Ni^0(P_2^{Ph}N_2^{Bz})_2]$ were prepared according to literature methods.[74,111] $[Ni^0(P_2^{Ph}N_2^{Bz})_2]$ is not soluble in acetonitrile directly, for experiments with $[Ni^0(P_2^{Ph}N_2^{Bz})_2]$, the solid was first dissolved in 0.1 ml tetrahydrofuran and then transferred to acetonitrile. $[Ni^0(P_2^{Ph}N_2^{Bz})_2]$ was never observed to precipitate from solution on the timescale of the experiments performed.

NMR spectra were recorded on either a Bruker 400 or 500 MHz spectrometer. ^{1}H NMR were referenced to proteo solvent impurities and ^{31}P and ^{31}P$\{^1$H$\}$ were referenced to a standard of phosphoric acid. UV-Vis absorbance measurements and spectrophotometric titrations[67] were performed on an Agilent Cary 60 UV-vis spectrophotometer using 1 cm pathlength quartz cuvettes.

5.5.2. Preparation of $[Ni^{II}(P_2^{Ph}N_2^{Bz})H_2(MeCN)][BF_4]_4$ ($Ni^{II}(H)_2$)

200 mg (0.16 mmol) of $[Ni^{II}(P_2^{Ph}N_2^{Bz})_2(MeCN)][BF_4]_2$ was dissolved in ~3 ml of acetonitrile. 3 ml of diethyl ether was then added to this solution to reduce polarity. To this solution was then added 2 equivalents (0.32 mmol, 47 mg) of tetrafluoroboric acid diethyl ether

complex. $[Ni^{II}(P_2^{Ph}N_2^{Bz}H)_2(MeCN)][BF_4]_4$ immediately precipitates out after addition as a red solid. The solid was filter out and washed with approximately 10 ml of diethyl ether. NMR confirmed isolated $[Ni^{II}(P_2^{Ph}N_2^{Bz}H)_2(MeCN)][BF_4]_4$ with a single $^{31}P\{^1H\}$ peak at -16 ppm.

5.5.3. Electrochemistry

. Electrochemical experiments were performed under a nitrogen atmosphere in an inert atmosphere glovebox using dry acetonitrile with 0.25 M $[Bu_4N][PF_6]$ electrolyte on a Pine Instruments Wavedriver potentiostat with a silver wire pseudo-reference separated from the main solution by a glass frit, a glassy carbon counter electrode and a 1mm disk glassy carbon working electrode. A freshly polished working electrode was used for every voltammogram recorded. Electrodes were polished before experiments with 0.05 μm alumina powder (CH Instruments, contained no agglomerating agents) Milli-Q water slurries. They were then rinsed and sonicated to remove residual alumina. Before measurements were taken, electrodes were pretreated by scanning two cycles from 1 V to -2 V (vs. Ag wire) at 400 mV/s in electrolyte solution.[67] In a generic experiment, a 5 ml solution of 0.6 mM $[Ni(P_2^{Ph}N_2^{Bz})_2(MeCN)][BF_4]_2$, acid:base buffer, ferrocene (internal reference), and electrolyte was prepared. The cyclic voltammogram was then collected at a scan rate of 50 mV/s, scanned cathodically first to view the reactivity of $Ni(P_2^{Ph}N_2^{Bz})_2$ before scanning through the internal reference. All scans were referenced to the ferrocene/ferrocenium couple.

5.5.4. Stopped-Flow Experiments

Stopped-Flow experiments were performed on a Hi-Tech Scientific SF-61 DX2 double mixing stopped-flow in single mixing mode with Kinetic Studio data acquisition software (v2.33). The instrument was outfitted with a photo-diode array for data collection and a 75 W

xenon lamp light source. Stopped-flow measurements were all performed under an N_2 atmosphere. This was accomplished by preparing solutions inside an inert-atmosphere glovebox in septum-sealed bottles. PEEK tubing was used to transfer solutions directly from sealed bottles to the stopped flow syringes to avoid exposure to air. To ensure purity, the syringe was purged three times with each solution prior to each measurement. In a typical experiment, one syringe was loaded with the $[Ni^0P_2^{Ph}N_2^{Ph})_2]$ solution and the other was loaded with a solution of acid and base. Upon injection, spectra were recorded from 350 nm to 700 nm using a 3 ms integration time.

5.5.5. Preparation of $[\boldsymbol{HNi^{II}(P_2^{Ph}N_2^{Bz})H_2(MeCN)][BF_4]_4}$ $\boldsymbol{(HNi^{II})}$

200 mg (0.16 mmol) of $[Ni^{II}(P_2^{Ph}N_2^{Bz})_2(MeCN)][BF_4]_2$ was dissolved in ~3 ml of acetonitrile. 31 mg (0.8 mmol) of sodium borohydride was dissolved in 5 ml of acetonitrile. 1 ml of the sodium borohydride solution (1 equivalent) was then added drop-wise with stirring to the solution of Ni^{II}. Upon addition the solution changes from red to golden yellow. Immediately after mixing the solvent was removed under vacuum. No additional purification was performed. Due to the decay of the hydride to Ni^I and H_2 (Appendix D.3), addition of the sodium borohydride solution was performed directly prior to experiments utilizing HNi^{II} without removing the solvent under vacuum.

APPENDIX A. SUPPLEMENTAL INFORMATION FOR CHAPTER 2

A.1 Cyclic Voltammogram of $[\mathbf{Ni}(\mathbf{P_2^{Ph}N_2^{Ph}})_2]^{2+}$

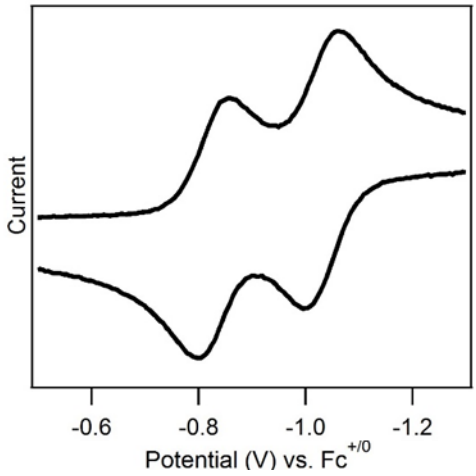

Figure A.1. Cyclic voltammogram of 1 mM $[Ni(P_2^{Ph}N_2^{Ph})_2]^{2+}$. $[Ni(P_2^{Ph}N_2^{Ph})_2]^{2+}$ has two reversible, one electron reduction waves at –0.83 V and –1.03 V vs. $Fc^{+/0}$ corresponding to the $Ni^{II/I}$ and $Ni^{I/0}$ couples. Voltammograms recorded at 100 mV/s in 0.2 M $[NBu_4][PF_6]$ CH_3CN solutions.

A.2. Effect of Added Base on the Rate of Ni^0 Protonation

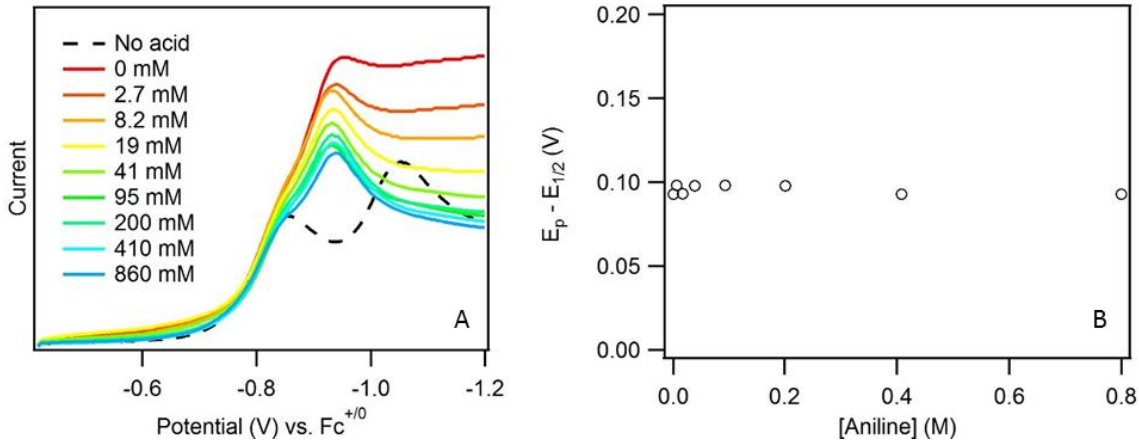

Figure A.2. Effect of added base on Ni^0 protonation rate. A) Cyclic voltammograms of 0.33 mM $[Ni(P_2^{Ph}N_2^{Ph})_2]^{2+}$ with 10 mM anilinium tetrafluoroborate with various concentrations of aniline (0- 860 mM). B) Peak potential plotted versus aniline concentration. These data indicate that the peak potential, and thus the rate of Ni^0 protonation, is not affected by the concentration of base. Voltammograms recorded at 100 mV/s in 0.2 M $[NBu_4][PF_6]$ CH_3CN solutions.

A.3. Validating Foot-of-the-Wave Analysis with Two Closely Spaced Redox Events

As its name suggest, foot-of-the-wave analysis examines the data at the earliest points in the catalytic wave. In this work, the catalytic wave is expected to originate at the $Ni^{I/0}$ redox event, which is 200 mV negative of the $Ni^{II/I}$. FOWA has not been investigated in the cases where there is an underlying redox event, and hence, another electrochemical equilibrium. Here we illustrate the anticipated error under these conditions by simulating this scenario for an *EECC* process, in the electrochemical simulation software DigiElch, with various rate constants for k_1 for the mechanism shown below.

Simulation parameters:

$O + e \rightleftharpoons P; \qquad E^0 = 0\ V$
$P + e \rightleftharpoons Q; \qquad E^0 = 0.2\ V$
$Q + X \rightarrow QX; \qquad k_1 = varied\ M^{-1}s^{-1}$
$QX + X \rightarrow O + X_2; \qquad k_2 = 50\ M^{-1}s^{-1}$

[O] = 0.001 M, [X] = 1 M, D_O = 1 x 10^{-5} cm^2 s^{-1}, k^0 = 10,000 cm s^{-1}, A = 1 cm^2

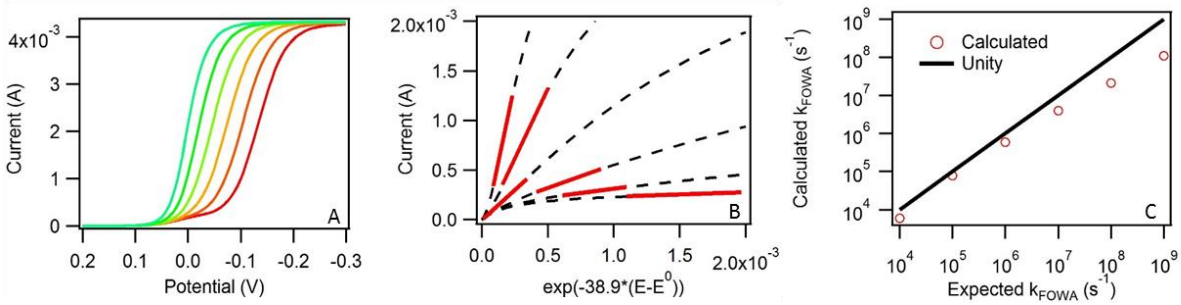

Figure A.3. Simulated FOWA with two closely spaced redox events. A) Simulated voltammograms with k_1 ranging from 1 x 10^4 (red) to 1 x 10^9 M^{-1} s^{-1} (green). For the lower rates, the O ⇌ P redox wave is still visible at the foot of the wave. B) FOWA for the simulated voltammograms. For the lower rates, the linear region is fit after the contribution from the O ⇌ P wave. C) The expected k_{FOWA} against the calculated k_{FOWA}. All calculated points are within 1 order of magnitude. Accuracy between FOWA calculated rates and actual rate constants are best at ca. 1 x 10^5 s^{-1}. The rates calculated in this work for the relevant data points were between 1 x 10^5 and 5 x 10^5 s^{-1}, the best location according to simulated examples.

A.4. Stopped-Flow Measurements and Kinetics Analysis

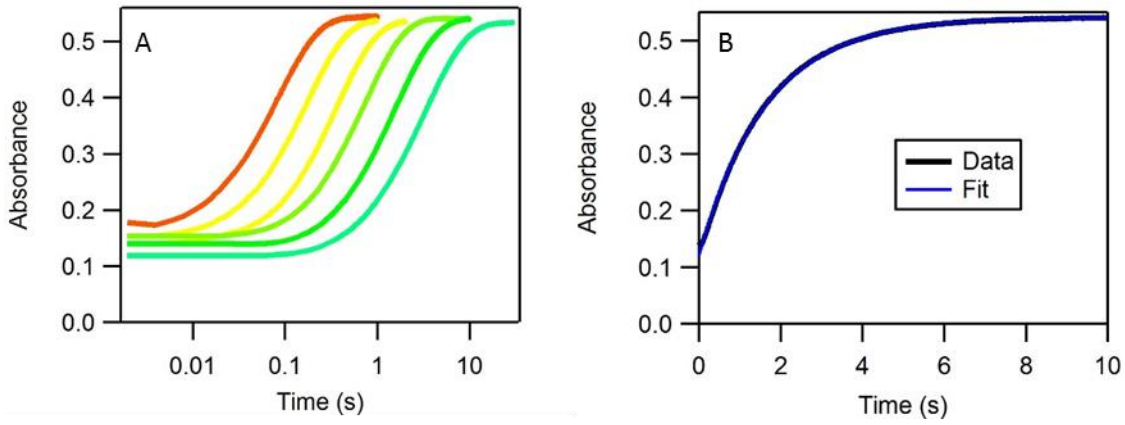

Figure A.4. Stopped-Flow Kinetics for $Ni^{II}H$ and Anilinium. A) Absorbance (λ_{obs} = 500 nm) versus time traces of the reaction of 0.1 mM $[HNi(P_2^{Ph}N_2^{Ph})_2]^+$ with 6 mM (cyan)–0.2 M (red) anilinium. B) Example kinetics fit of the stopped flow data. Datasets were fit with a single exponential ($Abs_t = Abs_\infty - \Delta Abs * e^{-k_{SF}*t}$, where Abs_t is the absorbance value at time t, Abs_∞ is the final absorbance, ΔAbs is the overall change).

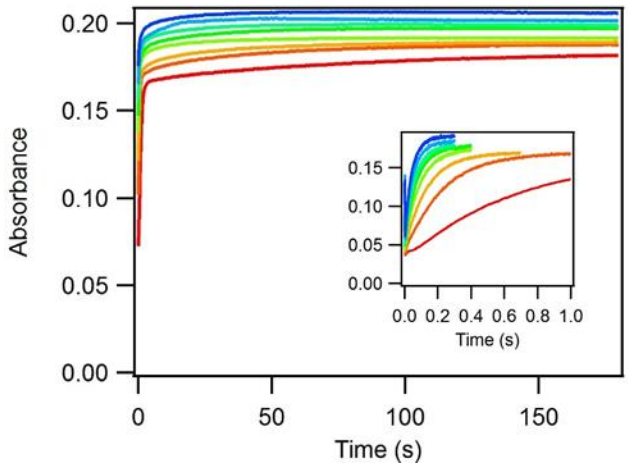

Figure A.5. Long term reactivity in stopped-flow of $Ni^{II}H$ and Anilinium. Absorbance (λ_{obs} = 500 nm) versus time traces for the reaction of 0.1 mM $[HNi(P_2^{Ph}N_2^{Ph})_2]^+$ with 13 mM (red)–0.2 M (blue) anilinium on longer timescales. The absorbance continues to increase beyond the initial kinetics regime highlighted in Figure A.4, indicating that another process is required for full conversion to $[Ni(P_2^{Ph}N_2^{Ph})_2]^{2+}$. This process is attributed to the conversion of the exo-protonated hydride species $H_{exo}NiH$ back to $[HNi(P_2^{Ph}N_2^{Ph})_2]^+$, followed by protonation in the endo position and H_2 release (see main text). The inset shows the initial kinetics (sub 1s) for these particular traces. Over the course of this particular experiment, the overall absorption value was shifted upward; this is attributed to decay of the $Ni^{II}H$ species, likely from a small amount of oxygen seeping into the system.

Table A.1. Percentage of stopped-flow traces representing the fast kinetics. Absorbance (λ_{obs} = 500 nm) at the start of the stopped-flow measurements (from Figure A.5), the end of the first kinetic regime and the end of the second kinetic regime for the reaction of 0.1 mM $[\boldsymbol{HNi(P_2^{Ph}N_2^{Ph})_2}]^+$ with various concentrations of anilinium. These values were used to calculate what percent of the net $[\boldsymbol{Ni(P_2^{Ph}N_2^{Ph})_2}]^{2+}$ product is generated in the fast reaction. The percent of the reaction completed during the fast kinetic regime has no dependence on the concentration of the acid.

[Anilinium] (M)	**Initial Absorbance**	**Absorbance after fast kinetics**	**Final Absorbance**	Percent complete after fast kinetics
0.013	0.036	0.167	0.182	**90.2**
0.040	0.037	0.169	0.188	**87.3**
0.067	0.042	0.170	0.189	**86.6**
0.095	0.044	0.174	0.192	**88.1**
0.121	0.049	0.180	0.197	**88.1**
0.149	0.052	0.180	0.200	**86.9**
0.175	0.058	0.186	0.203	**88.2**
0.203	0.065	0.193	0.207	**90.1**
			Average	**88.2**

A.5. Derivation of Equation 2.8.

To extract the overall rate constant (k_{pl}) from the plateau current (i_{pl}), the equation for the current plateau with an EECC mechanism (Eq. A.6) was first divided by the Randles-Sevcik Equation (Eq. A.2) to obtain Eq. A.7. When Eq. A.7 is solved for k_{pl}, the resulting Eq. A.8 can be used to convert i_{pl}/i_p to the overall rate constant for catalysis.

$$i_{pl} = 2FAC_{cat}\sqrt{k_{pl}D_{cat}}; \quad Eq.A.6$$

$$\frac{i_{pl}}{i_p} = \frac{4.48}{n}\sqrt{\frac{RTk_{pl}}{nFv}}; \quad Eq.A.7$$

Constants: R = 8.3145 J mol^{-1} K^{-1}, T = 298 K, F = 96485 C mol^{-1}

$$\frac{i_{pl}}{i_p} = \frac{0.7179}{n}\sqrt{\frac{k_{pl}}{n\upsilon}}$$

n=1, υ = 0.05 V/s and thus

$$k_{pl} = \left(\frac{i_{pl}/i_p}{3.212}\right)^2; \quad Eq.A.8 \text{ (Eq. 2.8)}$$

A.6. Kinetics Analysis of Cyclic Voltammetry and Stopped Flow Kinetics Accounting for an Off-Cycle Intermediate

Kinetics Analysis of observed rate constants obtained from catalytic cyclic voltammograms

The following differential equations describe the change in concentration of various reactants, intermediates and products as a function of time. We assume that the reduction to Ni^0 and subsequent protonation to form $Ni^{II}H$ are fast such that they do not influence the observed rate (reduction to Ni^0 is accounted for by Eq. 2.8, and thus, we only consider the reduced forms of nickel in our kinetics analysis as k_{pl} is representative of the rate at which Ni^0 is converted back to Ni^{II} through the catalytic process). Thus formation of Ni^{II} immediately results in the formation of $Ni^{II}H$ and the terms corresponding to $-k_2[Ni^{II}H][BH^+]$ and $k_1[Ni^0][BH^+]$ are not included the expression describing the concentration of $Ni^{II}H$ vs. time. Further, because monitoring base (B) concentration in these electrochemical experiments is exceedingly difficult, its contribution to the deprotonation of $H_{exo}Ni^{II}H$ is not included and $k_{-3}[B]$ is replaced by $k_{obs,-3}$.

$$\frac{d[Ni^{II}H]}{dt} = -k_3[Ni^{II}H][BH^+] + k_{obs,-3}[H_{exo}Ni^{II}H]$$

$$\frac{d[H_{exo}Ni^{II}H]}{dt} = -\frac{d[Ni^{II}H]}{dt}$$

Assuming that release of H_2 from $H_{endo}Ni^{II}H$ is rapid,

$$\frac{d[H_2]}{dt} = k_2[Ni^{II}H][BH^+]$$

Assuming that $Ni^{II}H$ and $H_{exo}Ni^{II}H$ are in equilibrium and their concentrations are at steady state:

$$\frac{d[Ni^{II}H]}{dt} = 0 = -k_3[Ni^{II}H][BH^+] + k_{obs,-3}[H_{exo}Ni^{II}H]$$

$$[Ni]_{total} = [Ni^{II}H] + [H_{exo}Ni^{II}H]$$

Solving for $[Ni^{II}H]$:

$$0 = -k_3[Ni^{II}H][BH^+] + k_{obs,-3}([Ni]_{total} - [Ni^{II}H])$$

$$k_3[Ni^{II}H][BH^+] + k_{obs,-3}\,[Ni^{II}H] = k_{obs,-3}[Ni]_{total}$$

$$(k_3[BH^+] + k_{obs,-3}\,)[Ni^{II}H] = k_{obs,-3}[Ni]_{total}$$

$$[Ni^{II}H] = \frac{k_{obs,-3}[Ni]_{total}}{k_3[BH^+] + k_{obs,-3}}$$

Substituting into hydrogen formation rate equation yields:

$$\frac{d[H_2]}{dt} = \frac{k_2 k_{obs,-3}[Ni]_{total}[BH^+]}{k_3[BH^+] + k_{obs,-3}} = k_{pl}[Ni]_{total}$$

$$k_{pl} = \frac{k_2 k_{obs,-3}[BH^+]}{k_3[BH^+] + k_{obs,-3}}$$

Analysis of Stopped-Flow Kinetics

Experimental data indicate that there are two kinetic regimes for the conversion of $Ni^{II}H$ to Ni^{II}. We assign the first regime to direct protonation of $Ni^{II}H$ in the endo position to form $H_{endo}Ni^{II}H$, followed by rapid H_2 release and production of Ni^{II}. The slower kinetics are assigned to reactivity of in the exo position to form $H_{exo}Ni^{II}H$, which must be deprotonated to reform $Ni^{II}H$ before $H_{endo}Ni^{II}H$ can be formed and H_2 released. We assume that the

deprotonation of $H_{exo}Ni^{II}H$ to $Ni^{II}H$ occurs on a substantially slower timescale such that it does not interfere in the fast regime of the kinetics, and as such, the relevant differential equations describing the change in concentrations of $Ni^{II}H$ and Ni^{II} on the fast timescale then become:

$$\frac{d[Ni^{II}H]}{dt} = -k_2[Ni^{II}H][HB] - k_3[Ni^{II}H][HB]; \quad Eq.A.9$$

$$\frac{d[Ni^{II}]}{dt} = k_2[Ni^{II}H][HB]$$

To solve for $[Ni^{II}]$ at any time *t* assuming we are under pseudo first order conditions such that $[BH^+] >> [Ni^{II}H]$.

$$\frac{d[Ni^{II}]}{dt} = k_2[Ni^{II}H]_t[BH^+]; \quad Eq.A.10$$

$[Ni^{II}H]_t$ is found by integrating $Eq.A.9$

$$\int_0^t \frac{d[Ni^{II}H]}{[Ni^{II}H]} = \int_0^t -(k_2 + k_3)[BH^+]dt$$

$$\ln[Ni^{II}H]_t = \ln[Ni^{II}H]_0 - (k_2 + k_3)[BH^+]t$$

$$[Ni^{II}H]_t = [Ni^{II}H]_0 e^{-(k_2+k_3)[BH^+]t}$$

Plugging this expression back into Eq. A.10 reveals:

$$\frac{d[Ni^{II}]}{dt} = k_2[Ni^{II}H]_0[BH^+]e^{-(k_2+k_3)[HB]t}$$

Integrating for $[Ni^{II}]_t$

$$\int_0^t d[Ni^{II}] = k_2[Ni^{II}H]_0[BH^+] * \int_0^t e^{-(k_2+k_3)[BH^+]t}dt$$

$$[Ni^{II}]_t - [Ni^{II}]_0 = k_2[Ni^{II}H]_0[BH^+]\left(-\frac{e^{-(k_2+k_3)[BH^+]t}}{(k_2 + k_3)[BH^+]} + \frac{1}{(k_2 + k_3)[BH^+]}\right)$$

$$[Ni^{II}]_t = [Ni^{II}]_0 + \frac{k_2[Ni^{II}H]_0[BH^+]}{(k_2 + k_3)[BH^+]} - \frac{k_2[Ni^{II}H]_0[BH^+]}{(k_2 + k_3)[BH^+]}e^{-(k_2+k_3)[HB]t}$$

$$[Ni^{II}]_t = [Ni^{II}]_0 + \frac{k_2[Ni^{II}H]_0\cancel{[BH^+]}}{(k_2+k_3)\cancel{[BH^+]}}[1 - e^{-(k_2+k_3)[BH^+]t}]$$

$$[Ni^{II}]_t = [Ni^{II}]_0 + \frac{k_2[Ni^{II}H]_0}{(k_2+k_3)}\left[1 - e^{-(k_2+k_3)[BH^+]t}\right]$$

$$[Ni^{II}]_0 = 0$$

$$[Ni^{II}]_t = \frac{k_2[Ni^{II}H]_0}{(k_2+k_3)}\left[1 - e^{-(k_2+k_3)[BH^+]t}\right]; \qquad Eq.A.11$$

As is described above (Figure A.4), stopped-flow data was fit to Eq. A.12. In our datasets, we have, presumably, three absorbing species, Ni^{II}, $Ni^{II}H$, and $H_{exo}Ni^{II}H$. We believe that the extinction coefficient (ε) for $Ni^{II}H$ and $H_{exo}Ni^{II}H$ are reasonably close to assume they are equal and thus:

$$Abs_t = Abs_\infty - \Delta Abs e^{-k_{SF}t}; \qquad Eq.A.12$$

$$Abs = (\varepsilon_{Ni^{II}}[Ni^{II}] + \varepsilon_{Ni^{II}H}([Ni^{II}H] + [H_{exo}Ni^{II}H]))l$$

Our path length was always 1 cm, thus;

$$Abs = \varepsilon_{Ni^{II}}[Ni^{II}] + \varepsilon_{Ni^{II}H}([Ni^{II}H] + [H_{exo}Ni^{II}H])$$

$$Abs_t = \varepsilon_{Ni^{II}}[Ni^{II}]_t + \varepsilon_{Ni^{II}H}([Ni^{II}H]_t + [H_{exo}Ni^{II}H]_t)$$

Because only $Ni^{II}H$ is present at the start of the experiment:

$$Abs_0 = \varepsilon_{Ni^{II}H}[Ni^{II}H]_0$$

ΔAbs corresponds to the total change in absorbance over the whole timeframe for the fast kinetics, which we will assume to be infinity for simplicity. At time infinity (end of the long timescale data), the concentrations of Ni^{II}, $Ni^{II}H$ and $H_{exo}Ni^{II}H$ are equal to:

$$[Ni^{II}]_\infty = \frac{k_2}{k_2+k_3}[Ni^{II}H]_0$$

$$[Ni^{II}H]_\infty = 0$$

$$[H_{exo}Ni^{II}H]_{\infty} = \frac{k_3}{k_2 + k_3}[Ni^{II}H]_0$$

Which gives an Abs_{∞} of:

$$Abs_{\infty} = \varepsilon_{Ni^{II}} \frac{k_2}{k_2 + k_3}[Ni^{II}H]_0 + \varepsilon_{Ni^{II}H} \frac{k_3}{k_2 + k_3}[Ni^{II}H]_0$$

And therefore a ΔAbs of:

$$\Delta Abs = Abs_{\infty} - Abs_0$$

$$\Delta Abs = \varepsilon_{Ni^{II}} \frac{k_2}{k_2 + k_3}[Ni^{II}H]_0 + \varepsilon_{Ni^{II}H} \frac{k_3}{k_2 + k_3}[Ni^{II}H]_0 - \varepsilon_{Ni^{II}H}[Ni^{II}H]_0$$

$$\Delta Abs = \varepsilon_{Ni^{II}} \frac{k_2[Ni^{II}H]_0}{k_2 + k_3} - \varepsilon_{Ni^{II}H} \frac{k_2[Ni^{II}H]_0}{k_2 + k_3}$$

$$\Delta Abs = (\varepsilon_{Ni^{II}} - \varepsilon_{Ni^{II}H}) * \frac{k_2[Ni^{II}H]_0}{k_2 + k_3}$$

Substituting into the right side of Eq. A.12 we obtain:

$$Abs_t = \varepsilon_{Ni^{II}} \frac{k_2[Ni^{II}H]_0}{k_2 + k_3} + \varepsilon_{Ni^{II}H} \frac{k_3[Ni^{II}H]_0}{k_2 + k_3} - (\varepsilon_{Ni^{II}} - \varepsilon_{Ni^{II}H}) \frac{k_2[Ni^{II}H]_0}{k_2 + k_3} * e^{-k_{SF}t}$$

$$Abs_t = \varepsilon_{Ni^{II}H} \frac{k_3[Ni^{II}H]_0}{k_2 + k_3} + \varepsilon_{Ni^{II}H} \frac{k_2[Ni^{II}H]_0}{k_2 + k_3} * e^{-k_{SF}t}$$

$$+ \varepsilon_{Ni^{II}} \frac{k_2[Ni^{II}H]_0}{k_2 + k_3}[1 - e^{-k_{SF}t}]; \quad Eq. A. 13$$

Considering that

$$\varepsilon_{Ni^{II}H} \frac{k_3[Ni^{II}H]_0}{k_2 + k_3} = \varepsilon_{Ni^{II}H}[Ni^{II}H]_0 - \varepsilon_{Ni^{II}H} \frac{k_2[Ni^{II}H]_0}{k_2 + k_3}$$

We can rearrange Eq. A.13 to obtain

$$Abs_t = \varepsilon_{Ni^{II}H}[Ni^{II}H]_0 - (\varepsilon_{Ni^{II}} - \varepsilon_{Ni^{II}H}) * \frac{k_2[Ni^{II}H]_0}{k_2 + k_3}[1 - e^{-k_{SF}*t}]$$

We also know from considering the system:

$$Abs_t = \varepsilon_{Ni^{II}H}[Ni^{II}H]_0 - (\varepsilon_{Ni^{II}} - \varepsilon_{Ni^{II}H}) * [Ni^{II}]_t$$

And thus,$[Ni^{II}]_t$ equals

$$[Ni^{II}]_t = \frac{k_2[Ni^{II}H]_0}{k_2+k_3}[1 - e^{-k_{SF}*t}]; \quad Eq.A.14$$

By comparison of Eq. A.11 and A.14, we find that:

$$k_{SF} = (k_2 + k_3)[BH^+]$$

A.7. Stopped-Flow Spectroscopy: Optically Searching for the Off-Cycle intermediate Signal

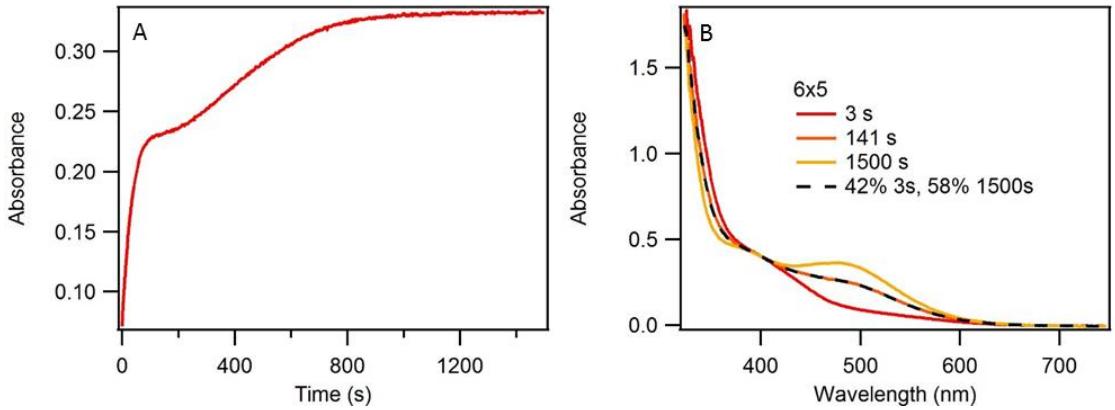

Figure A.6. Stopped-flow at high base concentration for $Ni^{II}H$. Left: Absorbance at 500 nm versus time for 0.22 mM $[HNi(P_2^{Ph}N_2^{Ph})_2]^+$, 5 mM anilinium, and 50 mM aniline. Plot shows the short and long timescale kinetics. Right: The full absorbance spectra at 3 s, 141s and 1500s for the reaction shown on the left. The spectra at 141s was shown to be a linear combination of the traces recorded at 3s ($[HNi(P_2^{Ph}N_2^{Ph})_2]^+$), and 1500s ($[Ni(P_2^{Ph}N_2^{Ph})_2]^{2+}$), the absorbance of any intermediate is indistinguishable from the reactant or product.

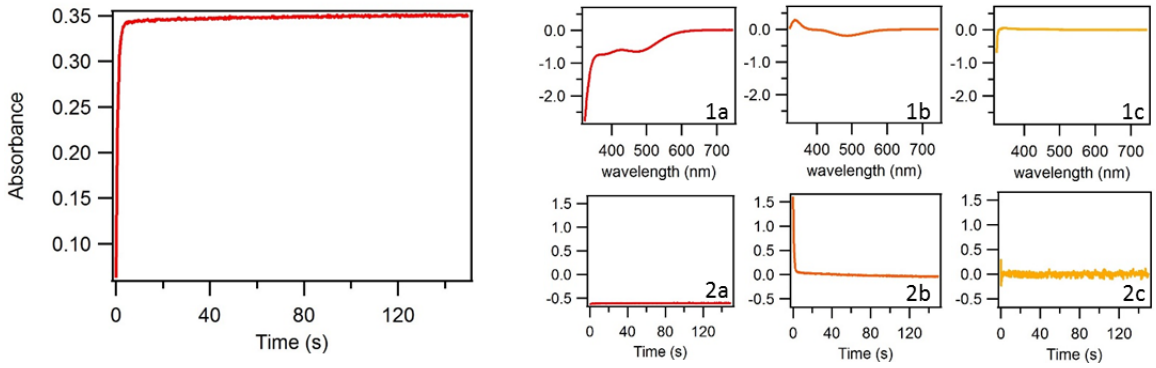

Figure A.7. SVD of stopped flow spectra for $Ni^{II}H$ and anilinium reaction. Left: Absorbance measured at 500 nm over the course of the reaction of 0.22 mM $[HNi(P_2^{Ph}N_2^{Ph})_2]^+$ with 5 mM anilinium. Trace extracted from 3 dimensional data, absorbance vs. wavelength vs. time, between 380 nm and 800 nm and 0 and 150 s. 1-2: Singular value decomposition (SVD) was performed on the 3 dimensional data set. 3 contributors to the overall spectra were identified. 1a and 1b represent the $[HNi(P_2^{Ph}N_2^{Ph})_2]^+$ and $[Ni(P_2^{Ph}N_2^{Ph})_2]^{2+}$ spectra, however, the actual spectra is misdiagnosed for them because SVD cannot differentiate two related species and the result is some linear combination of the two actual spectra(1a) and the overall change in the spectra (1b). 1c corresponds to the drift of the xenon light source over the course of the experiment. 2a-2c represent the contributions of each 1a-1c over the course of the experiment. SVD again suggests that if there is an off-cycle intermediate, its spectra must be indistinguishable from that of $[HNi(P_2^{Ph}N_2^{Ph})_2]^+$.

A.8. k_{-3} from Stopped Flow Simulations.

$$Ni^{II}H + BH \xrightarrow{k_2} Ni^{II} + H_2 + B$$

$$Ni^{II}H + BH \underset{k_{-3}}{\overset{k_3}{\rightleftharpoons}} H_{exo}Ni^{II}H + B$$

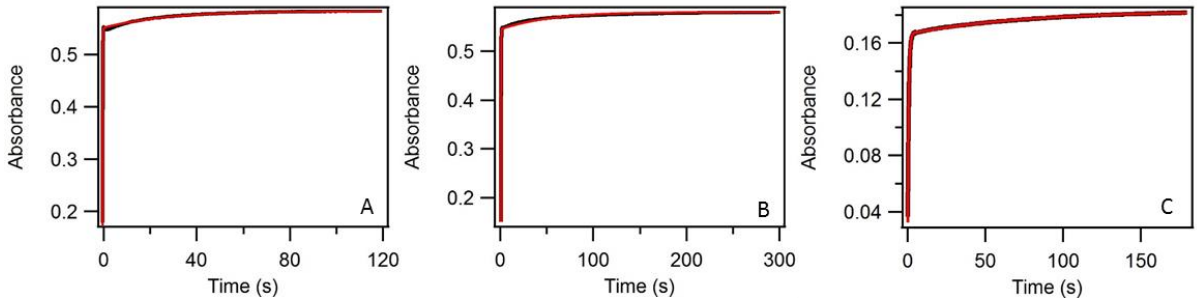

Figure A.8. k_{-3} from Stopped Flow Simulations. Three datasets were simulated using the mechanism shown above, allowing $H_{exo}Ni^{II}H$ to be formed and then deprotonated by the generated base before proceeding on to hydrogen evolution. Simulations were performed in MATLAB using an ordinary differential equation solver with the corresponding rate equations for Ni^{II}, $Ni^{II}H$, and $H_{exo}Ni^{II}H$. Fitting was accomplished by the least squares curve fitting function in MATLAB (lsqcurvefit). The resulting rate constants for each dataset were: A) k_2 55 M^{-1} s^{-1}, k_3 = 4.7 M^{-1} s^{-1}, k_{-3} = 110 M^{-1} s^{-1}. B) k_2 53 M^{-1} s^{-1}, k_3 = 4.7 M^{-1} s^{-1}, k_{-3} = 56 M^{-1} s^{-1}. C) k_2 52 M^{-1} s^{-1}, k_3 = 6.3 M^{-1} s^{-1}, k_{-3} = 150 M^{-1} s^{-1}. k_{-3} values were relatively scattered, but an average of the three was ~105 $M^{-1}s^{-1}$. Experimental Conditions: A): $[Ni^{II}H]$ = 0.392 mM, [anilinium] = 0.2 M; Center: $[Ni^{II}H]$ = 0.392 mM, [anilinium] = 0.1 M; Right: $[Ni^{II}H]$ = 0.1 mM, [anilinium] = 0.025 M.

A.9. Obtaining k_{-2} and [H_{exo}NiH] from NMR Equilibrium Experiment.

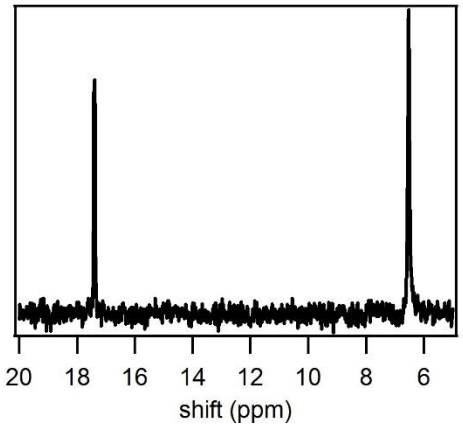

Figure A.9. ^{31}P NMR taken after allowing equilibration (6 hours after mixing) of 2.5 mM $Ni^{II}H$, 2.5 mM anilinium and 25 mM aniline. Relative integrations of the two peaks were 1 for Ni^{II} (6.6 ppm) and 0.58 for $Ni^{II}H$ (17.4 ppm); no other species were detected.

Integration of the peaks in Figure A.9, assuming that no degradation occurred, gave the following estimated concentrations at equilibrium.

$[Ni^{II}H] = 9.2x10^{-4}$ M

$[Ni^{II}] = 1.58x10^{-3}$ M

$[BH^{+}] = 9.2x10^{-4}$ M

$[B] = 2.66x10^{-2}$ M

The concentration of H_2 in solution is estimated using Henry's Law[199] as follows

$$P = kX$$

Where P = partial pressure, k = 5700 atm,[199] X = mol fraction of dissolved H_2.

$$P = \frac{n_{gas}RT}{V}$$

$$X = \frac{n_{dissolved}}{n_{MeCN}}$$

Where $n_{dissolved}$ is the moles of dissolved H_2, n_{gas} is the moles of H_2 in the headspace, and n_{MeCN} is the moles of solvent (acetonitrile) in the NMR tube.

R = 0.0821 L atm mol^{-1} K, T = 298 K

The total volume of the NMR tube was measured to be 2.8 mL and there was 1 mL liquid and thus 1.8 mL of headspace. The density of acetonitrile is 0.786 g/ml

V = 0.0018 L, n_{MeCN} = 0.01915 mol

$$\frac{n_{gas}RT}{V} = k\frac{n_{dissolved}}{n_{MeCN}}$$

$$1.359\ x\ 10^4 * n_{gas} = 2.977\ x\ 10^5 * n_{dissolved}$$

$$\frac{n_{dissolved}}{n_{gas}} = 0.04566$$

$$n_{total} = 1.58x10^{-6}\ mol = n_{gas} + n_{dissolved}$$

$$n_{dissolved} = 1.58x10^{-6} - n_{gas}$$

Solving for $n_{dissolved}$ by substituting $n_{gas} = \frac{n_{dissolved}}{0.04566}$ gives

$n_{dissolved}$ = 6.9 x 10^{-8} mol

$[H_2]$ = 6.9 x 10^{-5} M

The equilibrium we expect to be forming can be described by:

$$H_{exo}Ni^{II}H\ +\ B \overset{K_3}{\rightleftharpoons} Ni^{II}H\ +\ BH \overset{K_2}{\rightleftharpoons} Ni^{II} +\ H_2 + B$$

Solving the relevant equilibrium equations using the concentrations found above along with k_2 = 50 $M^{-1}s^{-1}$, k_3 = 10 $M^{-1}s^{-1}$ (averages of values from stopped-flow and current plateau analysis), and k_{-3} = 100 $M^{-1}s^{-1}$ (Appendix A.8) gives a k_{-2} of:

$$K_2 = \frac{k_2}{k_{-2}} = \frac{[Ni^{II}][H_2][B]}{[Ni^{II}H][BH]}$$

$$k_{-2} = \frac{k_2[Ni^{II}H][BH]}{[Ni^{II}][H_2][B]} = 1.5x10^4\ M^{-2}s^{-1}$$

and a concentration for $H_{exo}Ni^{II}H$ of:

$$K_3 = \frac{k_3}{k_{-3}} = \frac{[HNi^{II}H][B]}{[Ni^{II}H][BH]}$$

$$[H_{exo}Ni^{II}H] = \frac{k_3[Ni^{II}H][BH]}{k_{-3}[B]} = 3.2x10^{-6}\ M$$

With a concentration this low, we would not expect to see any signal for the $H_{exo}Ni^{II}H$ via NMR.

APPENDIX B. SUPPLEMENTAL INFORMATION FOR CHAPTER 3

B.1 Homoconjugation

Determination of the homoconjugation constant for 4-cyanoanilinium

^{1}H NMR was used to determine the homoconjugation constant for 4-cyanoanlinium. In the case that a proton is rapidly exchanging between multiple locations, only one peak will appear. The shift of that peak is dependent upon the shift of each pure species and the percentage of protons in each state. For 4-cyanoanilinium, this is represented as Eq. B.1, where δ is the observed shift, $\%H_X$ is the percentage of protons in state X, δ_X is the shift for pure X. For 4-cyanoanilinium, there are three possible states, B (4-cyanoaniline), BH (4-cyanonanilinium), and BHB (homoconjugated species).

$$\delta = \%H_B\delta_B + \%H_{BH}\delta_{BH} + \%H_{BHB}\delta_{BHB} \qquad (Eq.B.1)$$

Because each of the species present contains a different number of protons participating in the exchange process, we have to account for this using Eq. B.2, where n represents the number of exchanging protons on species X and χ_X represents the mole fraction of species X.

$$\%H_X = \frac{n\chi_X}{2\chi_B + 3\chi_{BH} + 5\chi_{BHB}} \qquad (Eq.B.2)$$

$$\delta = \frac{2\chi_B\delta_B + 3\chi_{BH}\delta_{BH} + 5\chi_{BHB}\delta_{BHB}}{2\chi_B + 3\chi_{BH} + 5\chi_{BHB}} \qquad (Eq.B.3)$$

To relate Eq. B.3 to the homoconjugation constant, we must solve for the concentration of the homoconjugated species in the equilibrium equation. As is explained below in the experiment description, we simplified our analysis by using a 1:1 ratio of B and BH and then varied the

total concentration. Thus, we simplify the input concentration of B and BH to be represented as $[I]_0$

$$[I]_0 = [B]_0 = [BH]_0 \qquad (Eq.B.4)$$

$$K = \frac{[BHB]}{[B][BH]} = \frac{[BHB]}{([I]_0 - [BHB])^2} \qquad (Eq.B.5)$$

$$[BHB] = [I]_0 + \frac{1 - \sqrt{1 + 4K[I]_0}}{2K} \qquad (Eq.B.6)$$

$$\chi_B = \chi_{BH} = \frac{([I]_0 - [BHB])}{2([I]_0 - [BHB]) + [BHB]} = \frac{([I]_0 - [BHB])}{2[I]_0 - [BHB]} \qquad (Eq.B.7)$$

$$\chi_{BHB} = \frac{[BHB]}{2([I]_0 - [BHB]) + [BHB]} = \frac{[BHB]}{2[I]_0 - [BHB]} \qquad (Eq.B.8)$$

Substituting S7 and S8 into S3 results in:

$$\delta = \frac{2([I]_0 - [BHB])\delta_B + 3([I]_0 - [BHB])\delta_{BH} + 5[BHB]\delta_{BHB}}{5[I]_0} \qquad (Eq.B.9)$$

Eq. B.9 can be further simplified by acknowledging that δ_B and δ_{BH} can be represented as a single parameter, δ_I.

$$\delta_I = \frac{2}{5}\delta_B + \frac{3}{5}\delta_{BH} \qquad (Eq.B.10)$$

$$\delta = \frac{([I]_0 - [BHB])}{[I]_0}\delta_I + \frac{[BHB]}{[I]_0}\delta_{BHB} \qquad (Eq.B.11)$$

Substituting in B.6 into B.11 we obtain our fitting equation for our NMR shift, with three dependent variables K, δ_I, and δ_{BHB}.

$$\delta = \frac{\sqrt{1 + 4K[I]_0} - 1}{2K[I]_0}\delta_I + \left(1 + \frac{1 - \sqrt{1 + 4K[I]_0}}{2K[I]_0}\right)\delta_{BHB} \qquad (Eq.B.12)$$

The homoconjugation constant was therefore determined by the average of three separate experiments. Each experiment followed a generic procedure in which 1 mL of a deuterated acetonitrile stock solution of 1:1 4-cyanoaniline:4-cyanoanilinium was prepared in an inert atmosphere glovebox. To three separate J-Young tubes, 0.125 mL, 0.25 mL, and 0.5 mL of stock solution were added. Each was then diluted to 0.5 mL total. After taking NMRs, the solutions were each then diluted by 0.1 mL. This was repeated 5-6 times to complete a dataset. After referencing the proteo-impurity of acetonitrile to 1.94 ppm,[137] the peak location of the acidic protons was recorded. After plotting the chemical shift against the input concentration, $[I]_0$, the datasets were fit using Eq. B.12 (Figure B.1).

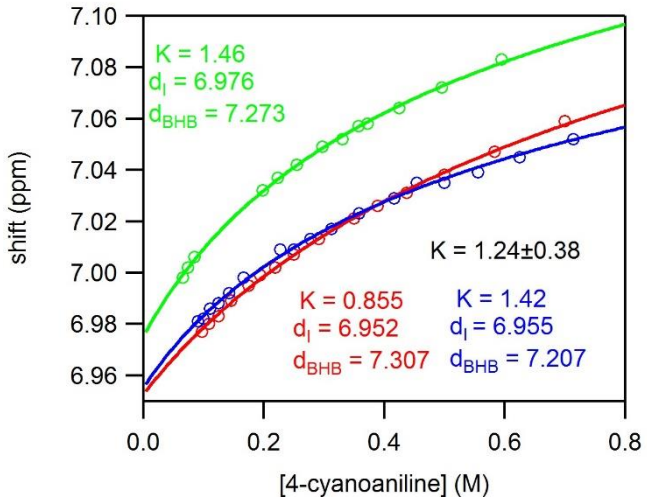

Figure B.1. Three titrations of 1:1 mixtures of 4-cyanoaniline:4-cyanoanilinium in deuterated acetonitrile. The fits represent Eq. B.12. The average value for K from the three datasets was $1.24 \pm 0.38\ M^{-1}$.

Tosic Acid Kinetic Trace

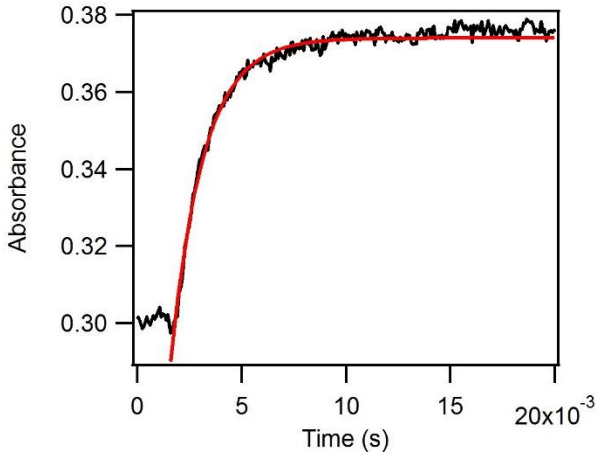

Figure B.2. Stopped-flow kinetics trace for the reaction of $Ni^{II}H$ with 5 mM of tosic acid to generate H_2 and Ni^{II} (λ_{obs} = 500 nm). Fit, shown in red, gives an observed rate constant of 640 s^{-1}.

B.2 Acid Concentration Independence

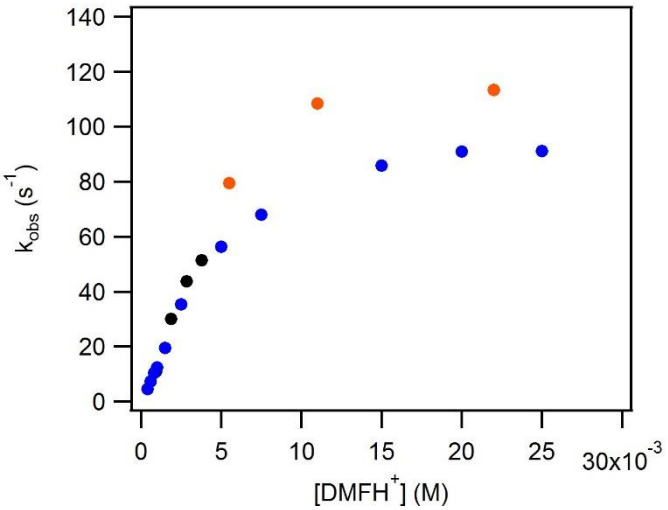

Figure B.3. Observed rate constant plotted against dimethylformamidium concentration; rate data obtained from stopped-flow kinetics traces monitoring the appearance Ni^{II} (λ_{obs} = 500 nm). The colored data points represent separate experiments. While the observed rate constant always plateaued around 10 mM $DMFH^+$, the rate constant at which it plateaued at was inconsistent.

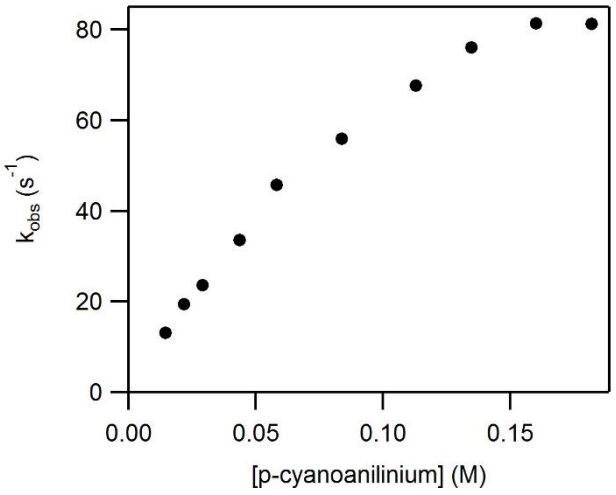

Figure B.4. Observed rate constant plotted against p-cyanoanilinium concentration; rate data obtained from stopped-flow kinetics traces monitoring the appearance of Ni^{II} (λ_{obs} = 500 nm).

B.3 Water in acetonitrile

Water addition to anilinium

Figure 3.4 shows that adding water to strong acids (pK_a < 8) results in an increase in the catalytic rate. As discussed, this is attributed to hydronium (or hydronium hydrate) formation in solution. In support of this statement, we find that the addition of water to anilinium (pK_a = 10.6) does not result in an increase in rate constant (Figure B.5).

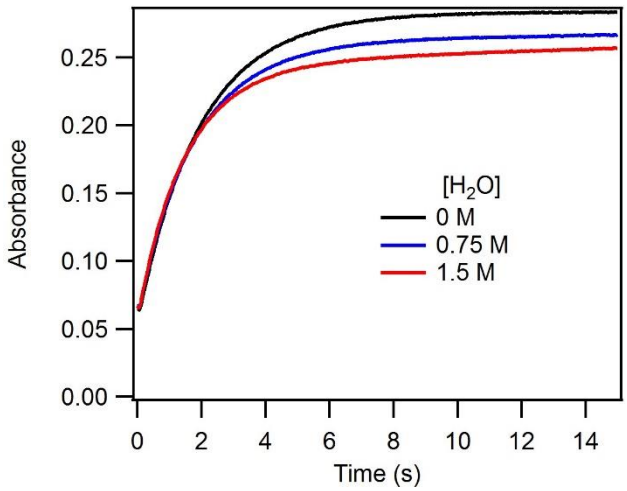

Figure B.5. Stopped-flow kinetics traces for the reaction of $Ni^{II}H$ with 10 mM anilinium in the presence of H_2O to generate H_2 and Ni^{II}.

B.4 Trifluoroacetic acid dimerization

Second Order Reactivity and Dimerization

It was reported in the literature than no dimerization is observed with trifluoroacetic acid in acetonitrile. Obtaining second order kinetics for the acids only has two possible explainations, either a termolecular reaction is occurring (i.e. Rate = $k[Ni^{II}H][AH]^2$) or the acid is dimerizing (i.e. Rate = $k[Ni^{II}H][(AH)_2]$) with a small enough dimerization constant such that $[(AH)_2] \propto [AH]^2$. We obtained an upper bound for the dimerization constant of 1 M^{-1} to see second order reactivity by determining that point at which $[(AH)_2] \propto [AH]^2$ no longer held true (Figure B.6).

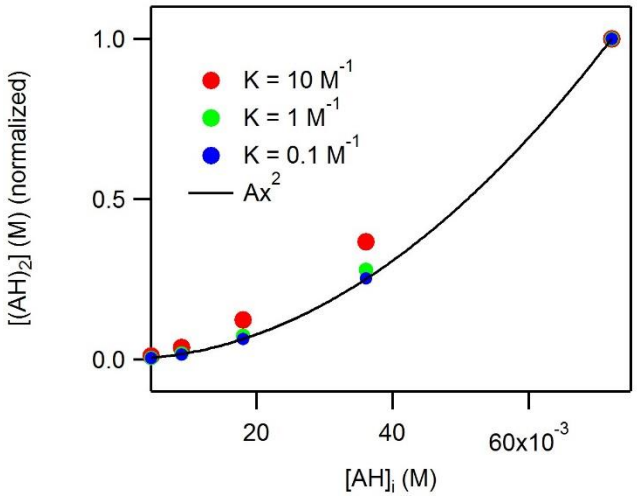

Figure B.6. Expected concentration of $(AH)_2$, normalized to one at the highest input concentration of AH, $[AH]_I$, (chosen to match the concentrations in the trifluoroacetic acid experiment), given a dimerization constant of 10, 1, and 0.1 M^{-1}. The black line represents a true second order curve. At 1 M^{-1} we see a slight deviation from second order and anything higher than that would no longer give a satisfactory fit to second order kinetics, suggesting that if trifluoroacetic acid and trichloroacetic acid are dimerizing, the dimerization constant is below 1 M^{-1}.

APPENDIX C. SUPPLEMENTAL INFORMATION FOR CHAPTER 4

C.1 Determination of Electrochemical Parameters for Simulations

Diffusion coefficient of 1 determined via cyclic voltammetry

The diffusion coefficient (D) of **1** was determined from a series of cyclic voltammograms recorded at scan rates between 0.01 and 7.5 V/s. Per the Randles-Sevcik equation (Eq. C.1), which relates the peak current i_p (amperes) of a reversible, diffusion controlled redox process to the scan rate υ, the diffusion coefficient was calculated as 9.22 x 10^{-6} cm^2/s. This value differs slightly from the reported value which was determined via electrochemical simulation (D = 8 x 10^{-6} cm^2/s).[94]

$$i_p = 0.4463nFA[1]\left(\frac{nF\upsilon D}{RT}\right)^{1/2} \qquad \text{Eq. C.1}$$

n is the number of electrons in the redox process, *F* is the Faraday constant, T is temperature, and R is the universal gas constant.

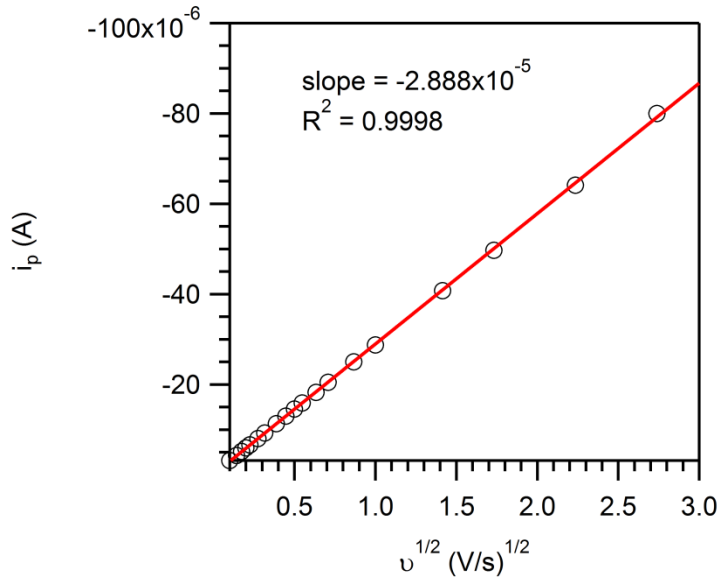

Figure C.1. The peak current of the 10/– cathodic wave plotted vs. υ1/2. The baseline currents of the voltammograms were subtracted from the peak intensities of the 10/– reduction ($\boldsymbol{i_p}$). The slope of this line corresponds to $\mathbf{0.4463}\boldsymbol{nFA}[\mathbf{1}]\left(\frac{\boldsymbol{nFD}}{\boldsymbol{RT}}\right)^{\mathbf{1/2}}$ per the Randles-Sevcik equation and can be used to determine the diffusion coefficient D.

Standard rate constant k_s for heterogeneous electron transfer determined via trumpet plot analysis

The peak potentials of the oxidation and reduction waves of **1** were determined for a 0.5 mM solution of **1** in 0.25 M [Bu_4N][PF_6] from CVs recorded at various scan rates υ. A plot of $E_p - E_{1/2}$ vs. log (υ) was then overlaid with a simulated working curve for which $D_{sim} = 1 \times 10^{-5}$ cm^2/s and $k_{s,sim} = 1$ cm/s. The x-axes (log (υ)) of the two plots were translated until the $E_p - E_{1/2}$ data overlapped (Figure C.9). At the overlap, $\Lambda_{s,Co} = \Lambda_{s,sim}$, where Λ_s is a dimensionless parameter defined as follows[22]

$$\Lambda_s = k_s \sqrt{\frac{RT}{F\upsilon D}}$$

where k_s is the standard rate constant, R is the gas constant, T is temperature, F is Faraday's constant, and D is the diffusion constant. At the overlap

$$k_{s,Co}\sqrt{\frac{RT}{F\upsilon_{Co}D_{Co}}} = k_{s,sim}\sqrt{\frac{RT}{F\upsilon_{sim}D_{sim}}}$$

And it follows that

$$log\left(\frac{k_{s,sim}\sqrt{D_{Co}}}{\sqrt{D_{sim}}k_{s,Co}}\right) = \frac{1}{2}(\log(\upsilon_{sim}) - \log(\upsilon_{Co}))$$

From this analysis, a standard rate constant for heterogeneous electron transfer for **1** was estimated ($k_{s,Co} = 0.054$ cm/s).

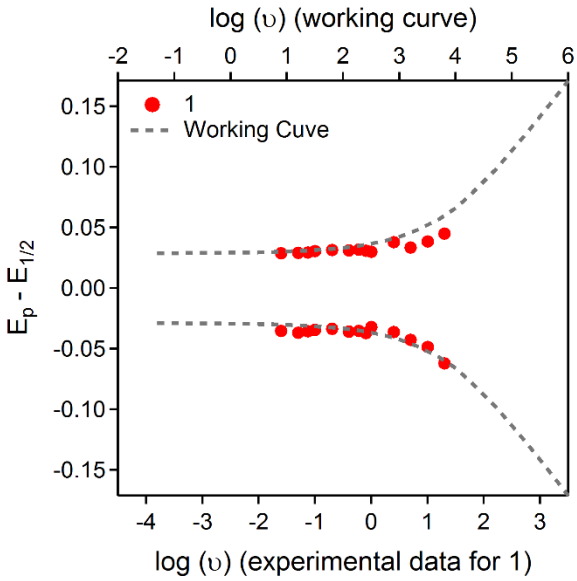

Figure C.2. Trumpet plot of 1 overlaid with the working curve described above.

C.2 Reactions of 1 with aniline

The aniline bases were shown, both electrochemically (Figures 4.1, C.10) and spectroscopically (Figure C.11), to coordinate to **1**. Prior to the addition of an aniline base, the $Co^{III/II}$ redox wave is electrochemically irreversible and centered at ~0.2 V vs. Fc^{+}/Fc, consistent with previous reports.[94] After aniline addition, the $Co^{III/II}$ wave shifts cathodically and gains electrochemical reversibility. The location of the $Co^{III/II}$ wave depends on the identity of the aniline added, stronger bases shift the wave to more negative potentials (Figure C.9). Unexpectedly, the $Co^{II/I}$ redox is unaffected by aniline addition. We attribute this to a rapid equilibrium between the coordinated and uncoordinated species, with coordination favored for cobaloximes in higher oxidation states.

Co^{III} Equilibrium

$$[Co(dmgBF_2)_2(CH_3CN)_2]^+ + \text{aniline} \rightleftharpoons [Co(dmgBF_2)_2(CH_3CN)(\text{aniline})]^+ + CH_3CN$$

Co^{II} Equilibrium

$$Co(dmgBF_2)_2(CH_3CN)_2 + \text{aniline} \rightleftharpoons Co(dmgBF_2)_2(CH_3CN)(\text{aniline}) + CH_3CN$$

Co^{I} Equilibrium

$$[Co(dmgBF_2)_2(CH_3CN)]^- + \text{aniline} \rightleftharpoons [Co(dmgBF_2)_2(\text{aniline})]^- + CH_3CN$$

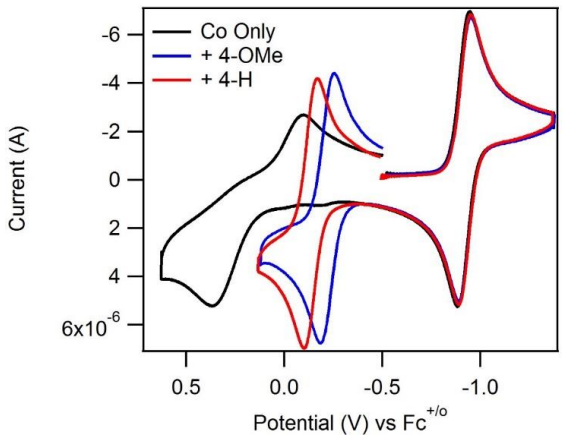

Figure C.3. Cyclic voltammograms of 0.38 mM **1** in the absence of added base (black), in the presence of 2 mM 4-methoxyaniline (blue), and in the presence of 5 mM aniline (red). Voltammograms recorded at 100 mV/s in 0.25 M $[Bu_4N][PF_6]$.

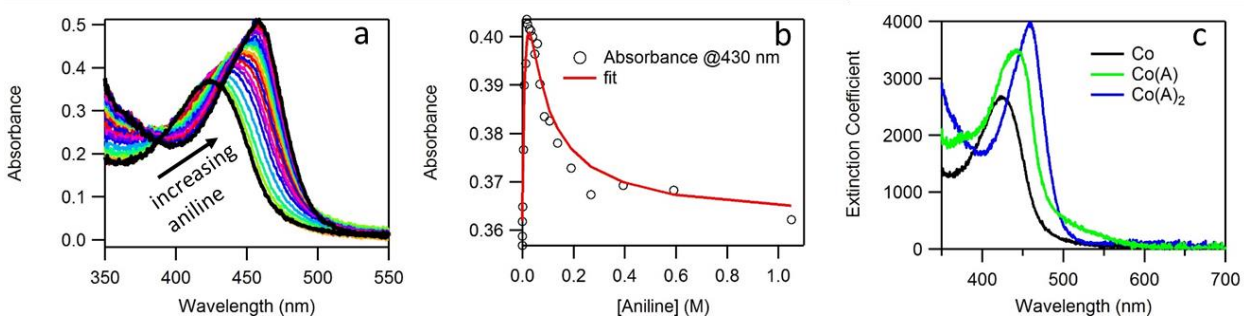

Figure C.4. a) Titration of 0.11 mM **1** with aniline (up to 1 M), monitored via UV-Vis absorption spectroscopy. b) Absorbance at 430 nm corresponding to presumed isosbestic point of **1(CH$_3$CN)$_2$** and **1(aniline)$_2$**. c) absorbance of **1**, **1(aniline)$_2$** and intermediate **1(aniline)**. Fitting of the dataset in (b) using the equilibrium equations for a singly and doubly bound species allowed for the determination of the spectra of the intermediate (**1(aniline)** in panel c). A linear combination of each of these three spectra in accordance with the fit in panel b is sufficient to derive each spectrum in panel a. The values for $K_{Co(A)}$ and $K_{Co(A)2}$ are not reported here as the fit also required the fitting of the absorbance for **1(aniline)** at 430 nm. The interdependency of these three parameters prevented an exact value from being determined. Thus the spectrum for **1(aniline)** in plot c is qualitative.

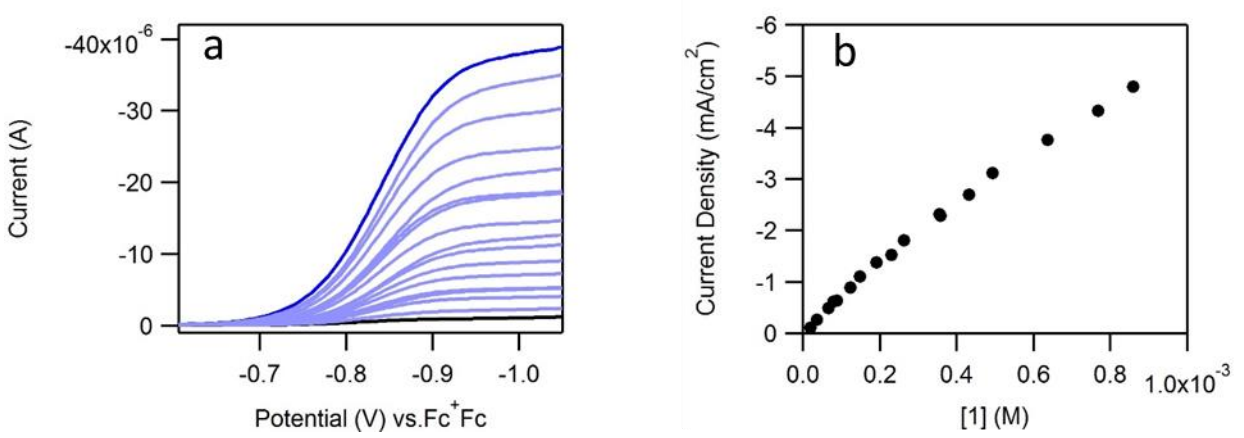

Figure C.5. a) Linear sweep voltammograms of varied concentrations of **1** in the presence of 140 mM 4-trifluoromethylanilinium. All traces recorded at 100 mV/s b) Plateau current obtained at -0.97 V vs. Fc/Fc$^+$ from the voltammograms in plot a.

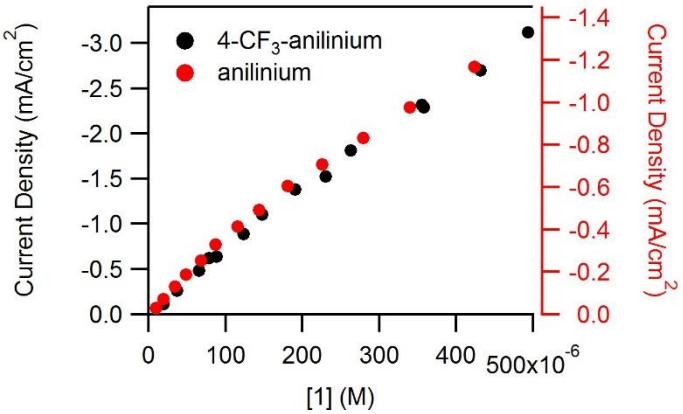

Figure C.6. Comparison of the data from Figure 4.3 and Figure C.5b showing different curvature.

C.3 Optically Monitoring the Decomposition of 1

Compound **1** is known to decompose in the presence of moderately strong acids in acetonitrile,[94,141,143] and the phenyl-substituted version of **1** has been reported to degrade to cobalt-containing nanoparticles in the presence of perchloric acid under reducing conditions.[200] Consequently, the stability of **1** was carefully evaluated under the conditions explored for this work. First, the stability of **1** in acetonitrile electrolyte solution without added acid was monitored by UV-vis spectroscopy over a period of approximately two weeks. Slow loss of the primary absorption peak of **1** was observed (Figure C.16), corresponding to a rate of ca. 3 x 10^{-5} mM/hr assuming the product does not absorb in the same region. Any 1.0 mM solutions of cobaloxime were utilized within three and a half weeks during which less than 1.8% of the sample degraded.

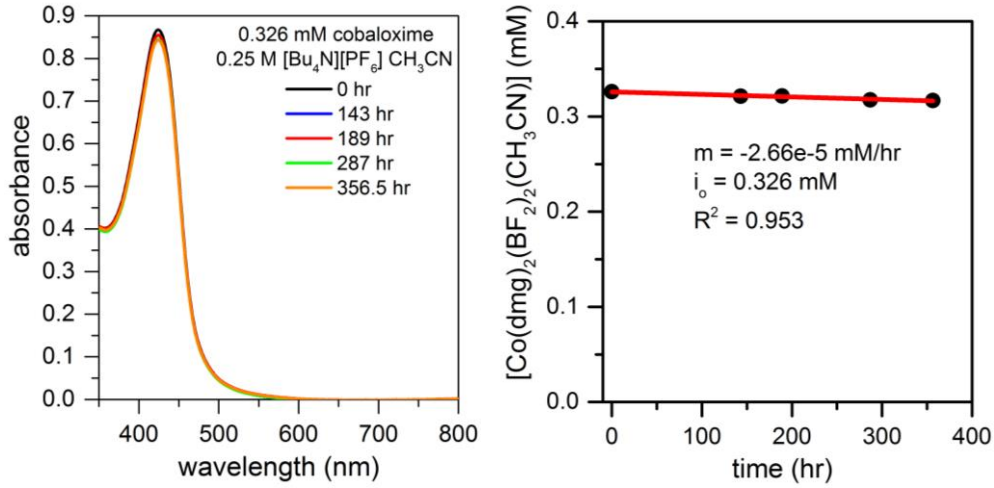

Figure C.7. Left) UV-vis spectra of **1** (initial concentration of 0.326 mM) in 0.25 M $[Bu_4N][PF_6]$ CH_3CN solution over time. Right) Calculated concentration of **1** (assuming that the decomposition products do not absorb at 423 nm) over time.

Next, the stability of **1** was studied in acetonitrile electrolyte solutions with added acid. Decomposition was observed for both 4-trifluoromethylanilinium (pK_a = 8.03; Figure C.17) and 4-cyanoanilinium (pK_a = 7; Figure C.17) on the timescale of minutes, with decomposition accelerated with the stronger acid 4-cyanoanilinium. In response to these observations, data collection procedures were modified for samples containing these acids. See experimental section for details.

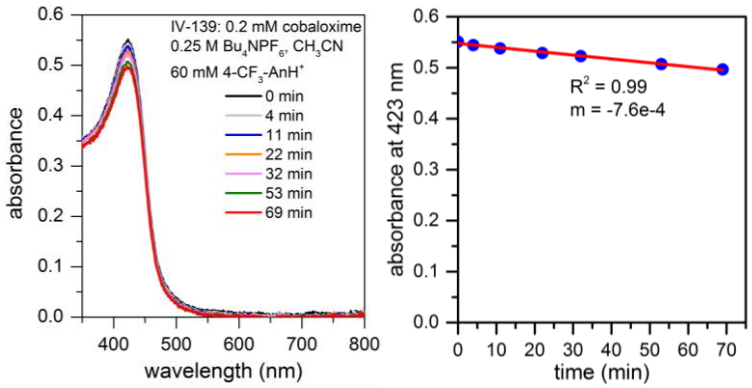

Figure C.8. Left) UV-vis spectra of **1** (initial concentration of 0.2 mM) in 0.25 M $[Bu_4N][PF_6]$ acetonitrile solution with 60 mM 4-trifluoromethylanilinium. Right) Absorbance at 423 nm over time.

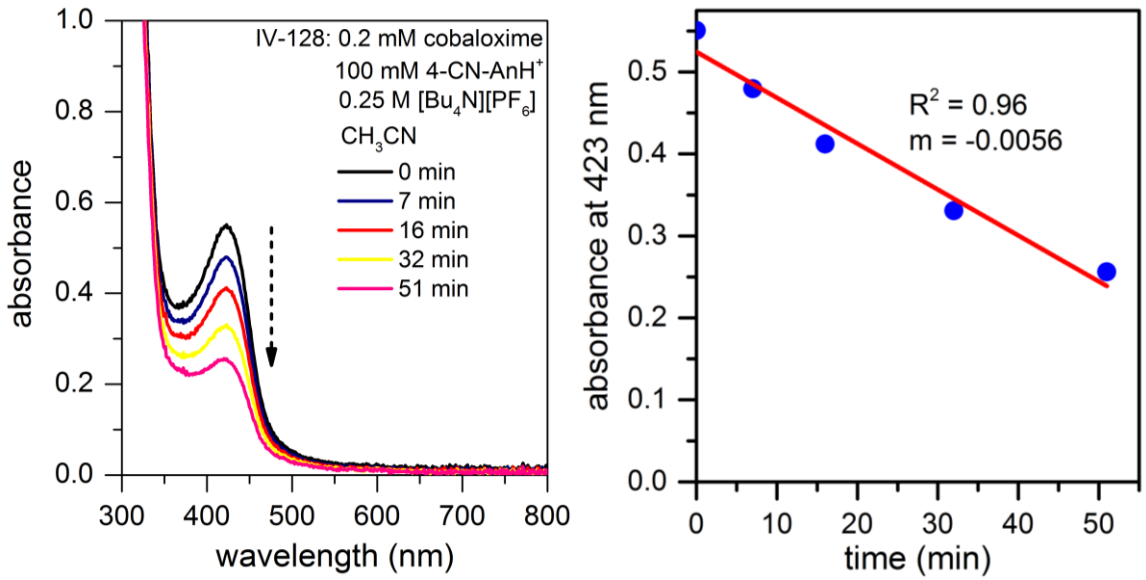

Figure C.9. Left) UV-vis spectra of **1** (initial concentration of 0.2 mM) in 0.25 M $[Bu_4N][PF_6]$ acetonitrile solution with 100 mM p-cyanoanilinium. Right) Absorbance at 423 nm over time.

C.4 Determination of Global Rate Constants from Plateau Currents

Catalytic cyclic voltammograms of 1 with substituted aniliniums

The catalytic voltammograms were recorded for **1** with 8 acids. Each voltammograms was recorded using a freshly pretreated electrode in order to minimize any potential fouling. Voltammograms were recorded at high acid concentrations in order to access plateau currents that are acid concentration and pK_a independent. As there is literature precedent for the degradation of **1** in strongly acidic solutions with proton sources such as HBF_4, HCl and $HClO_4$, these experiments were performed with great caution. We directly evaluated catalyst decomposition for strong acids (Appendix C.3). Relatedly, we found little evidence for catalyst decomposition for weak acids during the course of experiments. In response, to minimize the time frame in which **1** could potentially decompose, **1** was exposed to acid only for relatively brief periods. For these titration experiments involving high acid concentrations, multiple,

identical solutions of **1** were used in which a single addition of acid and a single scan were taken, substantially reducing the net exposure time of **1** to acid.

Plateau currents as a function of acid concentration

First-order dependence of plateau current on (acid concentration)$^{1/2}$ is expected for reactions that are first order in acid. By contrast, first-order dependence of plateau current i_{pl} (or peak current, in the absence of a plateau) on acid concentration is expected for solutions in which the peak current is governed by the diffusion of substrate into the reaction layer. Experimentally, for weak acids, we observe the half-order dependence with a current density dependent upon acid strength (Figure C.34). However, for stronger acids, the current density approaches a pK_a independent value and is linear with acid concentration (Figure c.35).

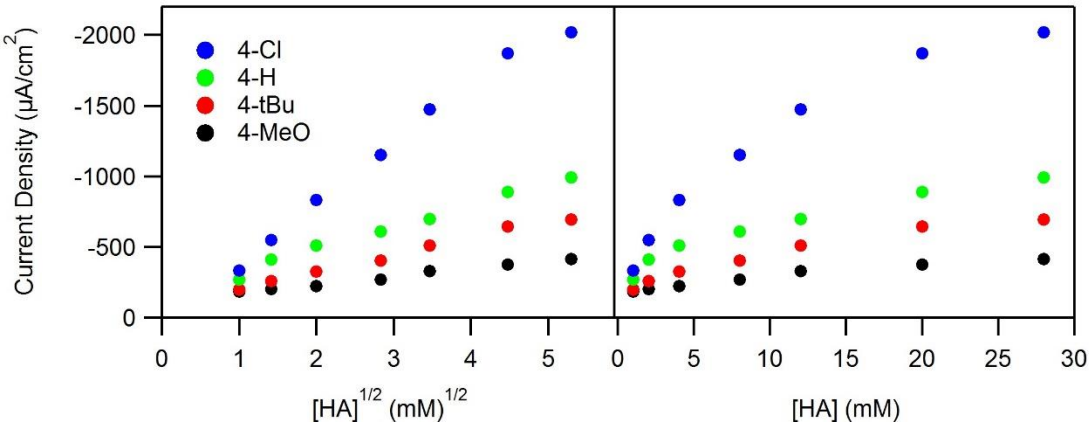

Figure C.10. Current density as a function of [HA]$^{1/2}$ and [HA] for the four weaker acids, 4-methoxyanilinium, 4-tertbutylanilinium, anilinium, and 4-chloroanilinium.

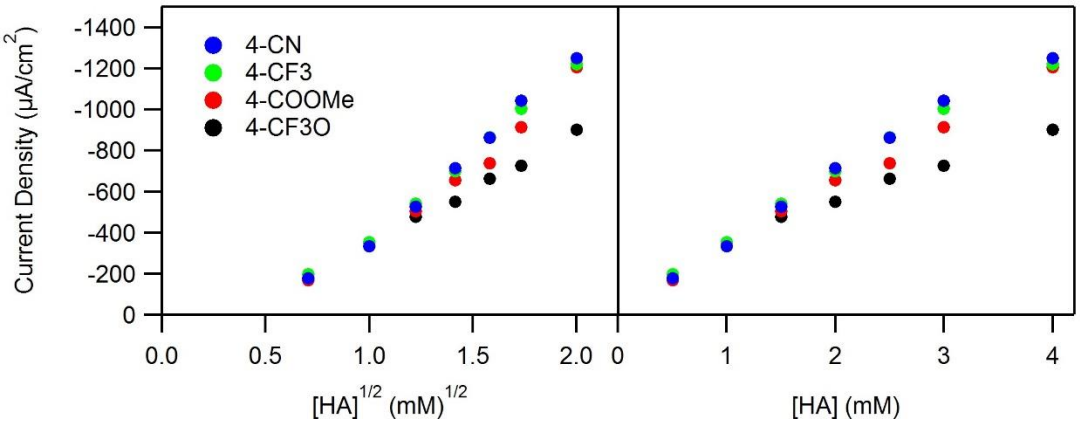

Figure C.11. Current density as a function of $[HA]^{1/2}$ and [HA] for the four stronger acids, 4-trifluoromethoxyanilinium, 4-(methylbenzoate)anilinium, 4-trilfluoromethylanilinium, and 4-cyanoanilinium. Note that the current–$[HA]^{1/2}$ plot does not intercept the origin.

C.5 Evaluating k_1 via foot-of-the-wave analysis

As is shown in Appendix C.2, when aniline bases are present in solution, the $Co^{III/II}$ ($\mathbf{1}^{0/+}$) redox wave shifts to a position that overlaps the ferrocene/ferrocenium couple. Because FOWA results are significantly impacted by any deviations in applied potential, each wave must be referenced to an internal standard already present in solution. It has been our general practice first to scan cathodically in our catalytic measurements and scan through the ferrocene reference on the reverse trace. However, as seen in Figure C.33, this made referencing to ferrocene very difficult as catalysis produces the aniline base, which coordinates to **1** and shifts the $Co^{III/II}$ ($\mathbf{1}^{0/+}$) wave to overlap the ferrocene wave. For improved accuracy, we scanned through the ferrocene wave first in our voltammetric measurements to minimize the interference arising from the production of aniline. Results for each anilinium are shown below in Figures C.34 and C.35. Voltammograms of two samples, 4-methoxyanilinium, and 4-tertbutylanilinium, suggest a small amount of aniline is available to bind cobaloxime prior to catalysis, inhibiting precise referencing and the result of this can be seen in the rate constant vs. concentration data shown below.

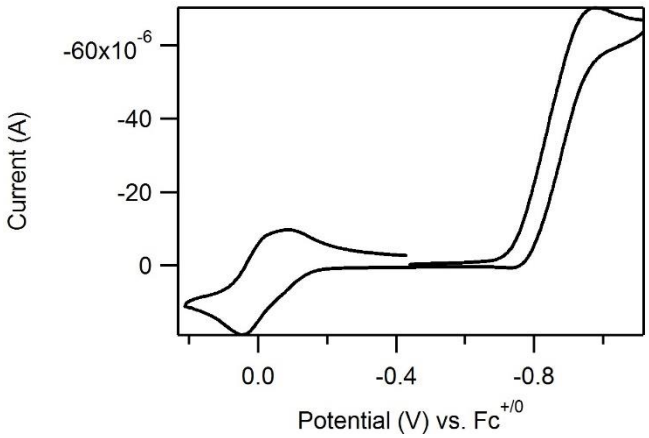

Figure C.12. Cyclic voltammogram of 0.5 mM **1** with 28 mM anilinium. After scanning through the catalytic wave, referencing to ferrocene becomes difficult; as can be seen here, the $Co^{III/II}$ wave, with aniline bound, overlaps with the ferrocene wave and prevents precise referencing.

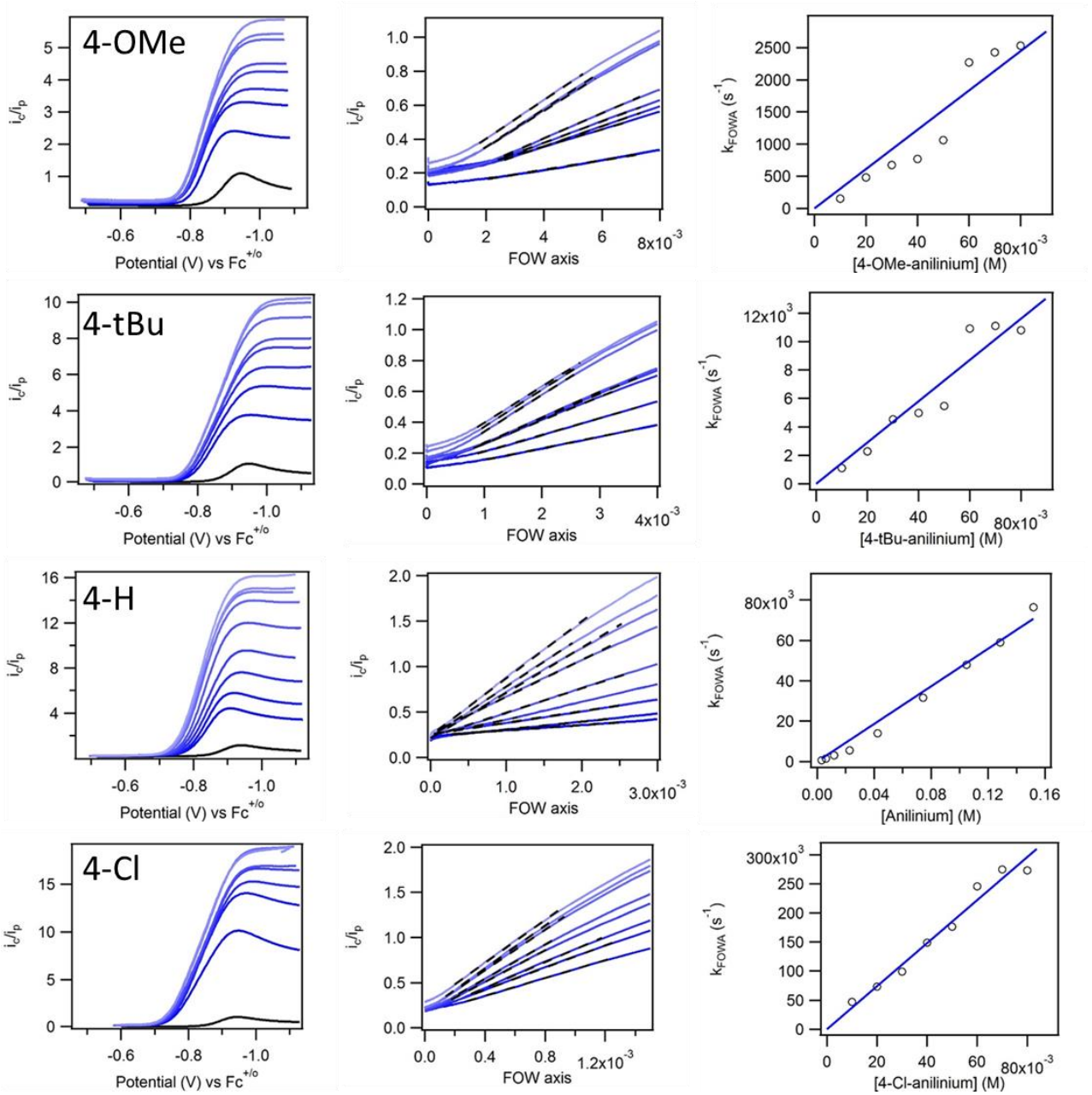

Figure C.13. FOWA of the four weaker acids, 4-methoxyanilinium, 4-tertbutylanilinium, anilinium, and 4-chloroanilinium. Plots, from left to right for each acid are the original catalytic waves (left), conversion to the FOWA axis, $\exp\left[-\frac{F}{RT}\left(E - E^{0\prime}_{\mathbf{1}^{0/-}}\right)\right]$, (center), and the resulting rate constant vs. acid concentration plot (right).

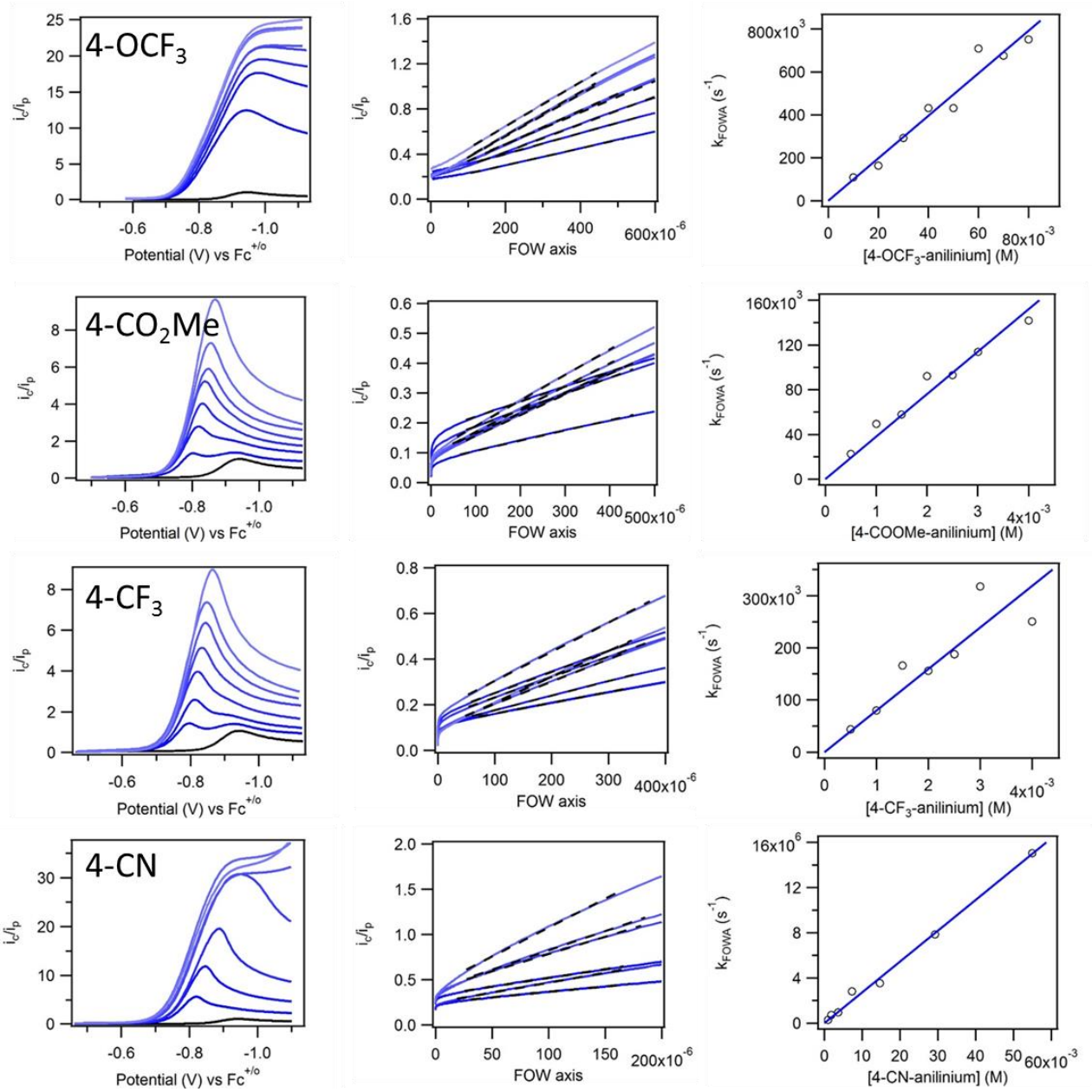

Figure C.14. FOWA of the four stronger acids, 4-trifluoromethoxyanilinium, 4-methylbenzoateanilinium, 4-trilfluoromethylanilinium, and 4-cyanoanilinium. Plots, from left to right for each acid are the original catalytic waves (left), conversion to the FOW axis, $\exp\left[-\frac{F}{RT}\left(E - E^0_{\mathbf{1}^{0/-}}\right)\right]$, (center), and the resulting rate constant vs. acid concentration plot (right).

C.6 Oxidation of unreacted $\mathbf{1}^{2-}(\mathbf{H}^{+})$

For solutions containing **1** and a weaker acid (pK_a > 9.5), a broad oxidation wave is observed on the anodic scan at potentials positive of the anodic feature of the reversible $\mathbf{1}^{0/-}$ wave recorded in the absence of acid. This feature is most pronounced at low acid concentrations. We assign this feature to the oxidation of unreacted $\mathbf{1}^{2-}(\mathbf{H}^{+})$. Because the rate constant k_{global} is on the order of 3.39 x 10^1 to 1.76 x 10^3 M^{-1} s^{-1} for acids in this range, turnover is expected to be slow with respect to the timescale of the experiment when low concentrations of acid are employed (ca. 1–10 mM, depending on k_{global}). As scan rate is increased, this feature becomes more pronounced and shifts to more positive potentials (Figure C.15).

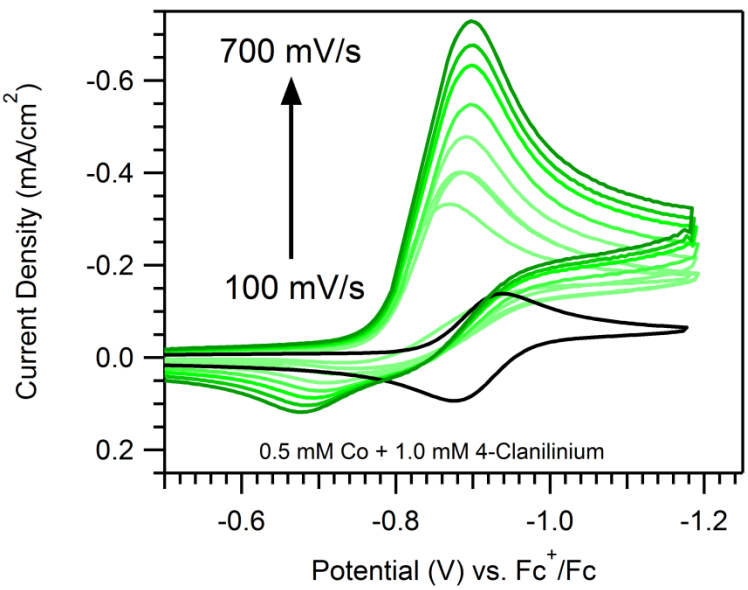

Figure C.15. Cyclic voltammograms of a solution containing 1 (black trace) and 4-chloroanilinium, as denoted. Voltammograms were taken at (increasing): 100, 150, 200, 300, 400, 500, 600, and 700 mV/s. All voltammograms recorded in 0.25 M [Bu4N][PF6].

APPENDIX D. SUPPLEMENTAL INFORMATION FOR CHAPTER 5

D.1 Degradation of $[Ni^{II}(P_2^{Ph}N_2^{Bz})H_2]^{4+}$

While $[Ni^{II}(P_2^{Ph}N_2^{Bz})H_2]^{4+}$ can be stored as a solid, dissolution in acetonitrile immediately begins to cause degradation, this was noted in a previous study it was shown that the degradation involved removal of the ligands which are then digested to form some unknown product. We observed that same trend by NMR and monitored the reaction by UV-Vis to get an understanding of how quickly experiments needed to be done with the complex to avoid interference by degradation (Figure D.1).

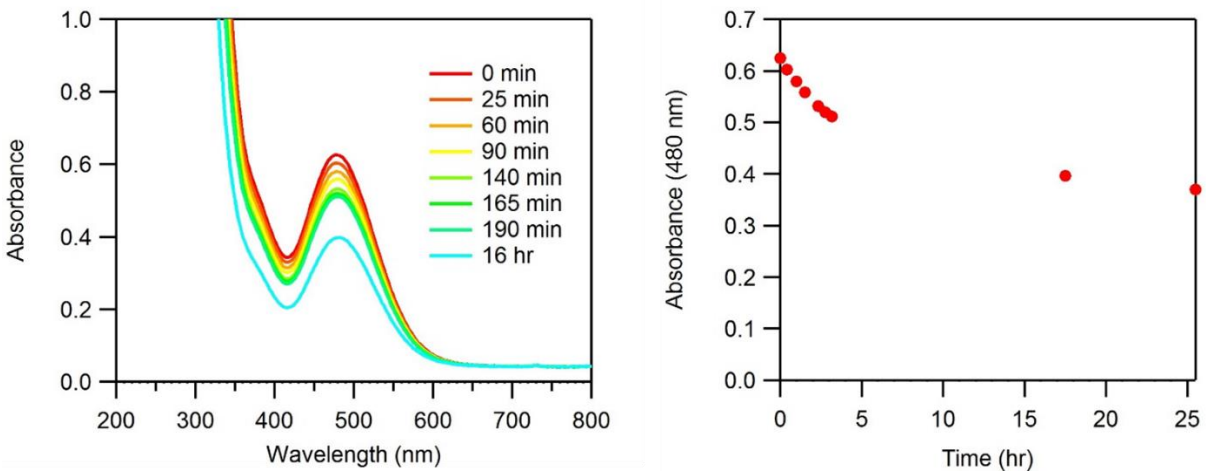

Figure D.1. UV-vis absorption of a solution of 0.35 mM $[Ni^{II}(P_2^{Ph}N_2^{Bz})H_2]^{4+}$ over time. Left: Full UV-Vis traces. Right: Absorbance at 480 nm as a function of time.

D.2 Spectrophotometric titration of $[\mathbf{N}i^{II}(\mathbf{P}_2^{\mathbf{Ph}}\mathbf{N}_2^{\mathbf{Bz}})_2]^{2+}$

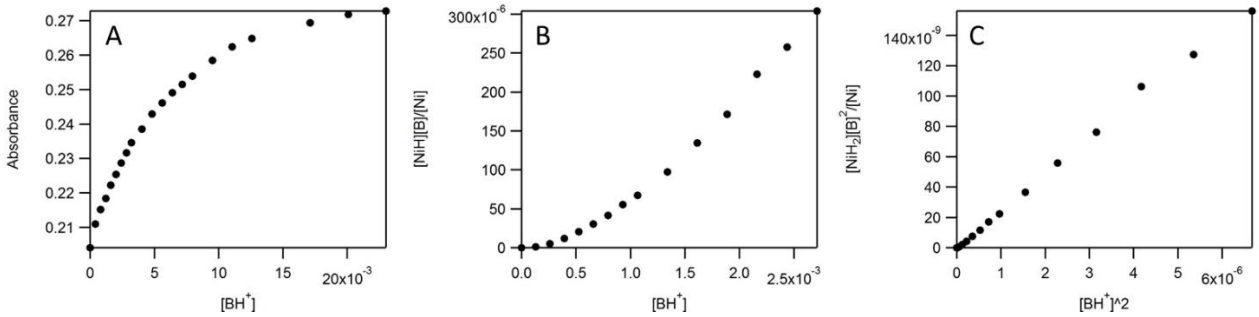

Figure D.2. Spectrophotometric titration of 0.25 mM $[\mathrm{N}i^{II}(\mathrm{P}_2^{\mathrm{Ph}}\mathrm{N}_2^{\mathrm{Bz}})_2]^{2+}$ with 4-cyanoanilinium. A) Absorbance at 425 nm as a function of acid concentration. B) Data work-up assuming the transfer of a single proton. C) Data work-up assuming the transfer of two protons.

D.3. Identification of $[\mathbf{N}i^{I}(\mathbf{P}_2^{\mathbf{Ph}}\mathbf{N}_2^{\mathbf{Bz}})_2]^{+}$ spectrum

Through a combination of UV-vis absorbance and NMR spectroscopies, the isolated nickel hydride HNi^{II} was observed to react to form Ni^{I} and H_2. Qualitatively, the rate of reaction was impeded by H_2 and accelerated at higher concentrations of hydride.

$$2HNi^{II} \rightleftharpoons 2Ni^{I} + H_2$$

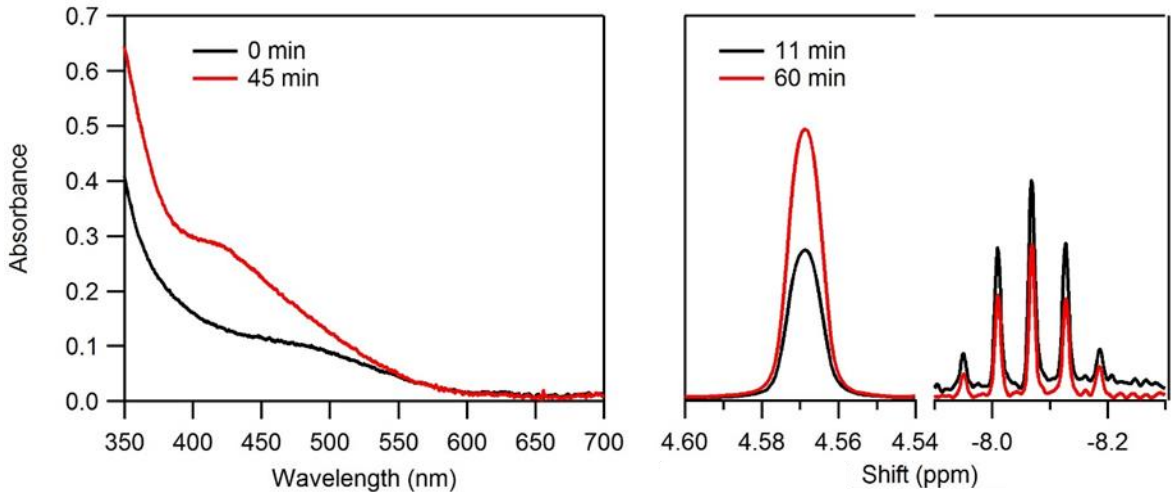

Figure D.3. Left: Conversion of $[HNi^{II}(P_2^{Ph}N_2^{Bz})_2]^{+}$ to $[Ni^{I}(P_2^{Ph}N_2^{Bz})_2]^{+}$, monitored by UV-Vis. Substoichiometric $NaBH_4$ (0.076mM) was added to a 0.122 mM solution of Ni^{II}. The

spectra at 0 min can be described as a mixture of $[HNi^{II}(P_2^{Ph}N_2^{Bz})_2]^+$and $[Ni^{II}(P_2^{Ph}N_2^{Bz})_2]^{2+}$, while the spectra at 45 min is a mixture of $[Ni^{II}(P_2^{Ph}N_2^{Bz})_2]^{2+}$ and $[Ni^{I}(P_2^{Ph}N_2^{Bz})_2]^{+}$. Right: Growth of H_2 (4.57 ppm) coinciding with the disappearance of HNi^{II} (hydride peak, -8.07 ppm) as monitored by NMR. The solution as prepared was equimolar in $[Ni^{II}(P_2^{Ph}N_2^{Bz})_2]^{2+}$ and $NaBH_4$ at 21 mM. Time steps represent the time after addition of $NaBH_4$.

In order to analyze the resulting UV-Vis spectrum in Figure D.3 recorded at 45 min, the absorbance spectrum of Ni^I was obtained by the titration of Ni^0 with Ni^{II} (and vice versa) in order to promote disproportionation to Ni^I. The resulting spectra were then deconvoluted (Figure D.4) because the $Ni^{II/I}$ and $Ni^{I/0}$ redox couples were too close together to cleanly isolate Ni^I.

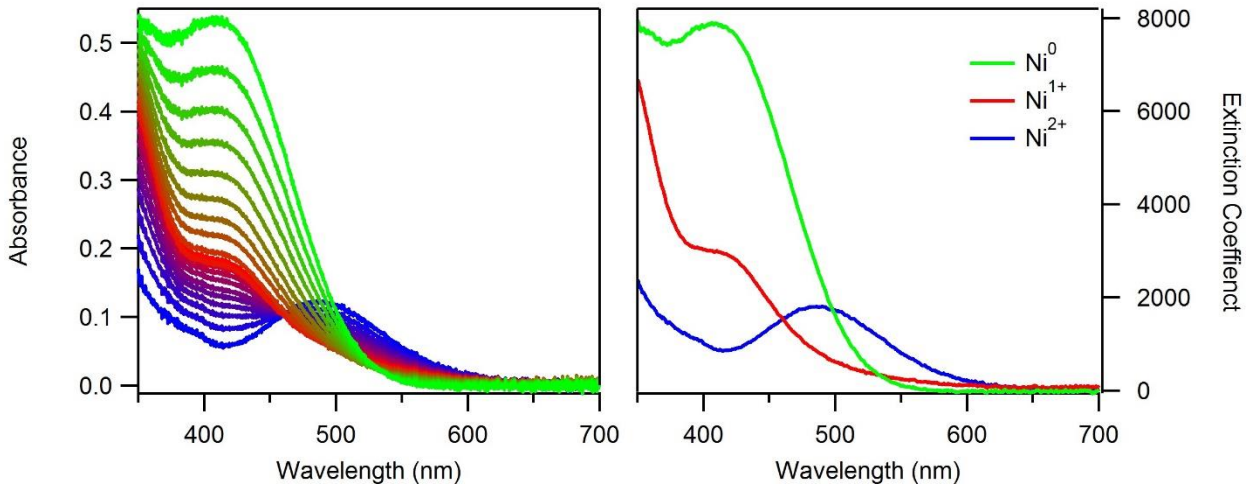

Figure D.4. Left: Titration of 2 ml of a 0.048 mM solution of $[Ni^0(P_2^{Ph}N_2^{Bz})_2]$ with a 0.068 mM solution of Ni^{II}, 10 x 0.2 ml additions (green to red) and vice versa (blue to red) monitored by UV-Vis spectroscopy. Right: Deconvolution of the spectra shown in Panel A, using the independently recorded spectra for $[Ni^{II}(P_2^{Ph}N_2^{Bz})_2]^{2+}$ and $[Ni^0(P_2^{Ph}N_2^{Bz})_2]$, reveal the third component, assigned as the absorbance spectrum of $[Ni^{I}(P_2^{Ph}N_2^{Bz})_2]^{+}$.

Because Ni^I disproportionates into Ni^{II} and Ni^0. Its spectrum could never be fully isolated. In order to deconvoluted the resulting spectra in Figure D.4, linear combination biased singular value decomposition (LCB-SVD) was employed. SVD is used across many fields of research and in many applications to reduce a matrix down to its principle parts. If we consider A to be

a matrix of absorbance versus titration step, we know that the entire matrix can be represented more simply as the extinction coefficients of each species observed in the titration, the corresponding concentration, and the instrumental noise, as such:

$$\text{wavelength}\begin{bmatrix} a_{1,1} & \cdots & a_{1,n,} \\ \cdots & \cdots & \cdots \\ a_{m,1} & \cdots & a_{m,n} \end{bmatrix} = \begin{bmatrix} \varepsilon_{1,1} & \varepsilon_{1,2} & \varepsilon_{1,3} \\ \cdots & \cdots & \cdots \\ \varepsilon_{m,1} & \varepsilon_{m,2} & \varepsilon_{m,3} \end{bmatrix} \begin{bmatrix} C_{1,1} & \cdots & C_{1,n} \\ C_{2,1} & \cdots & C_{2,n} \\ C_{3,1} & \cdots & C_{3,n} \end{bmatrix} + \begin{bmatrix} E_{1,1} & \cdots & E_{1,n,} \\ \cdots & \cdots & \cdots \\ E_{m,1} & \cdots & E_{m,n} \end{bmatrix}$$

$$\text{titration}$$

$$A = \mathrm{E} * C + e$$

Performing SVD allows us to generate a new set of matrices from matrix A that can be broken down into linear combinations of the extinction coefficients and concentrations and then the noise.

$$A \overset{SVD}{\Longrightarrow} E', Y, Z; \quad E' * Y * Z^T = A \quad \Rightarrow \quad E' * C' = A$$

Using the notation above, E' would represent the linear combination of extinction coefficients, Y is a diagonal matrix that represents the overall contribution of each spectrum in E' to the original matrix A and Z represents the "contribution corrected" linear combinations of the concentration. Multiplying Y and the transpose of Z then gives a matrix C', representing linear combinations of the concentration. Both matrix E' and C' are ordered such that the largest contributing factors are in the first ranks of the matrix. Therefore, we can visually inspect the ranks of E' to determine the transition point from linear combination of spectra to instrumental noise and subsequently cut off all extra ranks from each matrix E', and C', so that, if you have three species in solution, you will have three ranks in each matrix.

The resulting linear combinations are not recognizable as the spectra for your species, however, known species can be used to recompute the linear combinations, thereby biasing the result towards the real spectra. This is accomplished by uniting the known spectra with matrix A prior to performing SVD. This is represented below with E representing the matrix of known species. Performing the operations from before results in the matrix C'' that is united with C'.

$$E \cup A \overset{SVD}{\Longrightarrow} E', Y, Z; \quad E' * Y * Z^T = E \cup A \quad \Rightarrow \quad E' * C'' \cup C' = E \cup A$$

If all species are known, C'' is an n*n, where n is the number of species in solution. C'' can be applied to the matrices E' and C' to generate E and C, the true spectra and concentration.

$$\boldsymbol{E' * C'' = E}; \qquad \boldsymbol{(C'')^{-1} * C' = C}$$

When only some of the spectra are known, C'' still exists and finding C'' is made easier by biasing the analysis, using the known spectra. If two of three spectra are known, the first two columns of C'' can be directly determined through the union of E and A. The final column of C'' can then be determined by fitting the three values in the final column in order to satisfy experimental properties, such as:

1. The spectrum must contain all positive extinction coefficient values.

2. The concentration must never go below 0.

3. The total concentration of all species must sum to the known value.

For many datasets, these three values are sufficient to get an accurate spectrum for the unknown. When multiple unknown exists, it helps to include other parameters, such as:

4. The reaction concentrations are single exponential vs time (For a kinetic profile)

5. Specific species only increase, others only decrease.

The number of fitting parameters is limited by the previous knowledge of the system, but can include anything that can be quantified using the concentration or the resulting spectra.

Example Matlab Functions for LCB-SVD.

```
function [C, s,Cstack, gof,nA,nB] = LCB_SVD_Main( X, n1, n2, iter,ran,
total)
%LCB_SVD_Main Call function to fit for unknown spectra in a 2D matrix
%(e.g. Wavelength vs. Time, Wavelength vs. Titration, ppm vs. time).
%
% Input
%   X - Matrix with initial columns being the known spectra
%   n1 - number of known spectra
%   n2 - number of expected species in data
%   iter - number of attempted fits desired
%   ran - basis for a random number generator for initial starting points.
%       This value should be determined using the values for the known
%       species that appear in matrix C.
%   total - Total concentration for all species present.
%
% Output
%   C - Matrix used for rotation of the SVD matrices with the best fit
%       acheived
%   s - List of the parameters used in determining the value of the fit.
%       These will be experiment dependent
%   Cstack - Rotation matrices for all attempted fits
%   gof - recorded goodness of fit for all attempted fits
%   nA - Matrix containing the resulting spectra (including those already
%       known)
%   nB - Matrix containing the fit concentrations for each species.

% Perfom SVD and remove all excess columns and rows from the spectral and
% concentration matrices. Then arrange the initial rotation matrix with
% zeros in place of the unknowns.
[A,B,C] = svd(X);
D = B*C';
A = A(:,1:n2);
B = D(1:n2,:);
C = B(1:n2,1:n2);
C(:,(n1+1:n2))= zeros(n2,(n2-n1));
for i = (n1+1):n2
    C(i,i) = 1;
end
a = size(X);
nA = A(:,1:n2);
nB = B(1:n2,(n1+1):a(2));
b = size(nX);

%set up values for fitting. See documentation for suggested parameters
```

```
ydata(1,1) = total;
ydata(2,1) = 0;
ydata(3,1) = total;
ydata(4,1) = 0;
ydata(5,1) = 1;
ydata(6,1) = 0;

%Generate matrices to be used by the least squares fitter as the time
%series and input values for the rotation matrix
xdata = zeros(2,b(2));
In = C(:,(n1+1:n2));

%Expand the tolerances of the least squares fitter.
options = optimoptions('lsqcurvefit','MaxFunEvals',
10000,'MaxIter',10000,'TolFun', 1e-10,'TolX', 1e-10);
lb = In-10000000;
ub = In+10000000;

% Generate matrices for storage of fitting results
Cstack = zeros(n2,n2,iter);
gof = zeros(iter,1);

% Fit for the rotation matrix the preset number of times.
for i = 1:iter
    In = random('norm',0,ran,n2,n2-n1);
    fit =
lsqcurvefit(@(In,xdata)ConstraintChecker_ER_4_195(In,xdata,nA,nB,C,n1,n2),
In,xdata,ydata,lb,ub,options);
    s = ConstraintChecker_ER_4_195( fit, xdata,nA, nB, C,n1, n2);
    C(:,(n1+1:n2))= fit;
    Cstack(:,:,i) = C;
    gof(i,1) = goodnessOfFit(s,ydata, 'NRMSE');
end

%determine the best result and store it for output.
[~,I] = max(gof);
C = Cstack(:,:,I);
s = ConstraintChecker_ER_4_195( C(:,(n1+1):n2), xdata,nA, nB, C,n1, n2);
nB = C^-1*nB;
nA = nA*C;
end


function [ Constraint ] = ConstraintChecker( var, xdata,A, B, C,n1, n2)
%Constraint Checker Evaluates the spectra and concentration profiles to
%compare to the desired results for fitting
%
%   This function is called from LCB_SVD_Main
%
% Input
%   var - rotation matrix being examined
%   xdata - does nothing, but is required for lsqcurvefit function to
%       operate
%   A - SVD output spectra
%   B - SVD output concentrations
%   C - Contains rotation matrix values that are already known with the
```

```
%       unknown values as zeros
%   n1 - number of known spectra
%   n2 - expected number of species
%
% Output
%   Constraint - Contains the evaluated parameters for fitting, this will
%   be experiment dependent and should be set to match the values that
have
%   been logged in "ydata" in LCB_SVD_Main.

%Determine new spectra and concentration matrices and their absolute
values
C(:,(n1+1:n2))= var;
A = A*C;
B = C^-1*B;
D = abs(B);
E = abs(A);

%The parameters below are only general parameters and are not necessarily
%appropriate for any given experiment, they should be determined for each
%individual experiment.

%correct total concentration
Constraint(1,1) = mean(sum(B));
%Correct across whole set
Constraint(2,1) = std(sum(B));
%Absolute Value Matches(no negative concentrations)
Constraint(3,1) = mean(sum(D));
Constraint(4,1) = std(sum(D));
%No negative absorbance spectra values
Constraint(5,1) = ((sum(sum(A+1)))/(sum(sum(E+1))))^9;
%only one species in solution at beginning
Constraint(6,1) = B(1,1);

end
```

D.4. Spectrophotometric titration of $[\mathrm{N}i^{0}(\mathrm{P}_{2}^{\mathrm{Ph}}\mathrm{N}_{2}^{\mathrm{Bz}})_{2}]$

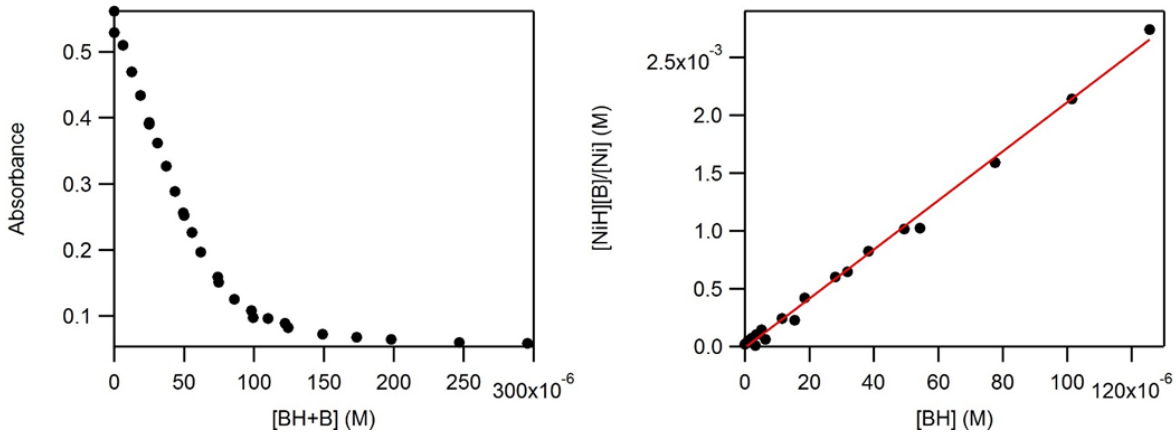

Figure D.5. Spectrophotometric titration of 0.08 mM $[\mathrm{N}i^{0}(\mathrm{P}_{2}^{\mathrm{Ph}}\mathrm{N}_{2}^{\mathrm{Bz}})_{2}]$ with triethylammonium. Left: Absorbance at 430 nm as a function of total triethylammonium added. Right: Plot of $[HNi^{II}][B]/[Ni^{0}]$ against $[BH^{+}]$. Slope of the linear fit shown in red is 20.15, yielding a pK_s of 20.15.

D.5. Electrochemistry of $[Ni^{II}(P_2^{Ph}N_2^{Bz}H)_2]^{4+}$

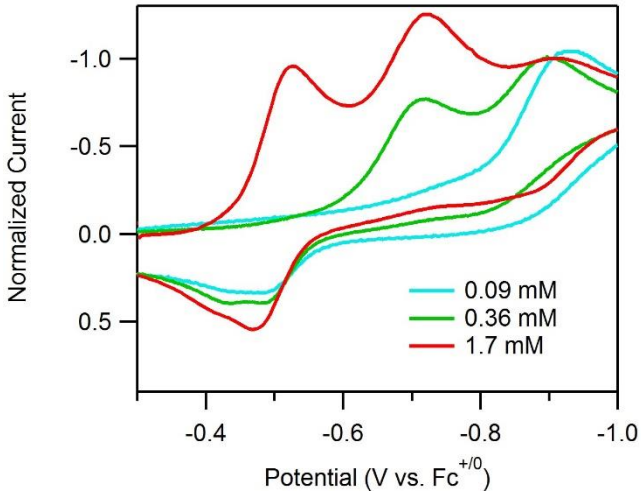

Figure D.6. Cyclic voltammograms of $[Ni^{II}(P_2^{Ph}N_2^{Bz}H)_2]^{4+}$ at 0.09 mM, 0.36 mM and 1.7 mM. Voltammograms recorded at 800 mV/s in 0.25 M $[NBu_4][PF_6]$ acetonitrile solution and normalized to the cathodic current at -0.9 V for comparison.

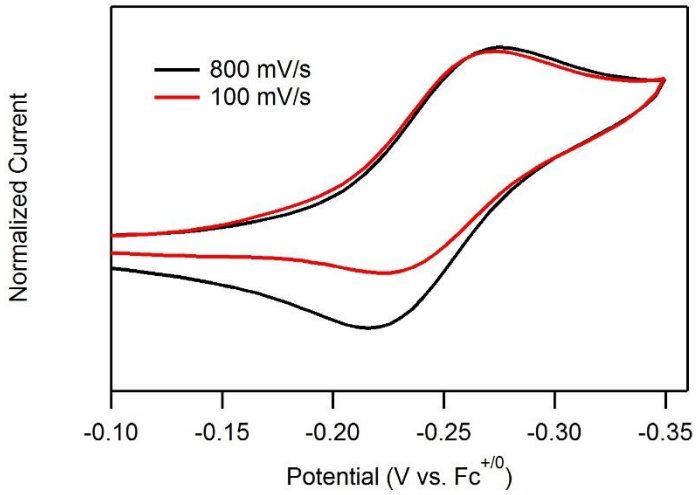

Figure D.7. Cyclic voltammograms of $[Ni^{II}(P_2^{Ph}N_2^{Bz}H)_2]^{4+}$ at 800 mV/s and 100 mV/s demonstrating the loss of reversibility at lower scan rates. Voltammograms recorded in 0.25 M [NBu4][PF6] acetonitrile solution and normalized to the peak of the anodic ferrocene wave for comparison (not shown).

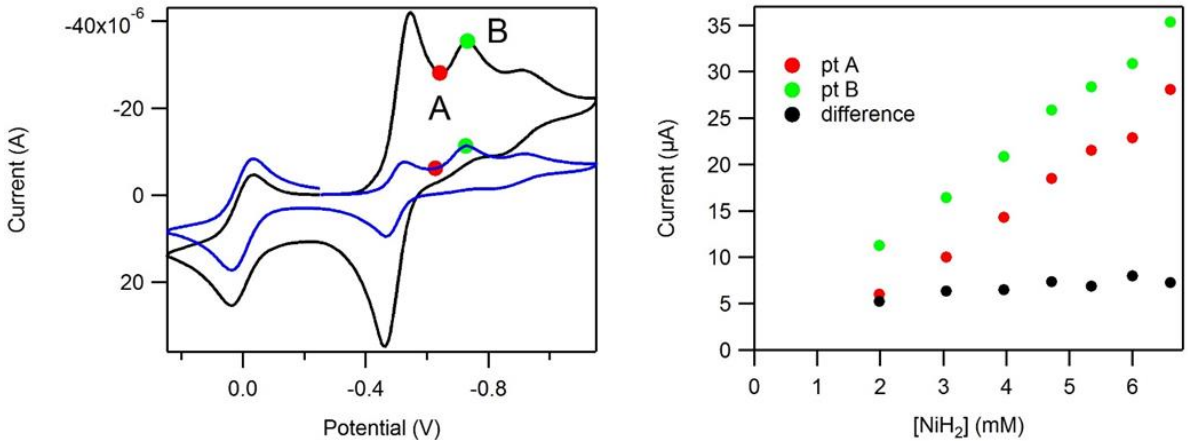

Figure D.8. Left: Cyclic voltammograms of $[Ni^{II}(P_2^{Ph}N_2^{Bz}H)_2]^{4+}$ at 2 mM, and 6.6 mM. Voltammograms recorded at 800 mV/s in 0.25 M [NBu4][PF6] acetonitrile solution. Right: Plot of the current at the valley (red points) between the reversible peak at -0.52 V and the irreversible peak at -0.7 V and the current of the peak at -0.7 V (green points). The difference (black points) reveals a fixed size for this reduction feature.

D.6. Diffusion Coefficient of $[Ni^{II}(P_2^{Ph}N_2^{Bz})_2]^{2+}$

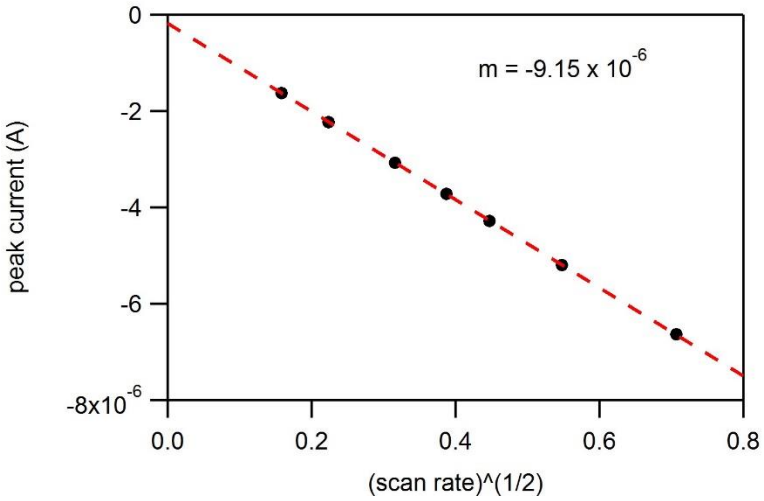

Figure D.9. Peak current for the $Ni^{II/I}$ reduction of 1.8 mM $[Ni^{II}(P_2^{Ph}N_2^{Bz})_2]^{2+}$ plotted against the square root of the scan rate. Analysis of the slope using the Randles-Sevcik equation yields a diffusion coefficient of 6 x 10^{-6} cm^2 s^{-1}. Voltammograms recorded in 0.25 M $[NBu_4][PF_6]$ acetonitrile solution with a 1 mm glassy carbon disk used as the working electrode.

D.7. Cyclic voltammograms of $[Ni^{II}(P_2^{Ph}N_2^{Bz})_2]^{2+}$ and 4-*t*-butylanilinium: Substrate concentration dependence

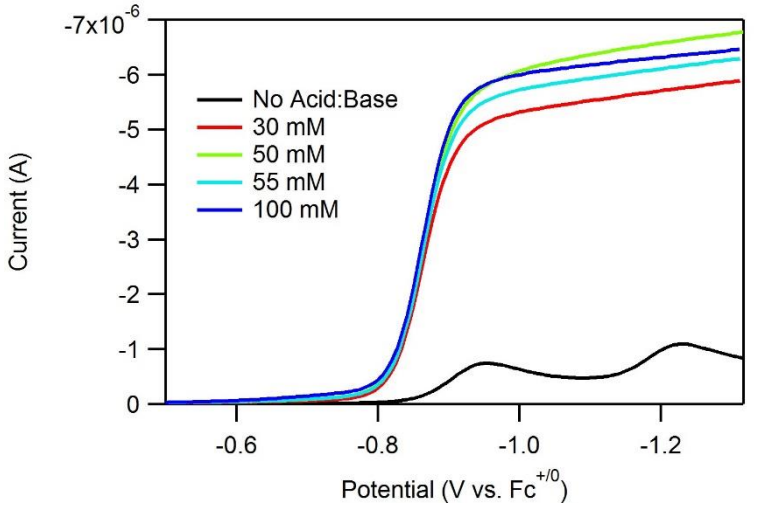

Figure D.10. Cyclic voltammograms of $[Ni^{II}(P_2^{Ph}N_2^{Bz})_2]^{2+}$ (0.6 mM) in 1:1 4-tertbutylanilinium:4-tertbutylaniline solutions at 30 mM, 50 mM, 55 mM and 100 mM acid concentrations. Voltammograms recorded at 50 mV/s in 0.25 M $[NBu_4][PF_6]$ acetonitrile solution.

D.8. Obtaining Rate of Hydride Formation with Triethylammonium

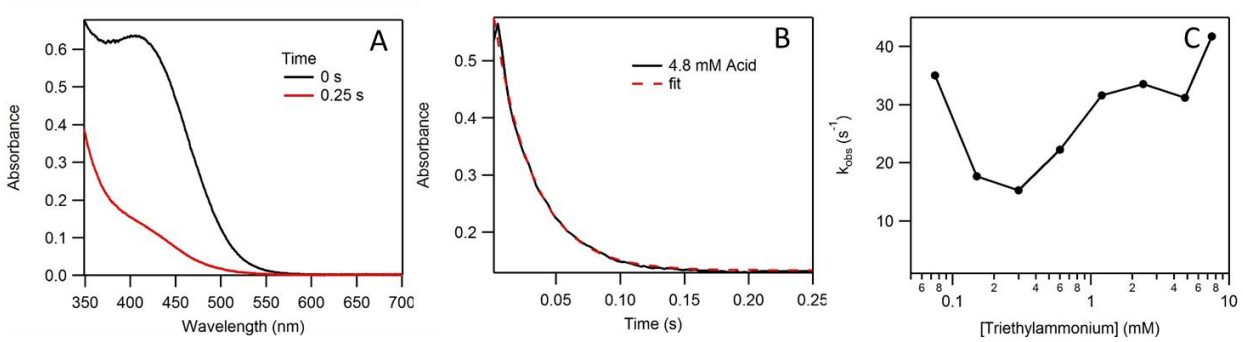

Figure D.11. A) Representative spectra for the direct conversion of $[Ni^0(P_2^{Ph}N_2^{Bz})_2]$ to $[HNi(P_2^{Ph}N_2^{Bz})_2]^+$ upon mixing with 4.8 mM triethylammonium. B) Kinetics trace at 410 nm for the same experiment shown in plot A. The dashed red trace represents a single exponential fit. C) Observed rate constants for the formation of $[HNi(P_2^{Ph}N_2^{Bz})_2]^+$ from reaction of $[Ni^0(P_2^{Ph}N_2^{Bz})_2]$ with triethylammonium. Rate constants obtained from fitting the kinetics profile at 410 nm to a single exponential function. Experiments performed using 0.075 mM Ni^0 and from 0.075 to 7.5 mM triethylammonium.

D.9. Stopped-flow Reactions: $[Ni^0(P_2^{Ph}N_2^{Bz})_2]$ vs. $[HNi^{II}(P_2^{Ph}N_2^{Bz})_2]^+$

To aid in the assignment of our unknown reaction intermediates observed optically, some stopped-flow reactions were performed to compare the reactivity of Ni^0 to HNi^{II}, including reactions with 2,4,6-collidinium (pK_a = 15.0, Figure D.12), anilinium (pK_a = 10.6, Figure 5.11), and 4-cyanoanilinium (pK_a = 7.0, Figure D.13).

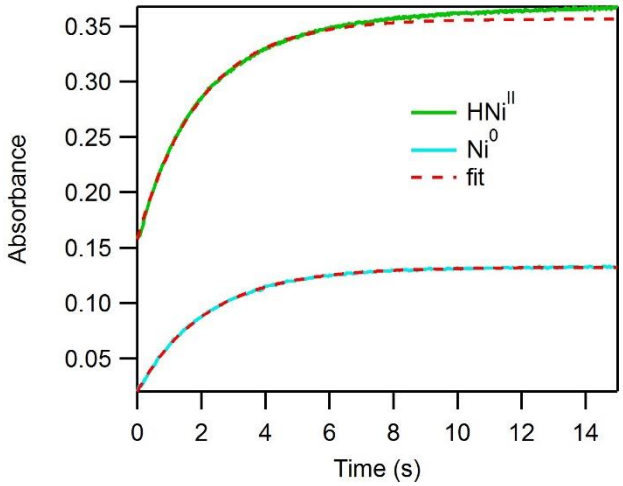

Figure D.12. Absorbance traces at 500 nm corresponding to the growth of Ni^{II} signal for the comparison of 0.2 mM HNi^{II} and 0.07 mM Ni^0 in a solution of 26 mM 2,4,6-collidinium. Dashed red traces represent single exponential fits (k_{obs} = 0.46 s^{-1} for Ni^0 and k_{obs} = 0.51 s^{-1} for HNi^{II}).

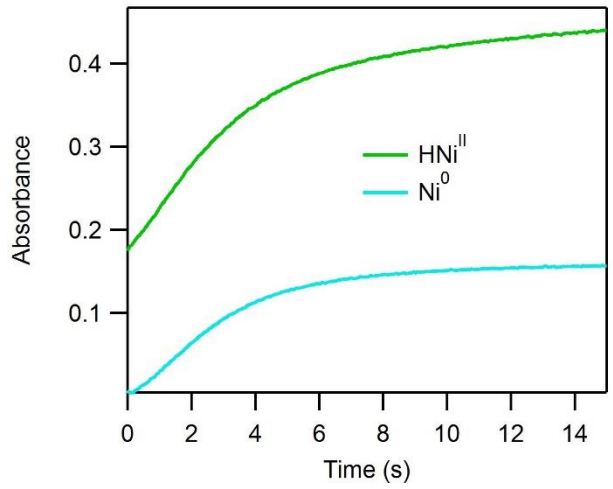

Figure D.13. Absorbance traces at 500 nm corresponding to the growth of Ni^{II} signal for reactions of 0.23 mM HNi^{II} or 0.09 mM Ni^0 with 11.5 mM 4-cyanoanilinium.

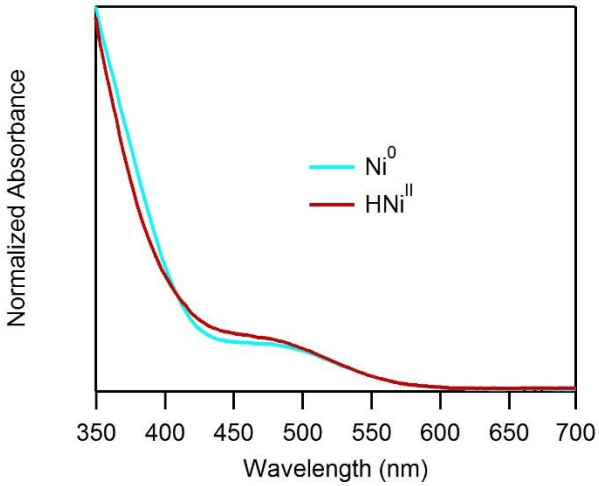

Figure D.14. Absorbance spectra at t = 2 s corresponding to the growth of Ni^{II} signal for the reaction of 0.23 mM HNi^{II} or 0.09 mM Ni^{0} with 11.5 mM 4-cyanoanilinium.

D.10. Intermediates observed in stopped-flow experiments for the reaction of $[Ni^{0}(P_2^{Ph}N_2^{Bz})_2]$ with 4-terbutylanilinium, anilinium, and 4-chloroanilinium

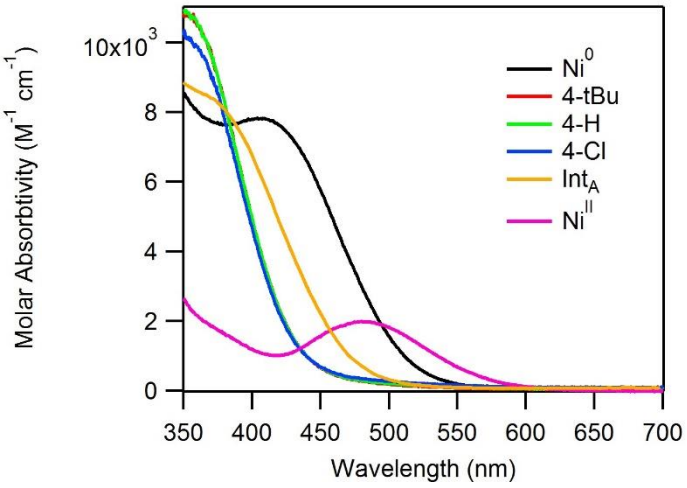

Figure D.15. Upon reaction of 0.1 mM $[Ni^{0}(P_2^{Ph}N_2^{Bz})_2]$ with 4-tertbutylanilinium (pK_a = 11.1, 4-tBu), anilinium (pK_a = 10.6, 4-H), and 4-chloroanilinium (pK_a = 9.7, 4-Cl), the initially recorded absorbance spectra (t = 1.5 ms) reveal a common intermediate for all acid and base concentrations. The intermediate (Int_B) is characterized by an absorbance shoulder from 350 to 450 nm. The absorbance of Int_A (Figure 9A), is included for comparison to Int_B.

D.11. Stopped-flow rapid mixing reaction of $[\mathbf{Ni^0(P_2^{Ph}N_2^{Bz})_2}]$ with 4-cyanoanilinium

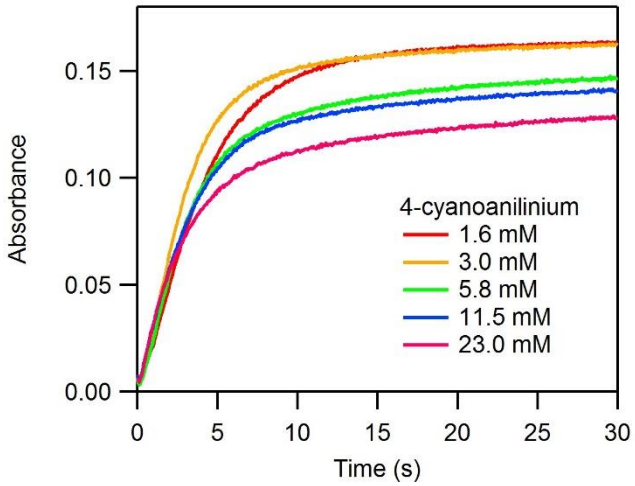

Figure D.16. Absorbance-time traces recorded at 500 nm upon rapid mixing of 0.09 mM Ni^0 with 4-cyanoanilinium (1.6 – 23.0 mM). Absorbance at 500 nm corresponds to the appearance of the Ni^{II} reaction product.

D.12. Obtaining $E_{cat/2}$, $E_{1/2}$ and peak potentials from cyclic voltammograms

Many of the cyclic voltammograms were difficult to obtain potential from and as such, we tried to be consistent in how they were assigned by developing a method for each type of reactivity. For reversible waves, the $E_{1/2}$ was used as is customary. For clean catalytic waves, the entire wave was fit with a sigmoid and the half height potential taken (Figure D.17). For messier voltammograms (those obtained below pH 7), we isolated the sigmoidal fit to only the first half of the wave. Between pH 14 and 17, voltammograms that clearly did not reach their Nernstian equilibria were see, the peak potential for the $Ni^{I/0}$ wave was used and the known value of $Ni^{II/I}$ was used.

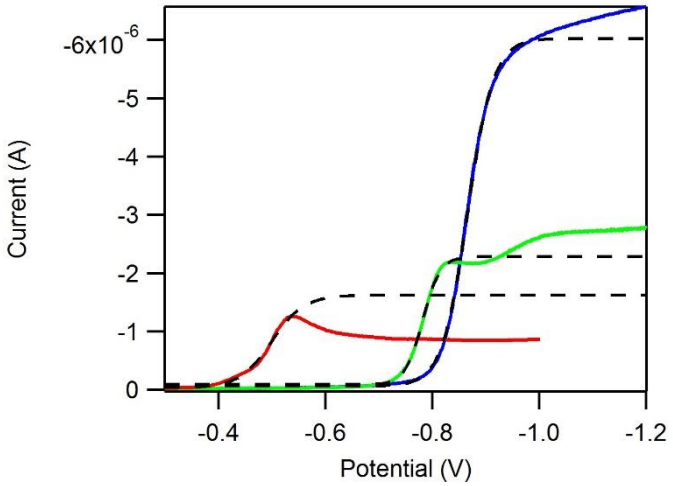

Figure D.17. Representative sigmoidal fits (black dashed line) for the 50 mM Acid:Base for 2,6-dichloroanilnium (red), 4-chloroanilinium (green), and 4-tertbutylanilinium (blue). the potential at half height of the sigmoidal fit was used as the value for $E_{cat/2}$.

D.13. 30 mV and 60 mV per decade slopes in experimental data

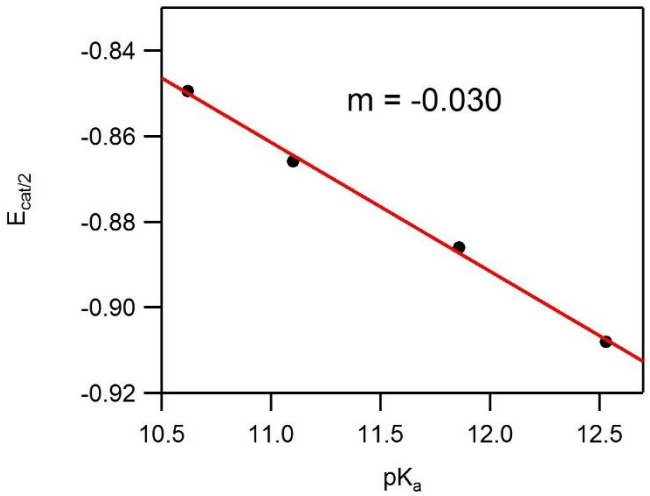

Figure D.18. $E_{cat/2}$ as a function of pK_a between 10.6 and 12.5. Linear fit results in a 30 mV per decade slope.

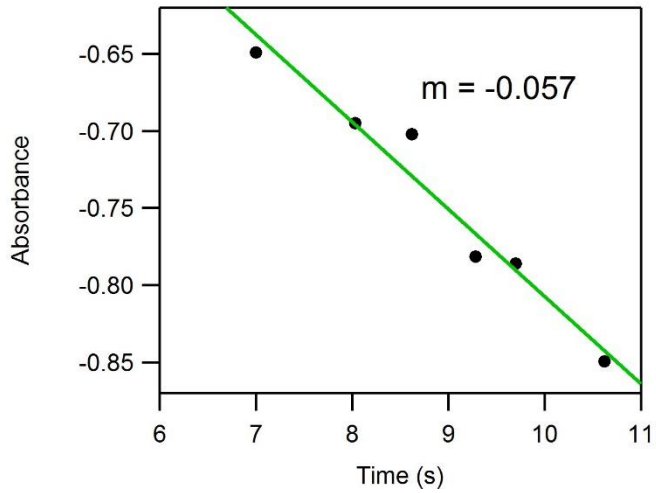

Figure D.19. $E_{cat/2}$ as a function of pK_a between 7 and 10.6. Linear fit results in a 57 mV per decade slope.

APPENDIX E. KINETIC MODELING OF ELECTROCATALYSIS IN CHRONOAMPEROGRAMS

E.1 Introduction

Recent efforts to develop sunlight-to-fuel technologies have brought the study of molecular electrocatalysts into the spotlight.[13,51,131,138,201] A number of coordination complexes have demonstrated catalytic activity towards water oxidation,[202,203] the hydrogen evolution reaction,[50,201,202,204,205] and the reduction of carbon dioxide.[9,13] Optimal catalysts should have a combination of low operating potentials, high turnover frequency, and low decomposition rates.[128] As a single catalyst bearing all of these attributes is unlikely to be discovered serendipitously, the solar fuels community has undertaken intensive mechanistic studies to better understand how these electrocatalytic reactions proceed.[43,50,62,91,206,207,111] With a few exceptions,[92,206] the primary mode of mechanistic study has involved electrochemical analysis, typically cyclic voltammetry (CV). In general, two methods for extracting mechanistic information from electrochemical data are utilized.[68]

The first and most commonly employed method is the use of pseudo-first-order analysis. Nicholson and Shain[28] developed theoretical methods for obtaining kinetic information from the canonical plateau in cyclic voltammograms obtained under steady-state catalytic conditions. An extension, known as foot-of-the-wave analysis,[34] has recently been reported as a method to determine catalytic rates for well-defined systems in which a plateau region proves inaccessible. Use of the pseudo-first-order analysis is often preferred because of its simplicity—the theory behind the method is fairly easy to conceptualize and only the measurement of catalytic cyclic voltammograms is required for analysis. However, a number of difficulties are encountered in practice.[68] As was thoroughly explained in the presentation

of the foot-of-the-wave method, the canonical plateau is rarely witnessed as numerous side-phenomena (substrate depletion, catalyst decomposition, and product inhibition) suppress the current.[34] Foot-of-the-wave analysis provides a response to this obstacle by allowing the kinetics prior to the onset of these adverse phenomena to be assessed. However, this approach can only provide kinetic information for the chemical step immediately following a reduction event, does not allow for the kinetic assessment of catalyst decomposition, and necessitates some mechanistic insight for proper application.[44,68]

The second method for mechanistic study is the use of digital simulation programs to model the current response of postulated mechanisms. While more robust than pseudo-first-order analysis, this approach does have its limitations.[208] The advantage of digital simulation of electrochemical catalysis is the ability to accurately handle the intricacy of mass transport while simultaneously modeling the thermodynamics at the electrode and the kinetics of homogeneous reactions. Unfortunately, the complexity of the calculations necessary and the level of programming required is enough to prevent most chemists, especially those not formally trained in electrochemistry, from developing their own simulation program. Professionally prepared and commercially marketed simulation programs, such as DigiElch (ElchSoft), which will be used throughout this work, and DigiSim (BASi) are widely trusted but the high cost prohibits many researchers from utilizing this tool. Free simulation programs can be found on the internet, but use of these programs without an understanding of their unique inner complexities is not advised.[208]

In response, we have developed a new approach for the mechanistic analysis of homogeneous molecular electrocatalysis in an effort to combine the advantages of digital simulation and pseudo-first-order methods into an accessible and versatile method. This

approach of kinetic modeling, herein denoted as Kinetic Modeling of Electrocatalysis in Chronoamperograms (KMEC), allows the user to postulate a reaction mechanism and utilize conceptually simple ordinary differential equations (along with an ordinary differential equation solver included in a technical computing software package, which many institutions have site licenses for) to generate an expected chronoamperogram for a given set of initial conditions. By adjusting rate constants for the elementary reaction steps or varying the mechanistic proposal, the chronoamperogram simulation can be optimized and key kinetic and mechanistic information gleaned. This is very similar in practice to modeling transient absorption spectra in which differential rate expressions describing the concentrations of reactants, intermediates and products as a function of time are related to experimental measurements through extinction coefficients.[206,169,209] In a chronoamperogram, the current versus time response provides a similar experimental handle. Importantly, rather than simply providing an observed rate constant, this method provides key mechanistic information which is inherently more valuable for catalyst design than situation-dependent rate data. Herein we a) discuss the theoretical origins and requirements for use of KMEC, b) highlight the benefits of chronoamperoemetry measurements over CV for analyzing molecular electrocatalysts, c) present a step-by-step guide for how to generate and interpret simulated chronoamperograms for both simple and complex systems, d) confirm its viability through comparison to data generated by both an analog of the Sand equation and with a commercial digital simulation program for several electrocatalytic reaction scenarios, and e) present equations to translate this method to the analysis of homolytic reaction pathways. In addition to describing this new approach and its application to electrocatalysis, it is hoped that this presentation provides

readers with insight into the various processes near the electrode surface that dictate current responses in electrocatlytic systems.

E.2. Results and Discussion

Pseudo-first-order kinetic analysis. Pseudo-first-order kinetic analysis was developed by Delahay and Stiehl to analyze current response measurements for an EC´ reaction mechanism (Scheme E.1). With both brief and thorough accounts of the theory readily available,[26,28,31,72] the discussion here will focus on the aspects and assumptions essential to incorporating pseudo-first-order kinetic analysis into KMEC. The analysis was prepared for Scheme E.1 in which electroactive species P is reduced at the electrode to Q and Q then reacts with some substrate A to reform P and product B. (All catalysis discussed in this work will be in the form of reductive catalysis, however, all concepts are directly applicable to oxidative catalysis.)

Scheme E.1. EC' catalytic reaction.

$$P + e^- \rightleftharpoons \mathrm{Q}$$

$$Q + A \xrightarrow{k_r} P + B$$

Most important to this work is Eq. E.1[26] which describes the current vs. time profile for pseudo-first-order catalysis.

$$i = nFSD_P^{1/2}C_P\left\{(k_{obs})^{1/2}\,\mathrm{erf}\left[(k_{obs}t)^{\frac{1}{2}}\right] + \frac{\exp(-k_{obs}t)}{(\pi t)^{1/2}}\right\} \quad (E.1)$$

n is the number of electrons transferred to the catalysis for each turnover, *F* is Faraday's constant, S is the surface area of the electrode, D_P is the diffusion coefficient for both P and Q (they are expected to be approximately equal), C_P is the concentration of catalyst, and t is time. For an EC′ mechanism, $k_{obs} = k_r[A]$, but Equation 1 has been adapted to analyze more complicated multi-step and multi-electron catalytic reaction mechanisms[13] wherein k_{obs} more generally represents the rate at which Q is converted back to P.[22,68]

Eq. E.1 has two controlling components — the diffusional and the kinetic responses; as $k_{obs}t \rightarrow 0$, Equation 1 is reduced to the familiar Cottrell equation (Eq. E.2, used to describe the current response due to diffusional flux of the electroactive species during chronoamperometry measurements) and as $k_{obs}t \rightarrow \infty$, it reduces to Eq. E.3 which is commonly used to extract rate data from the plateau in a catalytic cyclic voltammetric wave.

$$i = \frac{nFSD_P{}^{1/2}C_P}{(\pi t)^{1/2}} \qquad (E.2)$$

$$i = nFSC_P^0\sqrt{D_P k_{obs}} \qquad (E.3)$$

There are six assumptions and requirements to highlight for correct application of Eq. E.1:

1) The electrode is planar and mass transport is solely linear, semi-infinite diffusion.

2) The reduction of the substrate at the electrode occurs at potentials sufficient not to interfere with the catalytic current.

3) Electron transfer to the catalyst is fast such that it does not limit the reaction kinetics.

4) Consumption of substrate is negligible on the timescale of the experiment.

5) The summed concentration of the oxidized and reduced form of the catalyst is constant.

6) The product of catalysis does not influence the rate of reaction.

It is uncommon for a catalytic system to satisfy all of these assumptions. Most often, conditions 4, 5 and 6 are not met; consumption of substrate near the electrode surface occurs rapidly, reaction intermediates undergo degradation which leads to fluxional concentrations of catalyst, and reaction products inhibit catalysis. The technique presented in this work allows Eq. E.1 to be used to model catalysis without requiring conditions 4, 5 and 6 be met, and also provides kinetic assessment of the responsible phenomena (substrate depletion, catalyst decomposition, product inhibition).

Chronoamperometry. CV is frequently utilized to analyze electrocatalysts. In this technique, the response current is a function of both applied potential (and thus the relative ratio of oxidized and reduced catalyst at the electrode surface) and the timescale of the experiment. In chronoamperometry, the potential step essentially acts as an on-off switch for catalysis and the resulting current response only depends on time, in effect simplifying the interpretation of the data collected. In the simplest case, where electron transfer is fast and Nernstian, the potential dependent form of Eq. E.3 is shown as Eq. E.4 where $E_{1/2}$ represents the potential where half of the catalyst at the electrode surface is in its active form (this is often, but not always, synonymous with standard potential of the catalyst). [34,44,68]

$$i = \frac{nFSC_P^0\sqrt{D_P k_{obs}}}{1 + exp\left[\frac{nF}{RT}(E - E_{1/2})\right]} \quad (E.4)$$

Three regions are formed surrounding the redox potential of the catalyst; the region in which no catalysis is observable, the region where catalyst activity (the term activity here represents the ratio of reduced to oxidized catalyst at the surface of the electrode) varies in accordance with the Nernst equation, and the region where the potential is sufficient such that the catalytic current has no dependence upon potential (and thus forms the canonical sigmoidal wave in a cyclic voltammogram, Figure E.1). By stepping the potential from the region where virtually no catalysis is occurring to the region where virtually no current enhancement is achieved upon altering the potential (if we consider 1%, and 99% activity our reference points, the required potential step is 235 mV for an electrochemically reversible system), we effectively shift from no active catalyst to ~100% activity and thereby generate data that is entirely a result of the homogeneous kinetics and diffusive properties of the system, allowing evaluation to be performed simply on a time basis. As is demonstrated in Figure E.1, it can also be envisioned

that reactions with slow electron transfer kinetics can be studied in this manner simply by applying the necessary driving force to achieve the virtual 100% activity (of note on this topic, catalytic cyclic voltammograms have been described for slow electrode kinetics in equation form by Costentin *et al.*[34]). However, extra caution must be taken in this scenario to ensure there is no interference by substrate redox activity at the electrode surface.

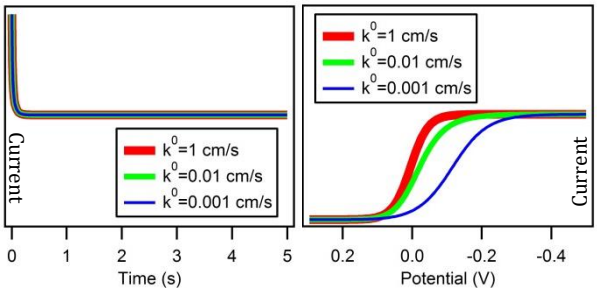

Figure E.1. Slow electron transfer kinetics significantly impact the results shown for linear sweep voltammetry (LSV, right plot) under pseudo-first-order catalytic conditions. However, no difference is seen between the fast (k^0=1 cm/s) and slow (k^0=0.001 cm/s) systems in chronoamperometry (CA, left plot) with a potential step from 0.3 to –0.5 V. Data simulated for an EC′ mechanism. Current axes on equivalent scale. [P] = 0.001 M, [A] = 1 M, $E_{P/Q}^{0\prime} = 0\ V$, k_r=50 $M^{-1}s^{-1}$.

Kinetic Modeling of Electrocatalysis in Chronoamperograms. The failure to witness a plateau in the large majority of electrocatalytic systems analyzed with CV results from the transience of the reactant (catalyst and substrate) concentrations near the electrode surface (the reaction layer,[210] see below), which can be due to both catalyst degradation and substrate consumption. Without knowledge of the available reactant concentrations at $t > 0$, it is difficult to obtain valuable information from Eq. E.1. However, if the available concentration at any time t can be ascertained, we can still apply Eq. E.1 at infinitesimally small time fragments within which steady-state conditions hold. To approach this, we begin with a postulated mechanism and associated rate constants for the elementary steps. From this we can

predict the available concentrations of reactants (catalyst and substrate), and subsequently the expected current as a function of time. Eq. E.5 approximates the reactant concentrations in the reaction layer during chronoamperometric measurements. Its evaluation results in a dataset representing the concentration of the species of interest over time.

$$\frac{dC^{\mu}}{dt} = \frac{D^{1/2}(C^{0} - C^{\mu})}{\mu(\pi t)^{1/2}} - (1 - e^{-1})C_{P}^{\mu}k \qquad (E.5)$$

C^{μ} is the concentration of the reaction species (catalyst, substrate, or product) in the reaction layer, C^{0} the bulk solution concentration, D is the diffusion coefficient, and C_{P}^{μ} is the concentration of catalyst in the reaction layer, and k represents the rate of consumption or appearance of the species of interest (see below). The differential equation can be evaluated using an ordinary differential equation solver (here we use ode45, implemented in the MATLAB software package; an example function for this is shown under section E.4. Eq. E.5 can be rewritten as Eq. E.6 to provide a conceptually complete picture of the reaction layer. Eq. E.6 is composed of three components which describe volume, flux into the reaction layer due to diffusion, and "flux" out of the reaction layer due to a homogeneous chemical reaction.

$$\frac{dC^{\mu}}{dt} = \frac{S\frac{D^{1/2}(C^{0} - C^{\mu})}{(\pi t)^{1/2}} - S(1 - e^{-1})\mu C_{P}^{\mu}k}{S\mu} \qquad (E.6)$$

i. Volume

$$\frac{dC^{\mu}}{dt} = \frac{S\frac{D^{1/2}(C^{0} - C^{\mu})}{(\pi t)^{1/2}} - S(1 - e^{-1})\mu C_{P}^{\mu}k}{\boldsymbol{S\mu}}$$

Because we are modeling the rate at which species are diffusing into the reaction layer and subsequently being consumed by a chemical reaction, we must define a volume in which these

processes occur. We represent this as $V = S\mu$ where S is the area of the electrode and μ is the depth of the reaction layer which is defined as Eq. E.7 (Section E.4). D_P is the diffusion coefficient of the catalyst and k_{obs} represents the rate at which the reduced form of the catalyst (Q) is converted back to the oxidized form (P).

$$\mu = \sqrt{\frac{D_P}{k_{obs}}} \quad (E.7)$$

The concept of the reaction layer was first presented for catalysis by Brdicka and Weisner[210] and is defined by applying the assumption that the active form of the catalyst exists in uniform concentration near the electrode surface.

ii. Diffusion

$$\frac{dC^{\mu}}{dt} = \frac{S\frac{\boldsymbol{D^{\frac{1}{2}}(C^0 - C^{\mu})}}{\boldsymbol{(\pi t)^{1/2}}} - S(1 - e^{-1})\mu C_P^{\mu} k}{S\mu}$$

Diffusion, the only form of mass transport considered in the analysis, is modeled with dependence on three parameters— the diffusion coefficient, the concentration difference between the bulk solution and the reaction layer ($C^0 - C^{\mu}$) and the time elapsed since the potential step (t). The relationship $\frac{D^{\frac{1}{2}}(C^0 - C^{\mu})}{(\pi t)^{1/2}}$ represents the flux through a plane at a fixed point by natural diffusion, and is commonly known as the Cottrell Equation. In solving for this equation, the initial boundary condition, "at any time t, the concentration (C^{μ}) is equal to a specific value that is unchanging," is applied (Section E.4). As a result, this expression is only an approximation because C^{μ} is actively changing, but we contend that this approximation holds by the nature of diffusion layer growth. The diffusion layer grows at a fixed rate,

regardless of the gradient present,[72] and thus, even as the difference gradually increases, no effect will be seen in the size of the diffusion layer, only a slightly different contour to the concentration profile. As such, the rate of flux into the reaction layer should not see an appreciable effect. It is important to note here that this equation remains true even for the case that C^{μ} is larger than C^{0}, allowing for the approximation of diffusion of product *out* of the reaction layer as well.

iii. Homogeneous reaction

$$\frac{dC^{\mu}}{dt} = \frac{S\frac{D^{1/2}(C^{0} - C^{\mu})}{(\pi t)^{1/2}} - S(\mathbf{1} - \boldsymbol{e^{-1}})\boldsymbol{\mu C_P^{\mu} k}}{S\mu}$$

Consumption of species in the reaction layer is modeled as the quantity of active catalyst, μC_P^{μ} (where C_P^{μ} represents the summed total of all forms of the catalyst contained within the reaction layer) multiplied by the observed rate of reaction responsible for the consumption or appearance (k) and a correction factor ($1 - e^{-1}$). The rate at which substrate is consumed has long been known to be $\mu C_P^{\mu} k$,[210] however, this has not been extended to other phenomena such as the catalyst decomposition. The correction factor $1 - e^{-1}$ represents the amount being consumed within the reaction layer by only considering the actual quantity of catalyst within this defined reaction layer. The derivation for this term can be found under SI–3 (Section E.4), and it can be more broadly applied to the consumption of any species related to the catalyst. A visual representation is shown in Figure E.2.

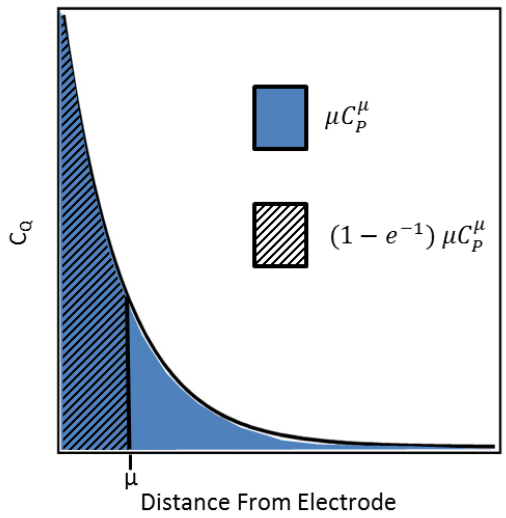

Figure E.2. Concentration vs. distance profile for the concentration of the reduced form of the catalyst in the EC´ pathway. The shaded blue region represents the total quantity of reduced catalyst. The striped region represents the catalyst located in the region we have defined as the reaction layer.

Application of KMEC. KMEC can be applied to a real system by following the steps outlined herein. Its use will be outlined for three catalytic scenarios: 1) an introductory system comprised of the EC′ mechanism (Figure E.3A) along with a catalyst degradation pathway 2) a mechanism comprised of multiple rate-influencing steps and 3) a complex catalytic system requiring more rigorous considerations (Scheme E.3). In the subsequent section, *Comparison of KMEC to Simulated Chronoamperograms* (and Section E.4), we apply KMEC to these and a variety of additional systems and compare the results to digital simulations. By comparing results from KMEC to digital simulations, we demonstrate the application of this approach to a wide range of catalytic scenarios and verify its robustness. Application of KMEC to analyze the mechanisms of molecular catalysts for hydrogen evolution is the focus of current work in our laboratory.

KMEC for EC' with catalyst degradation. For our first example we will examine the mechanism shown in Figure E.3A. It is comprised of three steps: first the reversible reduction of P to Q, followed by the irreversible interaction of Q with A to form P and B (with rate constant k_r) and the parallel irreversible degradation of Q to some species R (with rate constant k_d). This system was chosen because it provides a straightforward illustration of how Equations E.1 and E.5 cooperate to generate an expected chronoamperogram (Figure E.3C).

A) Reaction Scheme

$$P + e^- \rightleftharpoons Q$$

$$Q + A \xrightarrow{k_r} P + B \qquad k_r = 1000\ M^{-1}s^{-1}$$

$$Q \xrightarrow{k_d} R \qquad k_d = 2\ s^{-1}$$

B) Concentrations from KMEC equations

$$\frac{d[A]^{\mu}}{dt} = \frac{D_A^{1/2}([A]^0 - [A]^{\mu})}{\mu(\pi t)^{1/2}} - (1 - e^{-1})[P_T]^{\mu} * k_r[A]^{\mu}$$

$$\frac{d[P_T]^{\mu}}{dt} = \frac{D_{P_T}^{1/2}([P_T]^0 - [P_T]^{\mu})}{\mu(\pi t)^{1/2}} - (1 - e^{-1})[P_T]^{\mu} * k_d$$

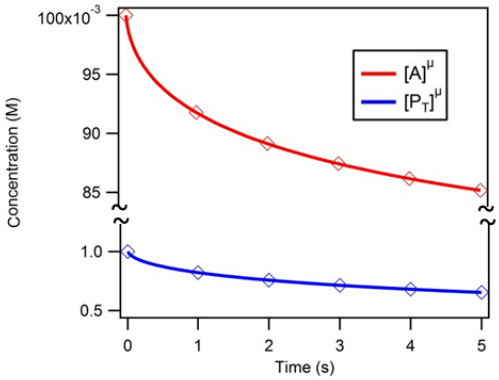

C) Calculation of Current

$$i = nFAD_P^{1/2}[P_T]^{\mu}\left\{(k_r[A]^{\mu})^{1/2}\,\mathrm{erf}\left[(k_r[A]^{\mu}t)^{\frac{1}{2}}\right] + \frac{\exp(-k_r[A]^{\mu}t)}{(\pi t)^{1/2}}\right\}$$

t	$[P_T]^{\mu}$ (mM)	$[A]^{\mu}$ (mM)	i (μA)
0	100.0	1.000	320.1
1	91.8	0.822	240.1
2	89.1	0.758	218.2
3	87.4	0.714	203.7
4	86.2	0.681	192.7
5	85.2	0.653	184.0

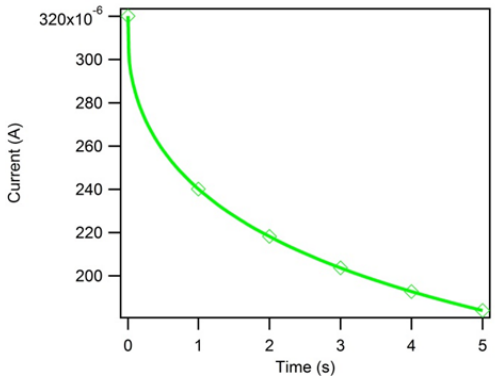

Figure E.3. Step by step illustration of how to generate a simulated chronoamperogram from a postulated mechanism using the KMEC method. Diamonds on plots do not represent all data points used in calculation, only those shown in the table.

Generating the KMEC equations (Figure E.3B) for this system can be accomplished easily. The only portion of the KMEC equations that requires attention from case to case is the homogeneous reaction expression. As was discussed earlier, the rate constant must represent the rate by which a given species of interest is consumed. For substrate A, this is simply $k_r[A]^{\mu}$ as was discussed for the EC′ analysis developed by Delahay and Stiehl.[26] For the catalyst P, the KMEC equation represents the concentration of all forms combined (P_T = P+Q) and the first-order rate constant describing the homogeneous reaction (degradation) causing its concentration change is k_d.

Evaluation of the KMEC equations (by ode45 function in MATLAB) using the initial concentrations [A] = 0.1 M, and [P] = 0.001 M results in the concentration profiles shown in Figure E.3B. With this time-dependent concentration data, Eq. E.1 can be used to calculate the expected chronoamperogram. k_{obs} for this equation is also $k_r[A]^{\mu}$, as the rate of consumption of A and regeneration of P from Q are equal. Current can be directly calculated using the three vectors— time, $[A]^{\mu}$, and $[P_T]^{\mu}$— and Eq. E.1 (Figure E.3C).

KMEC for multi-step reactions. Applying this method to mechanisms which contain multiple steps that influence the observed rate of reaction requires additional treatment beyond that shown in Figure E.3. In essence, the observed rate can generally be summarized utilizing the single step that results in the formation of product and regeneration of P; however, this requires that the concentration of the species involved in this step be known. Therefore, when considering multistep reactions, it thus becomes necessary to determine the concentrations of catalytic intermediates to generate time dependent concentration profiles like that in Figure E.3B. This will be illustrated using Scheme E.2 where we have a reversible addition of substrate prior to the irreversible formation of product.

Scheme E.2. Reaction for simple simulation

$$P + e^- \rightleftharpoons \mathrm{Q}$$

$$Q + A \rightleftharpoons QA; \quad k_1, k_2$$

$$QA \overset{k_3}{\rightarrow} P + B$$

With this mechanism, the crucial step of product formation can be described by the expression $k_3[QA]$. Because not all active (reduced) forms of the catalyst are manifested as species QA (Q and QA are in equilibrium), we cannot directly write an expression describing the observed rate constant from reactant concentrations (as opposed to in Figure E.3 where $k_r[A]$ describes the rate of product formation and regeneration of P).

For use in Eq. E.1 the observed rate constant *k* is presented in the units of s^{-1}. For a complex reaction the observed rate constant can be determined by dividing rate expression v by $[P_T]$ ($k_{obs} = v/[P_T]$). This was not explicitly demonstrated in Figure E.3, however, the practice was adhered to; the full form of k_{obs} for the first example was $k_{obs} = k_r[Q][A]/[P_T]$ where the observed rate $v = k_r[Q][A]$. For the example in Figure E.3, we can consider [Q] = $[P_T]$ because the reaction contains no intermediates and we are therefore left with only $k_{obs} = k_r[A]$ because $[Q]/[P_T]$ is unity. With a multi-step reaction such as the one in Scheme E.2 this is no longer the case. Therefore $k_{obs} = k_r[QA]/[P_T]$. While $[P_T]$ simply gets factored back in when implementing k_{obs} into the KMEC equation (Eq. E.5), it is very important for use of Eq. E.1 to derive k_{obs} in this manner as the current has a half order dependence on observed rate (which has substrate concentration factored in), while the dependence on catalyst concentration is first order.

To determine the observed rate constant we must know the percentage of active catalyst in the form of QA. In the scenario presented in Figure E.3, 100% of the active catalyst was

assumed to be in the form of Q. We can obtain the concentration of QA by two different methods− the first is to solve for it in closed form using pre-equilibrium approximations; this type of analysis, along with steady state approximations, is the subject of numerous textbooks and will not be discussed here.[211] The second and perhaps less taxing method is to calculate the equilibrium concentrations with an ordinary differential equation solver like that used to numerically solve the KMEC equations. The equations to be evaluated for Scheme E.2 are shown here:

$$\frac{d[Q]}{dt} = -k_1[Q][A] + k_2[QA] + k_3[QA]$$

$$\frac{d[QA]}{dt} = k_1[Q][A] - k_2[QA] - k_3[QA]$$

Notice that these equations do not encompass the whole of the reaction mechanism, but rather only the equations that represent the equilibrium between different forms of the catalyst. When evaluating for the equilibrium, all expressions that represent the net loss or gain of bulk species should be removed (they will be represented with KMEC equations). For Scheme E.2, this is simply the equation for $\frac{d[A]}{dt}$; including this would result in a transient concentration for species *A* and would therefore prohibit the reaction from reaching equilibrium. This is discussed in further detail in the next section and Section E.4.

The change in concentration of species *A*, which we excluded from the equilibrium equations is then accounted for by the KMEC equation below, where A is lost irreversibly at the same rate as product is formed ($k_{obs} = k_r[QA]/[P_T]$):

$$\frac{d[A]^\mu}{dt} = \frac{D_A^{1/2}([A]^0 - [A]^\mu)}{\mu(\pi t)^{1/2}} - (1 - e^{-1})[P_T]^\mu * k_3[QA]/[P_T]$$

The equilibrium equations and the KMEC equations are evaluated in tandem; from the equilibrium equations we obtain the value for [QA] which allows for the calculation of the observed rate ($k_{obs} = k_3[QA]/[P_T]$) and subsequently the change in concentration of *A* $\left(\frac{d[A]^{\mu}}{dt}\right)$. After the new concentration of species *A* is determined, the equilibrium equations can be re-evaluated with the new initial conditions. This process is repeated over the entire time window of the experiment to produce the time dependent concentration in the reaction layer. At the end, just like is shown for Figure E.3C, the observed rate over time is combined with the catalyst concentration (which is constant for this mechanism) to produce the expected chronoamperogram from Eq. E.1.

KMEC for complex, multi-step reactions. This method can also be applied to complex reaction schemes beyond the two cases outlined above, such as those responsible for hydrogen production, CO_2 reduction and water oxidation or other multi-electron, multi-substrate scenarios. To demostrate how to approach such a system, a hypothetical mechanism (Scheme E.3) has been envisioned that includes substrate consumption, catalyst decomposition, solution electron transfer processes (it is important to note that solution electron transfer processess can prevent the data from being analyzed by KMEC and a detailed discussion of when it is and is not appropriate can be found below), and product inhibition, along with reversible steps generating stable intermediates. In this reaction, species *A* is catalytically reduced to *C* by catalyst *P*. The reduction process involves two reaction series operating in tandem. Catalyst *P* reduces *A* to *B* by the reversible binding of *A* followed by addition of *Z* from co-substrate *YZ*, a solution electron transfer, and finally a second addition of *Z*, which forms *Y*, *B* and oxidized catalyst. Once *B* is available in solution, it is reduced to *C* through a tandem catalytic pathway. The rate constants selected dictate that both the generation of species *Y* and *B* slow the process

of catalysis (i.e. product inhibition) as the rate constant k_6 is greater than k_5 and $INT5$ is treated as a more stable intermediate than $INT1$. The reduced form of the catalyst, *Q*, can also interact with *YZ* to resulting in decomposition product *DEC*; this equivalent of *P* no longer participates in catalysis.

Scheme E.3. Reaction for mock simulation.

Scheme 3

$$P + e^- \rightleftharpoons Q$$
$$Q + YZ \rightarrow DEC + Y; \qquad k_{11}$$

$A \rightarrow B$		$B \rightarrow C$
$Q + A \rightleftharpoons INT1$	$k_1, k_2 \mid k_3, k_4$	$Q + B \rightleftharpoons INT5$
$INT1 + YZ \rightleftharpoons INT2 + Y$	$k_5, k_6 \mid k_8$	$INT5 + YZ \rightarrow INT6 + Y$
$INT2 \rightarrow INT3$	$k_7 \mid k_e$	$INT6 + Q \rightarrow INT7 + P$
$INT3 + Q \rightarrow INT4 + P$	$k_e \mid k_{10}$	$INT7 + YZ \rightarrow P + Y + C$
$INT4 + YZ \rightarrow P + Y + B$	k_9	

$k_1(M^{-1}s^{-1})$	$k_2(s^{-1})$	$k_3(M^{-1}s^{-1})$	$k_4(s^{-1})$	$k_5(M^{-1}s^{-1})$	$k_6(M^{-1}s^{-1})$
900	1800	200	20	400	8000
$k_7(M^{-1}s^{-1})$	$k_8(M^{-1}s^{-1})$	$k_9(M^{-1}s^{-1})$	$k_{10}(M^{-1}s^{-1})$	$k_{11}(M^{-1}s^{-1})$	
250	250	1000	1200	5	

1. Decide which species need KMEC equations

After a mechanism has been proposed, the species that need to be evaluated by KMEC equations must be identified. This includes all species that are *not* intermediates, have transient concentrations and *do* affect the rate of catalysis. For the mechanism in Scheme E.3, this includes the catalyst *P* (which will be denoted as P_T, to represent the sum of all forms with the exception of *DEC*), *A*, *B*, *YZ*, and *Y*. We do not include *C* because it does not participate in the catalytic cycle beyond formation and we *do* include *B* because though it is an intermediate in the full reaction, it exists in the bulk solution and its concentration affects the catalytic rate.

2. Determining homogenous reaction expressions

With the mechanism shown in Scheme E.3, the analysis becomes significantly more complex. Just as in Figure E.3, each species whose concentration is modeled with a KMEC equation (catalyst and substrates—P_T, *A*, *B*, *YZ*, and *Y*) must have a unique homogenous reaction expression and rate constant describing its rate of disappearance (or in the case of *Y* and *B*, rate of appearance)—k in Eq. E.5. From Scheme E.3, we can determine these rate constants to be:

$$k_B = \frac{v_B}{[P_T]^\mu} = k_9[INT4][YZ]^\mu/[P_T]^\mu \qquad (E.8.A)$$

$$k_C = \frac{v_C}{[P_T]^\mu} = k_{10}[INT7][YZ]^\mu/[P_T]^\mu \qquad (E.8.B)$$

$$k_{DEC} = \frac{v_{DEC}}{[P_T]^\mu} = k_{11}[Q][YZ]^\mu/[P_T]^\mu \qquad (E.8.C)$$

$$k_Y = 2 * (k_B + k_C) + k_{DEC} \qquad (E.8.D)$$

$$k_P = 2 * (k_B + k_C) \qquad (\text{a.k.a. } k_{obs}) \qquad (E.8.E)$$

where k_B represents the rate of consumption of *A* and formation of *B*, k_C represents the consumption of *B* (and formation of *C*), k_{DEC} represents the degradation of the catalyst to species *DEC*, k_Y represents the formation of *Y* and the consumption of *YZ*, and k_P represents the rate at which the oxidized form of the catalyst *P* is formed by homogeneous reaction pathways. k_Y and k_P can be adequately described through combinations of the other three rate constants. As discussed above, the rate constants are formed by dividing rate of formation (v) by $[P_T]^\mu$.

Examining the Equations E.8.A–E above, there are three species which are reaction intermediates ($INT4$, $INT7$, and Q see Figure E.S2) and thus have unknown concentrations. As was discussed in the previous section, we must determine these concentrations iteratively to generate the time dependent concentration data. For this purpose, a series of differential rate

expressions in full form (Section E.4) is derived and then all parts that result in a change of concentration of the species requiring KMEC equations (see above) are removed, resulting in Equations E.9.A-F.

$$\frac{d[Q]}{dt} = -k_1[Q][A] + k_2[INT1] - k_3[Q][B] + k_4[INT5] + k_9[INT4][YZ] + k_{10}[INT7][YZ] \quad (E.9.A)$$

$$\frac{d[INT1]}{dt} = k_1[Q][A] - k_2[INT1] - k_5[INT1][YZ] + k_6[INT2][Y] \quad (E.9.B)$$

$$\frac{d[INT5]}{dt} = k_3[Q][B] - k_4[INT5] - k_8[INT5][YZ] \quad (E.9.C)$$

$$\frac{d[INT2]}{dt} = k_5[INT1][YZ] - k_6[INT2][Y] - k_7[INT2] \quad (E.9.D)$$

$$\frac{d[INT4]}{dt} = k_7[INT2] - k_9[INT4][YZ] \quad (E.9.E)$$

$$\frac{d[INT7]}{dt} = k_8[INT5][YZ] - k_{10}[INT7][YZ] \quad (E.9.F)$$

Of note, the reaction steps in Scheme E.3 involving homogenous electron transfers (represented by the rate constant k_e) are not included in the Equations E.9.A-F. We made the assumption that these steps are much faster than the chemical steps and have no impact on overall rate; therefore, any species undergoing homogeneous electron transfer is automatically considered to be the reduced form (i.e. INT3 is automatically INT4 and INT6 is automatically INT7) in the differential rate expressions.

Equations E.9.A-F are solved numerically with an ordinary differential equation solver, wherein vectors describing current concentrations of bulk reactants in the reaction layer, the timespan and rate constants are provided as inputs to solve the initial value problem. Time-dependent concentration profiles are produced for each intermediate (Figure E.S2). As was

discussed for Scheme E.2, the concentrations of the catalyst and substrates approach equilibrium when the processes that prevent equilibrium are removed; these equilibrium concentrations can then be used in the evaluation of KMEC Equations E.10.A–E, shown below. This entire process is performed iteratively, each time with the new initial conditions obtained from the Equations E.10.A–E, to obtain the relevant concentrations of intermediates throughout the reaction. Note that Eq. E.10.C has two homogeneous reaction expressions to account for the formation and consumption of *B*. Evaluation of these equations, just as was performed in Figure E.3B results in Figure E.4 which illustrates both the concentrations of reactants and substrates (4A) and reaction rate constants from Equations E.8.A–E (4B) plotted versus time.

$$\frac{d[P_T]^{\mu}}{dt} = \frac{D_P^{1/2}([P_T]^0 - [P_T]^{\mu})}{\mu(\pi t)^{1/2}} - (1 - e^{-1})[P_T]^{\mu} * k_{DEC} \qquad (E.10.A)$$

$$\frac{d[A]^{\mu}}{dt} = \frac{D_A^{1/2}([A]^0 - [A]^{\mu})}{\mu(\pi t)^{1/2}} - (1 - e^{-1})[P_T]^{\mu} * k_B \qquad (E.10.B)$$

$$\frac{d[B]^{\mu}}{dt} = \frac{D_B^{1/2}([B]^0 - [B]^{\mu})}{\mu(\pi t)^{1/2}} + (1 - e^{-1})[P_T]^{\mu} * k_B - (1 - e^{-1})[P_T]^{\mu} * k_C \qquad (E.10.C)$$

$$\frac{d[YZ]^{\mu}}{dt} = \frac{D_{YZ}^{1/2}([YZ]^0 - [YZ]^{\mu})}{\mu(\pi t)^{1/2}} - (1 - e^{-1})[P_T]^{\mu} * k_Y \qquad (E.10.D)$$

$$\frac{d[Y]^{\mu}}{dt} = \frac{D_A^{1/2}([Y]^0 - [Y]^{\mu})}{\mu(\pi t)^{1/2}} + (1 - e^{-1})[P_T]^{\mu} * k_Y \qquad (E.10.E)$$

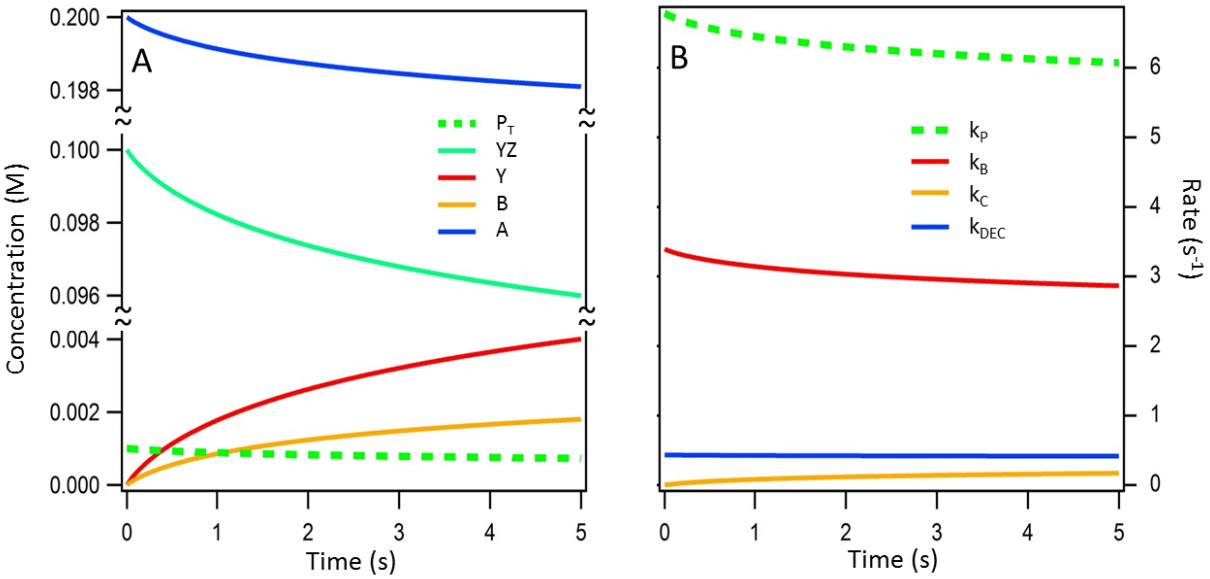

Figure E.4. A) The concentrations of the transient species within the reaction layer and B) the resulting rate constants describing formation of each species calculated using the Equations E.10.A-E, plotted as a function of time. The two green dashed traces (P_T concentration and k_P, n.b. P_T excludes DEC as it is inactive) will be used to calculate the expected current in a chronoamperogram. Initial conditions: [P] = 0.001 M; [YZ] = 0.1 M; [Y] = 0 M; [A] = 0.2 M; [B] = 0 M.

3. Generation of the expected chronoamperogram

In Figure E.4, special note should be taken of the dashed green trace in each plot. As was discussed above, only three vectors are required for the calculation of current vs. time per Eq. E.1— time, catalyst concentration within the reaction layer and observed rate constant for catalysis. Shown as the dashed green trace in Figure E.4A is the concentration of catalyst and shown as the dashed green trace in Figure E.4B is the observed rate of reformation of P after reduction to Q at the electrode, which is equal to k_{obs}. Following the principles illustrated in Figure E.3, these values in combination with Eq. E.1 can be used to produce the chronoamperogram shown in Figure E.5. At this point in the analysis, the chronoamperogram generated via the KMEC process can be compared to the experimental data and the rate constants and/or proposed mechanism input to the KMEC method can be iteratively adjusted to optimize the simulation.

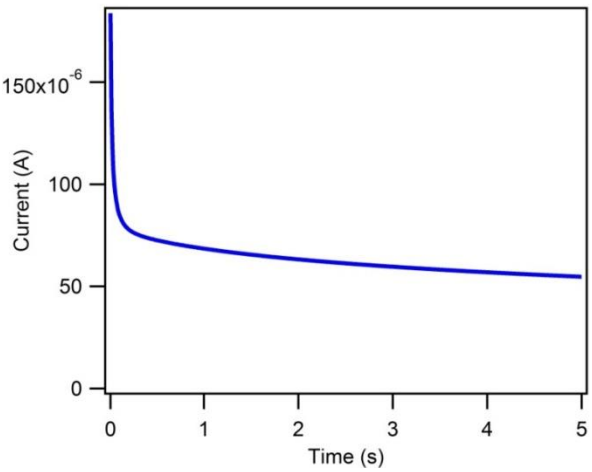

Figure E.5. Resulting chronoamperogram from KMEC analysis for Scheme E.2 with initial conditions: [P] = 0.001 M; [YZ] = 0.1 M; [Y] = 0 M; [A] = 0.2 M; [B] = 0 M.

Comparison of KMEC to simulated Chronoamperograms. As evidence that the assumptions and approximations that have been presented give reasonable results, the KMEC

method, as outlined, has been applied to several electrocatalytic scenarios. The first comparison will be to the true pseudo-first-order case in which substrate is consumed but the observed rate of reaction does not change (k_{obs} is not proportional to substrate concentration). This was accomplished by solving, in closed form, for the concentration of substrate over time and comparing the result from Eq. E.5 to this data. Next, several comparisons will be made for more complex catalytic systems, demonstrating that the KMEC approximations remain adequate under more strenuous circumstances by comparing KMEC results to data generated by DigiElch for a series of complex mechanisms, including the one presented in Scheme E.3. Comparison to DigiElch is the optimal way to verify the accuracy of this approach as it allows control of the influencing parameters for the datasets and is already trusted as a means for mechanistic analysis of real systems throughout the electrocatalysis literature.[126,212]

i. Ideal Scenario- True Pseudo-First-Order Catalysis

As a first proof of principle, the result of Eq. E.5 was tested under idealized conditions wherein the overall rate of catalysis is fixed as a constant value and has no dependence on the concentration of substrate. This was accomplished by solving for the concentration of substrate at the electrode surface in closed form from Fick's Laws. The derivation can be foundin Section E.4 and the result is Eq. E.11, where P represents the catalyst and S represents the substrate.

$$C_S(0,t) = C_S^0 - \frac{2C_P^0\sqrt{D_P k t}}{\sqrt{\pi D_S}} \qquad \text{(E. 11)}$$

Eq. E.11 is practically identical to the Sand Equation[72] developed for the determination of τ in chronopotentiometry, where the reaction rate *k* has been substituted for current via the relationship presented in Eq. E.2. Shown in Figure E.6 are the concentration versus time profiles for substrate *S* generated by Eq. E.5 (KMEC) and Equation 11 (closed-form) for six different reaction rates. It is clear from these results that the Eq. E.5 performs laudably.

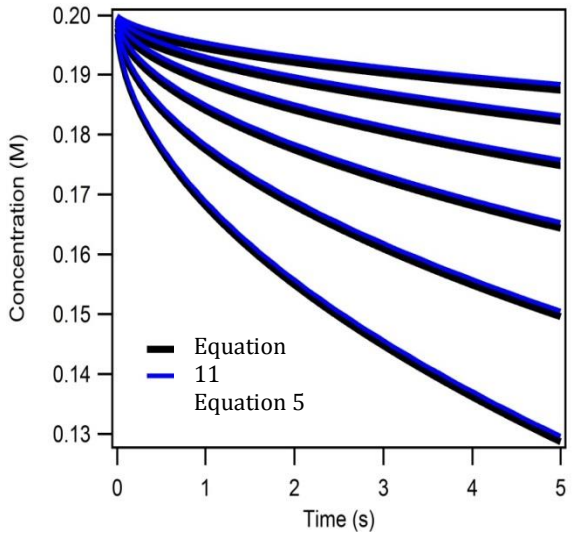

Figure E.6. Comparison of result from Eq. E.5 and Sand equation analog (E.11) for six different reaction rates. Vertical axis represents substrate concentration. From top to bottom k = 25, 50, 100, 200, 400, 800. C_P^0= 0.001 M . D_P=D_S=1e–5 cm^2/s.

ii. Complex Mechanisms

Several mechanisms were formulated to test the reliability of KMEC with regard to various phenomena that are expected to occur in catalyst systems of interest. A mechanism representing the culmination of these phenomena (presented in Scheme E.3) is then considered. Figure E.7 displays the comparison of chronoamperograms generated by KMEC method and by the digital simulation software DigiElch for mechanisms representing substrate consumption (E.7a, Section E.4), catalyst decomposition (E.7b, SI–9, Supporting Information), product inhibition (E.7c, Section E.4), and homogeneous electron transfers (E.7d, Section E.4). We can see from these datasets that KMEC is able to accurately portray the expected results for a variety of commonly encountered reaction types.

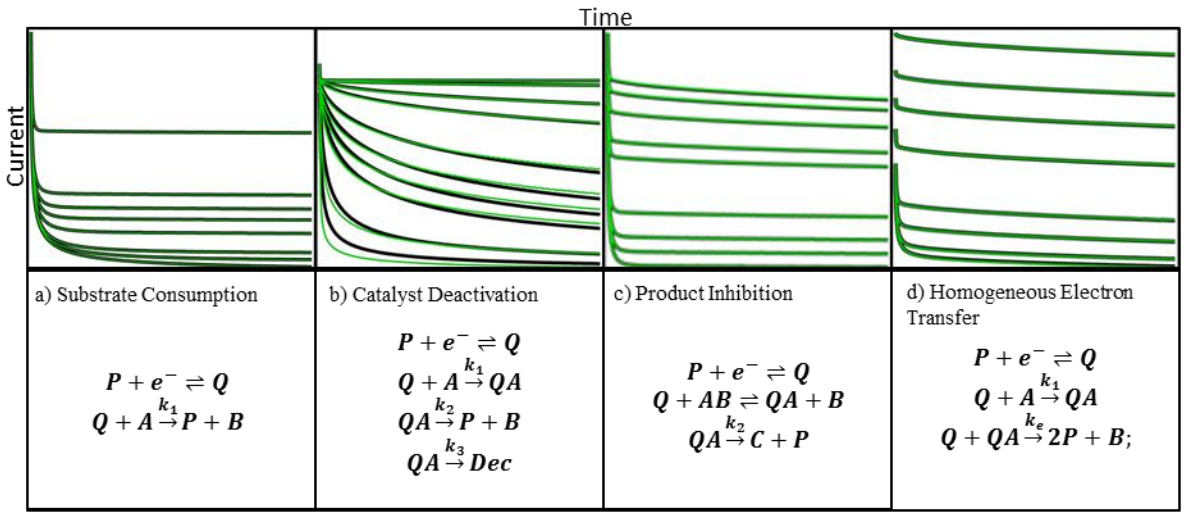

Figure E.7. Comparison of chronoamperograms generated by KMEC (green traces) to those generated by DigiElch (black traces) for four commonly encountered phenomena a) Substrate Consumption; k_1 = 50 $M^{-1}s^{-1}$, [P] = 0.001 M, [A] = 0.001 … 0.3 M (from bottom to top). B) Catalyst Deactivation; k_1 = 1e10 $M^{-1}s^{-1}$, k_2 = 75 s^{-1}, k_3 = 0.01 … 100 s^{-1} (from top to bottom) [P] = 0.001 M, [A] = 0.1 M. c) Product Inhibition; $k_1 = k_{-1}$ = 1e5 $M^{-1}s^{-1}$, k_2 = 50 s^{-1}, [P] = 0.001 M, [AB] = 0.1 M, [B] = 0 … 10 M (from top to bottom). d) Homogeneous Electron Transfer; k_1 = 1000 $M^{-1}s^{-1}$, k_e = 1e9 $M^{-1}s^{-1}$, [P] = 0.001 M, [A] = 0.001 M … 1 M (from bottom to top).

Figure E.8 displays the comparison of results from KMEC and DigiElch for four different experimental scenarios in the case of Scheme E.3. In each panel, data is simulated for a series of 'samples' between which the concentration of a single reactant is varied, as would typically be done in an experiment. In Figure E.8a, the initial concentration of catalyst concentration and *A* concentration are held constant at [P] = 0.001 M and [A] = 0.2 M with no initial *Y* or *B*, and the concentration of substrate *YZ* is varied between measurements. In Figure E.8b, the initial concentration of catalyst concentration and substrate *B* concentration are held constant at [P] = 0.001 M and [B] = 0.2 M, with no initial *Y* or *A*, and the concentration of substrate *YZ* is varied. In Figure E.8c, the catalyst and substrates *YZ* and *A* concentrations are held at [P] = 0.001 M, [YZ] = 0.1 M, and [A] = 0.2 M, with no *B* initially in solution and [Y] is varied. In

Figure E.8d, substrates *YZ*, and *A* are held constant at [YZ] = 0.1 M and [A] = 0.2 M, with no Y or B initially added to solution, and the concentration of catalyst is varied. In the face of this complex scenario, the KMEC method adequately matches the results of robust digital simulations.

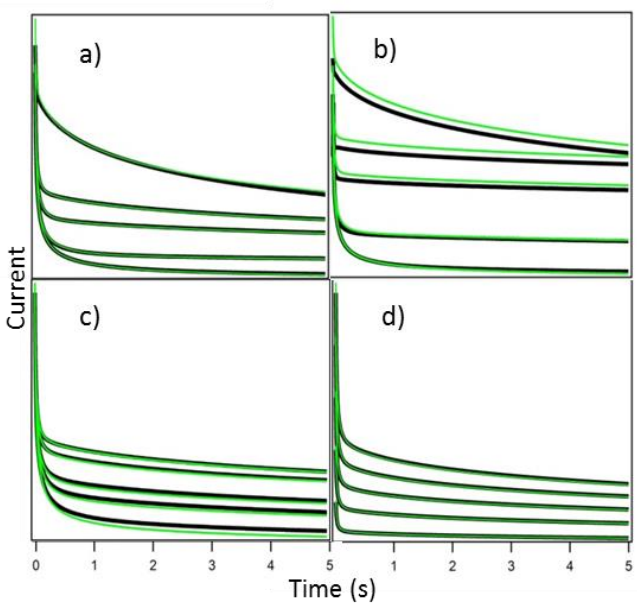

Figure E.8. Comparison of the results from the KMEC method (green traces) to those from DigiElch simulations (black traces) for the mechanism shown in Scheme E.3. Initial concentrations for a) [P] = 0.001 M, [Y] = 0 M, [A]=0.2 M, [B] = 0 M, and [YZ] = (from bottom to top) 0.001, 0.01, 0.05, 0.1, and 0.5 M. b) [P] = 0.001 M, [Y] = 0 M, [A]= 0 M, [B] = 0.2 M, and [YZ] = (from bottom to top) 0.001, 0.01, 0.05, 0.1, and 0.5 M. c) [P] = 0.001 M, [YZ] = 0.1 M, [A]=0.2 M, [B] = 0 M, and [Y] = (from top to bottom) 0.001, 0.01, 0.05, 0.1, and 0.5 M. d) [P] = (from bottom to top) 0.001, 0.002, 0.003, 0.004, 0.005 M, [YZ] = 0.1 M, [A]=0.2 M, [B] = 0 M, and [Y] = 0 M.

In order for any method to be relevant to solar fuel production, it must be able to handle multiple electron transfer processes as most catalytic processes of interest require at least two electrons. These multi-electron processes add increased complexity to electrochemical analysis. When evaluating these systems, it is important that the steady-state assumptions hold.

An example scenario of when steady state assumptions do not hold is illustrated in Section E.4. In this reaction a species QB forms irreversibly at a slow rate from intermediate QA and substrate B. This slow rate allows for the species QB to form some distance from the electrode where no reducing equivalents (Q or the electrode) are available and thus the intermediate (QB) is incapable of being turned over in the catalytic cycle. So, while a catalytic current will be witnessed, quantification in this (unexpected) scenario would prove impossible by this, or any other, steady-state method.

Solution Electron Transfers and Homolytic Reaction Pathways. As presented, the KMEC approach is suitable for reaction scenarios in which the rate-limiting step is first order in catalyst. This holds because Eq. E.1, which is used to generate the current vs. time profile, was derived for scenarios that are first order in catalyst.[26] As demonstrated, this equation remains applicable even with complex reaction pathways involving dynamic equilibria, provided the order in catalyst remains purely first order. In the case of slow solution electron transfer processes (species Q reduces a reaction intermediate) or the more likely scenario, a homolytic reaction pathway (2 equivalents of intermediate QA react to release product B and regenerate 2 equivalents of Q), Eq. E.1 and the definition of μ as defined by Eq. E.7 are no longer applicable. Fortunately, slow solution electron transfer processes are typically not limiting as facile reduction of intermediates at the electrode will take over as the dominate pathway.[44,68] However, homolytic reaction scenarios are particularly relevant to fuel-forming catalysis, especially hydrogen evolution where two metal hydride intermediates can react to release H_2.[51,169]

Eq. E.1 and Eq. E.7 are based upon a concentration profile of the active species that decays exponentially as a function of distance from the electrode (Figure E.2) and this

concentration profile is not valid for reactions that are second order in catalyst (SI-13, Appendix E.4). In order to account for a second order, rate-limiting process, Equations E.12 and E.13 were derived. Eq. E.12 incorporates the homolytic reaction analysis presented by Costentin et.al.[44] into Eq. E.1 and describes the current vs. time profile for a second order reaction. Eq. E.13 defines the reaction layer depth μ for a second order reaction (SI-14, Appendix E.4).

$$i = nFSD_P^{1/2}C_P\left\{(\frac{2}{3}k_{obs})^{1/2}\,\mathrm{erf}\left[\left(\frac{2}{3}k_{obs}t\right)^{\frac{1}{2}}\right] + \frac{\exp(-\frac{2}{3}k_{obs}t)}{(\pi t)^{1/2}}\right\} \quad (E.12)$$

$$\mu = \sqrt{\frac{2D_P}{3k_{obs}}} \quad (E.13)$$

The exchange of Eq. E.1 for Eq. E.12 and the use of the new form of μ presented in Eq E.13 are the only changes to KMEC needed to analyze a second order in catalyst reaction pathway; all other facets remain the same. Application of these equations with KMEC is demonstrated in Figure E.9 for a simple homolytic reaction scheme with a pre-equilibrium and is more thoroughly explored in the Supplemental Information (SI–15, SI–16).

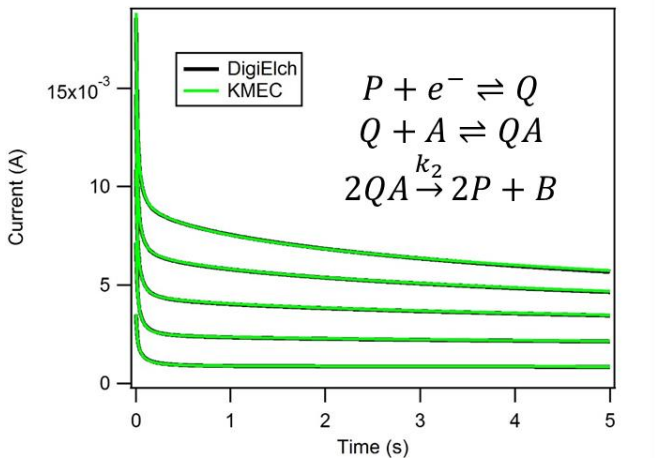

Figure E.9. Application of KMEC using Equations E.12 and E.13 to a homolytic reaction mechanism. k_1 = 1,000 $M^{-1}s^{-1}$, k_{-1} = 1,000 s^{-1}, k_2 = 1e5 $M^{-1}s^{-1}$,[A] = 0.1 M, [P] = 2 mM … 10 mM (from bottom to top)

When applying the KMEC approach, a reaction must be defined as either first order or second order in catalyst; an intermediate regime is not accessible by this analysis. In other words, if an elementary step in a catalytic cycle is second order in catalyst, whether it be a solution electron transfer process or a homolytic reaction, it must either be 1) the rate limiting step,[44] such that it can be analyzed with the second order Eq. E.12, or 2) occur sufficiently fast so as to avoid impacting the overall rate (as was the case for Scheme E.3) and the system can be analyzed with the first order Eq. E.1. Recent work to address intermediate regime has been put forth by Costentin et. al.[213]

Experimental Considerations. Perhaps the most important consideration for using chronoamperometry to study electrocatalytic cycles is the minimization of effects from double layer charging and uncompensated resistance. At short timescales, double-layer charging can contribute a non-trivial amount of current to the chronoamperogram. Reducing the contribution from double-layer charging is a matter of minimizing the potential traversed in the potential step. This is easily achieved by selecting a resting potential (potential prior to the step) that is as close to the catalytic redox event as possible without perturbing the system.

More challenging, but certainly not prohibitive, is the uncompensated resistance. First, all generic methods for the reduction of uncompensated resistance should be applied. Namely, the concentration of the supporting electrolyte should be made as high as possible and the current should be managed by using a small electrode (yet large enough to maintain semi-infinite linear diffusion) and minimizing the concentration of catalyst used in the measurements. After

minimizing the uncompensated resistance, it is important to have an approximate value of what the uncompensated resistance is; methods for its determination are available in the literature.[67] If the uncompensated resistance is known, the experimental parameters can be adjusted to account for the ohmic drop. A simple equation (Eq. E.14, SI-17, Appendix E.4) can be devised for approximating the necessary measured potential simply by calculating the required potential beyond the catalytic redox event to achieve 99% catalyst activity while accounting for the ohmic drop.

$$E_{measured} = E^0 - .118 - iR \qquad (Eq. E.14)$$

An approximate value for the current can be obtained simply by performing an exploratory cyclic voltammogram and using the highest attained current. It is important to note that the value obtained from this equation gives a minimum value for the the potential that is safe to use and it is preferred that the user extend a safe distance beyond to account for the contributions from the Cottrell current at early timescales. However, it is not expected that this contribution from the Cottrell current will significantly distort the result of the data as it only effects the earliest timepoints in the experiment prior to the establishment of an equilibrium (SI-18, Appendix E.4).

E.3. Conclusion

We have outlined the advantages of using chronoamperometric methods for the study of homogeneous electrocatalysis and have presented KMEC as a method which can be used to gain meaningful mechanistic insight. This was previously much more difficult (or impossible in the case of catalyst deactivation) without digital simulation programs. We have also presented new equations to address the current response and to define the reaction layer for homolytic reactions. KMEC can be likened to the methodology presented by Blackmond for

reaction progress kinetic analysis[214]—we have adapted a commonly practiced method of mechanistic analysis to the field of electrochemistry by approximating diffusive effects and calculating the current response through basic electrochemical relationships.

The use of Eq. E.5 and the KMEC method are not limited to the scenarios defined and have many possible adaptations, especially for water oxidation, proton reduction and CO_2 reduction catalysts. Ongoing work is focused on applying KMEC to electrocatalytic systems developed in our laboratory. We confidently assert after strenuous testing that this method gives reliable results in all cases that adequately satisfy the requirements outlined above and we believe that this technique will prove valuable in the growing field of electrode assisted catalysis.

E.4. Supporting Information

SI–1. Origin of the reaction layer depth, μ.

The reaction layer depth is defined as the distance from the electrode required to contain all of the active form (Q) of the catalyst at a uniform concentration equal to that of the species P in the bulk. It was originally defined by Brdicka and Weisner[210] and defined utilizing Eq. E.3 from the main text.

If we assume that:

$$\frac{i}{nFS} = \mu C_P^0 k$$

where μ is a correction factor representing the actual quantity of the reduced form of the catalyst, we can set this equal to Eq. E.3:

$$\frac{i}{nFS} = D_P^{1/2} C_P^0 k^{1/2}$$

and solve for μ to reveal Eq. E.7 (main text) in the units of cm:

$$\mu = \sqrt{\frac{D_P}{k_{obs}}}$$

SI–2. Cottrell Equation form found in Equation E.5 from the main text.

Boundary Conditions

$$C(x, 0) = C^0 \qquad E.A1$$

$$C(\infty, t) = C^0 \qquad E.A2$$

$$C(0,t) = C^{\mu} \qquad E.A3$$

Fick's Laws

$$\frac{\partial C(x,t)}{\partial t} = D\frac{\partial^2 C(x,t)}{\partial x^2} \qquad E.A4$$

$$-J(x,t) = D\left[\frac{\partial C(x,t)}{\partial x}\right]_{x=\mu} \qquad E.A5$$

Laplace transform of A.4

$$s\bar{C}(x,s) - C^0 = D\frac{\partial^2 \bar{C}(x,s)}{\partial x^2} \qquad E.A6$$

Manipulation through Partial Fractions[21]

$$\bar{C}(x,s) = \frac{C^0}{s} + A(s) * exp\left[-\sqrt{\frac{s}{D}}x\right] + B(s) * exp\left[\sqrt{\frac{s}{D}}x\right] \qquad E.A7$$

Boundary condition A.2 demands that B(s) =0

$$\bar{C}(x,s) = \frac{C^0}{s} + A(s) * exp\left[-\sqrt{\frac{s}{D}}x\right] \qquad E.A8$$

Laplace transform of A.5

$$-\bar{J}(x,s) = D\left[\frac{\partial \bar{C}(x,s)}{\partial x}\right]_{x=\mu} \qquad E.A9$$

Laplace transform of A.3

$$\bar{C}(0,s) = \frac{C^{\mu}}{s} \qquad E.A10$$

Substitute A.10 into A.8

$$\frac{C^{\mu}}{s} = \frac{C^0}{s} + A(s) * exp\left[-\sqrt{\frac{s}{D}}x\right] \qquad E.A11$$

Solve for A(s) with x = 0 (μ simplification)

$$A(s) = \frac{C^0 - C^{\mu}}{s} \qquad E.A12$$

Substitute A.12 into A.8, take the derivative and substitute in A.9

$$-\bar{J}(\mu,s) = \frac{C^0 - C^{\mu}}{\sqrt{Ds}} \qquad E.A13$$

Inverse Laplace Transform of A.13

$$-J(\mu,t) = \frac{D^{\frac{1}{2}}(C^0 - C^{\mu})}{\sqrt{\pi t}} \qquad E.A14$$

SI–3. Origin of correction factor on homogeneous reaction expression.

The correction factor $1 - e^{-1}$ represents the quantity of "active" catalyst that is contained within the defined reaction layer. This value was solved from the concentration equation presented by Delahay and Stiehl[26] by integrating from the electrode surface to μ as is shown below.

$$[Q]_x = [P]_\infty - [P]_\infty \left\{ 1 - \frac{1}{2}\exp\left[-x\left(\frac{k}{D}\right)^{\frac{1}{2}}\right] * erfc\left[\frac{x}{2(Dt)^{\frac{1}{2}}} - (kt)^{\frac{1}{2}}\right] - \frac{1}{2}\exp\left[-x\left(\frac{k}{D}\right)^{\frac{1}{2}}\right] * erfc\left[\frac{x}{2(Dt)^{\frac{1}{2}}} + (kt)^{\frac{1}{2}}\right] \right\}$$

as $t \to \infty$

$$erfc\left[\frac{x}{2(Dt)^{\frac{1}{2}}} - (kt)^{\frac{1}{2}}\right] = 2$$

$$erfc\left[\frac{x}{2(Dt)^{\frac{1}{2}}} + (kt)^{\frac{1}{2}}\right] = 0$$

therefore

$$[Q]_x = [P]_\infty - [P]_\infty \left\{ 1 - \exp\left[-x\left(\frac{k}{D}\right)^{\frac{1}{2}}\right] \right\}$$

$$\left(\frac{k}{D}\right)^{\frac{1}{2}} = \mu^{-1}$$

integrating for [Q] from 0 to μ gives

$$= \int_0^\mu [P]_\infty - [P]_\infty \{1 - \exp[-x\mu^{-1}]\}$$

$$= \langle [P]_\infty x - [P]_\infty x - \mu[P]_\infty \exp[-x\mu^{-1}] \rangle_0^\mu$$

$$= -\mu[P]_\infty e^{-1} + \mu[P]_\infty$$

$$= (1 - e^{-1})\mu[P]_\infty$$

SI–4. Comparison of result from Equation E.5 with and without $1 - e^{-1}$

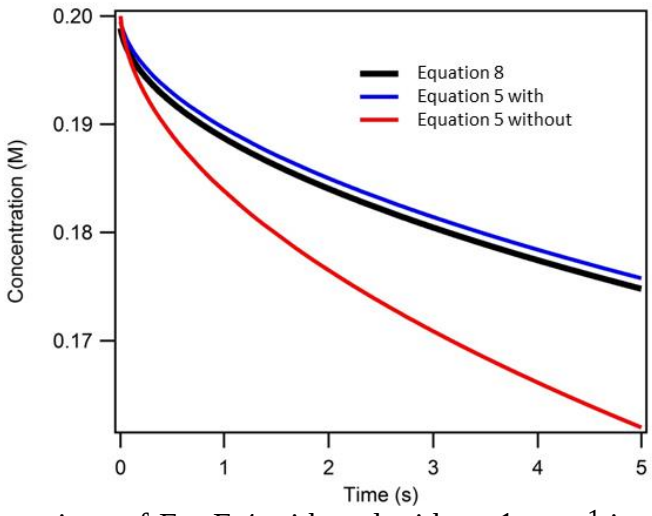

Figure E.S1. Comparison of Eq. E.4 with and without $1 - e^{-1}$ in the homogenous reaction expression to the result from Eq. E.7 with k = 100, D_P=D_S=1e-5, and C_P=0.001. It can be seen

here, as in Figure E.5, that the result of Eq. E.4 is slightly larger across the entire timeframe than the result from Eq. E.7. This is because Eq. E7 was solved for the concentration at the surface of the electrode and Equation E.4 represents the average concentration across the reaction layer. In fact, the difference between the result of Equations E.7 and E.4 is dependent upon the defined size of the reaction layer in Eq. E.4. If the reaction layer is made larger (say 2*μ instead), the difference will be larger, and vice versa.

SI–5. Generation of Differential Equations for Scheme E.3.

Scheme 3

$$P + e^- \rightleftharpoons Q$$
$$Q + YZ \rightarrow DEC + Y; \qquad k_{11}$$

$A \rightarrow B$			$B \rightarrow C$
$Q + A \rightleftharpoons INT1$	k_1, k_2	k_3, k_4	$Q + B \rightleftharpoons INT5$
$INT1 + YZ \rightleftharpoons INT2 + Y$	k_5, k_6	k_8	$INT5 + YZ \rightarrow INT6 + Y$
$INT2 \rightarrow INT3$	k_7	k_e	$INT6 + Q \rightarrow INT7 + P$
$INT3 + Q \rightarrow INT4 + P$	k_e	k_{10}	$INT7 + YZ \rightarrow P + Y + C$
$INT4 + YZ \rightarrow P + Y + B$	k_9		

$k_1(M^{-1}s^{-1})$	$k_2(s^{-1})$	$k_3(M^{-1}s^{-1})$	$k_4(s^{-1})$	$k_5(M^{-1}s^{-1})$	$k_6(M^{-1}s^{-1})$
900	1800	200	20	400	8000
$k_7(M^{-1}s^{-1})$	$k_8(M^{-1}s^{-1})$	$k_9(M^{-1}s^{-1})$	$k_{10}(M^{-1}s^{-1})$	$k_{11}(M^{-1}s^{-1})$	
250	250	1000	1200	5	

$$\frac{d[Q]}{dt} = -k_1[Q][A] + k_2[INT1] - k_3[Q][B] + k_4[INT5] + k_9[INT4][YZ] + k_{10}[INT7][YZ] - k_{11}[Q][YZ]$$

Note: As mentioned in the paper, P and Q are treated as the same species when making our differential equations such that any generation of P is considered to be directly converted to Q. This is because it is a diffusive process (i.e. P must travel to the electrode to become Q) and this conversion is handled by Eq. E.1. The final rate that we determine is meant to supply information on how fast the catalytic process is able to regenerate P after the creation of Q at the electrode surface.

$$\frac{d[INT1]}{dt} = k_1[Q][A] - k_2[INT1] - k_5[INT1][YZ] + k_6[INT2][Y]$$

$$\frac{d[INT5]}{dt} = k_3[Q][B] - k_4[INT5] - k_8[INT5][YZ]$$

$$\frac{d[INT2]}{dt} = k_5[INT1][YZ] - k_6[INT2][Y] - k_7[INT2]$$

$$\frac{d[INT4]}{dt} = k_7[INT2] - k_9[INT4][YZ]$$

$$\frac{d[INT7]}{dt} = k_8[INT5][YZ] - k_{10}[INT7][YZ]$$

$$\frac{d[YZ]}{dt} = k_6[INT2][Y] - k_5[INT1][YZ] - k_8[INT5][YZ] - k_9[INT4][YZ] - k_{10}[INT7][YZ] - k_{11}[Q][YZ]$$

$$\frac{d[Y]}{dt} = -k_6[INT2][Y] + k_5[INT1][YZ] + k_8[INT5][YZ] + k_9[INT4][YZ] + k_{10}[INT7][YZ] + k_{11}[Q][YZ]$$

$$\frac{d[A]}{dt} = -k_1[Q][A] + k_2[INT1]$$

$$\frac{d[B]}{dt} = -k_3[Q][B] + k_4[INT5] + k_9[INT4][YZ]$$

$$\frac{d[C]}{dt} = k_{10}[INT7][YZ]$$

$$\frac{d[DEC]}{dt} = k_{11}[Q][YZ]$$

The above equations represent the entirety of the mechanism outlined in Scheme E.3. The differential equations shown in black are those found in the main text and represent the necessary ones for use in KMEC (These are shown in the Matlab script *Equilibrate.m* below). The equations in red represent those that would prevent the evaluation of these equations from reaching equilibrium and they also represent the species whose concentration in the reaction layer has a diffusional dependence that must be accounted for by Eq. E.5. The equations in blue represent the species whose formation dictates the consumption of other molecules. For example, the formation of one *B* results in the loss of two *YZ*, and one *A*, and the formation of two *Y* and two *P*.

Evaluation of the equations in black results in the equilibrium concentrations of each intermediate as is shown below in Figure E.S2. This equilibrium must be calculated for every time point in the reaction with the new initial conditions.

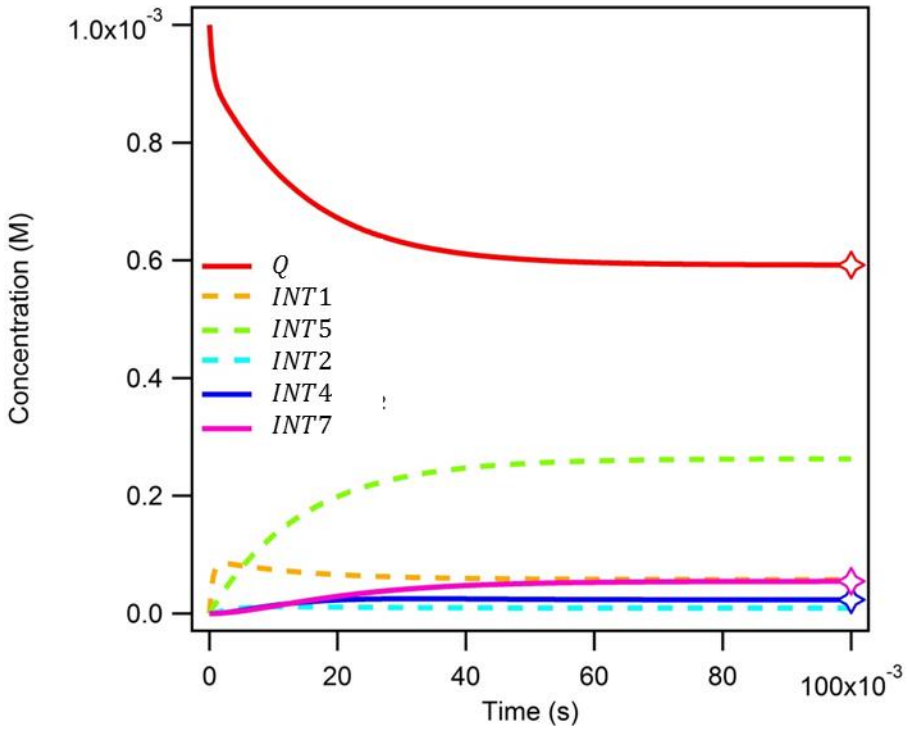

Figure E.S2. Evaluation of the differential equations shown above in black with the initial conditions [P] =0.001 M, [YZ] = 0.1 M, [Y] = 0 M, [A] = 0.2 M, and [B] = 0.1 M, allows one to obtain the steady state equilibrium concentrations of the intermediates. The species shown as solid lines are the ones that are then used to calculate the rate constants (See blue equations above).

Using the starred points shown in Figure E.2S, the rate constants ($k_B, k_C, k_{DEC}, k_Y, k_P$, Equations E.8.A-E) can then be determined and the subsequent change in concentration of each of the bulk species can be evaluated.

SI–6. Structuring the calculation in Matlab.

For our calculations we use three primary functions (KMECexecute.m, which calls upon KMEC.m and CreateCurrent.m) plus one optional function (equilibrate.m) representing the equilibrium calculation (as stated in the main text, if the rates are solved for by steady state approximations, this function is not needed). The calculations shown below are for the example presented in Scheme E.3, but can be adapted for any proposed mechanism. The first function, KMECexecute, is simply to initiate the calculation and then convert the appropriate information into the expected current response:

(The files below were copied directly from their *.m source and can be copied directly back into MATLAB. The example values given in the annotation can be used to recreate the plot in Figure E.4.)

KMECexecute.m

KMECexecute.m first evaluates the function “KMEC” using the ode45 solver implemented in MATLAB to produce the expected chronoamperogram.

```
function [ current ] = KMECexecute( time, k,D, iC, Earea)
%KMECexecute generates expected chronoamperogram for given conditions
%       inputs as vectors
%   time = timepoints for experiment in seconds (e.g. .01:.01:5 provides a
%           time vector 0.01-5 s with 0.01 s intervals).
%   k = rate constants for mechanism, listed in order k1-k11
%       (e.g. [900;1800;200;20;400;8000;250;250;1000;1200;5])
%   D = diffusion coefficients (in cm^2/s) of species being evaluated
%       (e.g. [1e-5;1e-5;1e-5;1e-5;1e-5])
%   iC = initial Concentrations of bulk species [P;YZ;Y;A;B]
%       (e.g. [.001;.1;0;.23;0])
%   Earea = electrode area in cm^2 (e.g. 0.1)

%KMECexecute calls upon function KMEC to Obtain time-dependent
concentrations %and rate information. The last column of data in
%'Conc' represents kp to be used for generating current, but in its
%integral form (i.e. it must be divided by time, this calculation can
%be seen in the function "CreateCurrent"). The first 5 columns represent
the %concentrations over time starting with the values from 'iC'.
[~,Conc] = ode45(@(t,Conc)KMEC(t,Conc,k,D,iC),time,...
[iC(1);iC(2);iC(3);iC(4);iC(5);0]);
%CreateCurrent converts concentration and rate data (from 'Conc')  and
%initial inputs time, %diffusion coefficients and electrode area into
%expected current response
[current]= CreateCurrent(time, Conc, D(1), Earea);
end
```

KMEC.m

KMEC.m defines the KMEC equations

```
function [ dConc ] = KMEC(t,Conc,k,D,iC)
%KMEC for use with ode solver to generate Concentration vs. time data
% inputs
%   t = timepoint array: for use by ode
%   Conc = Concentration and observed rate array for use by ode
%       [P;YZ;Y;A;B]
%   k  = array of rate constants
%   D  = array of Diffusion coefficients
%       [P;YZ;Y;A;B]
%   iC = array of initial concentrations
%       [P;YZ;Y;A;B]

%c0 = initial conditions vector for evaluating the equilibrium
concentrations %of the intermediates
%c0 = [Q;INT1;INT5;INT2;INT4;INT7]
c0 = [Conc(1);0;0;0;0;0];
%Species to be held constant in equilibrium calculation
%Fixed = [YZ;Y;A;B]
```

```
Fixed = [Conc(2);Conc(3);Conc(4);Conc(5)];
%Calculates equilibrium concentrations, calculation extends to 1s to
ensure equilibration. (ode23s was used for expediency)
[~, EqConc]=ode23s(@(t,EqConc)equilibrate(t,EqConc,k,Fixed),.01:.03:1,c0);
%Calculates turnover rate for each product and the Rate Constant
%using the last timpoint in EqConc.
%
%generation of B
kb = (k(9)*EqConc(length(EqConc),5)*Conc(2))/Conc(1);
%generation of C
kc = (k(10)*EqConc(length(EqConc),6)*Conc(2))/Conc(1);
%generation of DEC
kdec = (k(11)*EqConc(length(EqConc),1)*Conc(2))/Conc(1);
%generation of Y
ky = 2*(kb+kc)+kdec;

%total turnover rate
kp = 2*(kb+kc);
%KMEC equations shown in paper (.632 = 1-e^-1)
%Catalyst
dConc(1) = (D(1).^.5*(iC(1)-Conc(1)))/(pi.^.5*sqrt(D(1)/kp)*(t).^.5)...
-(.632)*Conc(1)*kdec;
%YZ
dConc(2) = (D(2).^.5*(iC(2)-Conc(2)))/(pi.^.5*sqrt(D(1)/kp)*(t).^.5)...
-(.632)*Conc(1)*ky;
%Y
dConc(3) = (D(3).^.5*(iC(3)-Conc(3)))/(pi.^.5*sqrt(D(1)/kp)*(t).^.5)...
+(.632)*Conc(1)*ky;
%A
dConc(4) = (D(4).^.5*(iC(4)-Conc(4)))/(pi.^.5*sqrt(D(1)/kp)*(t).^.5)...
-(.632)*Conc(1)*kb;
%B
dConc(5) = (D(5).^.5*(iC(5)-Conc(5)))/(pi.^.5*sqrt(D(1)/kp)*(t).^.5)...
+(.632)*Conc(1)*kb-(.632)*Conc(1)*kc;
%retains kobs for use when evaluating for current
dConc(6) = kp;

dConc = dConc(:);
end
```

Equilibrate.m

This function is used by KMEC to calculate the equilibrium values

```
function [ dEqConc ] = equilibrate( t, EqConc, k, Fixed )
%equilibrate used by ode solver to find equilibrium values
%    inputs
%   t = timepoint array: to be used by ode
%   EqConc = Concentration Array: to be used by ode
%       [Q;INT1;INT5;INT2;INT4;INT7]
%   k = rate constants
```

```
%       [900;1800;200;20;400;8000;250;250;1000;1200;5]
%   Fixed = fixed concentrations
%       [YZ;Y;A;B]

%d[P]/dt =
dEqConc(1) = -k(1)*EqConc(1)*Fixed(3)+k(2)*EqConc(2)-k(3)*EqConc(1)...
*Fixed(4)+k(4)*EqConc(3)+k(9)*EqConc(5)*Fixed(1)+k(10)*EqConc(6)*Fixed(1);
%d[INT1]/dt =
dEqConc(2) = k(1)*EqConc(1)*Fixed(3)-k(2)*EqConc(2)-...
k(5)*EqConc(2)*Fixed(1)+k(6)*EqConc(4)*Fixed(2);
%d[INT5]/dt =
dEqConc(3) = k(3)*EqConc(1)*Fixed(4)-k(4)*EqConc(3)-
k(8)*EqConc(3)*Fixed(1);
%d[INT2]/dt =
dEqConc(4) = k(5)*EqConc(2)*Fixed(1)-k(6)*EqConc(4)*Fixed(2)-
k(7)*EqConc(4);
%d[INT4]/dt =
dEqConc(5) = k(7)*EqConc(4)-k(9)*EqConc(5)*Fixed(1);
%d[INT7]/dt =
dEqConc(6) = k(8)*EqConc(3)*Fixed(1)-k(10)*EqConc(6)*Fixed(1);

dEqConc = dEqConc(:);
end
```

CreateCurrent.m

After the Concentrations and observed rate have been calculated, “CreateCurrent” is called to generate the expected current response.

```
function [ current] = CreateCurrent(time, Conc, D, Earea)
%CreateCurrent Converts vectors of time, catalyst concentration and
%observed rate constant into current.
%
%   input
%   Conc= matrix containing concentration and rate over time, the first
%   column should be catalyst concentration and the last column should be
the
%   observed rate constant.
%   D = catalyst diffusion coefficient
%
%Generates empty array
current = zeros(length(time),1);
%determines size of matrix to identify column containing the observed rate
a = size(Conc);
%loop iteratively determines concentration
for i = 1:length(Conc);
%divides differential rate by time to obtain actual rate. The last
```

```
%datapoint and the next to last datapoint have the same rate by neccessity
if i == length(Conc)
    kobs = (Conc(i,a(2))-Conc(i-1,a(2)))/(time(i)-time(i-1));
else
    kobs = (Conc(i+1,a(2))-Conc(i,a(2)))/(time(i+1)-time(i));
end
%calculates current using equation 1 from paper
current(i,1)=1*96.485*Earea*(D)^(.5)*Conc(i,1)*(kobs^(.5)...
*erf((kobs*time(i))^(.5))+(exp(-kobs*time(i))/((pi*time(i))^(.5))));
end
end
```

As noted above, if the functions presented are executed using the example values given in the "KMECexecute" annotation, the time and current datasets can be plotted to obtain figure E.4 from the main text.

SI–7. Equation E.8 from Fick's Laws

Boundary Conditions & assumptions

$$C_S(x,0) = C_S^0 \qquad E.B1$$

$$C_S(\infty,t) = C_S^0 \qquad E.B2$$

$$i = nFAC_P^{\mu}\sqrt{D_P k_{obs}} \qquad E.B3$$

Fick's Laws

$$\frac{\partial C(x,t)}{\partial t} = D\frac{\partial^2 C(x,t)}{\partial x^2} \qquad E.B4$$

$$-J(x,t) = \frac{i}{nFA} = C_P^{\mu}\sqrt{D_P k_{obs}} = D\left[\frac{\partial C(x,t)}{\partial x}\right]_{x=\mu} \qquad E.B5$$

Laplace transform of B.4

$$s\bar{C}(x,s) - C^0 = D\frac{\partial^2 \bar{C}(x,s)}{\partial x^2} \qquad E.B6$$

Manipulation through Partial Fractions[21]

$$\bar{C}(x,s) = \frac{C^0}{s} + A(s) * exp\left[-\sqrt{\frac{s}{D}}x\right] + B(s) * exp\left[\sqrt{\frac{s}{D}}x\right] \qquad E.B7$$

Boundary condition B.2 demands that B(s) =0

$$\bar{C}(x,s) = \frac{C^0}{s} + A(s) * exp\left[-\sqrt{\frac{s}{D}}x\right] \qquad E.B8$$

Laplace Transform of B.5

$$C_P^{\mu}\sqrt{D_P\bar{k}_{obs}(s)} = D\left[\frac{\partial \bar{C}_S(x,s)}{\partial x}\right]_{x=\mu} \qquad E.B9$$

Taking the derivative of B.8 and substituting in B.9 to solve for A(s) reveals

$$\bar{C}_S(x,s) = \frac{C_S^0}{s} + \left[\frac{C_P^{\mu}\sqrt{D_P\bar{k}_{obs}(s)}}{D_S^{1/2}s^{1/2}}\right] * exp\left[-\sqrt{\frac{s}{D}}x\right] \qquad E.B10$$

If k_{obs} is held constant $\bar{k}_{obs}(s) = \frac{k_{obs}}{s}$

$$\bar{C}_S(x,s) = \frac{C_S^0}{s} + \left[\frac{C_P^{\mu}\sqrt{D_P k_{obs}}}{D_S^{1/2}s^{3/2}}\right] * exp\left[-\sqrt{\frac{s}{D}}x\right] \qquad E.B11$$

The inverse transform of B.11 Yields

$$C_S(x,t) = C_S^0 - \frac{C_P^{\mu}\sqrt{D_P k_{obs}}}{D_S}\left\{2\sqrt{\frac{D_S t}{\pi}} * exp\left(-\frac{x^2}{4D_S t}\right) - x * erfc\left(\frac{x}{2\sqrt{D_S t}}\right)\right\} \qquad E.B12$$

Solving for x = 0 gives

$$C_S(0,t) = C_S^0 - \frac{2C_P^{\mu}\sqrt{D_P k_{obs}}t^{\frac{1}{2}}}{\sqrt{D_S\pi}} \qquad E.B13$$

For comparison, the Sand Equation is Shown as E.B14.

$$C(0,t) = C^0 - \frac{2it^{\frac{1}{2}}}{nFA\sqrt{D_S\pi}} \qquad E.B14$$

SI–8. DigiElch vs. KMEC: Substrate Consumption

Mechanism Used:

$P + e^- \rightleftharpoons Q$

$Q + A \rightarrow P + B; \qquad k_1 = 50\ M^{-1}s^{-1}$

KMEC equation Used:

$$\frac{d[A]^{\mu}}{dt} = \frac{D_A^{1/2}([A]^0 - [A]^{\mu})}{\mu(\pi t)^{1/2}} - (1 - e^{-1})[P_T]^{\mu} * k_1[A]^{\mu}$$

k_{obs} for Eq. E.1:

$k_{obs} = k_1[A]^{\mu}$

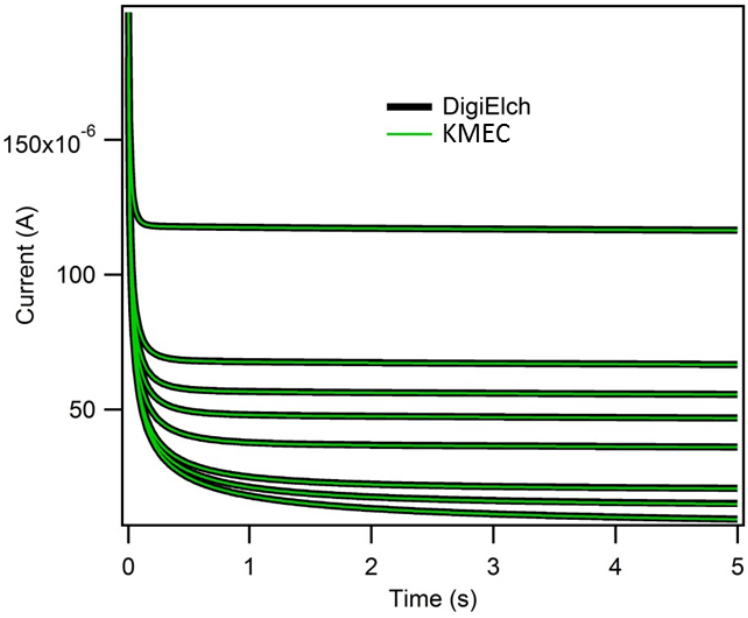

Figure E.S3. Comparison of DigiElch to KMEC in the case of substrate consumption. [P] = 0.001 M, [A] = (from bottom to top) 0.001, 0.05, 0.01, 0.03, 0.05, 0.07, 0.1, and 0.3 M.

SI–9. DigiElch vs. KMEC: Catalyst Decomposition

Mechanism Used:

$P + e^- \rightleftharpoons Q$

$Q + A \rightarrow QA; \quad k_1 = 1e10\ M^{-1}s^{-1}$

$QA \rightarrow P + B; \quad k_2 = 75\ s^{-1}$

$QA \rightarrow Dec; \quad k_3 = varied$

KMEC equation used:

$$\frac{d[P_T]^\mu}{dt} = \frac{D_P^{1/2}([P_T]^0 - [P_T]^\mu)}{\mu(\pi t)^{1/2}} - (1 - e^{-1})[P_T]^\mu * k_3$$

Note: Substrate equation not needed because turnover rate has neglible dependence on substrate concentration. This was forced on the system by making k_1 10^8 greater than k_2, which when including the concentration of species A results in rate ~10^7 greater than k_2 throughout the entire experiment.

k_{obs} for Eq. E.1:

$k_{obs} = k_2$

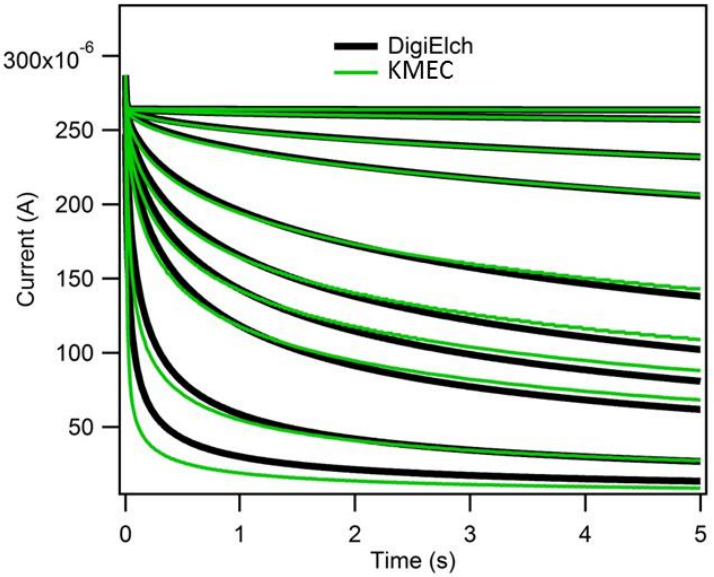

Figure E.S4. Comparison of DigiElch to KMEC for catalyst Decomposition. [P] = 0.001 M, [A] = 0.1 M, k_3 = (from top to bottom) 0.01, 0.1, 0.5, 1, 3, 5, 7, 10, 30, 100 s^{-1}.

SI–10. DigiElch vs. KMEC: Product Inhibition

Mechanism Used:

$P + e^- \rightleftharpoons Q$

$Q + AB \rightleftharpoons QA + B; \quad K = 1, k_1 = 1e5\ M^{-1}s^{-1},$

$QA \rightarrow C + P; \quad k_3 = 50\ s^{-1}$

KMEC equations used:

$$\frac{d[AB]^{\mu}}{dt} = \frac{D_{AB}^{1/2}([AB]^{0} - [AB]^{\mu})}{\mu(\pi t)^{1/2}} - (1 - e^{-1})[P_T]^{\mu} * k_3[QA]/[P_T]^{\mu}$$

$$\frac{d[B]^{\mu}}{dt} = \frac{D_{B}^{1/2}([B]^{0} - [B]^{\mu})}{\mu(\pi t)^{1/2}} + (1 - e^{-1})[P_T]^{\mu} * k_3[QA]/[P_T]^{\mu}$$

Note 1: We can simplify the homogeneous reaction expression to cancel $[P_T]^{\mu}$ here. This is also true for the equations shown in the main text, however, perhaps less evident. The importance of including this division by $[P_T]^{\mu}$ is described in the main text.[26]

Note 2: In order to obtain the value for [QA], an equilibration function similar to the one discussed for Scheme E.3 was used. The differential equations used for this function were:

$$\frac{d[Q]}{dt} = \frac{d[AB]}{dt} = -k_1[Q][AB] + k_2[QA][B] + k_3[QA]$$

$$\frac{d[QA]}{dt} = \frac{d[B]}{dt} = k_1[Q][AB] - k_2[QA][B] - k_3[QA]$$

k_{obs} for Eq. E.1:

$$k_{obs} = k_3[QA]/[P_T]^{\mu}$$

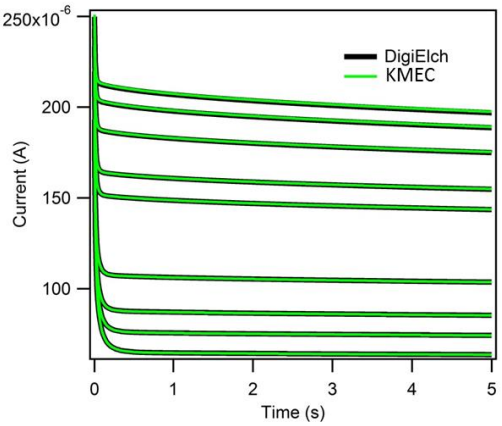

Figure E.S5. Comparison of DigiElch to KMEC for product inhibition. [P] = 0.001 M, [AB] = 0.1 M [B] = (from top to bottom) 0, 0.01, 0.03, 0.07, 1, 3, 5, 7, and 10

SI–11. DigiElch vs. KMEC: homogeneous electron transfer

Mechanism Used:

$$P + e^{-} \rightleftharpoons Q$$

$$Q + A \rightarrow QA; \quad k_1 = 1000 M^{-1}s^{-1}$$

$$Q + QA \rightarrow 2P + B; \quad k_e = 1e9\ M^{-1}s^{-1}$$

KMEC equation used:

$$\frac{d[A]^{\mu}}{dt} = \frac{D_{A}^{1/2}([A]^{0} - [A]^{\mu})}{\mu(\pi t)^{1/2}} - (1 - e^{-1})[P_T]^{\mu} * k_1[A]^{\mu}$$

k_{obs} for Eq. E.1:

$$k_{obs} = 2 * k_1[A]^{\mu}$$

Note: Because the electron transfer rate k_e is set to occur sufficiently fast such that it contributes negligibly to the observed rate, k_{obs} can be written as $2 * k_1[A]^{\mu}$ as two of species P are subsequently produced from every formation of QA.

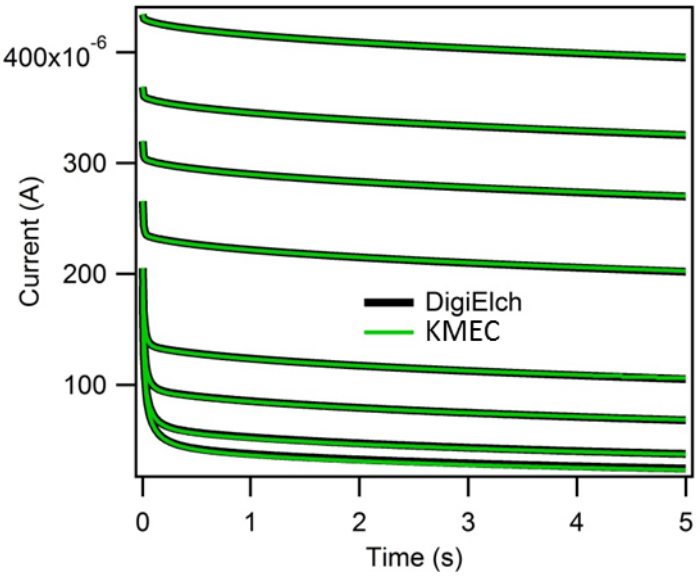

Figure E.S6. Comparison of DigiElch to KMEC for homogeneous electron transfers. [P]=0.001 M, [A]= (from bottom to top) 0.001, 0.002, 0.005, 0.01, 0.03, 0.05, 0.07, and 0.1 M.

SI–12. KMEC fails when the steady state requirements fail.

Mechanism Used:

$P + e^- \rightleftharpoons Q$

$Q + A \rightarrow QA; \quad k_1 = 1000 M^{-1}s^{-1}$

$QA + B \rightarrow QB; \quad k_2 = 1000 M^{-1}s^{-1}$

$Q + QB \rightarrow 2P + C; \quad k_e = 1e10\ M^{-1}s^{-1}$

KMEC equations used:

$$\frac{d[A]^{\mu}}{dt} = \frac{D_A^{1/2}([A]^0 - [A]^{\mu})}{\mu(\pi t)^{1/2}} - (1 - e^{-1})[P_T]^{\mu} * k_2[QA][B]/[P_T]^{\mu}$$

$$\frac{d[B]^{\mu}}{dt} = \frac{D_B^{1/2}([B]^0 - [B]^{\mu})}{\mu(\pi t)^{1/2}} + (1 - e^{-1})[P_T]^{\mu} * k_2[QA][B]/[P_T]^{\mu}$$

Note 1: We can simplify the homogeneous reaction expression to cancel $[P_T]^{\mu}$ here. This is also true for the equations shown in the main text, however, perhaps less evident. The importance of including this division by $[P_T]^{\mu}$ is described in the main text.[26]

Note 2: In order to obtain the value for [QA], an equilibration function similar to the one discussed for Scheme E.3 was used. The differential equations used for this function are

shown below. Because the formation of QB immediately forms P which we consider to immediately become Q, the two reactions represented by k_1 and k_2 can be treated very similar to an equilibrium (i.e. reaction of Q and A makes QA and reaction of QA and B makes Q).

$$\frac{d[Q]}{dt} = -k_1[Q][A] + k_2[QA][B]$$

$$\frac{d[QA]}{dt} = k_1[Q][A] - k_2[QA][B]$$

k_{obs} for Eq. E.1:

$$k_{obs} = k_2[QA][B]/[P_T]^{\mu}$$

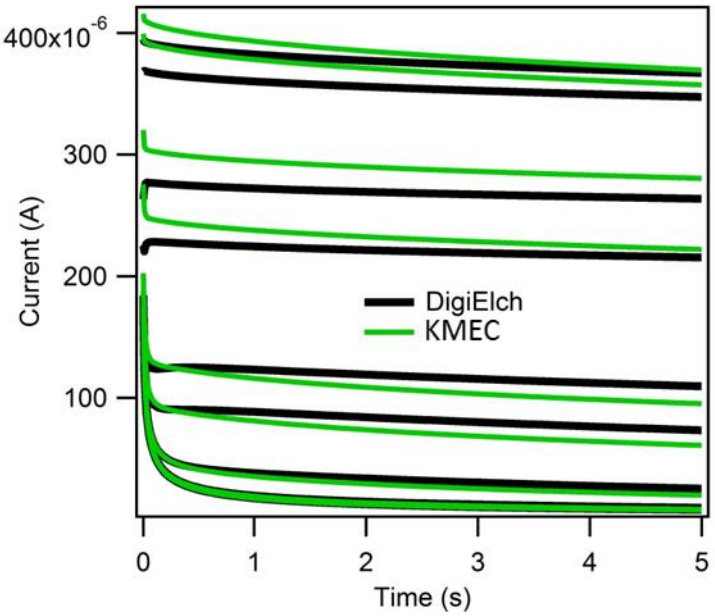

Figure E.S7. This figure demonstrates the result of KMEC against DigiElch in a scenario which steady state approximations cannot adequately describe. In the presented mechanism, QB is able to form far enough away from the electrode surface such that no Q is present to reduce it and thus QB will simply diffuse into solution without turning over. [P]=0.001 M, [A] =0.1 M, [B] = (from bottom to top) 1e-5, 1e-4, 1e-3, 5e-3, 0.01, 0.05, 0.1, 0.5, and 1 M.

SI-13. Concentration Profiles of Active species near the electrode surface for First Order and Second Order Processes.

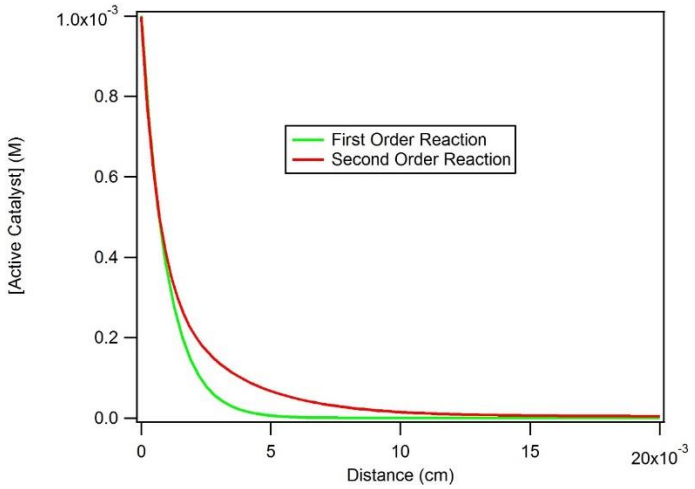

Figure E.S8. This figure shows the concentration of active catalyst vs. the distance from the electrode surface for a first order and second order reaction. The second order profile is lengthened as the reaction slows with decreasing concentration. This lengthened profile also results in results in the reaction taking longer to reach steady state (manifested in Eq. E.12 from the main text as the 2/3 within the error function and the exponential).

SI-14. μ for Second Order Reaction.

Solved just as in SI-1

$$\frac{i}{nFS} = \mu C_P^0 k$$

$$\frac{i}{nFS} = \sqrt{\frac{2}{3}} D_P^{1/2} C_P^0 k^{1/2}$$

Set equal and solve for μ

$$\mu = \sqrt{\frac{2D_P}{3k_{obs}}}$$

SI-15. Comparison of result from Equation E.1 and Equation E.12 for a Homolytic system

Mechanism Used:

$P + e^- \rightleftharpoons Q$

$Q + A \rightarrow QA; \quad k_1 = 1e10 M^{-1}s^{-1}$

$QA + QA \rightarrow 2P + B; \quad k_2 = 1e5\ M^{-1}s^{-1}$

KMEC equation used:

$$\frac{d[A]^{\mu}}{dt} = \frac{D_A^{1/2}([A]^0 - [A]^{\mu})}{\mu(\pi t)^{1/2}} - 2 * (1 - e^{-1})[P_T]^{\mu} * \frac{k_2[QA]^{\mu}[QA]^{\mu}}{[P_T]^{\mu}}$$

Equilibrium Equations used:

$$\frac{d[Q]}{dt} = -k_1[Q][A] + k_2[QA][QA]$$

$$\frac{d[QA]}{dt} = k_1[Q][A] - k_2[QA][QA]$$

k_{obs} for Equations E.1 and E.12:

$$k_{obs} = 2 * \frac{k_2[QA]^{\mu}[QA]^{\mu}}{[P_T]^{\mu}}$$

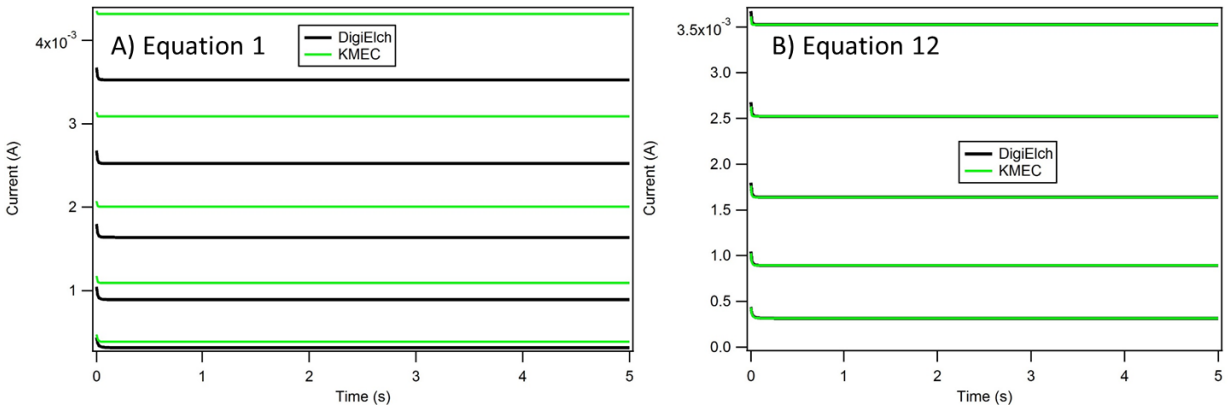

Figure E.S9. Comparison of DigiElch to KMEC with using Eq. E.1 (A) and Eq. E.12 (B) for the Homolytic mechanism outlined above. [A] = 1 M, [P] = 0.2 mM, 0.4 mM, 0.6 mM, 0.8 mM, and 1 mM (From bottom to top).

SI-16. Using Second Order equations for Rate Limiting Solution Electron Transfer.

Mechanism Used:

$P + e^- \rightleftharpoons Q$

$Q + A \rightleftharpoons QA; \quad k_1 = 1e10 M^{-1}s^{-1}, \; k_2 = \; varied$

$QA + Q \rightarrow 2P + B; \quad k_3 = 1e5 \; M^{-1}s^{-1}$

KMEC equation used:

$$\frac{d[A]^{\mu}}{dt} = \frac{D_A^{1/2}([A]^0 - [A]^{\mu})}{\mu(\pi t)^{1/2}} - 2 * (1 - e^{-1})[P_T]^{\mu} * \frac{k_2[QA]^{\mu}[Q]^{\mu}}{[P_T]^{\mu}}$$

k_{obs} for Eq. E.12:

$$k_{obs} = 2 * \frac{k_2[QA]^{\mu}[Q]^{\mu}}{[P_T]^{\mu}}$$

Equilibrium Equations used:

$$\frac{d[Q]}{dt} = \; -k_1[Q][A] + k_2[QA] + k_3[QA][Q]$$

$$\frac{d[QA]}{dt} = \; k_1[Q][A] - k_2[QA] - k_3[QA][Q]$$

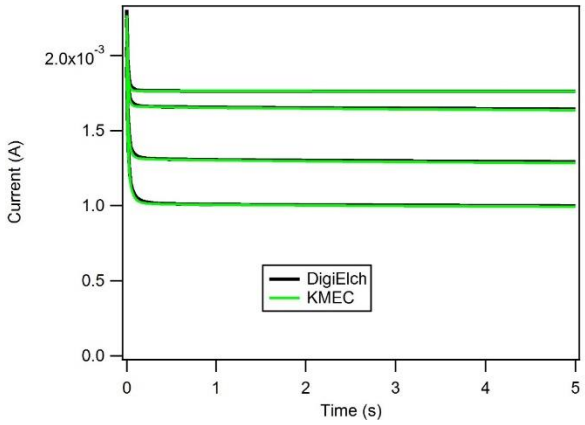

Figure E.S10. Comparison of DigiElch to KMEC using Eq. E.12 for current response demonstrating its accuracy even when two different forms of the catalyst with differing concentrations are reacting together. [A] = 0.1 M, [P] = 1 mM and k_2 = 1e10, 5e9, 2e9, and 1e9 s^{-1} (From bottom to top).

SI–17. Minimum required measured potential after factoring in uncompensated resistance.

Set minimum requirement for use of KMEC as 99% catalyst activity

$$.99 = \; \frac{1}{1 + \exp(\frac{R}{RT}\left(E_{applied} - E^0\right))}$$

$E_{measured} = E_{applied} - iR$

Substituting for $E_{applied}$

$$.99 = \frac{1}{1 + \exp(\frac{R}{RT}(E_{measured} + iR - E^0))}$$

Solving for $E_{measured}$

$E_{Measured} = E^0 - .118 - iR$

With this Equation and a reasonable catalytic current of 100 μA and a resistance of 50 Ω, the experimenter would need an additional measured potential of only 5 mV beyond the theoretical 118 mV past E^0 necessary for 99% activity.

SI–18. Cottrell contribution to current.

It is important to understand the timeframe over which the Cottrell current will have a significant contribution as its effect on the measured current and therefore the Ohmic drop is a less trivial prediction. In order to examine this we have plotted the percent of contribution to the total current originating from the Cottrell expression in Eq. E.1 from the main text. This is represented as the expression:

$$\frac{\frac{exp(-kt)}{(\pi t)^{1/2}}}{\frac{exp(-kt)}{(\pi t)^{1/2}} + (k_{obs})^{1/2}\, erf\left[(kt)^{\frac{1}{2}}\right]} = \%Cottrell$$

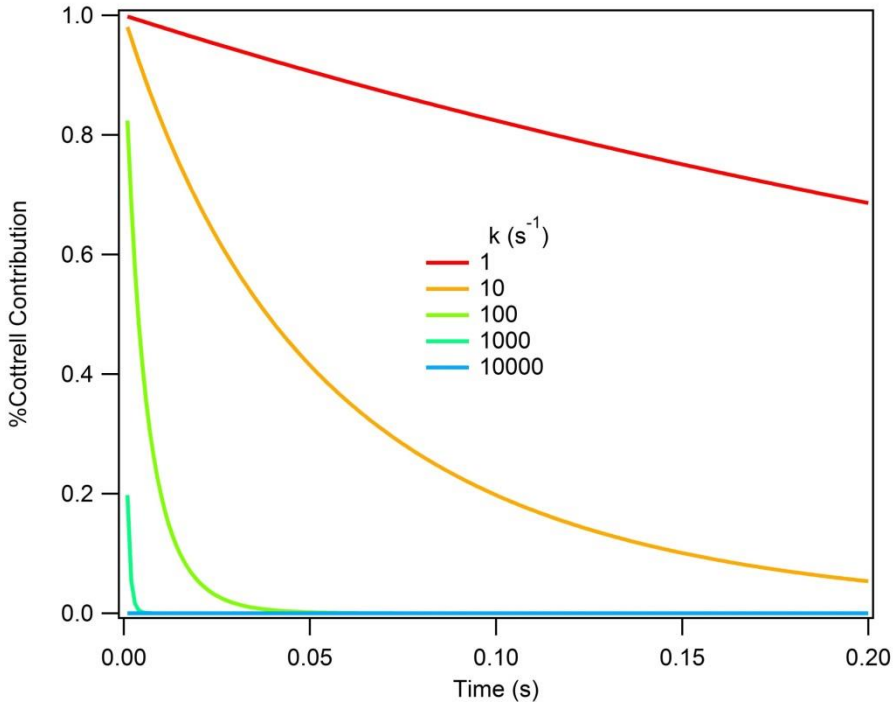

Figure E.S11. This figure demonstrates the percent contribution to the total current from Cottrell factors as a function of time. As can be seen in the figure, the contribution is only significant at short timescales and only for reactions with slow rates. This suggest that the Cottrell contribution will not significantly affect the overall result of the experiment through ohmic drop, provided that the mentioned precautions are taken. We consider this to be true because at slow catalytic rates the overall current should be significantly lower and therefore in the regime where the Cottrell current contributes significantly, the overall magnitude of the current is lower, and at fast catalytic rates the timescale for the Cottrell contribution is short.

APPENDIX F. LASER TABLE SOFTWARE

F.1 TA Software Overview

- The TA software can be accessed through matlab under the “apps” tab. It is titled “nsTA”

Summary

The software for the nanosecond TA was designed to perform a beginning to end TA/Luminescence experiment. When the nsTA icon is selected the software begins by establishing open connections to all necessary instruments; this includes the digital delay generator, monochromator, and NI USB (Shutters, PMT power supply, slow amp). This may take several seconds. If a connection fails, the user is notified of the faulty equipment and the user has the option to either close the program or correct the problem and proceed. The first window to appear is designed for instrument set-up and experiment organization. After selecting execute, the queued experiments are performed, saved at the requested location and the results are displayed for immediate viewing. Upon closing of the program at any point all instruments are disconnected.

Set-up Screen

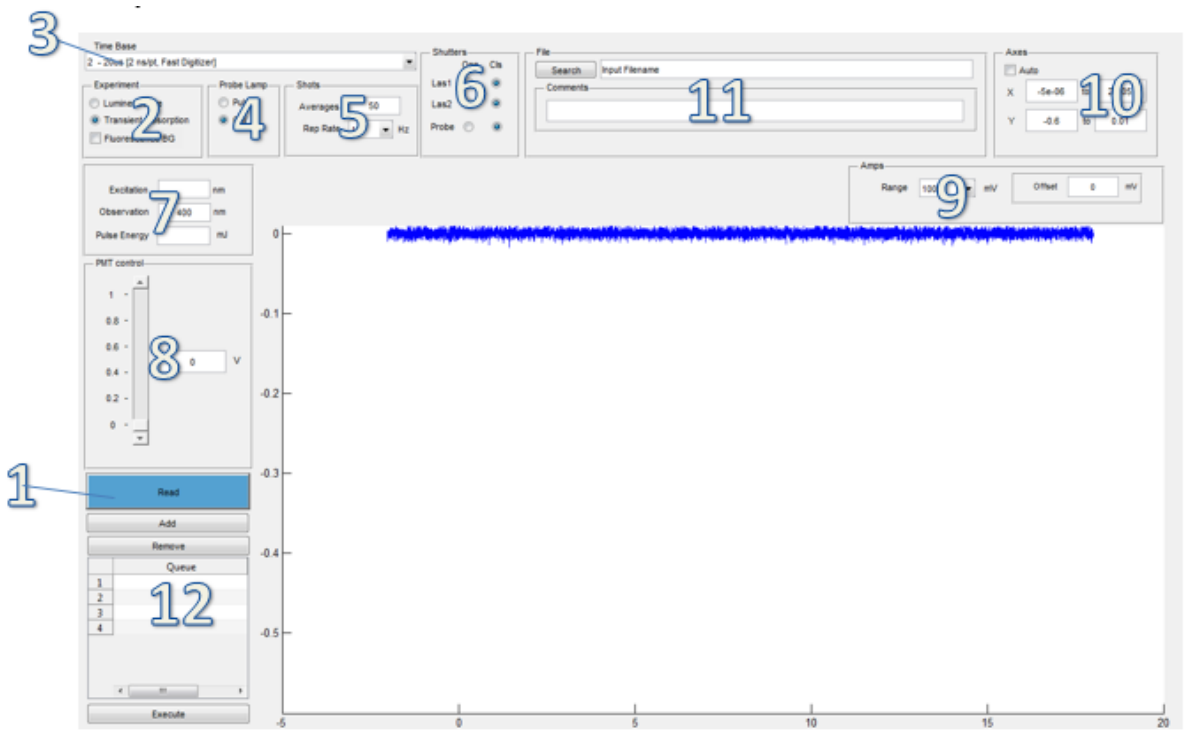

1. Read Button

The read button controls whether the data from the oscilloscope is actively being collected and retrieved and can be toggled on and off. If data is being retrieved, the button is red, otherwise it is blue. In the software when this button is activated, an internal timer begins and once each second the software either checks for complete data or initiates data collection. When data is retrieved it is displayed on the axis.

Data acquisition by the timer retrieves the necessary oscilloscope information from the timebase(3) menu, rep rate(5) menu, and range(9) menu. All other parameters for acquisition are controlled external to the oscilloscope and remain in their selected position indefinitely.

2. Experiment type

Three options available: transient absorption without fluorescence background, transient absorption with fluorescence background, and time resolved luminescence.

Default: transient absorption without fluorescence background

3. TimeBase

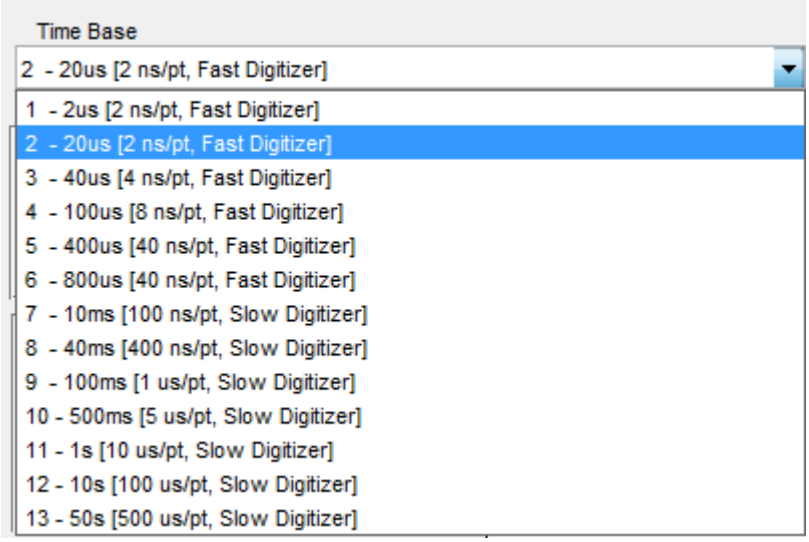

A set of 13 predetermined timeframes for experiments. The first six use the Gage CS12502 Oscilloscope and the rest use the Gage CS8422 Oscilloscope. The parameters for data acquisition that are set by this tab are managed through the setUpDigitizer.m function.

4. Probe Lamp

Two options: Pulsed or CW

Default: CW

Selection of this option has two functions, it both sets the probe lamp to the desired setting immediately and stores the selected option when queuing experiments.

5. Shots

The averages box stores the number of averages for queued experiments.

Default: 50

Rep Rate: 10 Hz, or 1 Hz.

Default: 10 Hz

At 10 Hz, data is collected for every laser pulse, at 1 Hz, the shutter is set to only allow one shot of every ten through. The digitizer triggers off of the photodiode, so each pulse that reaches the diode and sample is collected.

6. Shutters

Opens and closes shutters. This is for operational purposes only. The selected option is not stored, the type of experiment selected controls the shutters when experiments are being performed.

Note: Shutters must be set to remote. Control is through the NI card.

Default: Closed

7. Energy parameters

Excitation: This value is stored for documentation purposes and will appear at the top of the data file upon experiment completion

Observation: This value controls the monochromator. Changing this value both immediately changes the wavelength and stores it for queued experiments

Default: 400 nm

Pulse Energy: This value is stored for documentation purposes and will appear at the top of the data file upon experiment completion

8. PMT control

There are two options for setting the PMT voltage, the scroll bar and the edit box. It is preferable to use the scroll bar with “read” activated to ensure voltages do not exceed the PMT damage threshold.

Note: the PMT control box must be set to remote. Control of this box is through the NI card.

9. Amps

Range:

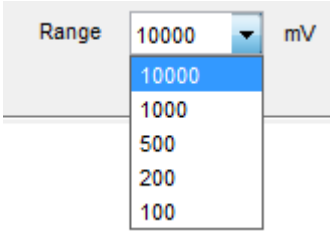

This is the range of voltage that the oscilloscope will be reading in. 10,000 mV is not an option for the fast digitizer.

Default: Fast Digitizer: 1,000 mV, Slow Digitizer: 10,000 mV

Offset: this option is only available when the slow digitizer is selected and it reads off the voltage offset from the slow amp. The software will add this voltage offset back into the final transient absorption data before calculating the delta OD.

10. Axes

This panel controls the axis viewer. Selection of auto selects the appropriate size for data viewing but may make the data difficult to look at as the size will change for every new set of data recorded.

Default: The vertical axis is set to manual and the horizontal is set to automatic. When this setting is changed it cannot be returned to default without reopening the program.

11. File

The filename box stores the location where the data will be saved after the experiment has completed. Selecting the “search” button brings up the file interface for selection.

The comment box is used to leave comments in the final file after the experiment has completed.

12. Queue

The queue table displays the experiments that have been programed by the user.

Add: The add button gathers all information necessary for experiment and stores this information in a global variable.

Remove: The remove button deletes the information for the selected variable, removing it from the queue

Execute: The execute button closes the set-up screen and opens a new window for gathering the requested data.

Note: once this button is selected the user cannot return to the set-up screen, new experiments must be performed by closing this window and re-selecting the nsTA icon.

Execute Screen

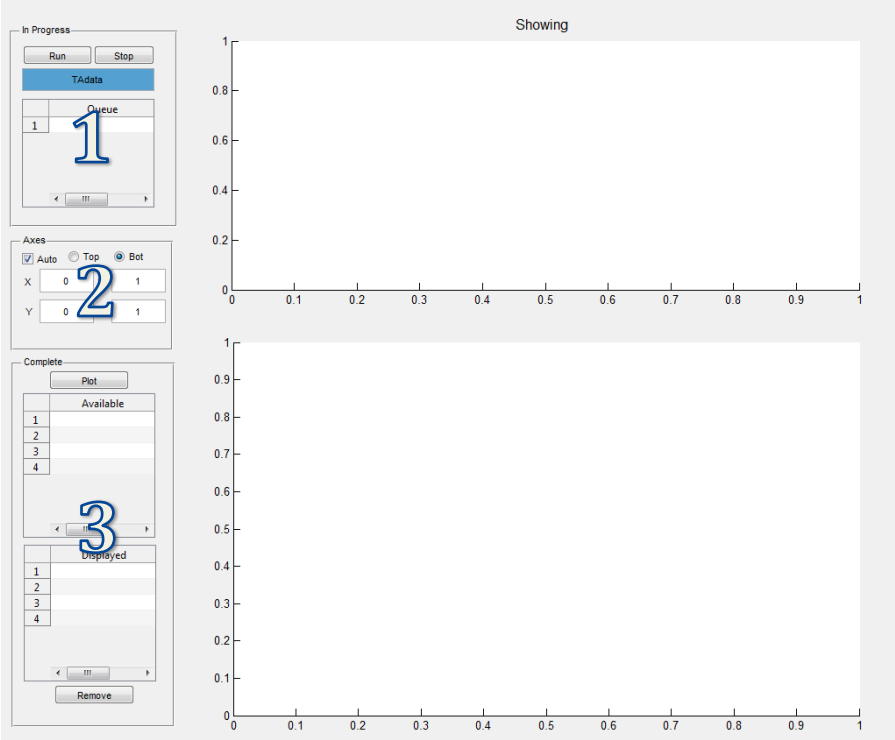

1. In Progress

Run/stop: turns on/off data collection timer

Queue: Same table as was shown on the set-up screen, except the data currently being collected is shown in the blue box (which is red when no data is being collected).

As data is collected it is displayed in the top axis.

2. Axes

The same function as the Axes on the set-up screen except in this one the option is selected to control either the top or the bottom axes.

3. Complete

Plot: plots the data selected in the “Available” table on the lower axis.

Available Table: Shows experiments that have been saved to file during the current session.

Displayed Table: Shows the data that is displayed in the lower axis

Remove: Removes the data selected in the “Displayed” table from the lower axis.

F.2 Matlab Functions

```
function varargout = TAsetupGUI(varargin)
% TASETUPGUI MATLAB code for TAsetupGUI.fig
%      TASETUPGUI, by itself, creates a new TASETUPGUI or raises the
%      existing singleton*.
%
%      H = TASETUPGUI returns the handle to a new TASETUPGUI or the handle
%      to the existing singleton*.
%
%      TASETUPGUI('CALLBACK',hObject,eventData,handles,...) calls the
%      local function named CALLBACK in TASETUPGUI.M with the given input
%      arguments.
%      TASETUPGUI('Property','Value',...) creates a new TASETUPGUI or
%      raises the existing singleton*.  Starting from the left, property
%      value pairs are applied to the GUI before TAsetupGUI_OpeningFcn
%      gets called.  An unrecognized property name or invalid value makes
%      property application stop.  All inputs are passed to
%      TAsetupGUI_OpeningFcn via varargin.
%
%      *See GUI Options on GUIDE's Tools menu.  Choose "GUI allows only
%      one instance to run (singleton)".
%
%       TAsetupGUI is the main function for operating Laser Table 1, it
%       provides control of the CS12502 and CS8422 Oscilloscopes, QC9514
%       Digital Delay Generator, CM112 Monochromator, PMT power supply and
%       shutter box.
%
% See also: GUIDE, GUIDATA, GUIHANDLES

% Last Modified by GUIDE v2.5 16-Jan-2014 11:39:56

% Begin initialization code - DO NOT EDIT
gui_Singleton = 1;
```

```
gui_State = struct('gui_Name',       mfilename, ...
                   'gui_Singleton',  gui_Singleton, ...
                   'gui_OpeningFcn', @TAsetupGUI_OpeningFcn, ...
                   'gui_OutputFcn',  @TAsetupGUI_OutputFcn, ...
                   'gui_LayoutFcn',  [] , ...
                   'gui_Callback',   []);
if nargin && ischar(varargin{1})
    gui_State.gui_Callback = str2func(varargin{1});
end

if nargout
    [varargout{1:nargout}] = gui_mainfcn(gui_State, varargin{:});
else
    gui_mainfcn(gui_State, varargin{:});
end
% End initialization code - DO NOT EDIT


% --- Executes just before TAsetupGUI is made visible.
function TAsetupGUI_OpeningFcn(hObject, eventdata, handles, varargin)
% This function has no output args, see OutputFcn.
% hObject    handle to figure
% eventdata  reserved - to be defined in a future version of MATLAB
% handles    structure with handles and user data (see GUIDATA)
% varargin   command line arguments to TAsetupGUI (see VARARGIN)

% Choose default command line output for TAsetupGUI
handles.output = hObject;

%This section initializes the monochromator
global Monochromator;
%Calls OpenCM112Link which locates the CM112 monochromator and then makes
an open
%connection. If the monochromator is not found, "device not found" is
%returned and a notification will appear asking that you connect the
%instrument, otherwise the handle to the instrument will be returned.
%This program cannot function without an active monochromator
%connection.
Monochromator = OpenCM112Link();
if isequal(Monochromator, 'device not found')
    selection = questdlg('Monochromator not on, please turn on and select
yes to continue.','Close','Yes','No','Yes');
    switch selection
        case 'Yes'
            Monochromator = OpenCM112Link();
            CM112set(Monochromator, 'Position', 400);
        case 'No'
            delete(gcf);
            return
    end
else
    CM112set(Monochromator, 'Position', 400);
end
%Sets initial Experiment radio button to Transient Adsorption
set(handles.TARadio, 'Value', 1);
%Sets initial timescale
```

```
set(handles.TimeBaseMenu, 'Value', 2);
%Sets initial probe lamp status to continuous wave
set(handles.ProbeLampStatic, 'Value', 1);
%Sets initial value for averages to 50
set(handles.AveragesBox, 'String', '50');
%Sets initial value for excitation wavelength to null
set(handles.ExcitationBox, 'String', '');
%Sets initial location of PMT to readout to 0
set(handles.PMTsetBox, 'String', '0');
%Sets initial color of Read button to Carolina Blue
set(handles.ReadButton, 'BackgroundColor', [.33 .63 .82])
%Sets Axes to specific y range
ylim([-.6, .01]);

%This section obtains the current axes properties and displays them
xLimits = get(gca, 'Xlim');
yLimits = get(gca, 'YLim');
set(handles.YlowBox, 'String', yLimits(1,1));
set(handles.YhighBox, 'String', yLimits(1,2));
set(handles.XlowBox, 'String', xLimits(1,1));
set(handles.XhighBox, 'String', xLimits(1,2));

%initialization of all gloval variables
%
%Scope is used to keep track of which Oscilloscope is currently active
%while using the timer object "updatePlotTimer"
global Scope;
Scope = 0;
%PMTcontrol, Las1Shutter, Las2Shutter, and Probe Shutter are all channels
%on the shutter box.
global PMTcontrol;
global Las1Shutter;
global Las2Shutter;
global ProbeShutter;
%PMTcontrol is an analog output channel, the shutterbox, which is an NI
USB
%6008, has two analog output channels ao0 and ao1, PMTcontrolLocation must
%match the output channel that the PMT power supply is plugged into.
PMTcontrolLocation = 'ao0';
%The shutters operate off of the Digital I/O channels on the NI USB 6008.
%The ShutterLocation variable must match the location of the physical
%shutter on the shutterbox. There are 8 channels, beginning with 0 which
%are labeled port0/line*, *=0,1...6,7.
Las1ShutterLocation = 'port0/line0';
Las2ShutterLocation = 'port0/line1';
ProbeShutterLocation = 'port0/line2';
%This try/catch block is designed to check if the shutter box is connected
%to the computer. If it is not, a notification will appear asking for you
%to plug in the box before proceeding. The setup cannot be opened without
%the shutter box being active.
try
    PMTcontrol = daq.createSession('ni');
    PMTcontrol.addAnalogOutputChannel('Dev1', 'ao0', 'Voltage');
    Las1Shutter = daq.createSession('ni');
    Las1Shutter.addDigitalChannel('Dev1','port0/line0', 'OutputOnly');
    set(handles.Las1Close, 'Value', 1)
```

```
    Las1Shutter.outputSingleScan(0);
    Las2Shutter = daq.createSession('ni');
    Las2Shutter.addDigitalChannel('Dev1','port0/line1', 'OutputOnly');
    set(handles.Las2Close, 'Value', 1)
    Las2Shutter.outputSingleScan(0);
    ProbeShutter = daq.createSession('ni');
    ProbeShutter.addDigitalChannel('Dev1','port0/line2', 'OutputOnly');
    set(handles.ProbeClose, 'Value', 1)
    ProbeShutter.outputSingleScan(0);
catch err
    selection = questdlg('DIO/Valve Driver not connected, please connect
and select yes to continue.','Close','Yes','No','Yes');
        switch selection
            case 'Yes'
                PMTcontrol = daq.createSession('ni');
                PMTcontrol.addAnalogOutputChannel('Dev1', 'ao0',
'Voltage');
                Las1Shutter = daq.createSession('ni');
                Las1Shutter.addDigitalChannel('Dev1','port0/line0',
'OutputOnly');
                set(handles.Las1Close, 'Value', 1)
                Las1Shutter.outputSingleScan(0);
                Las2Shutter = daq.createSession('ni');
                Las2Shutter.addDigitalChannel('Dev1','port0/line1',
'OutputOnly');
                set(handles.Las2Close, 'Value', 1)
                Las2Shutter.outputSingleScan(0);
                ProbeShutter = daq.createSession('ni');
                ProbeShutter.addDigitalChannel('Dev1','port0/line2',
'OutputOnly');
                set(handles.ProbeClose, 'Value', 1)
                ProbeShutter.outputSingleScan(0);
            case 'No'
                fclose(Monochromator);
                clear global Monochromator;
                delete(gcf);
                return
        end
end

%This section initializes the digital delay generator
global pausetime;
global delayGen;
pausetime = .1;
%Calls OpenQC9514Link which locates the QC9514 Digital Delay Generator and
then makes an open
%connection. If the DDG is not found, "device not found" is
%returned and a notification will appear asking that you connect the
%instrument, otherwise a handle to the instrument will be returned.
%This program cannot function without an active monochromator
%connection.
[delayGen] = OpenQC9514Link();
%try/catch block signals if "device not found" is used and asks the user
to
%turn on or connect the digital delay generator
try
    if isequal(delayGen, 'device not found')
```

```
        selection = questdlg('Digital Delay Generator not on, please turn
on and select yes to continue.','Close','Yes','No','Yes');
        switch selection
            case 'Yes'
                [delayGen] = OpenQC9514Link();
               %setting pulse generator screen to automatically update
                fprintf(delayGen, ':display:mode on<cr><lf>');
                pause(pausetime);
                fscanf(delayGen);
                %setting pulse generator brightness to 2.
                fprintf(delayGen, ':display:brightness 2<cr><lf>');
                pause(pausetime);
                fscanf(delayGen);
                %Updating On/Off status of Channels A and B
                fprintf(delayGen, ':pulse1:state 1<cr><lf>');
                fscanf(delayGen);
                fprintf(delayGen, ':pulse2:state 0<cr><lf>');
                fscanf(delayGen);
                %Running Digital Delay Generator
                fprintf(delayGen, ':spulse:state 1<cr><lf>');
                fscanf(delayGen);
            case 'No'
                fclose(Monochromator);
                clear global Monochromator;
                delete(gcf);
                return
        end
    else
        %setting pulse generator screen to automatically update
        fprintf(delayGen, ':display:mode on<cr><lf>');
        pause(pausetime);
        fscanf(delayGen);
        %setting pulse generator brightness to 2.
        fprintf(delayGen, ':display:brightness 2<cr><lf>');
        pause(pausetime);
        fscanf(delayGen);
        %Updating On/Off status of Channels A and B
        fprintf(delayGen, ':pulse1:state 1<cr><lf>');
        fscanf(delayGen);
        fprintf(delayGen, ':pulse2:state 0<cr><lf>');
        fscanf(delayGen);
        %Running Digital Delay Generator
        fprintf(delayGen, ':spulse:state 1<cr><lf>');
        fscanf(delayGen)
    end
catch err
%setting pulse generator screen to automatically update
fprintf(delayGen, ':display:mode on<cr><lf>');
pause(pausetime);
fscanf(delayGen);
%setting pulse generator brightness to 2.
fprintf(delayGen, ':display:brightness 2<cr><lf>');
pause(pausetime);
fscanf(delayGen);
%Updating On/Off status of Channels A and B
fprintf(delayGen, ':pulse1:state 1<cr><lf>');
fscanf(delayGen);
```

```
fprintf(delayGen, ':pulse2:state 0<cr><lf>');
fscanf(delayGen);
%Running Digital Delay Generator
fprintf(delayGen, ':spulse:state 1<cr><lf>');
fscanf(delayGen)
end

%global variables for information management.
%QueueInfo is a structure which stores all of the appropriate variables
%when the "Add" button is pressed for the Queue. QueueNames is a cell
array
%that stores the information for the Queued list.
global QueueInfo;
QueueInfo(1).dataset = 0;
global QueueNames;
QueueNames = cell(1);
QueueNames{1,1} = '';

%This sets the selection of a cell on the QueueTable to trigger
%CellSelect3, which stores the location of the selected cell.
set(handles.QueueTable, 'CellSelectionCallback',@CellSelect3);

%Generates the Timer which allows for the continual update of the plot
%after the read button is selected.
handles.updatePlotTimer = timer('ExecutionMode', 'FixedRate', 'Period',
.25, 'TimerFcn', {@updatePlot, handles});
%Triggers the closeGUI function when the option to close the gui is
%selected.
set(handles.figure1,'CloseRequestFcn',{@closeGUI,handles});
% Update handles structure
set(handles.ObservationBox, 'String', '400');
guidata(hObject, handles);

% UIWAIT makes TAsetupGUI wait for user response (see UIRESUME)
% uiwait(handles.figure1);

function CellSelect3(hObject, eventData, handles)
%CellSelect3 is called when cells are selected from the Queuetable. It
%subsequently stores them in the global variable QueueCellSelect.
global QueueCellSelect;
QueueCellSelect = eventData.Indices;

function updatePlot(hObject, eventdata, handles)
%updatePlot is managed by the updatePlot Timer generated in the opening
%function.
%
%The updatePlot Timer is triggered by pressing the read button. It is on
%when the read button is red and is off when the read button is blue. It
is
%used to repeatedly signal the selected oscilloscope to collect data and
%then displays it.

%Acquires global variable "Scope"
global Scope;
%If Scope does not contain a handle to an oscilloscope. The status is set
```

```
%to -1 to signal to the need to initialized data collection. If "Scope"
%does contain a handle, the status of the data acquisition is checked and
%recorded.
if Scope ~= 0;
    status = CsMl_QueryStatus(Scope);
else
    status = -1;
end

%Triggers if no oscilloscope is active
if status == -1
    %Obtains the Timebase that was selected
    selection = get(handles.TimeBaseMenu, 'Value');
    %Selects the appropriate oscilloscope for the desired Timescale
    if selection < 7
        Requested.Board = 1280; %CS12502
    else
        Requested.Board = 214;  %CS8422
    end
    %Initializes oscilloscope and checks for errors
    systems = CsMl_Initialize;
    CsMl_ErrorHandler(systems);
    %Obtains a handles to the desired oscillscope
    [ret, Scope] = CsMl_GetSystem(Requested);
    CsMl_ErrorHandler(ret);
    %calls setupDigitizer to prepare all data acquisition parameters for
the
    %oscilloscope
    setupDigitizer(selection, Scope);
    %transmits all parameters to the scope
    [ret] = CsMl_Commit(Scope);
    CsMl_ErrorHandler(ret, 1, Scope);
    %Signals the oscilloscope to begin looking for a trigger event.
    ret = CsMl_Capture(Scope);
    CsMl_ErrorHandler(ret, 1, Scope);
end
%Triggers if status ==0, meaning that the oscilloscope has completed its
%data acquisition.
if status == 0
    %obtains parameter info from oscilloscope
    [ret, acqInfo] = CsMl_QueryAcquisition(Scope);
    %transfer structure is created to obtain desired data from
oscilloscope
    transfer.Mode = CsMl_Translate('Default', 'TxMode');
    transfer.Segment = 1;
    transfer.Start = -acqInfo.TriggerHoldoff;
    transfer.Length = acqInfo.SegmentSize;
    %transfers from channel 2 on scope
    transfer.Channel = 2;
    % Transfer the data
    [ret, data, actual] = CsMl_Transfer(Scope, transfer);
    %obtains parameters describing timescale of experiment
    [depth, triggerHoldoff, between] = FindTime(get(handles.TimeBaseMenu,
'Value'));
    %creates dataset representing the time
    Time = ((-triggerHoldoff*between):between:((depth-1)*between))';
    %plots data on GUI plot
```

```
    plot(handles.axes1, Time, data);
    %disconnects from oscilloscope
    ret = CsMl_FreeSystem(Scope);
    %removes handle from global variable
    Scope = 0;
    %updates plot information
    autoupdate(hObject,eventdata, handles);
end


% --- Outputs from this function are returned to the command line.
function varargout = TAsetupGUI_OutputFcn(hObject, eventdata, handles)
% varargout  cell array for returning output args (see VARARGOUT);
% hObject    handle to figure
% eventdata  reserved - to be defined in a future version of MATLAB
% handles    structure with handles and user data (see GUIDATA)

% Get default command line output from handles structure
varargout{1} = handles.output;


% --- Executes on selection change in TimeBaseMenu.
function TimeBaseMenu_Callback(hObject, eventdata, handles)
% hObject    handle to TimeBaseMenu (see GCBO)
% eventdata  reserved - to be defined in a future version of MATLAB
% handles    structure with handles and user data (see GUIDATA)

%Frees any oscilloscopes that were in use to reinitialize with new
%parameters.
global Scope;
Scope = 0;
CsMl_FreeAllSystems;
plot(1,1);


% --- Executes during object creation, after setting all properties.
function TimeBaseMenu_CreateFcn(hObject, eventdata, handles)
% hObject    handle to TimeBaseMenu (see GCBO)
% eventdata  reserved - to be defined in a future version of MATLAB
% handles    empty - handles not created until after all CreateFcns called

% Hint: popupmenu controls usually have a white background on Windows.
%       See ISPC and COMPUTER.
if ispc && isequal(get(hObject,'BackgroundColor'),
get(0,'defaultUicontrolBackgroundColor'))
    set(hObject,'BackgroundColor','white');
end


% --- Executes on button press in AxesAuto.
function AxesAuto_Callback(hObject, eventdata, handles)
% hObject    handle to AxesAuto (see GCBO)
% eventdata  reserved - to be defined in a future version of MATLAB
% handles    structure with handles and user data (see GUIDATA)
if get(hObject, 'Value') == 1
```

```
    axis auto
else
    axis manual
end
autoupdate(hObject,eventdata, handles);



function XlowBox_Callback(hObject, eventdata, handles)
% hObject    handle to XlowBox (see GCBO)
% eventdata  reserved - to be defined in a future version of MATLAB
% handles    structure with handles and user data (see GUIDATA)
new = str2double(get(hObject, 'String'));
opposite = get(handles.XhighBox, 'String');
oppositenum = str2double(opposite);
while (new > oppositenum) || isnan(new)
    new = str2double(inputdlg(strcat('invalid bounds, enter value less
than ', opposite,')')));
    if isempty(new)
        return;
    end
end
xlim([new,oppositenum]);
set(handles.AxesAuto, 'Value', 0);
autoupdate(hObject,eventdata, handles);


% --- Executes during object creation, after setting all properties.
function XlowBox_CreateFcn(hObject, eventdata, handles)
% hObject    handle to XlowBox (see GCBO)
% eventdata  reserved - to be defined in a future version of MATLAB
% handles    empty - handles not created until after all CreateFcns called

% Hint: edit controls usually have a white background on Windows.
%       See ISPC and COMPUTER.
if ispc && isequal(get(hObject,'BackgroundColor'),
get(0,'defaultUicontrolBackgroundColor'))
    set(hObject,'BackgroundColor','white');
end



function YlowBox_Callback(hObject, eventdata, handles)
% hObject    handle to YlowBox (see GCBO)
% eventdata  reserved - to be defined in a future version of MATLAB
% handles    structure with handles and user data (see GUIDATA)
new = str2double(get(hObject, 'String'));
opposite = get(handles.YhighBox, 'String');
oppositenum = str2double(opposite);
while (new > oppositenum) || isnan(new)
    new = str2double(inputdlg(strcat('invalid bounds, enter value less
than ', opposite,')')));
    if isempty(new)
        return;
    end
```

```
end
ylim([new,oppositenum]);
set(handles.AxesAuto, 'Value', 0);
autoupdate(hObject,eventdata, handles);


% --- Executes during object creation, after setting all properties.
function YlowBox_CreateFcn(hObject, eventdata, handles)
% hObject    handle to YlowBox (see GCBO)
% eventdata  reserved - to be defined in a future version of MATLAB
% handles    empty - handles not created until after all CreateFcns called

% Hint: edit controls usually have a white background on Windows.
%       See ISPC and COMPUTER.
if ispc && isequal(get(hObject,'BackgroundColor'),
get(0,'defaultUicontrolBackgroundColor'))
    set(hObject,'BackgroundColor','white');
end



function XhighBox_Callback(hObject, eventdata, handles)
% hObject    handle to XhighBox (see GCBO)
% eventdata  reserved - to be defined in a future version of MATLAB
% handles    structure with handles and user data (see GUIDATA)
new = str2double(get(hObject, 'String'))
opposite = get(handles.XlowBox, 'String');
oppositenum = str2double(opposite)
while (new < oppositenum) || isnan(new)
    new = str2double(inputdlg(strcat('invalid bounds, enter value greater
than ', opposite,')')));
    if isempty(new)
        return;
    end
end
xlim([oppositenum,new]);
set(handles.AxesAuto, 'Value', 0);
autoupdate(hObject,eventdata, handles);


% --- Executes during object creation, after setting all properties.
function XhighBox_CreateFcn(hObject, eventdata, handles)
% hObject    handle to XhighBox (see GCBO)
% eventdata  reserved - to be defined in a future version of MATLAB
% handles    empty - handles not created until after all CreateFcns called

% Hint: edit controls usually have a white background on Windows.
%       See ISPC and COMPUTER.
if ispc && isequal(get(hObject,'BackgroundColor'),
get(0,'defaultUicontrolBackgroundColor'))
    set(hObject,'BackgroundColor','white');
end
```

```
function YhighBox_Callback(hObject, eventdata, handles)
% hObject    handle to YhighBox (see GCBO)
% eventdata  reserved - to be defined in a future version of MATLAB
% handles    structure with handles and user data (see GUIDATA)
new = str2double(get(hObject, 'String'));
opposite = get(handles.YlowBox, 'String');
oppositenum = str2double(opposite);
while (new < oppositenum) || isnan(new)
    new = str2double(inputdlg(strcat('invalid bounds, enter value greater
than ', opposite,')')));
    if isempty(new)
        return;
    end
end
ylim([oppositenum,new]);
set(handles.AxesAuto, 'Value', 0);
autoupdate(hObject,eventdata, handles);


% --- Executes during object creation, after setting all properties.
function YhighBox_CreateFcn(hObject, eventdata, handles)
% hObject    handle to YhighBox (see GCBO)
% eventdata  reserved - to be defined in a future version of MATLAB
% handles    empty - handles not created until after all CreateFcns called

% Hint: edit controls usually have a white background on Windows.
%       See ISPC and COMPUTER.
if ispc && isequal(get(hObject,'BackgroundColor'),
get(0,'defaultUicontrolBackgroundColor'))
    set(hObject,'BackgroundColor','white');
end

function autoupdate(hObject,eventdata, handles)
%updates plot information for display
xLimits = get(handles.axes1, 'Xlim');
yLimits = get(handles.axes1, 'YLim');
set(handles.YlowBox, 'String', yLimits(1,1));
set(handles.YhighBox, 'String', yLimits(1,2));
set(handles.XlowBox, 'String', xLimits(1,1));
set(handles.XhighBox, 'String', xLimits(1,2));



function FilenameBox_Callback(hObject, eventdata, handles)
% hObject    handle to FilenameBox (see GCBO)
% eventdata  reserved - to be defined in a future version of MATLAB
% handles    structure with handles and user data (see GUIDATA)


% --- Executes during object creation, after setting all properties.
function FilenameBox_CreateFcn(hObject, eventdata, handles)
% hObject    handle to FilenameBox (see GCBO)
% eventdata  reserved - to be defined in a future version of MATLAB
% handles    empty - handles not created until after all CreateFcns called
```

```
% Hint: edit controls usually have a white background on Windows.
%       See ISPC and COMPUTER.
if ispc && isequal(get(hObject,'BackgroundColor'),
get(0,'defaultUicontrolBackgroundColor'))
    set(hObject,'BackgroundColor','white');
end


% --- Executes on button press in SearchFilename.
function SearchFilename_Callback(hObject, eventdata, handles)
% hObject    handle to SearchFilename (see GCBO)
% eventdata  reserved - to be defined in a future version of MATLAB
% handles    structure with handles and user data (see GUIDATA)

%opens Save menu
filename = GetFileName();
%displays selected location to user
set(handles.FilenameBox, 'String', filename);



function ExcitationBox_Callback(hObject, eventdata, handles)
% hObject    handle to ExcitationBox (see GCBO)
% eventdata  reserved - to be defined in a future version of MATLAB
% handles    structure with handles and user data (see GUIDATA)


% --- Executes during object creation, after setting all properties.
function ExcitationBox_CreateFcn(hObject, eventdata, handles)
% hObject    handle to ExcitationBox (see GCBO)
% eventdata  reserved - to be defined in a future version of MATLAB
% handles    empty - handles not created until after all CreateFcns called

% Hint: edit controls usually have a white background on Windows.
%       See ISPC and COMPUTER.
if ispc && isequal(get(hObject,'BackgroundColor'),
get(0,'defaultUicontrolBackgroundColor'))
    set(hObject,'BackgroundColor','white');
end



function ObservationBox_Callback(hObject, eventdata, handles)
% hObject    handle to ObservationBox (see GCBO)
% eventdata  reserved - to be defined in a future version of MATLAB
% handles    structure with handles and user data (see GUIDATA)

global Monochromator;
%obtains value that user input into Observation wavelength box
uiInput = str2double(get(hObject,'String'));
%If value is invalid, a new value is requested before proceeding
if ~(uiInput < 1000) || ~(uiInput > 200)
```

```
    answer = inputdlg('Invalid Value, input a number between 200 and
1000','Error',1);
    uiInput =str2double(answer);
    if isempty(answer)
        set(hObject, 'String', CM112get(Monochromator, 'Position'));
        return;
    end
    while ~(uiInput < 1000) || ~(uiInput > 200)
        answer = inputdlg('Invalid Value, input a number between 200 and
1000','Error',1);
        if isempty(answer)
        set(hObject, 'String', CM112get(Monochromator, 'Position'));
        return;
        end
        uiInput =str2double(answer);
    end
    set(hObject, 'String', answer);
end
%new position is set on Monochromator
CM112set(Monochromator, 'Position', uiInput);


% --- Executes during object creation, after setting all properties.
function ObservationBox_CreateFcn(hObject, eventdata, handles)
% hObject    handle to ObservationBox (see GCBO)
% eventdata  reserved - to be defined in a future version of MATLAB
% handles    empty - handles not created until after all CreateFcns called

% Hint: edit controls usually have a white background on Windows.
%       See ISPC and COMPUTER.
if ispc && isequal(get(hObject,'BackgroundColor'),
get(0,'defaultUicontrolBackgroundColor'))
    set(hObject,'BackgroundColor','white');
end



function AveragesBox_Callback(hObject, eventdata, handles)
% hObject    handle to AveragesBox (see GCBO)
% eventdata  reserved - to be defined in a future version of MATLAB
% handles    structure with handles and user data (see GUIDATA)



% --- Executes during object creation, after setting all properties.
function AveragesBox_CreateFcn(hObject, eventdata, handles)
% hObject    handle to AveragesBox (see GCBO)
% eventdata  reserved - to be defined in a future version of MATLAB
% handles    empty - handles not created until after all CreateFcns called

% Hint: edit controls usually have a white background on Windows.
%       See ISPC and COMPUTER.
if ispc && isequal(get(hObject,'BackgroundColor'),
get(0,'defaultUicontrolBackgroundColor'))
    set(hObject,'BackgroundColor','white');
```

```
end



function RepRateBox_Callback(hObject, eventdata, handles)
% hObject    handle to RepRateBox (see GCBO)
% eventdata  reserved - to be defined in a future version of MATLAB
% handles    structure with handles and user data (see GUIDATA)


% --- Executes during object creation, after setting all properties.
function RepRateBox_CreateFcn(hObject, eventdata, handles)
% hObject    handle to RepRateBox (see GCBO)
% eventdata  reserved - to be defined in a future version of MATLAB
% handles    empty - handles not created until after all CreateFcns called

% Hint: edit controls usually have a white background on Windows.
%       See ISPC and COMPUTER.
if ispc && isequal(get(hObject,'BackgroundColor'),
get(0,'defaultUicontrolBackgroundColor'))
    set(hObject,'BackgroundColor','white');
end


% --- Executes on button press in TARadio.
function TARadio_Callback(hObject, eventdata, handles)
% hObject    handle to TARadio (see GCBO)
% eventdata  reserved - to be defined in a future version of MATLAB
% handles    structure with handles and user data (see GUIDATA)
set(hObject, 'Value', 1);
set(handles.LumRadio, 'Value', 0);
set(handles.FluorCheckbox, 'Visible', 'on');


% --- Executes on button press in LumRadio.
function LumRadio_Callback(hObject, eventdata, handles)
% hObject    handle to LumRadio (see GCBO)
% eventdata  reserved - to be defined in a future version of MATLAB
% handles    structure with handles and user data (see GUIDATA)
set(hObject, 'Value', 1);
set(handles.TARadio, 'Value', 0);
set(handles.FluorCheckbox, 'Value', 0);
set(handles.FluorCheckbox, 'Visible', 'off');


% --- Executes on button press in FluorCheckbox.
function FluorCheckbox_Callback(hObject, eventdata, handles)
% hObject    handle to FluorCheckbox (see GCBO)
% eventdata  reserved - to be defined in a future version of MATLAB
% handles    structure with handles and user data (see GUIDATA)
if get(handles.LumRadio, 'Value') ==1
    set(hObject, 'Value', 0)
end
```

```
% --- Executes on button press in ProbeLampPulsed.
function ProbeLampPulsed_Callback(hObject, eventdata, handles)
% hObject    handle to ProbeLampPulsed (see GCBO)
% eventdata  reserved - to be defined in a future version of MATLAB
% handles    structure with handles and user data (see GUIDATA)
set(hObject, 'Value', 1);
set(handles.ProbeLampStatic, 'Value', 0);
global pausetime;
global delayGen;
pausetime = .1;
%Updating On/Off status of ChannelB
fprintf(delayGen, ':pulse2:state 1<cr><lf>');
pause(pausetime);
fscanf(delayGen);


% --- Executes on button press in ProbeLampStatic.
function ProbeLampStatic_Callback(hObject, eventdata, handles)
% hObject    handle to ProbeLampStatic (see GCBO)
% eventdata  reserved - to be defined in a future version of MATLAB
% handles    structure with handles and user data (see GUIDATA)
set(hObject, 'Value', 1);
set(handles.ProbeLampPulsed, 'Value', 0);
global pausetime;
global delayGen;
pausetime = .1;
%Updating On/Off status of ChannelB
fprintf(delayGen, ':pulse2:state 0<cr><lf>');
pause(pausetime);
fscanf(delayGen);


% --- Executes on slider movement.
function PMTSlider_Callback(hObject, eventdata, handles)
% hObject    handle to PMTSlider (see GCBO)
% eventdata  reserved - to be defined in a future version of MATLAB
% handles    structure with handles and user data (see GUIDATA)
global PMTcontrol;
sliderValue = get(hObject,'Value');
%Adjusting for Scaler on PMT power supply
inputValue = 4.02*sliderValue;
PMTcontrol.outputSingleScan(inputValue);
set(handles.PMTsetBox,'String', num2str(sliderValue));


% --- Executes during object creation, after setting all properties.
function PMTSlider_CreateFcn(hObject, eventdata, handles)
% hObject    handle to PMTSlider (see GCBO)
% eventdata  reserved - to be defined in a future version of MATLAB
% handles    empty - handles not created until after all CreateFcns called

% Hint: slider controls usually have a light gray background.
if isequal(get(hObject,'BackgroundColor'),
get(0,'defaultUicontrolBackgroundColor'))
```

```
    set(hObject,'BackgroundColor',[.9 .9 .9]);
end



function PMTsetBox_Callback(hObject, eventdata, handles)
% hObject    handle to PMTsetBox (see GCBO)
% eventdata  reserved - to be defined in a future version of MATLAB
% handles    structure with handles and user data (see GUIDATA)
global PMTcontrol;
setValue = get(hObject,'String');
setValue = str2double(setValue);
%checking to ensure value is between 0 and 1.
if (setValue > 1) || (setValue < 0)
    warndlg('Value invalid, voltage not altered')
    set(hObject,'String',num2str(get(handles.PMTSlider,'Value')));
else
    %Adjusting for Scaler on PMT power supply
    inputValue = 4.02*setValue;
    PMTcontrol.outputSingleScan(inputValue);
    set(handles.PMTSlider, 'Value',setValue);
end



% --- Executes during object creation, after setting all properties.
function PMTsetBox_CreateFcn(hObject, eventdata, handles)
% hObject    handle to PMTsetBox (see GCBO)
% eventdata  reserved - to be defined in a future version of MATLAB
% handles    empty - handles not created until after all CreateFcns called

if ispc && isequal(get(hObject,'BackgroundColor'),
get(0,'defaultUicontrolBackgroundColor'))
    set(hObject,'BackgroundColor','white');
end



% --- Executes on selection change in CommentBox.
function CommentBox_Callback(hObject, eventdata, handles)
% hObject    handle to CommentBox (see GCBO)
% eventdata  reserved - to be defined in a future version of MATLAB
% handles    structure with handles and user data (see GUIDATA)



% --- Executes during object creation, after setting all properties.
function CommentBox_CreateFcn(hObject, eventdata, handles)
% hObject    handle to CommentBox (see GCBO)
% eventdata  reserved - to be defined in a future version of MATLAB
% handles    empty - handles not created until after all CreateFcns called

if ispc && isequal(get(hObject,'BackgroundColor'),
get(0,'defaultUicontrolBackgroundColor'))
    set(hObject,'BackgroundColor','white');
```

```
end


% --- Executes on button press in AddButton.
function AddButton_Callback(hObject, eventdata, handles)
% hObject    handle to AddButton (see GCBO)
% eventdata  reserved - to be defined in a future version of MATLAB
% handles    structure with handles and user data (see GUIDATA)
%
%function stores all selected parameters for use during data acquisition
%and file saving.

%initializes global data storage variables
global QueueInfo;
global QueueNames;
%obtains filename
Filename = get(handles.FilenameBox,'String');
%checks to ensure filename has been input
if isequal(Filename, 'Input Filename')
    warndlg('File not named');
    return;
end
%selects correct location for data storage
if QueueInfo(1).dataset == 0
    dataset = 1;
else
    dataset = length(QueueInfo)+1;
end
%removes location String from filename for QueueNames Cell
name = Filename;
breaks = regexp(name, '\');
lengthBreaks = length(breaks);
lengthName = length(name);
name = name((breaks(1,lengthBreaks)+1):(lengthName-4));
%determines if filename has already been selected
for i = 1:length(QueueNames)
    if isequal(name, QueueNames{i,1})
        warndlg('Filename already exist')
        return;
    end
end
%stores dataset number
QueueInfo(dataset).dataset = dataset;
%Stores timebase value
QueueInfo(dataset).TimeBase = get(handles.TimeBaseMenu, 'Value');
%Stores whether a Fluorescence background will be taken
QueueInfo(dataset).FluorescenceBG = get(handles.FluorCheckbox, 'Value');
%stores whether the probelamp will be pulsed ore continuous wave
if get(handles.ProbeLampPulsed, 'Value') == 1
    QueueInfo(dataset).ProbeLamp = 'Pulsed';
else
    QueueInfo(dataset).ProbeLamp = 'CW';
end
%Stores the type of experiment that will be performed
if get(handles.TARadio, 'Value') ==1
    QueueInfo(dataset).Experiment = 'TA';
```

```
else
    QueueInfo(dataset).Experiment = 'Lum';
end
%Stores the number of averages to be taken
QueueInfo(dataset).Averages =
str2double(get(handles.AveragesBox,'String'));
%Stores the RepRate
if get(handles.RepRateBox, 'Value') == 1
    QueueInfo(dataset).RepRate = 10;
else
    QueueInfo(dataset).RepRate = 1;
end
%Stores the complete filename and location for saving
QueueInfo(dataset).Filename = get(handles.FilenameBox,'String');
%stores the comments from the user
QueueInfo(dataset).Comments = get(handles.CommentBox, 'String');
%stores the excitation wavelength
QueueInfo(dataset).Excitation = get(handles.ExcitationBox, 'String');
%stores the observation wavelength
QueueInfo(dataset).Observation = str2double(get(handles.ObservationBox,
'String'));
%stores the pulse energy
QueueInfo(dataset).PulseEnergy = get(handles.PulseEnergyBox, 'String');
if isequal(QueueNames{1,1}, '')
    QueueNames{1,1} = name;
else
    QueueNames{length(QueueNames)+1,1} = name;
end
%renews the QueueTable data.
set(handles.QueueTable,'data',QueueNames);


% --- Executes on button press in ReadButton.
function ReadButton_Callback(hObject, eventdata, handles)
% hObject    handle to ReadButton (see GCBO)
% eventdata  reserved - to be defined in a future version of MATLAB
% handles    structure with handles and user data (see GUIDATA)
%
%Turns the timer on and off for updating the plot.
Value = get(hObject, 'value');
if Value == 1
    global Scope;
    Scope = 0;
    CsMl_FreeAllSystems;
    set(hObject, 'BackgroundColor', [1 .2 .2])
    start(handles.updatePlotTimer);
else
    set(hObject, 'BackgroundColor', [.33 .63 .82])
    stop(handles.updatePlotTimer);
    CsMl_FreeAllSystems;
end

function closeGUI(src, evt, handles)
%executes upon selection of closeout button. disconnects from instruments,
%stops timers and clears global variables.
selection = questdlg('Are you sure?','Close','Yes','No','Yes');
```

```
switch selection
    case 'Yes'
        if isequal(get(handles.updatePlotTimer, 'Running'),'on')
            stop(handles.updatePlotTimer);
        end
        CsMl_FreeAllSystems();
        global Monochromator;
        fclose(Monochromator);
        global delayGen;
        fprintf(delayGen, ':pulse2:state 0<cr><lf>');
        fclose(delayGen);
        clear global QueueInfo;
        clear global QueueNames;
        global PMTcontrol
        PMTcontrol.outputSingleScan(0);
        delete(gcf)
    case 'No'
        return
end


% --- Executes on button press in ExecuteButton.
function ExecuteButton_Callback(hObject, eventdata, handles)
% hObject    handle to ExecuteButton (see GCBO)
% eventdata  reserved - to be defined in a future version of MATLAB
% handles    structure with handles and user data (see GUIDATA)
%
% Deletes current GUI and opens the data acquisition GUI.
global QueueNames;
if isequal(QueueNames{1,1}, '')
    warndlg('No job queued');
    return;
end
selection = questdlg('Are you sure you want to
continue?','Execute','Yes','No','Yes');
switch selection
    case 'Yes'
        global QueueInfo
        if isequal(get(handles.updatePlotTimer, 'Running'),'on')
            stop(handles.updatePlotTimer);
        end
        delete(gcf);
        CsMl_FreeAllSystems();
        ExecuteGui(QueueInfo);
    case 'No'
        return
end


% --- Executes on button press in Las1Open.
function Las1Open_Callback(hObject, eventdata, handles)
% hObject    handle to Las1Open (see GCBO)
% eventdata  reserved - to be defined in a future version of MATLAB
% handles    structure with handles and user data (see GUIDATA)
global Las1Shutter;
set(hObject, 'Value', 1);
```

```
set(handles.Las1Close, 'Value', 0);
Las1Shutter.outputSingleScan(1);


% --- Executes on button press in Las1Close.
function Las1Close_Callback(hObject, eventdata, handles)
% hObject    handle to Las1Close (see GCBO)
% eventdata  reserved - to be defined in a future version of MATLAB
% handles    structure with handles and user data (see GUIDATA)
global Las1Shutter;
set(hObject, 'Value', 1);
set(handles.Las1Open, 'Value', 0);
Las1Shutter.outputSingleScan(0);


% --- Executes on button press in Las2Open.
function Las2Open_Callback(hObject, eventdata, handles)
% hObject    handle to Las2Open (see GCBO)
% eventdata  reserved - to be defined in a future version of MATLAB
% handles    structure with handles and user data (see GUIDATA)
global Las2Shutter;
set(hObject, 'Value', 1);
set(handles.Las2Close, 'Value', 0);
Las2Shutter.outputSingleScan(1);


% --- Executes on button press in Las2Close.
function Las2Close_Callback(hObject, eventdata, handles)
% hObject    handle to Las2Close (see GCBO)
% eventdata  reserved - to be defined in a future version of MATLAB
% handles    structure with handles and user data (see GUIDATA)
global Las2Shutter;
set(hObject, 'Value', 1);
set(handles.Las2Open, 'Value', 0);
Las2Shutter.outputSingleScan(0);


% --- Executes on button press in ProbeOpen.
function ProbeOpen_Callback(hObject, eventdata, handles)
% hObject    handle to ProbeOpen (see GCBO)
% eventdata  reserved - to be defined in a future version of MATLAB
% handles    structure with handles and user data (see GUIDATA)
global ProbeShutter;
set(hObject, 'Value', 1);
set(handles.ProbeClose, 'Value', 0);
ProbeShutter.outputSingleScan(1);


% --- Executes on button press in ProbeClose.
function ProbeClose_Callback(hObject, eventdata, handles)
% hObject    handle to ProbeClose (see GCBO)
% eventdata  reserved - to be defined in a future version of MATLAB
% handles    structure with handles and user data (see GUIDATA)
global ProbeShutter;
set(hObject, 'Value', 1);
```

```
set(handles.ProbeOpen, 'Value', 0);
ProbeShutter.outputSingleScan(0);


function PulseEnergyBox_Callback(hObject, eventdata, handles)
% hObject    handle to PulseEnergyBox (see GCBO)
% eventdata  reserved - to be defined in a future version of MATLAB
% handles    structure with handles and user data (see GUIDATA)


% --- Executes during object creation, after setting all properties.
function PulseEnergyBox_CreateFcn(hObject, eventdata, handles)
% hObject    handle to PulseEnergyBox (see GCBO)
% eventdata  reserved - to be defined in a future version of MATLAB
% handles    empty - handles not created until after all CreateFcns called
if ispc && isequal(get(hObject,'BackgroundColor'),
get(0,'defaultUicontrolBackgroundColor'))
    set(hObject,'BackgroundColor','white');
end


% --- Executes on button press in RemoveButton.
function RemoveButton_Callback(hObject, eventdata, handles)
% hObject    handle to RemoveButton (see GCBO)
% eventdata  reserved - to be defined in a future version of MATLAB
% handles    structure with handles and user data (see GUIDATA)
%
%Removes selected data from the QueueTable
global QueueCellSelect;
global QueueInfo;
global QueueNames;
if isempty(QueueCellSelect);
    warndlg('No selection made');
    return;
end
sizeSelect = size(QueueCellSelect);
if sizeSelect(1) > 1
    warndlg('only one item may be selected');
    return;
end

QueueInfo(QueueCellSelect(1,1)) = '';
if length(QueueNames) == 1
    QueueNames{1,1} = '';
    QueueInfo(1).dataset = 0;
else
QueueNames =
QueueNames(~strcmp(QueueNames,QueueNames{QueueCellSelect(1,1),1}));
end
set(handles.QueueTable, 'data',QueueNames);


function varargout = ExecuteGui(varargin)
% EXECUTEGUI MATLAB code for ExecuteGui.fig
```

```
%      EXECUTEGUI, by itself, creates a new EXECUTEGUI or raises the
existing
%      singleton*.
%
%      H = EXECUTEGUI returns the handle to a new EXECUTEGUI or the handle
to
%      the existing singleton*.
%
%      EXECUTEGUI('CALLBACK',hObject,eventData,handles,...) calls the
local
%      function named CALLBACK in EXECUTEGUI.M with the given input
arguments.
%
%      EXECUTEGUI('Property','Value',...) creates a new EXECUTEGUI or
raises the
%      existing singleton*.  Starting from the left, property value pairs
are
%      applied to the GUI before ExecuteGui_OpeningFcn gets called.  An
%      unrecognized property name or invalid value makes property
application
%      stop.  All inputs are passed to ExecuteGui_OpeningFcn via varargin.
%
%      *See GUI Options on GUIDE's Tools menu.  Choose "GUI allows only
one
%      instance to run (singleton)".
%
%       Cannot run as standalone, must be opened from TAsetupGUI
%
% See also: GUIDE, GUIDATA, GUIHANDLES

% Last Modified by GUIDE v2.5 16-Jan-2014 10:37:22

% Begin initialization code - DO NOT EDIT
gui_Singleton = 1;
gui_State = struct('gui_Name',       mfilename, ...
                   'gui_Singleton',  gui_Singleton, ...
                   'gui_OpeningFcn', @ExecuteGui_OpeningFcn, ...
                   'gui_OutputFcn',  @ExecuteGui_OutputFcn, ...
                   'gui_LayoutFcn',  [] , ...
                   'gui_Callback',   []);
if nargin && ischar(varargin{1})
    gui_State.gui_Callback = str2func(varargin{1});
end

if nargout
    [varargout{1:nargout}] = gui_mainfcn(gui_State, varargin{:});
else
    gui_mainfcn(gui_State, varargin{:});
end
% End initialization code - DO NOT EDIT


% --- Executes just before ExecuteGui is made visible.
function ExecuteGui_OpeningFcn(hObject, eventdata, handles, varargin)
% This function has no output args, see OutputFcn.
% hObject    handle to figure
```

```
% eventdata  reserved - to be defined in a future version of MATLAB
% handles    structure with handles and user data (see GUIDATA)
% varargin   command line arguments to ExecuteGui (see VARARGIN)

% Choose default command line output for ExecuteGui
handles.output = hObject;

guidata(hObject, handles);

%Initializes global variables
global QueueNames;
global dataset;
dataset = 1;
global complete;
complete = 1;
global progress;
progress = 0;
global cluster;
cluster = parcluster();
global CompletedNames;
CompletedNames{1,1} = '';
global PlottedDataNames;
PlottedDataNames{1,1} = '';
global color;
color = 0;
global cstring;
cstring = 'krbgmc';

%set axes control to lower plot
set(handles.PastRadio, 'Value', 1);
%set axis to auto
set(handles.AutoAxes, 'Value', 1);
%update display for plot values
xLimits = get(handles.PastAxes, 'Xlim');
yLimits = get(handles.PastAxes, 'YLim');
set(handles.YlowBox, 'String', yLimits(1,1));
set(handles.YhighBox, 'String', yLimits(1,2));
set(handles.XlowBox, 'String', xLimits(1,1));
set(handles.XhighBox, 'String', xLimits(1,2));

%displays queuelist
set(handles.QueueTable,'data',QueueNames);
%This sets the selection of a cell on the DisplayedTable to trigger
%CellSelect, which stores the location of the selected cell.
set(handles.DisplayedTable, 'CellSelectionCallback',@CellSelect);
%This sets the selection of a cell on the AvailableTable to trigger
%CellSelect, which stores the location of the selected cell.
set(handles.AvailableTable, 'CellSelectionCallback',@CellSelect2);
%Creates Timer to operate second core for dataacquisition
handles.ExecuteTimer = timer('ExecutionMode', 'FixedRate', 'Period', 1,
'TimerFcn', {@Execute, handles});
% Update handles structure
guidata(hObject, handles);
%executes closeGUI function when GUI closeout is selected
set(handles.figure1,'CloseRequestFcn',{@closeGUI,handles});
%Starts data acquisition
```

```
start(handles.ExecuteTimer);

% UIWAIT makes ExecuteGui wait for user response (see UIRESUME)
% uiwait(handles.figure1);
function CellSelect(hObject,eventData,handles)
%stores location of selected cell on displayed table
global DisplayedCellSelect;
DisplayedCellSelect = eventData.Indices;

function CellSelect2(hObject,eventData,handles)
%stores location of selected cell on available table
global AvailableCellSelect;
AvailableCellSelect = eventData.Indices;

function Execute(hObject, eventdata, handles)
%Executes on for Execute Timer. Controls operation of 2nd core.
%Acquires all global variables
global QueueInfo;
global dataset;
if dataset > length(QueueInfo);
    return
end
global QueueNames;
global complete;
global Monochromator;
global PMTcontrol;
global Las1Shutter;
global Las2Shutter;
global ProbeShutter;
global delayGen;
global CurrentData;
global progress;
global cluster;
global job;
global CompletedData;
global CompletedNames;
global PlottedDataNames;
global PlottedData;
global color;
global cstring;
%Proceeds if there is no active data acquistions
if complete == 1;
    %sets currently active box to next dataset
    set(handles.CurrentDataBox, 'String', QueueNames{1,1});
    %sets currently active box to carolina blue
    set(handles.CurrentDataBox, 'BackgroundColor', [.33 .63 .82])
    %stores dataset name for display in available table
    if isequal(CompletedNames{1,1},'')
        CompletedNames{1,1} = QueueNames{1,1};
    else
        CompletedNames{length(CompletedNames)+1,1} = QueueNames{1,1};
    end
    %deletes dataset from queue list
    if length(QueueNames)>1
        QueueNames = QueueNames(~strcmp(QueueNames,QueueNames{1,1}));
    else
```

```
        QueueNames{1,1} = '';
    end
    set(handles.QueueTable,'data',QueueNames);
    %Sets Monochromator to appropriate wavelength
    CM112set(Monochromator,'Position', QueueInfo(dataset).Observation);
    pause(1.4)
    %Opens Las1Shutter
    Las1Shutter.outputSingleScan(1);
    %Ensures Laser is receiving pulse signal
    fprintf(delayGen, ':pulse1:state 1<cr><lf>');
    fscanf(delayGen);
    %sets probe lamp to desired state
    if isequal(QueueInfo(dataset).ProbeLamp, 'Pulsed');
        fprintf(delayGen, ':pulse2:state 1<cr><lf>');
        fscanf(delayGen);
    else
        fprintf(delayGen, ':pulse2:state 0<cr><lf>');
        fscanf(delayGen);
    end
    %selects appropriate oscilloscope
    if QueueInfo(dataset).TimeBase < 7
        QueueInfo(dataset).Board = 'CS12502';
    else
        QueueInfo(dataset).Board = 'CS8422';
    end
    complete = 0;
end
%Data Acquisition Switchboard
%Experiment Switch: Case TA or Lum

switch QueueInfo(dataset).Experiment
    case 'TA'
        %TA First Switch: Case Fluorescence Background Yes or No
        switch QueueInfo(dataset).FluorescenceBG
            %No Fluorescence Background
            case 0
                %TA Second Switch: Progress 0,1,2,3
                switch progress
                    %Data Acquisition has not began
                    case 0
                        %Open Laser and Probe Shutters
                        Las2Shutter.outputSingleScan(1);
                        ProbeShutter.outputSingleScan(1);
                        %Generate Time Data
                        [depth, triggerHoldoff, between] =
FindTime(QueueInfo(dataset).TimeBase);
                        QueueInfo(dataset).SegmentSize =
depth+triggerHoldoff;
                        QueueInfo(dataset).TotalTime =(depth-
1)*between+triggerHoldoff*between;
                        CurrentData.Time = ((-
triggerHoldoff*between):between:((depth-1)*between))';
                        %Generate Empty datasets for storage
                        CurrentData.Final =
zeros(1,QueueInfo(dataset).SegmentSize);
                        CurrentData.TA =
zeros(1,QueueInfo(dataset).SegmentSize);
```

```
                        CurrentData.ProbeBG =
zeros(1,QueueInfo(dataset).SegmentSize);
                        %sends job to 2nd core for acquisition of
Transient
                        %Absorption data
                        job = batch(cluster,@CollectAverage, 1,
{QueueInfo(dataset).Averages,QueueInfo(dataset).TimeBase});
                        %Sets progress to 1
                        progress = 1;
                    %Data Acquisition of Transient Absorption data has
been
                    %initialized
                    case 1
                        %try/catch to determine if job is complete, if
yes,
                        %proceed, if no, delay until next call
                        try
                            fetched = fetchOutputs(job);
                        catch err
                            return;
                        end
                        %stores data gathered from job
                        CurrentData.TA = fetched{1,1};
                        %close Laser shutter
                        Las2Shutter.outputSingleScan(0);
                        %plot raw TA data on top Axes
                        hold(handles.NowAxes, 'off');
                        set(handles.ShowingText, 'String',
get(handles.CurrentDataBox, 'String'));
                        plot(handles.NowAxes, CurrentData.Time,
CurrentData.TA, 'Color', 'blue');
                        %sends job to 2nd core for acquisition of probe
                        %background
                        job = batch(cluster,@CollectAverage, 1,
{QueueInfo(dataset).Averages,QueueInfo(dataset).TimeBase});
                        %sets progress to 2
                        progress = 2;
                    %Data acquisition for Probe Background data has been
                    %initialized
                    case 2
                        %try/catch to determine if job is complete, if
yes,
                        %proceed, if no, delay until next call
                        try
                            fetched = fetchOutputs(job);
                        catch err
                            return;
                        end
                        %Stores data obtained from job
                        CurrentData.ProbeBG = fetched{1,1};
                        %plots result on top Axes
                        hold(handles.NowAxes, 'on');
                        plot(handles.NowAxes, CurrentData.Time,
CurrentData.ProbeBG, 'Color', 'green');
                        %creates deltaOD dataset
                        CurrentData.Final = -
log(CurrentData.TA./CurrentData.ProbeBG);
```

```
                        plot(handles.NowAxes, CurrentData.Time,
CurrentData.Final, 'Color', 'black');
                        %sends job to 2nd core for creation of output csv
                        %file for saving
                        job = batch(cluster,@CreateFileTA1, 1,
{QueueInfo(dataset).SegmentSize, QueueInfo(dataset).TotalTime,
QueueInfo(dataset).Board, QueueInfo(dataset).ProbeLamp,
QueueInfo(dataset).Averages, QueueInfo(dataset).RepRate,
QueueInfo(dataset).Filename, QueueInfo(dataset).Comments,
QueueInfo(dataset).PulseEnergy, QueueInfo(dataset).Excitation,
QueueInfo(dataset).Observation, CurrentData.Time, CurrentData.Final,
CurrentData.TA, CurrentData.ProbeBG});
                        %sets progress to 3
                        progress = 3;
                    %csv file creation has been initialized
                    case 3
                        %try/catch to determine if job is complete, if
yes,
                        %proceed, if no, delay until next call
                        try
                            fetched = fetchOutputs(job);
                        catch err
                            return;
                        end
                        %retreives document that has been created
                        doc = fetched{1,1};
                        %saves document as a csv file
                        dlmcell(QueueInfo(dataset).Filename,doc);
                        %plots final result on lower Axes
                        hold(handles.PastAxes, 'on');
                        CompletedData(dataset).Time = CurrentData.Time;
                        CompletedData(dataset).data = CurrentData.Final;
                        %selects color for plot
                        if color > 6
                            color = 0;
                        end
                        col = cstring(mod(color,6)+1);
                        color = color +1;
                        if isequal(PlottedDataNames{1,1},'')
                            PlottedDataNames{1,1} =
get(handles.CurrentDataBox,'String');
                            PlottedData{1,1} = plot(handles.PastAxes,
CompletedData(dataset).Time, CompletedData(dataset).data, 'Color', col);
                        else

PlottedDataNames{length(PlottedDataNames)+1,1}=get(handles.CurrentDataBox,
'String');
                            PlottedData{length(PlottedData)+1,1} =
plot(handles.PastAxes, CompletedData(dataset).Time,
CompletedData(dataset).data, 'Color', col);
                        end
                        %renews data tables
                        set(handles.AvailableTable, 'data',
CompletedNames);
                        set(handles.DisplayedTable, 'data',
PlottedDataNames);
```

```
                        %if this was the last dataset to be taken,
shutters
                        %are closed, probe lamp is set to CW and the user
                        %is notified that data acquisition has ceased.
                        if dataset == length(QueueInfo)
                            PMTcontrol.outputSingleScan(0);
                            Las2Shutter.outputSingleScan(0);
                            Las1Shutter.outputSingleScan(0);
                            ProbeShutter.outputSingleScan(0);
                            fprintf(delayGen, ':pulse2:state 0<cr><lf>');
                            set(handles.CurrentDataBox, 'BackgroundColor',
[1 .2 .2]);
                            set(handles.CurrentDataBox, 'String', '');
                        end
                        %all variables are renewed for next data set
                        clear global CurrentData;
                        progress = 0;
                        complete = 1;
                        dataset = dataset+1;
                end
            %Fluorescence background will be taken
            case 1
                switch progress
                    %data acquisition has not begun
                    case 0
                        %Shutters opened
                        Las2Shutter.outputSingleScan(1);
                        ProbeShutter.outputSingleScan(1);
                        %Time values created
                        [depth, triggerHoldoff, between] =
FindTime(QueueInfo(dataset).TimeBase);
                        QueueInfo(dataset).SegmentSize =
depth+triggerHoldoff;
                        QueueInfo(dataset).TotalTime =(depth-
1)*between+triggerHoldoff*between;
                        CurrentData.Time = ((-
triggerHoldoff*between):between:((depth-1)*between))';
                        %datasets initialized
                        CurrentData.Final =
zeros(1,QueueInfo(dataset).SegmentSize);
                        CurrentData.TA =
zeros(1,QueueInfo(dataset).SegmentSize);
                        CurrentData.ProbeBG =
zeros(1,QueueInfo(dataset).SegmentSize);
                        CurrentData.FluorBG =
zeros(1,QueueInfo(dataset).SegmentSize);
                        %job for data acquisition of Transient absorption
                        %data sent to 2nd core
                        job = batch(cluster,@CollectAverage, 1,
{QueueInfo(dataset).Averages,QueueInfo(dataset).TimeBase});
                        %progress updated to 1
                        progress = 1;
                    %data acquisition for TA data has been initialized
                    case 1
                        %try/catch to determine if job is complete, if
yes,
                        %proceed, if no, delay until next call
```

```
                        try
                            fetched = fetchOutputs(job);
                        catch err
                            return;
                        end
                        %retreives data from job
                        CurrentData.TA = fetched{1,1};
                        %closes Laser shutter for Probed Background
                        Las2Shutter.outputSingleScan(0);
                        %plots data
                        hold(handles.NowAxes, 'off');
                        set(handles.ShowingText, 'String',
get(handles.CurrentDataBox, 'String'));
                        plot(handles.NowAxes, CurrentData.Time,
CurrentData.TA, 'Color', 'blue');
                        %sends probe background job to 2nd core
                        job = batch(cluster,@CollectAverage, 1,
{QueueInfo(dataset).Averages,QueueInfo(dataset).TimeBase});
                        %progress updated to 2
                        progress = 2;
                    %data acquisition for probe background initialized
                    case 2
                        %try/catch to determine if job is complete, if
yes,
                        %proceed, if no, delay until next call
                        try
                            fetched = fetchOutputs(job);
                        catch err
                            return;
                        end
                        %data retreived from job
                        CurrentData.ProbeBG = fetched{1,1};
                        %Laser shutter opened and probe shutter closed
                        Las2Shutter.outputSingleScan(1);
                        ProbeShutter.outputSingleScan(0);
                        %plots data
                        hold(handles.NowAxes, 'on');
                        plot(handles.NowAxes, CurrentData.Time,
CurrentData.ProbeBG);
                        %sends data acquisition job for fluorescence
                        %background to 2nd core
                        job = batch(cluster,@CollectAverage, 1,
{QueueInfo(dataset).Averages,QueueInfo(dataset).TimeBase});
                        %progress updated to 3
                        progress = 3;
                    %data acquisition for fluorescence BG initialized
                    case 3
                        %try/catch to determine if job is complete, if
yes,
                        %proceed, if no, delay until next call
                        try
                            fetched = fetchOutputs(job);
                        catch err
                            return;
                        end
                        %retreives job data
                        CurrentData.FluorBG = fetched{1,1};
```

```
                        %plots job data
                        plot(handles.NowAxes, CurrentData.Time,
CurrentData.FluorBG, 'Color', 'red');
                        %corrects to deltaOD and plots
                        CurrentData.Final = -log((CurrentData.TA-
CurrentData.FluorBG)./CurrentData.ProbeBG);
                        plot(handles.NowAxes, CurrentData.Time,
CurrentData.Final, 'Color', 'black');
                        %sends job to 2nd core for file creation
                        job = batch(cluster,@CreateFileTA2, 1,
{QueueInfo(dataset).SegmentSize, QueueInfo(dataset).TotalTime,
QueueInfo(dataset).Board, QueueInfo(dataset).ProbeLamp,
QueueInfo(dataset).Averages, QueueInfo(dataset).RepRate,
QueueInfo(dataset).Filename, QueueInfo(dataset).Comments,
QueueInfo(dataset).PulseEnergy, QueueInfo(dataset).Excitation,
QueueInfo(dataset).Observation, CurrentData.Time, CurrentData.Final,
CurrentData.TA, CurrentData.ProbeBG, CurrentData.FluorBG});
                        %progress updated to 4
                        progress = 4;
                    %file creation job initialized
                    case 4
                        %try/catch to determine if job is complete, if
yes,
                        %proceed, if no, delay until next call
                        try
                            fetched = fetchOutputs(job);
                        catch err
                            return;
                        end
                        %retreive job data
                        doc = fetched{1,1};
                        %saves as csv file
                        dlmcell(QueueInfo(dataset).Filename,doc);
                        %plots data on lower plot
                        hold(handles.PastAxes, 'on');
                        CompletedData(dataset).Time = CurrentData.Time;
                        CompletedData(dataset).data = CurrentData.Final;
                        %selects color for plotting
                        if color > 6
                            color = 0;
                        end
                        col = cstring(mod(color,6)+1);
                        color = color +1;
                        if isequal(PlottedDataNames{1,1},'')
                            PlottedDataNames{1,1} =
get(handles.CurrentDataBox,'String');
                            PlottedData{1,1} = plot(handles.PastAxes,
CompletedData(dataset).Time, CompletedData(dataset).data,'Color',col);
                        else

PlottedDataNames{length(PlottedDataNames)+1,1}=get(handles.CurrentDataBox,
'String');
                            PlottedData{length(PlottedData)+1,1} =
plot(handles.PastAxes, CompletedData(dataset).Time,
CompletedData(dataset).data,'Color', col);
                        end
                        %renews data tables
```

```
                        set(handles.AvailableTable, 'data',
CompletedNames);
                        set(handles.DisplayedTable, 'data',
PlottedDataNames);
                        %if this was the last dataset to be taken,
shutters
                        %are closed, probe lamp is set to CW and the user
                        %is notified that data acquisition has ceased.
                        if dataset == length(QueueInfo)
                            PMTcontrol.outputSingleScan(0);
                            Las2Shutter.outputSingleScan(0);
                            Las1Shutter.outputSingleScan(0);
                            ProbeShutter.outputSingleScan(0);
                            fprintf(delayGen, ':pulse2:state 0<cr><lf>');
                            set(handles.CurrentDataBox, 'BackgroundColor',
[1 .2 .2]);
                            set(handles.CurrentDataBox, 'String', '');
                        end
                        %resets data acquisition variables for next job
                        clear global CurrentData;
                        progress = 0;
                        complete = 1;
                        dataset = dataset+1;
                end
            end
            autoupdate2(hObject,eventdata, handles);
        %Luminescence Acquisition
        case 'Lum'
            switch progress
                %data acquisition has not begun
                case 0
                    %Opens Laser shutter, closes probe shutter
                    Las2Shutter.outputSingleScan(1);
                    ProbeShutter.outputSingleScan(0);
                    %generates time data
                    [depth, triggerHoldoff, between] =
FindTime(QueueInfo(dataset).TimeBase);
                    QueueInfo(dataset).SegmentSize = depth+triggerHoldoff;
                    QueueInfo(dataset).TotalTime =(depth-
1)*between+triggerHoldoff*between;
                    CurrentData.Time = ((-
triggerHoldoff*between):between:((depth-1)*between))';
                    CurrentData.Lum = zeros(1,QueueInfo(dataset).SegmentSize);
                    %sends job to 2nd core for acquistion of luminescence data
                    job = batch(cluster,@CollectAverage, 1,
{QueueInfo(dataset).Averages,QueueInfo(dataset).TimeBase});
                    %progress updated to 1
                    progress = 1;
                case 1
                    %try/catch to determine if job is complete, if yes,
                    %proceed, if no, delay until next call
                    try
                        fetched = fetchOutputs(job);
                    catch err
                        return;
                    end
                    %retreives data from job
```

```
                CurrentData.Lum = fetched{1,1};
                set(handles.ShowingText, 'String',
get(handles.CurrentDataBox, 'String'));
                %plots data
                hold(handles.NowAxes, 'off');
                plot(handles.NowAxes, CurrentData.Time, CurrentData.Lum,
'Color', 'blue');
                %sends job for file creation
                job = batch(cluster,@CreateFileLum, 1,
{QueueInfo(dataset).SegmentSize, QueueInfo(dataset).TotalTime,
QueueInfo(dataset).Board, QueueInfo(dataset).ProbeLamp,
QueueInfo(dataset).Averages, QueueInfo(dataset).RepRate,
QueueInfo(dataset).Filename, QueueInfo(dataset).Comments,
QueueInfo(dataset).PulseEnergy, QueueInfo(dataset).Excitation,
QueueInfo(dataset).Observation, CurrentData.Time, CurrentData.Lum});
                progress = 2;
            case 2
                %try/catch to determine if job is complete, if yes,
                %proceed, if no, delay until next call
                try
                    fetched = fetchOutputs(job);
                catch err
                    return;
                end
                %retreives file from job
                doc = fetched{1,1};
                %saves file as csv
                dlmcell(QueueInfo(dataset).Filename,doc);
                %plots data on lower axes
                hold(handles.PastAxes, 'on');
                CompletedData(dataset).Time = CurrentData.Time;
                CompletedData(dataset).data = CurrentData.Lum;
                if color > 6
                    color = 0;
                end
                col = cstring(mod(color,6)+1);
                color = color +1;
                if isequal(PlottedDataNames{1,1},'')
                    PlottedDataNames{1,1} =
get(handles.CurrentDataBox,'String');
                    PlottedData{1,1} = plot(handles.PastAxes,
CompletedData(dataset).Time, CompletedData(dataset).data, 'Color', col);
                else

PlottedDataNames{length(PlottedDataNames)+1,1}=get(handles.CurrentDataBox,
'String');
                    PlottedData{length(PlottedData)+1,1} =
plot(handles.PastAxes, CompletedData(dataset).Time,
CompletedData(dataset).data, 'Color', col);
                end
                %renews data tables
                set(handles.AvailableTable, 'data', CompletedNames);
                set(handles.DisplayedTable, 'data', PlottedDataNames);
                clear global CurrentData;
                %if this was the last dataset to be taken, shutters
                %are closed, probe lamp is set to CW and the user
                %is notified that data acquisition has ceased.
```

```
                if dataset == length(QueueInfo)
                    PMTcontrol.outputSingleScan(0);
                    Las2Shutter.outputSingleScan(0);
                    Las1Shutter.outputSingleScan(0);
                    ProbeShutter.outputSingleScan(0);
                    fprintf(delayGen, ':pulse2:state 0<cr><lf>');
                    set(handles.CurrentDataBox, 'BackgroundColor', [1 .2
.2]);
                    set(handles.CurrentDataBox, 'String', '');
                end
                %resets parameters for next dataset
                progress = 0;
                complete = 1;
                dataset = dataset+1;
        end
        autoupdate2(hObject,eventdata, handles);
end




% --- Outputs from this function are returned to the command line.
function varargout = ExecuteGui_OutputFcn(hObject, eventdata, handles)
% varargout  cell array for returning output args (see VARARGOUT);
% hObject    handle to figure
% eventdata  reserved - to be defined in a future version of MATLAB
% handles    structure with handles and user data (see GUIDATA)

% Get default command line output from handles structure
varargout{1} = handles.output;

function closeGUI(src,evnt, handles)
%called on closing of GUI, clears all global parameters and sits
%instruments to default states
selection = questdlg('Are you sure?','Close','Yes','No','Yes');
switch selection
    case 'Yes'
        if isequal(get(handles.ExecuteTimer, 'Running'),'on')
            stop(handles.ExecuteTimer);
        end
        CsMl_FreeAllSystems();
        global Monochromator;
        fclose(Monochromator);
        clear global Monachromator;
        global delayGen;
        fprintf(delayGen, ':pulse2:state 0<cr><lf>');
        fclose(delayGen);
        clear global delayGen;
        global PMTcontrol;
        PMTcontrol.outputSingleScan(0);
        clear global PMTcontrol;
        clear global Las1Shutter;
        clear global Las2Shutter;
        clear global ProbeShutter;
        clear global dataset;
        clear global complete;
```

```
        clear global progress;
        clear global cluster;
        clear global job;
        clear global CompletedData;
        clear global CompletedNames;
        clear global PlottedDataNames;
        clear global PlottedData;
        clear global QueueInfo;
        clear global QueueNames;
        clear global AvailableCellSelect;
        clear global DisplayedCellSelect;
        clear global color;
        clear global cstring;
        clear global col;
        delete(gcf)
    case 'No'
        return
end


function CurrentDataBox_Callback(hObject, eventdata, handles)
% hObject    handle to CurrentDataBox (see GCBO)
% eventdata  reserved - to be defined in a future version of MATLAB
% handles    structure with handles and user data (see GUIDATA)



% --- Executes during object creation, after setting all properties.
function CurrentDataBox_CreateFcn(hObject, eventdata, handles)
% hObject    handle to CurrentDataBox (see GCBO)
% eventdata  reserved - to be defined in a future version of MATLAB
% handles    empty - handles not created until after all CreateFcns called
if ispc && isequal(get(hObject,'BackgroundColor'),
get(0,'defaultUicontrolBackgroundColor'))
    set(hObject,'BackgroundColor','white');
end


% --- Executes on button press in GoButton.
function GoButton_Callback(hObject, eventdata, handles)
% hObject    handle to GoButton (see GCBO)
% eventdata  reserved - to be defined in a future version of MATLAB
% handles    structure with handles and user data (see GUIDATA)
%
%starts timer for data acquisition
if isequal(get(handles.ExecuteTimer, 'Running'),'off')
    set(handles.CurrentDataBox, 'BackgroundColor', [.33 .63 .82]);
    start(handles.ExecuteTimer);
else
    warndlg('Already Running');
end


% --- Executes on button press in StopButton.
function StopButton_Callback(hObject, eventdata, handles)
```

```
% hObject    handle to StopButton (see GCBO)
% eventdata  reserved - to be defined in a future version of MATLAB
% handles    structure with handles and user data (see GUIDATA)
%
%stops timer for data acquisition
if isequal(get(handles.ExecuteTimer, 'Running'),'on')
    set(handles.CurrentDataBox, 'BackgroundColor', [1 .2 .2]);
    stop(handles.ExecuteTimer);
else
    warndlg('Not Running');
end


% --- Executes on button press in PlotButton.
function PlotButton_Callback(hObject, eventdata, handles)
% hObject    handle to PlotButton (see GCBO)
% eventdata  reserved - to be defined in a future version of MATLAB
% handles    structure with handles and user data (see GUIDATA)
global PlottedData;
global PlottedDataNames;
global AvailableCellSelect;
global CompletedData;
global CompletedNames;
global color;
global cstring;
if isempty(AvailableCellSelect);
    warndlg('No selection made');
    return;
end
sizeSelect = size(AvailableCellSelect);
if sizeSelect(1) > 1
    warndlg('only one dataset may be selected');
    return;
end
hold(handles.PastAxes, 'on');
if color > 6
    color = 0;
end
col = cstring(mod(color,6)+1);
color = color +1;
if isequal(PlottedDataNames{1,1}, '')
    PlottedData{1,1} = plot(handles.PastAxes,
CompletedData(AvailableCellSelect(1,1)).Time,CompletedData(AvailableCellSe
lect(1,1)).data, 'Color', col);
    PlottedDataNames{1,1} = CompletedNames{AvailableCellSelect(1,1),1};
else
    PlottedData{length(PlottedData)+1,1} = plot(handles.PastAxes,
CompletedData(AvailableCellSelect(1,1)).Time,CompletedData(AvailableCellSe
lect(1,1)).data, 'Color', col);
    PlottedDataNames{length(PlottedDataNames)+1,1} =
CompletedNames{AvailableCellSelect(1,1),1};
end
set(handles.DisplayedTable, 'data', PlottedDataNames);
autoupdate2(hObject,eventdata, handles);

% --- Executes on button press in RemoveButton.
```

```
function RemoveButton_Callback(hObject, eventdata, handles)
% hObject    handle to RemoveButton (see GCBO)
% eventdata  reserved - to be defined in a future version of MATLAB
% handles    structure with handles and user data (see GUIDATA)
global PlottedData;
global PlottedDataNames;
global DisplayedCellSelect;
if isempty(DisplayedCellSelect);
    warndlg('No selection made');
    return;
end
sizeSelect = size(DisplayedCellSelect);
if sizeSelect(1) > 1
    warndlg('only one dataset may be selected');
    return;
end
delete(PlottedData{DisplayedCellSelect(1,1),1})
PlottedData{DisplayedCellSelect(1,1),1} = '';
PlottedDataNames{DisplayedCellSelect(1,1),1} = '';
if length(PlottedData) ~= 1
    PlottedData =
PlottedData(~strcmp(PlottedData,PlottedData{DisplayedCellSelect(1,1),1}));
end
if length(PlottedDataNames) ~= 1
    PlottedDataNames =
PlottedDataNames(~strcmp(PlottedDataNames,PlottedDataNames{DisplayedCellSe
lect(1,1),1}));
end
set(handles.DisplayedTable, 'data', PlottedDataNames);
autoupdate2(hObject,eventdata, handles);


% --- Executes on button press in AutoAxes.
function AutoAxes_Callback(hObject, eventdata, handles)
% hObject    handle to AutoAxes (see GCBO)
% eventdata  reserved - to be defined in a future version of MATLAB
% handles    structure with handles and user data (see GUIDATA)
if get(handles.NowRadio, 'Value') ==1
    if get(hObject, 'Value') == 1
        axis(handles.NowAxes, 'auto')
    else
        axis(handles.NowAxes, 'manual')
    end
else
    if get(hObject, 'Value') == 1
        axis(handles.PastAxes, 'auto')
    else
        axis(handles.PastAxes, 'manual')
    end
end
autoupdate2(hObject,eventdata, handles);
% Hint: get(hObject,'Value') returns toggle state of AutoAxes



function XlowBox_Callback(hObject, eventdata, handles)
```

```
% hObject    handle to XlowBox (see GCBO)
% eventdata  reserved - to be defined in a future version of MATLAB
% handles    structure with handles and user data (see GUIDATA)
new = str2double(get(hObject, 'String'));
opposite = get(handles.XhighBox, 'String');
oppositenum = str2double(opposite);
while (new > oppositenum) || isnan(new)
    new = str2double(inputdlg(strcat('invalid bounds, enter value less
than ', opposite,')')));
    if isempty(new)
        return;
    end
end
if get(handles.PastRadio, 'Value') == 1
    xlim(handles.PastAxes, [new,oppositenum]);
else
    xlim(handles.NowAxes, [new,oppositenum]);
end
set(handles.AutoAxes, 'Value', 0);
autoupdate2(hObject,eventdata, handles);



% --- Executes during object creation, after setting all properties.
function XlowBox_CreateFcn(hObject, eventdata, handles)
% hObject    handle to XlowBox (see GCBO)
% eventdata  reserved - to be defined in a future version of MATLAB
% handles    empty - handles not created until after all CreateFcns called
if ispc && isequal(get(hObject,'BackgroundColor'),
get(0,'defaultUicontrolBackgroundColor'))
    set(hObject,'BackgroundColor','white');
end



function YlowBox_Callback(hObject, eventdata, handles)
% hObject    handle to YlowBox (see GCBO)
% eventdata  reserved - to be defined in a future version of MATLAB
% handles    structure with handles and user data (see GUIDATA)
new = str2double(get(hObject, 'String'));
opposite = get(handles.YhighBox, 'String');
oppositenum = str2double(opposite);
while (new > oppositenum) || isnan(new)
    new = str2double(inputdlg(strcat('invalid bounds, enter value less
than ', opposite,')')));
    if isempty(new)
        return;
    end
end
if get(handles.PastRadio, 'Value') == 1
    ylim(handles.PastAxes, [new,oppositenum]);
else
    ylim(handles.NowAxes, [new,oppositenum]);
end
set(handles.AutoAxes, 'Value', 0);
autoupdate2(hObject,eventdata, handles);
```

```
% --- Executes during object creation, after setting all properties.
function YlowBox_CreateFcn(hObject, eventdata, handles)
% hObject    handle to YlowBox (see GCBO)
% eventdata  reserved - to be defined in a future version of MATLAB
% handles    empty - handles not created until after all CreateFcns called

% Hint: edit controls usually have a white background on Windows.
%       See ISPC and COMPUTER.
if ispc && isequal(get(hObject,'BackgroundColor'),
get(0,'defaultUicontrolBackgroundColor'))
    set(hObject,'BackgroundColor','white');
end



function XhighBox_Callback(hObject, eventdata, handles)
% hObject    handle to XhighBox (see GCBO)
% eventdata  reserved - to be defined in a future version of MATLAB
% handles    structure with handles and user data (see GUIDATA)
new = str2double(get(hObject, 'String'))
opposite = get(handles.XlowBox, 'String');
oppositenum = str2double(opposite)
while (new < oppositenum) || isnan(new)
    new = str2double(inputdlg(strcat('invalid bounds, enter value greater
than ', opposite,')')));
    if isempty(new)
        return;
    end
end
if get(handles.PastRadio, 'Value') == 1
    xlim(handles.PastAxes, [oppositenum,new]);
else
    xlim(handles.NowAxes, [oppositenum,new]);
end
set(handles.AutoAxes, 'Value', 0);
autoupdate2(hObject,eventdata, handles);


% --- Executes during object creation, after setting all properties.
function XhighBox_CreateFcn(hObject, eventdata, handles)
% hObject    handle to XhighBox (see GCBO)
% eventdata  reserved - to be defined in a future version of MATLAB
% handles    empty - handles not created until after all CreateFcns called
if ispc && isequal(get(hObject,'BackgroundColor'),
get(0,'defaultUicontrolBackgroundColor'))
    set(hObject,'BackgroundColor','white');
end



function YhighBox_Callback(hObject, eventdata, handles)
% hObject    handle to YhighBox (see GCBO)
% eventdata  reserved - to be defined in a future version of MATLAB
```

```
% handles    structure with handles and user data (see GUIDATA)
new = str2double(get(hObject, 'String'));
opposite = get(handles.YlowBox, 'String');
oppositenum = str2double(opposite);
while (new < oppositenum) || isnan(new)
    new = str2double(inputdlg(strcat('invalid bounds, enter value greater
than ', opposite,')')));
    if isempty(new)
        return;
    end
end
if get(handles.PastRadio, 'Value') == 1
    ylim(handles.PastAxes, [oppositenum,new]);
else
    ylim(handles.NowAxes, [oppositenum,new]);
end
set(handles.AutoAxes, 'Value', 0);


% --- Executes during object creation, after setting all properties.
function YhighBox_CreateFcn(hObject, eventdata, handles)
% hObject    handle to YhighBox (see GCBO)
% eventdata  reserved - to be defined in a future version of MATLAB
% handles    empty - handles not created until after all CreateFcns called
if ispc && isequal(get(hObject,'BackgroundColor'),
get(0,'defaultUicontrolBackgroundColor'))
    set(hObject,'BackgroundColor','white');
end


% --- Executes on button press in NowRadio.
function NowRadio_Callback(hObject, eventdata, handles)
% hObject    handle to NowRadio (see GCBO)
% eventdata  reserved - to be defined in a future version of MATLAB
% handles    structure with handles and user data (see GUIDATA)
set(hObject, 'Value', 1);
set(handles.PastRadio, 'Value', 0);
if isequal(get(handles.NowAxes,
'XLimMode'),'manual')||isequal(get(handles.NowAxes, 'YLimMode'),'manual')
    set(handles.AutoAxes, 'Value', 0);
else
    set(handles.AutoAxes, 'Value', 1);
end
autoupdate2(hObject,eventdata, handles);


% --- Executes on button press in PastRadio.
function PastRadio_Callback(hObject, eventdata, handles)
% hObject    handle to PastRadio (see GCBO)
% eventdata  reserved - to be defined in a future version of MATLAB
% handles    structure with handles and user data (see GUIDATA)
set(hObject, 'Value', 1);
set(handles.NowRadio, 'Value', 0);
if isequal(get(handles.PastAxes,
'XLimMode'),'manual')||isequal(get(handles.PastAxes, 'YLimMode'),'manual')
    set(handles.AutoAxes, 'Value', 0);
```

```
else
    set(handles.AutoAxes, 'Value', 1);
end
autoupdate2(hObject,eventdata, handles);


function autoupdate2(hObject,eventdata, handles)
%updates axes parameter display
if get(handles.PastRadio, 'Value') ==1
    xLimits = get(handles.PastAxes, 'Xlim');
    yLimits = get(handles.PastAxes, 'YLim');
else
    xLimits = get(handles.NowAxes, 'Xlim');
    yLimits = get(handles.NowAxes, 'YLim');
end
set(handles.YlowBox, 'String', yLimits(1,1));
set(handles.YhighBox, 'String', yLimits(1,2));
set(handles.XlowBox, 'String', xLimits(1,1));
set(handles.XhighBox, 'String', xLimits(1,2));



function [ Depth, TriggerHoldoff, between ] = setupDigitizer(
TimeRangeValue, handle )
if TimeRangeValue == 1
    SampleRate = 5e8;
    Depth = 912;
    TriggerHoldoff = 112;
    between = 2e-9;
elseif TimeRangeValue == 2
    SampleRate = 5e8;
    Depth = 9008;
    TriggerHoldoff = 1008;
    between = 2e-9;
elseif TimeRangeValue == 3
    SampleRate = 2.5e8;
    Depth = 9008;
    TriggerHoldoff = 1008;
    between = 4e-9;
elseif TimeRangeValue == 4
    SampleRate = 1.25e8;
    Depth = 11264;
    TriggerHoldoff = 1264;
    between = 8e-9;
elseif TimeRangeValue == 5
    SampleRate = 2.5e7;
    Depth = 9008;
    TriggerHoldoff = 1008;
    between = 4e-8;
elseif TimeRangeValue == 6
    SampleRate = 2.5e7;
    Depth = 18000;
    TriggerHoldoff = 2000;
    between = 4e-8;
elseif TimeRangeValue == 7
```

```
    SampleRate = 1e7;
    Depth = 90000;
    TriggerHoldoff = 10000;
    between = 1e-7;
elseif TimeRangeValue == 8
    SampleRate = 2.5e6;
    Depth = 90000;
    TriggerHoldoff = 10000;
    between = 4e-7;
elseif TimeRangeValue == 9
    SampleRate = 1e6;
    Depth = 90000;
    TriggerHoldoff = 10000;
    between = 1e-6;
elseif TimeRangeValue == 10
    SampleRate = 2e5;
    Depth = 90000;
    TriggerHoldoff = 10000;
    between = 5e-6;
elseif TimeRangeValue == 11
    SampleRate = 1e5;
    Depth = 90000;
    TriggerHoldoff = 10000;
    between = 1e-5;
elseif TimeRangeValue == 12
    SampleRate = 1e4;
    Depth = 90000;
    TriggerHoldoff = 10000;
    between = 1e-4;
elseif TimeRangeValue == 13
    SampleRate = 2e3;
    Depth = 90000;
    TriggerHoldoff = 10000;
    between = 5e-4;
else
    warndlg('Time Range Conversion Failed');
end
[ret, sysinfo] = CsMl_GetSystemInfo(handle);
CsMl_ErrorHandler(ret, 1, handle);

acqInfo.SampleRate = SampleRate;
acqInfo.ExtClock = 0;
acqInfo.Mode = CsMl_Translate('Dual', 'Mode');
acqInfo.SegmentCount = 1;
acqInfo.Depth = Depth;
acqInfo.SegmentSize = Depth + TriggerHoldoff;
acqInfo.TriggerTimeout = 1000000;
acqInfo.TriggerHoldoff = TriggerHoldoff;
acqInfo.TriggerDelay = 0;
acqInfo.TimeStampConfig = 0;

[ret] = CsMl_ConfigureAcquisition(handle, acqInfo);
CsMl_ErrorHandler(ret, 1, handle);

% Set up all the channels even though
% they might not all be used. For example
```

```
% in a 2 board master / slave system, in single channel
% mode only channels 1 and 3 are used.
for i = 1:sysinfo.ChannelCount
    chan(i).Channel = i;
    chan(i).Coupling = CsMl_Translate('DC', 'Coupling');
    chan(i).DiffInput = 0;
    chan(i).InputRange = 2000;
    chan(i).Impedance = 50;
    chan(i).DcOffset = 0;
    chan(i).DirectAdc = 0;
    chan(i).Filter = 0;
end;

[ret] = CsMl_ConfigureChannel(handle, chan);
CsMl_ErrorHandler(ret, 1, handle);

trig.Trigger = 1;
trig.Slope = CsMl_Translate('Positive', 'Slope');
trig.Level = 2;
trig.Source = 1;
trig.ExtCoupling = CsMl_Translate('DC', 'ExtCoupling');
trig.ExtRange = 2000;

[ret] = CsMl_ConfigureTrigger(handle, trig);
CsMl_ErrorHandler(ret, 1, handle);
end


function [ doc ] = CreateFileTA1(SegmentSize, TotalTime, Board, ProbeLamp,
Averages, RepRate, Filename, Comments, PulseEnergy, Excitation,
Observation, Time, deltaOD, TA, ProbeBG)
%UNTITLED5 Summary of this function goes here
%   Detailed explanation goes here
doc = cell(16+length(Time),1);
doc{1,1} = {'Transient Adsorption without Fluorescence Background'};
doc{2,1} = {''};
breaks = regexp(Filename, '\');
lengthBreaks = length(breaks);
lengthName = length(Filename);
name = Filename((breaks(1,lengthBreaks)+1):(lengthName-4));
doc{3,1} = {['Dataset: ' name]};
doc{4,1} = {['Comments: ' Comments]};
doc{5,1} = {['Datapoints: ' num2str(SegmentSize)]};
doc{6,1} = {['Total Time: ' num2str(TotalTime)]};
doc{7,1} = {['Scope: ' Board]};
doc{8,1} = {['Probe Lamp: ' ProbeLamp]};
doc{9,1} = {['Scope: ' Board]};
doc{10,1} = {['Averages: ' num2str(Averages)]};
doc{11,1} = {['Rep Rate: ' num2str(RepRate)]};
doc{12,1} = {['Pulse Energy: ' PulseEnergy]};
doc{13,1} = {['Excitation Wavelength: ' Excitation]};
doc{14,1} = {['Observation Wavelength: ' num2str(Observation)]};
doc{15,1} = {''};
doc{16,1} = {'Time , deltaOD , rawTA , Probe BG'};
j = 1;
for i = 17:(length(Time)+16)
```

```
    doc{i,1} = {[num2str(Time(j,1)) ' , ' num2str(deltaOD(j,1)) ' , '
num2str(TA(j,1)) ' , ' num2str(ProbeBG(j,1))]};
    j = j +1;
end

end


function [ Output ] = CollectAverage( Averages, TimeBase)
%UNTITLED Summary of this function goes here
%   Detailed explanation goes here
if TimeBase < 7
    Requested.Board = 1280; %CS12502
else
    Requested.Board = 214;  %CS8422
end
systems = CsMl_Initialize;
CsMl_ErrorHandler(systems);

[ret, Scope] = CsMl_GetSystem(Requested);
CsMl_ErrorHandler(ret);

[ret, sysinfo] = CsMl_GetSystemInfo(Scope);
CsMl_ErrorHandler(ret);
pause(.2)
for i = 1:Averages
    setupDigitizer(TimeBase, Scope);
    [ret] = CsMl_Commit(Scope);
    CsMl_ErrorHandler(ret, 1, Scope);
    ret = CsMl_Capture(Scope);
    CsMl_ErrorHandler(ret, 1, Scope);
        status = CsMl_QueryStatus(Scope);
    while status ~= 0
        status = CsMl_QueryStatus(Scope);
    end
    [ret, acqInfo] = CsMl_QueryAcquisition(Scope);
    transfer.Mode = CsMl_Translate('Default', 'TxMode');
    transfer.Segment = 1;
    transfer.Start = -acqInfo.TriggerHoldoff;
    transfer.Length = acqInfo.SegmentSize;
    transfer.Channel = 2;
    % Transfer the data
    [ret, data, actual] = CsMl_Transfer(Scope, transfer);
    if i == 1
        Output = data;
    else
        Output = ((i-1)*Output+data)/i;
    end
end
Output=Output';
CsMl_FreeSystem(Scope);
end


function [QC9514, location] = OpenQC9514Link(loc)
```

```
%OpenQC9514Link Opens communication with the QC9514 digital delay
generator
%   input
%       loc = com location of pulse generator, not required
%
%   output
%       QC9514 = object containing device
if nargin == 1
    %connecting
    location = loc;
    QC9514 = serial(loc);
    try
        %opening communication
        fopen(QC9514);
        %Executing monochromotar echo command
        fprintf(QC9514,'*IDN?<cr><lf>');
        %pausing to allow monochromator to process
        pause(.2);
        %retreiving echo
        response = fscanf(QC9514);
        read = regexp(response, '9514', 'once');
        if isempty(read)
            fclose(QC9514);
            clear QC9514;
            QC9514 = 'device not found';
        end
    catch
        %if an error occured, connections are closed
        fclose(QC9514);
        clear QC9514;
        QC9514 = 'device not found';
    end
%handles no input situation
else
    %serial locations to check
    COM ={'COM1','COM2','COM3','COM4','COM5','COM6','COM7','COM8'};
    %COM = {'COM6','COM7','COM8'};
    %value for looping
    i = 1;
    %boolean for connection made
    linked = 0;
    %while loop executes while link has not been made and all ports have
    %not been checked
    while (linked == 0)&&(i<=length(COM))
        %boolean for location possible
        available = 1;
        try
            %retreiving location to check from array
            location = COM{i};
            %Connection being made
            QC9514 = serial(location);
            %Opening communication
            fopen(QC9514);
            %executing echo to monochromotar
            fprintf(QC9514,'*IDN?<cr><lf>');
            %pausing to allow monochromator to process
            pause(.2);
```

```
            if QC9514.BytesAvailable > 5
                %retreiving echo
                response = fscanf(QC9514);
            end
        catch
            %closing connection if monochromotar not present
            try
                fclose(QC9514);
                clear CM112;
            catch
            end
            QC9514 = 'device not found';
            available = 0;
        end
        %opening connection if device detected
        if available == 1;
            fprintf(QC9514,'*IDN?<cr><lf>');
            %pausing to allow monochromator to process
            pause(.2);
            %retreiving echo
            if QC9514.BytesAvailable > 5
                response = fscanf(QC9514);
                read = regexp(response, '9514', 'once');
            else
                read = [];
            end
            %signifying link
            if ~isempty(read)
                linked = 1;
            else
                QC9514 = 'device not found';
            end
        end
        i = i+1;
    end
end

end


function [ outString] = ShiftDecimal( inString, places )
number = str2num(inString)*10^places;
if places < 0
    outString = num2str(number, '%.9f');
else
    outString = num2str(number);
end


function [ CM112 ] = OpenCM112Link( loc )
%OpenCM112Link opens communication with the CM112 Monochromator
%  input
%   loc = location of monochromator (i.e. 'COM3')
%  output
%   CM112 = device for use
%
```

```
%  If location is input, function searches location for monochromator, if
%  no location is input, function searches all available serial ports for
%  monochromator.

%handles input argument
if nargin == 1
    %connecting
    CM112 = serial(loc);
    try
        %opening communication
        fopen(CM112);
        %Executing monochromotar echo command
        fwrite(CM112, 27);
        %pausing to allow monochromator to process
        pause(.2)
        %retreiving echo
        response = fread(CM112, CM112.BytesAvailable);
    catch
        %if an error occured, connections are closed
        fclose(CM112);
        clear CM112;
        CM112 = 'device not found';
    end
%handles no input situation
else
    %serial locations to check
    COM ={'COM1','COM2','COM3','COM4','COM5','COM6','COM7','COM8'};
    %value for looping
    i = 1;
    %boolean for connection made
    linked = 0;
    %while loop executes while link has not been made and all ports have
    %not been checked
    while (linked == 0)&&(i<=length(COM))
        %boolean for location possible
        available = 1;
        try
            %retreiving location to check from array
            location = COM{i};
            %Connection being made
            CM112 = serial(location);
            %Opening communication
            fopen(CM112);
            %executing echo to monochromotar
            fwrite(CM112, 27);
            %pausing to allow instrument to respond
            pause(.2);
            %retreiving echo
            response = fread(CM112, CM112.BytesAvailable);
        catch
            %closing connection if monochromotar not present
            try
                fclose(CM112);
                clear CM112;
            catch
            end
            CM112 = 'device not found';
```

```
            available = 0;
        end
        %opening connection if device detected
        if available == 1;
            fwrite(CM112, 27);
            pause(.2)
            response = fread(CM112, CM112.BytesAvailable);
            %signifying link
            if response == 27
                linked = 1;
            else
                CM112 = 'device not found';
            end
        end
        i = i+1;
    end
end


function [Accepted] = CM112set( device, setting, setTo )
%CM112set sets instrument properties for the CM112 monochromator
%
%   input
%    device = object representing monochromator
%    setting = setting to be changed, options are:
%       'Position'  - sets the wavelength
%       'Units'     - sets the Units
%       (00=microns,01=nanometers,02=angstroms)
%
%    setTo = value to set setting to
%
%   output
%    Accepted = returns 1 if setting changed, 0 if not.
%
Answer = 0;
if isequal(setting, 'Position')
    byte = 16;
    [hibyte lowbyte] = readable2byte(setTo);
    Answer = 1;
end
if isequal(setting, 'Units')
    byte = 50;
    Answer = 2;
end
if Answer == 1;
    fwrite(device, [byte hibyte lowbyte]);
    pause(.4);
    response = fread(device, device.BytesAvailable);
end
if Answer == 2;
    fwrite(device, [byte setTo])
    pause(.4);
    response = fread(device, device.BytesAvailable);
end
if response(1) >128 || Answer ==0
    Accepted = 0;
```

```
else
    Accepted = 1;
end

end


function [ Answer ] = CM112get( device, query )
%CM112get returns requested information about the monochromator
%   input
%    device = object for the monochromator
%    query = requesed info
%
%    info that can be requested
%                - OUTPUT
%   'Position'   - wavelength
%   'Grooves'    - Grooves per mm on grating
%   'Blaze'      - not sure what this is
%   'Grating#'   - Current Grating Number
%   'Speed'      - Current Scan Speed
%   'Gratings'   - Number of Gratings
%   'Units'      - wavelength units (0=microns, 1=nanometers, 2=angstroms)
%   'Serial'     - Serial Number
%
%   output
%    Answer = OUTPUT
Answer = 'Invalid input argument';
if isequal(query, 'Position')
    byte = 00;
    Answer = 1;
end
if isequal(query, 'Grooves')
    byte = 02;
    Answer = 1;
end
if isequal(query, 'Blaze')
    byte = 03;
    Answer = 1;
end
if isequal(query, 'Grating#')
    byte = 04;
    Answer = 1;
end
if isequal(query, 'Speed')
    byte = 05;
    Answer = 1;
end
if isequal(query, 'Gratings')
    byte = 13;
    Answer = 1;
end
if isequal(query, 'Units')
    byte = 14;
    Answer = 1;
end
if isequal(query, 'Serial')
```

```
    byte = 19;
    Answer = 1;
end
if Answer == 1
    fwrite(device, [56 byte])
    pause(.2);
    response = fread(device, device.BytesAvailable);
    Answer = byte2readable(response(1), response(2));
end
end


function [ readable ] = byte2readable( hibyte,lowbyte )
%Converts hibyte to a readable number
readable = hibyte*256 +lowbyte;
end
```

APPENDIX G. FINITE DIFFERENCE ELECTROCHEMICAL SIMULATION

G.1 Extracting Kinetics Information from Voltammograms in the 'Total Catalysis' Zone

KT2: Simulation of concentration profiles

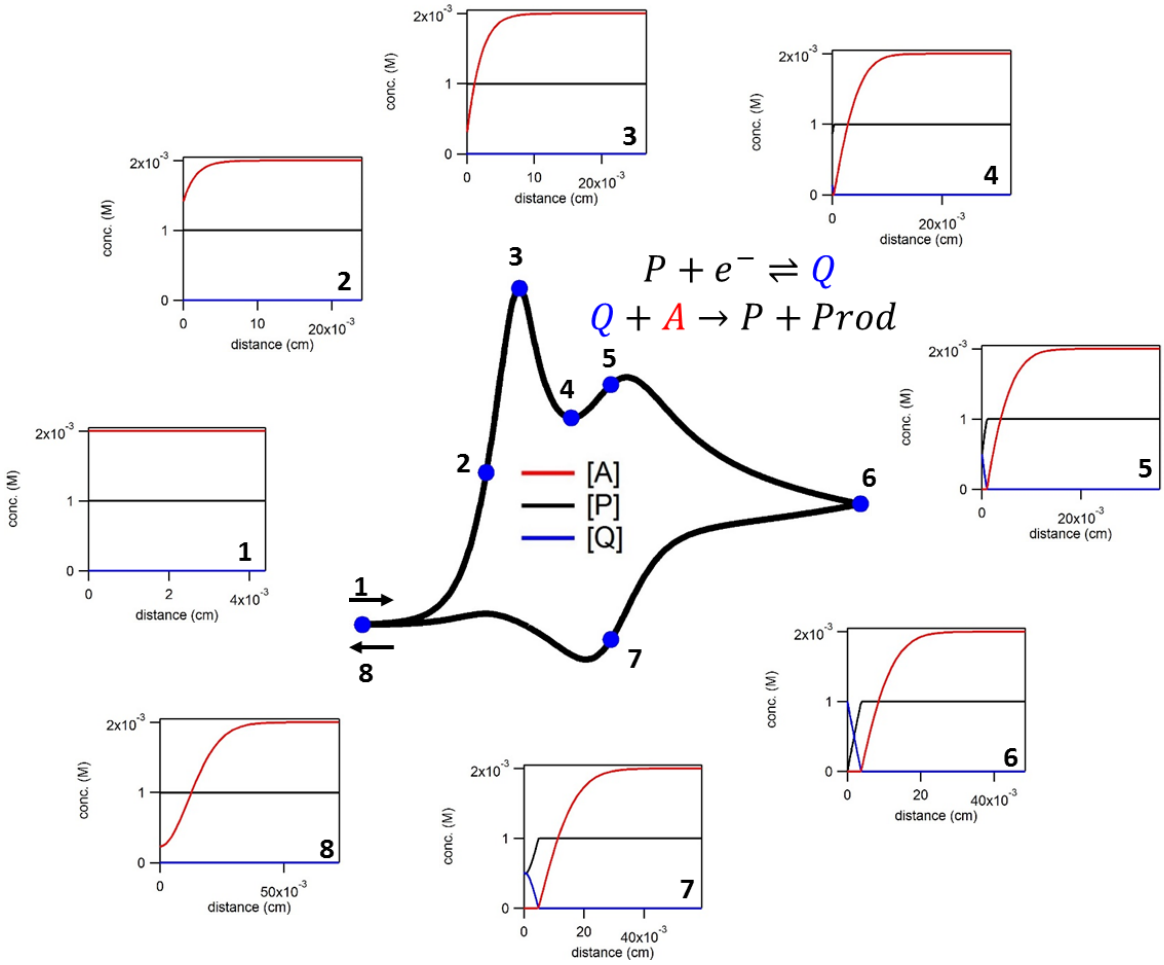

Figure G.1. This figure illustrates the kinetic, thermodynamic, and concentration factors that give rise to the KT2 voltammogram. The cyclic voltammogram in the center was generated using the *EC*' mechanism with a bulk concentration for the catalyst [P] of 0.001 M and for the substrate [A], a concentration of 0.002 M. The rate constant for the homogeneous reaction is k_e = 1x 10^8 M^{-1} s^{-1} and the scan rate is 100 mV/s. The surrounding plots show the concentration of the catalyst P, substrate A and reduced catalyst Q as a function of the distance from the electrode for each of the marked points on the cyclic voltammogram. At point 1, the scan has not begun, so the concentration is the same as bulk for each species. Points 5 and 7 both are both at the $E^{0'}$ of the catalyst (as such [P] = [Q] at distance = 0). In all of the plots, it can be seen that the concentrations of P and Q are defined by the Nernst Equation at the surface of the electrode (distance = 0 cm). As the voltammogram is scanned between points 2 and 4, the

substrate at the surface of the electrode is consumed before the concentration of active catalyst (Q) reaches a value visually different from point 0. Points 5–7 illustrate that once the potential is in a range that significantly alters the concentrations of P and Q from their bulk values, no substrate is available near the electrode. The depletion of substrate continues to grow over the course of the scan, leading to a Nernstian redox wave for the catalyst. Restated, the catalyst is reduced (and reoxidized) and has no substrate in the reaction layer to react with. At point 8, we can see that once Q is completely re-oxidized, either at the electrode during the anodic scan or via reaction with A, the substrate diffuses back towards the electrode surface.

Extending the KT2 Equation to an ECEC' mechanism.

In our efforts to extend the equation defining peak position for an *EC'* reaction exhibiting total catalysis (Eq. 4.4, Eq. G.1) to a two electron, two proton system, we empirically determined that the peak position is well described by Eq. 4.5 (G.2) for scenarios in which the second electron transfer is much easier than the first and k_2 is infinitely faster than k_1 (see below). Eq. G.2 differs from Eq. 4.4 in the catalyst concentration; the concentration of catalyst is multiplied by a factor of 2 for the *ECEC'* reaction. This can be understood by realizing that each 'active' catalyst consumes two equivalents of substrate. Simulated results presented in Figure G.2 show a comparison of an *EC*' reaction, an *EC'* reaction with twice the concentration of catalyst, and an *ECEC'* reaction in which the second electron transfer is much easier than the first. As illustrated below, we have determined that Eq. 4.5 can be more widely applied to scenarios beyond those in which the second electron transfer is much easier than the first and k_2 is infinitely faster than k_1 (see below).

$$E_p = E^0 - \frac{RT}{F}(0.409) + \frac{RT}{2F} ln\left(\frac{RTk_1 D_P (C_P^0)^2}{FvD_A C_A}\right) \qquad \text{Eq. G.1}$$

$$E_p = E^0 - \frac{RT}{F}(0.409) + \frac{RT}{2F} ln\left(\frac{RTk_1 D_P (2C_P^0)^2}{FvD_A C_A}\right) \qquad \text{Eq. G.2}$$

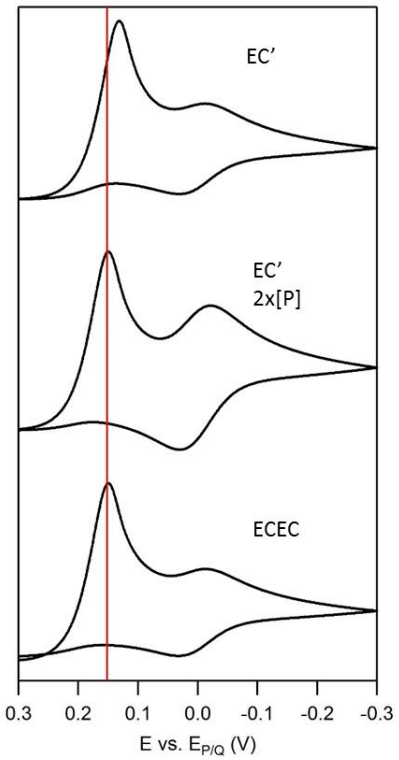

Figure G.2. Voltammograms for an EC' reaction with [P] = 0.001 M (top), an EC' reaction with [P] = 0.002 M (middle), and an ECEC reaction with [P] = 0.001 M (bottom) under conditions in which catalysis conforms to Zone KT2. The peak location of the middle and bottom voltammograms are identical. Other significant simulation parameters: [A] = 0.004 M, scan rate = 100 mV/s, and all diffusion coefficients = 1x10-5 cm2/s. The rate constants for chemical steps were $1x10^9$ M^{-1} s^{-1}. Simulations performed in DigiElch.

Identifying conditions for valid use of KT2 equation (Equation 4.5)

To determine the region in which the empirically determined KT2 equation (Eq. 4.5) is valid, voltammograms were simulated over the range of excess factors ($\gamma = [A]/[P]$) from 1 to 56 using a grid of k_1 and k_2 values each ranging from 10 to 1 x 10^{10} M^{-1} s^{-1}. The simplified two electron, two substrate, mechanism shown here was used for these simulations:

$$P + e \rightleftharpoons Q$$

$$Q + A \overset{k_1}{\rightarrow} PA$$

$$PA + e \rightleftharpoons QA$$

$$QA + A \overset{k_2}{\rightarrow} P + B$$

The simulations were performed with a diffusion coefficient for P of $D_P = 8x10^{-6}$ cm^2/s and for A of $D_A = 1.25x10^{-5}$ cm^2/s. It was assumed the second electron transfer was much significantly easier than the first ($E_{P/Q}$ = 0 V, and $E_{PA/QA}$ = 0.3 V). The script for generating grids of peak potential values was prepared in-house with MATLAB (The Mathworks, Inc.) using a higher order Crank-Nicolson finite differences method and is .[187,188] To confirm the accuracy of this method, results were checked against simulations with identical parameters using the

commercial DigiElch package. Scripts are provided in Section G.2. An example of one of these grids is shown here in Figure C.39.

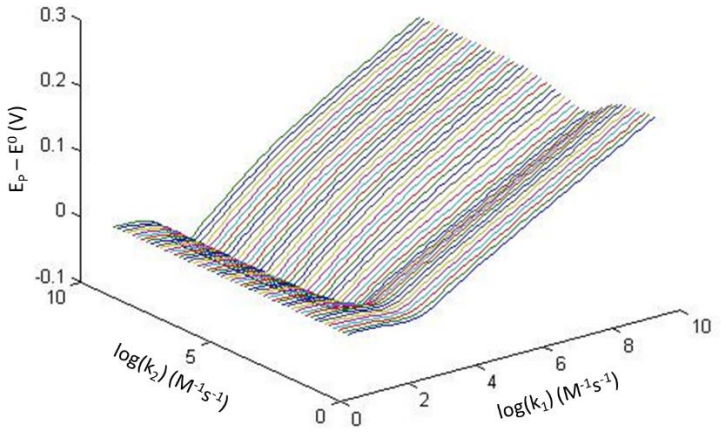

Figure G.3. The peak potential value is plotted against the log of k1 and k2. This particular dataset was obtained for concentrations [P] = 0.0005 M and [A] = 0.002, with a scan rate of 100 mV/s.

To simplify the analysis of this data, we examined the 2D cross sections where either k_1 = 1 x 10^{10} M^{-1} s^{-1} or k_2 = 1 x1 0^{10} M^{-1} s^{-1}, seen in Figure G.4.

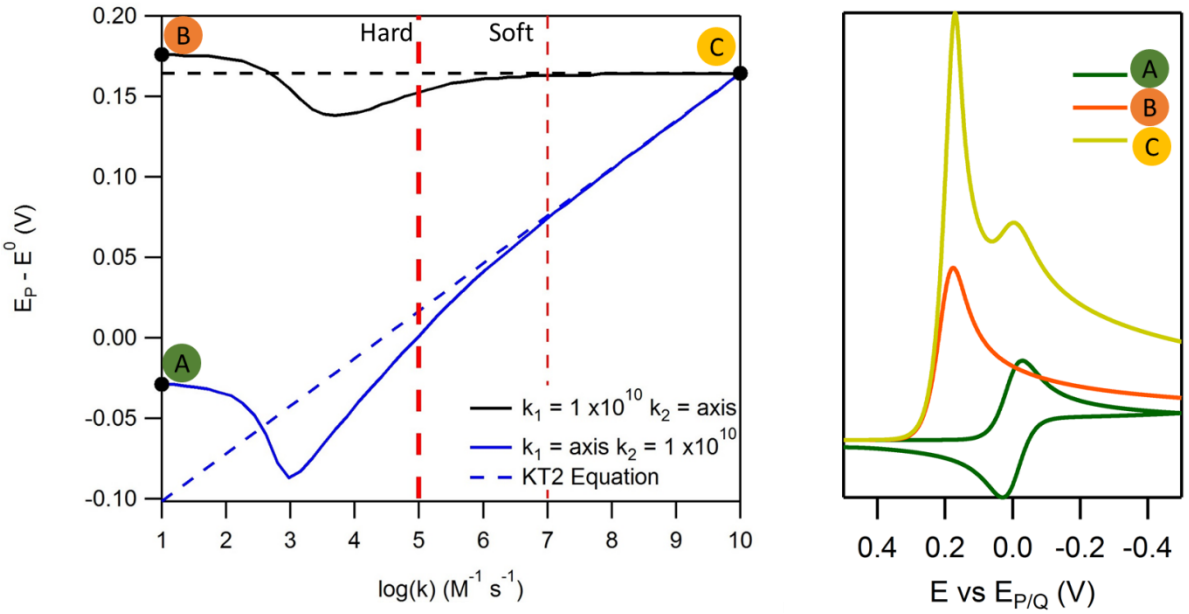

Figure G.4. (Right) Cross sections from Figure C.39 where k1 = 1 x 10^{10} M^{-1} s^{-1} (black) and k2 = 1 x 10^{10} M^{-1} s^{-1} (blue). The dashed lines represent the values determined from Eq. 4.5 (C.8) for identical conditions. The dashed red lines represent what we have assigned as our

'hard' ($k = 1x10^5\ M^{-1}s^{-1}$) and 'soft' ($k = 1x10^7\ M^{-1}s^{-1}$) boundaries for use of Eq. 4.5. (Left) The voltammograms at each of the points marked A, B, and C.

From Figure G.4, we have assigned boundaries for use of the KT2 equations; our hard boundary is defined by the region in which Eq. 4.5 and the simulation results are within half a log unit of one another (k_1 and $k_2 > 1 \times 10^5\ M^{-1}\ s^{-1}$) and our soft boundary is defined by the region in which Equation 5 and the simulation results are indistinguishable from one another (k_1 and $k_2 > 1 \times 10^7\ M^{-1}\ s^{-1}$). The voltammograms shown for points A, B, and C highlight that 1) for small values of k_1 (point A), a reversible wave is obtained, as the catalyst does not interact with the substrate fast enough to affect change, 2) for small values of k_2 (point B), the response is identical to that expected for an *ECE* reaction, whereby the peak current is proportional to two times the catalyst concentration and no redox wave is observed at $E_{P/Q}$, and 3) at or above our boundaries (point C), a "total catalysis" response is obtained, whereby the peak current is proportional to the substrate concentration and reduction of P to Q can be seen at $E_{P/Q}$.

As noted above, Eq. 4.5 was determined based on two assumptions: 1) the second electron transfer is much easier than the first ($E_{P/Q} < E_{PA/QA}$) and 2) the second chemical step is much faster than the first ($k_2 >> k_1$). Simulations were performed to quantify these conditions. Simulations were initially performed under conditions which Eq. 4.5 is valid: the simulated peak potential matched the value determined from Eq. 4.5. A series of voltammograms were then simulated in which value of k_2 and the potential of the second electron transfer ($E_{PA/QA}$) were altered (n.b. neither parameter is a factor in Equation 5). From these data, the difference between the peak potential obtained from the digital simulation and the peak potential determined from Eq. 4.5 (E(sim)–E(Eq. 4.5)) was determined as a function of both the ratio of the rate constants (k_2/k_1) and the difference between the potentials for the two electron transfer reactions ($E_{PA/QA} - E_{P/Q}$) (Figure G.5–G.7). From these data, we determined specific conditions in which Eq. 4.5 accurately predicts the peak potential, defined by $\log(k_2/k_1) + 32(E_2 - E_1) > 2.7$.

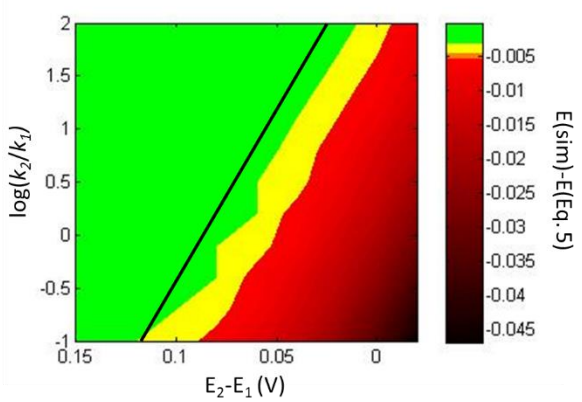

Figure G.5. Plot of the peak potential difference between the simulated value and the value predicted from Eq. 4.5 (colormap, green represents no deviation) as a function of the difference in potential between the first and second electron transfer (horizontal axis) and the logarithm of ratio of k_2 and k_1 (vertical axis). The black line represents the equation $\log(k_2/k_1) + 32(E_2 - E_1) = 2.7$. At values below 2.7, the simulated peak potentials no longer match the

predicted potential from Eq. 4.5. For this simulation, k_1 = 1 x 10^8 $M^{-1}s^{-1}$, E_1 = 0 V, υ= 0.1 V/s, and k_2 and E_2 were varied according to the axis.

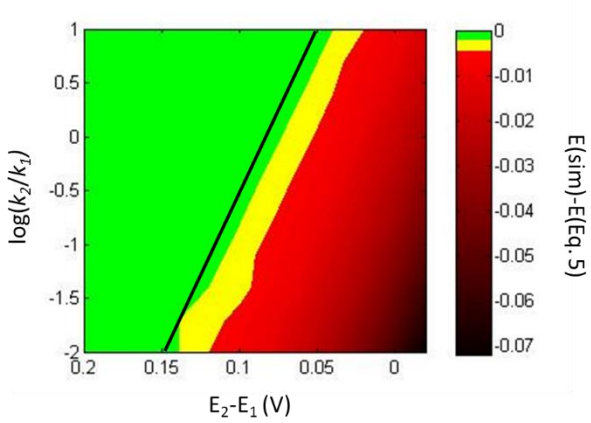

Figure G.6. Plot of the peak potential difference between the simulated value and the value predicted from Eq. 4.5 (colormap, green represents no deviation) as a function of the difference in potential between the first and second electron transfer (horizontal axis) and the logarithm of ratio of k_2 and k_1 (vertical axis). The black line represents the equation $\log(k_2/k_1) + 32(E_2 - E_1) = 2.7$. At values below 2.7, the simulated peak potentials no longer match the predicted potential from Eq. 4.5. For this simulation, k_1 = 1 x 10^9 M^{-1} s^{-1}, E_1 = 0 V, υ = 0.1 V/s, and k_2 and E_2 were varied according to the axis.

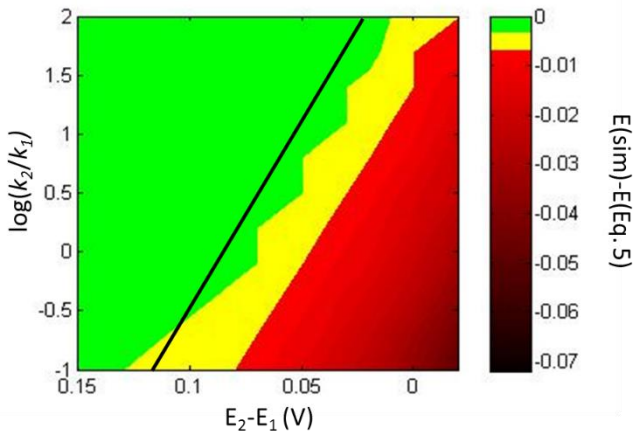

Figure G.7. Plot of the peak potential difference between the simulated value and the value predicted from Eq. 4.5 (colormap, green represents no deviation) as a function of the difference in potential between the first and second electron transfer (horizontal axis) and the logarithm of ratio of k_2 and k_1 (vertical axis). The black line represents the equation $\log(k_2/k_1) + 32(E_2 - E_1) = 2.7$. At values below 2.7, the simulated peak potentials no longer match the predicted potential from Eq. 4.5. For this simulation, k_1 = 1 x 10^8 M^{-1} s^{-1}, E_1 = 0 V, υ= 0.2 V/s, and k_2 and E_2 were varied according to the axis.

G.2 MATLAB functions for the finite difference simulations required for Figure G.3

```
function [ P,Q,PH,QH,H,x, Voltammogram, Potential ] =
CN_HO_KT_ECEC_Daniels( xcells, totalLength,exponential, timeSteps,
timeStep, scanRate, DiffusionCat,DiffusionSub, ConcCat,ConcSub, Rate1,
Rate2, Estart, EPHQH)
%CN_HO_KT_ECEC_Daniels.m
%Main file for simulations.
%All parameters necessary for simulation of a
%single voltammogram are sent here. This file generates a linear sweep
%voltammogram for an ECEC catalytic mechanism.
%
%The potential for the first electron tranfer is assumed to be zero volts.
%
%INPUT
%   xcells = number of concentration data points. (e.g 20)
%   totalLength = distance from electrode being modeled in cm. (e.g. 0.03)
%   exponential = exponential increase of data points for creating a
%       non-uniform concentration grid. (e.g 1.8)
%   timeSteps = number of time points to be calculated. (e.g 500)
%   timeStep = length of time step in seconds. (e.g. 0.01)
%   scanRate = scan rate for the voltammogram in V/s. (e.g. 0.1)
%   DiffusionCat = Diffusion coefficient for the catalyst (e.g. 8e-6)
%   DiffusionSub = Diffusion coefficient for the substrate (e.g. 1e-6)
%   ConcCat = initial concentration of the catalyst in molarity (e.g.
%   0.001)
%   ConcSub = initial concentration of the substrate in molarity (e.g.
%   0.01)
%   Rate1 = rate of the first chemical step (e.g. 1e8)
%   Rate2 = rate of the second chemical sep (e.g. 1e8)
%   Estart = starting potential for scan (e.g. 0.3)
%   EPHQH = redox potential of the second electron transfer (e.g. 0.3)
%
%OUTPUT
%   P = Final Concentration array for P
%   Q = Final Concentration array for Q
%   PH = Final Concentration array for PH
%   QH = Final Concentration array for QH
%   H = Final Concentration array for H
%   x = distance array
%   Voltammogram = Current array
%   Potential = Potential array

%Prepares distance grid for concentration profiles
x = PrapareNonUniformGrid( xcells, totalLength, exponential);
%Prepares Matrices for calculating diffusion (assuming all same D)
%A = left (future coefficients), B = right (Present Coefficients)
[ APBase, BPBase ] = PrepareDiffusionalMatrices( xcells, DiffusionCat,
timeStep, x);
[ AHBase, BHBase ] = PrepareDiffusionalMatrices( xcells, DiffusionSub,
timeStep, x);
AP = APBase;
AQ = APBase;
APH = APBase;
AQH = APBase;
AH = AHBase;
```

```
BP = BPBase;
BQ = BPBase;
BPH = BPBase;
BQH = BPBase;
BH = BHBase;

%Initialize concentration matrices and set to zero
P = zeros(length(x),1);
Q = zeros(length(x),1);
PH = zeros(length(x),1);
QH = zeros(length(x),1);
H = zeros(length(x),1);

%Set initial value for concentrations
P = P+ConcCat;
H = H+ConcSub;

%Initialize Matrices for newly calculate concentrations after each
timestep
PFnew = P;
QFnew = Q;
PHFnew = PH;
QHFnew = QH;
HFnew = H;

%Prepare kinetic parameter
kinetic1P = 0.5*Rate1/DiffusionCat;
kinetic2P = 0.5*Rate2/DiffusionCat;

kinetic1H = 0.5*Rate1/DiffusionSub;
kinetic2H = 0.5*Rate2/DiffusionSub;

%set initial potential
E = Estart;
%initialize Current and Potential arrays
Voltammogram = zeros(timeSteps,1);
Potential = Voltammogram;
%loop for stepping time
for j = 1:timeSteps
    %time from beginning
    t = j*timeStep;
    %set new potential
    Enow = E-t*scanRate;
    %determine boundary conditions for electroactive species
    RatioPQ = exp(38.941*Enow);
    RatioPHQH = exp(38.941*(Enow-EPHQH));
    change = 10;
    %loop to allow convergence to correct value for interdependent
    %parameters
    while change > .0000001

        PF = PFnew;
        QF = QFnew;
        PHF = PHFnew;
        QHF = QHFnew;
```

```
        HF = HFnew;

        %Calculating diffusion matrices
        for i = 2:xcells+1
            %Changes to P made in p below
            AQ(i,i) = APBase(i,i)+kinetic1P*(HF(i)+H(i));
            BQ(i,i) = BPBase(i,i)-kinetic1P*(HF(i)+H(i));
            %Changes to PH made in ph below
            AQH(i,i) = APBase(i,i)+kinetic2P*(HF(i)+H(i));
            BQH(i,i) = BPBase(i,i)-kinetic2P*(HF(i)+H(i));

            AH(i,i) =
AHBase(i,i)+kinetic1H*(QF(i)+Q(i))+kinetic2H*(QHF(i)+QH(i));
            BH(i,i) = BHBase(i,i)-kinetic1H*(QF(i)+Q(i))-
kinetic2H*(QHF(i)+QH(i));
        end
        %Solving for concentration
        p = BP*P+kinetic2P*(QHF+QH).*(HF+H);
        q = BQ*Q;
        ph = BPH*PH+kinetic1P*(QF+Q).*(HF+H);
        qh = BQH*QH;
        h = BH*H;
        Total = PF(2)+QF(2);
        %boundary conditions
        p(1) = RatioPQ*Total/(1+RatioPQ);
        q(1) = Total - p(1);
        Total = PHF(2)+QHF(2);
        ph(1) = RatioPHQH*Total/(1+RatioPHQH);
        qh(1) = Total - ph(1);
        h(1) = HF(2);
        p(xcells+2) = ConcCat;
        q(xcells+2) = 0;
        ph(xcells+2) = 0;
        qh(xcells+2) = 0;
        h(xcells+2) = ConcSub;

        PFnew = AP\p;
        QFnew = AQ\q;
        PHFnew = APH\ph;
        QHFnew = AQH\qh;
        HFnew = AH\h;

        changeP = abs(mean(PFnew-PF))/ConcCat;
        changeQ = abs(mean(QFnew-QF))/ConcCat;
        changePH = abs(mean(PHFnew-PHF))/ConcCat;
        changeQH = abs(mean(QHFnew-QHF))/ConcCat;
        changeH = abs(mean(HFnew-HF))/ConcSub;

        change =changeP+changeQ+changePH+changeQH+changeH;
    end
    %setting new concentations to current
    P = PFnew;
    Q = QFnew;
    PH = PHFnew;
    QH = QHFnew;
    H = HFnew;
```

```
    %Filling in Current and Potential arrays
    Voltammogram(j,1) = DiffusionCat*96485*(P(2)-P(1))*0.001/(x(2)-
x(1))+DiffusionCat*96485*(PH(2)-PH(1))*0.001/(x(2)-x(1));
    Potential(j,1) = Enow;
end
```

```
function [ x ] = PrapareNonUniformGrid( xcells, totalLength, exponential )
%PrepareNonUniformGrid
%Called by CN_HO_KT_ECEC_Daniels.
%Prepares non-uniform grid for concentration profile
%
%INPUT
%   xcells = number of concentration data points. (e.g 20)
%   totalLength = distance from electrode being modeled in cm. (e.g. 0.03)
%   exponential = exponential increase of data points for creating a
%       non-uniform concentration grid. (e.g 1.8)
%
%OUTPUT
%   x = non-uniform grid


a = 1:1:xcells-2;
a = a';
a = exponential.^a;
a = totalLength*a/a(xcells-2);
a = a-(2*a(1)-a(2));
a = a+0.5*a(1);
a = a*(totalLength-(a(xcells-2)-a(xcells-3))/2)/a(xcells-2);
x = zeros(xcells+2,1);
x(2,1) = 2*a(1)-a(2);
x(1,1) = -x(2,1);
for i = 3:length(a)+2
    x(i,1) = a(i-2,1);
end
x(xcells+1,1) = x(xcells,1)+(x(xcells,1)-x(xcells-1,1));
x(xcells+2,1) = x(xcells+1,1)+(x(xcells,1)-x(xcells-1,1));

end
```

```
function [ A, B ] = PrepareDiffusionalMatrices( xcells, Diffusion,
timeStep, x)
%PrepareDiffusionalMatrices
%Called by CN_HO_KT_ECEC_Daniels
%Prepares diffusional mattrices using a higher order Crank Nicolson
method,
%the details of which can be found at:
%Liu, J.; Pope, G.; Sepehrnoori, K. Appl. Math. Modelling, 1995, 19,
%162-172
%
```

```
%INPUT
%   xcells = number of concentration data points. (e.g 20)
%   Diffusion = Diffusion coefficient in cm^2/s. (e.g. 1e-5)
%   timeStep = length of time step in seconds. (e.g. 0.01)
%   x = non-uniform distance grid
%
%OUTPUT
%   A = Constant matrices for diffusion calculation
%   B = Constant matrices for diffusion calculation


A = zeros(xcells+2);
B = zeros(xcells+2);
A(1,1) = 0.5;
A(1,2) = 0.5;
delta = 1/(x(2)-x(1))^2;
A(2,1) = -delta;
A(2,2) = 2/(Diffusion*timeStep)+2*delta;
A(2,3) = -delta;
B(2,1) = delta;
B(2,2) = 2/(Diffusion*timeStep)-2*delta;
B(2,3) = delta;
for i = 3:length(x)-2
    dXl2 = abs(x(i-2)-x(i-1));
    dXl1 = abs(x(i-1)-x(i));
    dX = abs(x(i)-x(i+1));
    dXr1 = abs(x(i+1)-x(i+2));
    dl2 = dXl1+(dXl2+dX)/2;
    dl1 = (dXl1+dX)/2;
    dr1 = (dX+dXr1)/2;
    a = 2*(dr1-dl1)/(dl2*(dl2+dr1)*(dl2-dl1));
    b = 2*(dl2-dr1)/(dl1*(dl2-dl1)*(dl1+dr1));
    c = 2*(dl2+dl1)/(dr1*(dl1+dr1)*(dl2+dr1));

    A(i,i-2) = -a;
    A(i,i-1) = -b;
    A(i,i) = 2/(Diffusion*timeStep)+a+b+c;
    A(i,i+1) = -c;
    B(i,i-2) = a;
    B(i,i-1) = b;
    B(i,i) = 2/(Diffusion*timeStep)-a-b-c;
    B(i,i+1) = c;
end
A(length(x)-1,length(x)-2) = -delta;
A(length(x)-1,length(x)-1) = 2/(Diffusion*timeStep)+2*delta;
A(length(x)-1,length(x)) = -delta;
B(length(x)-1,length(x)-2) = delta;
B(length(x)-1,length(x)-1) = 2/(Diffusion*timeStep)-2*delta;
B(length(x)-1,length(x)) = delta;
A(xcells+2,xcells+1) = 0.5;
A(xcells+2,xcells+2) = 0.5;

end
```

REFERENCES

(1) Carter, J. In *Vital Speeches of the Day*; 1977; pp 418–420.

(2) Owen, N. A.; Inderwildi, O. R.; King, D. A. *Energy Policy* **2010**, *38* (8), 4743.

(3) Lewis, N. S. *Chem. Rev.* **2015**, *115* (23), 12631.

(4) Cook, T. R.; Dogutan, D. K.; Reece, S. Y.; Surendranath, Y.; Teets, T. S.; Nocera, D. G. *Chem. Rev.* **2010**, *110* (11), 6474.

(5) DuBois, D. L. *Inorg. Chem.* **2014**, *53* (8), 3935.

(6) Song, W.; Chen, Z.; Brennaman, M. K.; Concepcion, J. J.; Patrocinio, A. O. T.; Murakami Iha, N. Y.; Meyer, T. J. *Pure Appl. Chem.* **2011**, *83* (4), 749.

(7) McKone, J. R.; Marinescu, S. C.; Brunschwig, B. S.; Winkler, J. R.; Gray, H. B. *Chem. Sci.* **2014**, *5* (3), 865.

(8) Bard, A. J. **2010**, 7559.

(9) Benson, E. E.; Kubiak, C. P.; Sathrum, A. J.; Smieja, J. M. *Chem. Soc. Rev.* **2009**, *38* (1), 89.

(10) Tard, C.; Pickett, C. J. *Chem. Rev.* **2009**, *109* (6), 2245.

(11) Chen, L.; Chen, G.; Leung, C.; Yiu, S.; Ko, C.; Anxolabéhère-Mallart, E.; Robert, M.; Lau, T.-C. *ACS Catal.* **2015**, *5* (1), 356.

(12) Sathrum, A. J.; Kubiak, C. P. *J. Phys. Chem. Lett.* **2011**, 2372.

(13) Costentin, C.; Robert, M.; Savéant, J.-M. *Chem. Soc. Rev.* **2013**, *42* (6), 2423.

(14) Raugei, S.; Chen, S.; Ho, M.-H.; Ginovska-Pangovska, B.; Rousseau, R. J.; Dupuis, M.; DuBois, D. L.; Bullock, R. M. *Chem. - A Eur. J.* **2012**, *18* (21), 6493.

(15) Bediako, D. K.; Solis, B. H.; Dogutan, D. K.; Roubelakis, M. M.; Maher, A. G.; Lee, C. H.; Chambers, M. B.; Hammes-Schiffer, S.; Nocera, D. G. *Proc. Natl. Acad. Sci.* **2014**, *111* (42), 15001.

(16) Hammes-Schiffer, S. *Acc. Chem. Res.* **2009**, *42* (12), 1881.

(17) Compton, R. G.; Banks, C. E. *Understanding Voltammetry*, 2nd ed.; Imperial College Press: London, 2011.

(18) Mabbott, G. A. *J. Chem. Educ.* **1983**, *60* (9), 697.

(19) Felton, G. A. N.; Mebi, C. A.; Petro, B. J.; Vannucci, A. K.; Evans, D. H.; Glass, R. S.; Lichtenberger, D. L. *J. Organomet. Chem.* **2009**, *694* (17), 2681.

(20) Evans, D. H.; O'Connell, K. M.; Petersen, R. A.; Kelly, M. J. *J. Chem. Ed.* **1983**, *60* (4), 290.

(21) Bard, A. J.; Faulkner, L. R. *Electrochemical Methods: Fundamentals and Applications*, 2nd ed.; John Wiley & Sons, Inc.: Hoboken, 2001.

(22) Savéant, J.-M. *Elements of Molecular and Biomolecular Electrochemistry*; Wiley-Interscience: New York, 2006.

(23) Savéant, J.-M.; Su, K. B. *J. Electroanal. Chem.* **1984**, *171*, 341.

(24) Savéant, J.-M. *Chem. Rev.* **2008**, *108* (7), 2348.

(25) Stewart, M. P.; Ho, M.-H.; Wiese, S.; Lindstrom, M. Lou; Thogerson, C. E.; Raugei, S.; Bullock, R. M.; Helm, M. L. *J. Am. Chem. Soc.* **2013**, *135* (16), 6033.

(26) Delahay, P.; Stiehl, G. L. *J. Am. Chem. Soc.* **1952**, *74*, 3500.

(27) Schwarz, W. M.; Shain, I. *J. Phys. Chem.* **1965**, *69*, 30.

(28) Nicholson, R. S.; Shain, I. *Anal. Chem.* **1964**, *36*, 706.

(29) Savéant, J.-M.; Vianello, E. *Electrochim. Acta* **1965**, *10* (December 1964), 905.

(30) Savéant, J.-M.; Vianello, E. *Electrochim. Acta* **1967**, *12*, 629.

(31) Andrieux, C. P.; Blocman, C.; Dumas-Bouchiat, J. M.; M'Halla, F.; Savéant, J.-M. *J. Electroanal. Chem.* **1980**, *113*, 19.

(32) Savéant, J.-M.; Su, K. B. *J. Electroanal. Chem.* **1985**, *196*, 1.

(33) Helm, M. L.; Stewart, M. P.; Bullock, R. M.; DuBois, M. R.; DuBois, D. L. *Science (80-.).* **2011**, *333* (6044), 863.

(34) Costentin, C.; Drouet, S.; Robert, M.; Savéant, J.-M. *J. Am. Chem. Soc.* **2012**, *134* (27), 11235.

(35) Lexa, D.; Savéant, J.-M.; Schafer, H. J.; Su, I. K.-B.; Vering, B.; Wang, D. L. *J. Am. Chem. Soc.* **1990**, *112*, 6162.

(36) Martin, D. J.; McCarthy, B. D.; Rountree, E. S.; Dempsey, J. L. *Dalt. Trans.* **2016**, *45* (24), 9970.

(37) Elgrishi, N.; McCarthy, B. D.; Rountree, E. S.; Dempsey, J. L. *ACS Catal.* **2016**, *6* (6), 3644.

(38) Rountree, E. S.; Martin, D. J.; McCarthy, B. D.; Dempsey, J. L. *ACS Catal.* **2016**, *6* (5), 3326.

(39) Elgrishi, N.; Kurtz, D. A.; Dempsey, J. L. *J. Am. Chem. Soc.* **2017**, *139* (1), 239.

(40) Horvath, S.; Fernandez, L. E.; Appel, A. M.; Hammes-Schiffer, S. *Inorg. Chem.* **2013**, *52* (7), 3643.

(41) Pourbaix, M. *Atlas of Electrochemical Equilibria in Aqueous Solutions, 2nd Edition*, 2nd ed.; National Association of Corrosion, 1974.

(42) Rountree, E. S.; Dempsey, J. L. *J. Am. Chem. Soc.* **2015**, *137* (41), 13371.

(43) Costentin, C.; Drouet, S.; Passard, G.; Robert, M.; Savéant, J.-M. *J. Am. Chem. Soc.* **2013**, *135* (24), 9023.

(44) Costentin, C.; Savéant, J.-M. *ChemElectroChem* **2014**, *1* (7), 1226.

(45) Gagliardi, C. J.; Murphy, C. F.; Binstead, R. a.; Thorp, H. H.; Meyer, T. J. *J. Phys. Chem. C* **2015**, *119* (13), 7028.

(46) Wasylenko, D. J.; Rodr, C.; Pegis, M. L.; Mayer, J. M. *J. Am. Chem. Soc.* **2014**, *136*, 12544.

(47) Symes, M. D.; Surendranath, Y.; Lutterman, D. a.; Nocera, D. G. *J. Am. Chem. Soc.* **2011**, *133* (14), 5174.

(48) Bourrez, M.; Steinmetz, R.; Ott, S.; Gloaguen, F.; Hammarström, L. *Nat. Chem.* **2015**, *7* (2), 140.

(49) Mandal, S.; Shikano, S.; Yamada, Y.; Lee, Y.-M.; Nam, W.; Llobet, A.; Fukuzumi, S. *J. Am. Chem. Soc.* **2013**, *135* (41), 15294.

(50) Bullock, R. M.; Appel, A. M.; Helm, M. L. *Chem. Commun.* **2014**, *50* (24), 3125.

(51) Dempsey, J. L.; Brunschwig, B. S.; Winkler, J. R.; Gray, H. B. *Acc. Chem. Res.* **2009**, *42* (12), 1995.

(52) Wasylenko, D. J.; Palmer, R. D.; Berlinguette, C. P. *Chem. Commun.* **2013**, *49* (3), 218.

(53) Concepcion, J. J.; Jurss, J. W.; Brennaman, M. K.; Hoertz, P. G.; Patrocinio, A. O. T.; Murakami Iha, N. Y.; Templeton, J. L.; Meyer, T. J. *Acc. Chem. Res.* **2009**, *42* (12), 1954.

(54) Wilson, A. D.; Shoemaker, R. K.; Miedaner, a; Muckerman, J. T.; DuBois, D. L.; DuBois, M. R. *Proc. Natl. Acad. Sci. U. S. A.* **2007**, *104* (17), 6951.

(55) Rakowski DuBois, M.; DuBois, D. L. *Chem. Soc. Rev.* **2009**, *38* (1), 62.

(56) Kilgore, U. J.; Stewart, M. P.; Helm, M. L.; Dougherty, W. G.; Kassel, W. S.; Dubois, M. R.; Dubois, D. L.; Bullock, R. M. *Inorg. Chem.* **2011**, *50*, 10908.

(57) DuBois, D. L.; Bullock, R. M. *Eur. J. Inorg. Chem.* **2011**, *2011* (7), 1017.

(58) Yang, J. Y.; Bullock, R. M.; DuBois, M. R.; DuBois, D. L. *MRS Bull.* **2011**, *36* (1), 39.

(59) Rakowski DuBois, M.; DuBois, D. L. *Acc. Chem. Res.* **2009**, *42* (12), 1974.

(60) Ho, M. H.; Rousseau, R.; Roberts, J. A. S.; Wiedner, E. S.; Dupuis, M.; Dubois, D. L.; Bullock, R. M.; Raugei, S. *ACS Catal.* **2015**.

(61) Wilson, A. D.; Newell, R. H.; McNevin, M. J.; Muckerman, J. T.; Rakowski DuBois, M.; DuBois, D. L. *J. Am. Chem. Soc.* **2006**, *128* (1), 358.

(62) Pool, D. H.; DuBois, D. L. *J. Organomet. Chem.* **2009**, *694* (17), 2858.

(63) Ginovska-Pangovska, B.; Dutta, A.; Reback, M. L.; Linehan, J. C.; Shaw, W. J. *Acc. Chem. Res.* **2014**, *47* (8), 2621.

(64) Hou, J.; Fang, M.; Cardenas, A. J. P.; Shaw, W. J.; Helm, M. L.; Bullock, R. M.; Roberts, J. a. S.; O'Hagan, M. *Energy Environ. Sci.* **2014**, *7* (12), 4013.

(65) Wiese, S.; Kilgore, U. J.; Ho, M.; Raugei, S.; Dubois, D. L.; Bullock, R. M.; Helm, M. L. *ACS Catal.* **2013**, *3*, 2527.

(66) Chen, S.; Ho, M.; Bullock, R. M.; Dubois, D. L.; Dupuis, M.; Rousseau, R.; Raugei, S. *ACS Catal.* **2014**, *4*, 229.

(67) McCarthy, B. D.; Martin, D. J.; Rountree, E. S.; Ullman, A. C.; Dempsey, J. L. *Inorg. Chem.* **2014**, *53* (16), 8350.

(68) Rountree, E. S.; McCarthy, B. D.; Eisenhart, T. T.; Dempsey, J. L. *Inorg. Chem.* **2014**, *53* (19), 9983.

(69) Das, P.; Stolley, R. M.; van der Eide, E. F.; Helm, M. L. *Eur. J. Inorg. Chem.* **2014**, No. 27, 4611.

(70) Wiedner, E. S.; Yang, J. Y.; Chen, S.; Raugei, S.; Dougherty, W. G.; Kassel, W. S.; Helm, M. L.; Bullock, R. M.; Dubois, M. R.; Dubois, D. L. **2012**.

(71) Galan, B. R.; Sch, J.; Linehan, J. C.; Seu, C.; Appel, A. M.; Roberts, J. A. S.; Helm, M. L.; Kilgore, U. J.; Yang, J. Y.; Dubois, D. L.; Kubiak, C. P. *J. Am. Chem. Soc.* **2011**, *133*, 12767.

(72) Bard, A. J.; Faulkner, L. R. In *Electrochemical Methods: Fundamental and Applications*; Harris, D., Swain, E., Robey, C., Aiello, E., Eds.; John Wiley & Sons, Inc.: Hoboken, 2001; pp 471–533.

(73) Elgrishi, N.; Chambers, M. B.; Fontecave, M. *Chem. Sci.* **2015**, 2522.

(74) Fraze, K.; Wilson, A. D.; Appel, A. M.; Dubois, M. R.; Dubois, D. L. **2007**, No. 27, 3918.

(75) Kilgore, U. J.; Roberts, J. a S.; Pool, D. H.; Appel, A. M.; Stewart, M. P.; DuBois, M. R.; Dougherty, W. G.; Kassel, W. S.; Bullock, R. M.; DuBois, D. L. *J. Am. Chem. Soc.* **2011**, *133* (15), 5861.

(76) Wiedner, E. S. Pacific Northwest National Laboratory, Richland, WA. Unpublished work, 2015.

(77) Artero, V.; Saveant, J.-M. *Energy Environ. Sci.* **2014**, *7*, 3808.

(78) Hoffert, W. a.; Roberts, J. a. S.; Morris Bullock, R.; Helm, M. L. *Chem. Commun.* **2013**, *49* (71), 7767.

(79) O'Hagan, M.; Shaw, W. J.; Raugei, S.; Chen, S.; Yang, J. Y.; Kilgore, U. J.; DuBois, D. L.; Bullock, R. M. *J. Am. Chem. Soc.* **2011**, *133* (36), 14301.

(80) Smith, S. E.; Yang, J. Y.; Dubois, D. L.; Bullock, R. M. *Angew. Chemie Int. Ed.* **2012**, *51* (13), 3152.

(81) O'Hagan, M.; Ho, M.; Yang, J. Y.; Appel, A. M.; Dubois, M. R.; Raugei, S.; Shaw, W. J.; Dubois, D. L.; Bullock, R. M. *J. Am. Chem. Soc.* **2012**, *134*, 19409.

(82) Ho, M. H.; Rousseau, R.; Roberts, J. A. S.; Wiedner, E. S.; Dupuis, M.; Dubois, D. L.; Bullock, R. M.; Raugei, S. *ACS Catal.* **2015**, *5* (9), 5436.

(83) O'Hagan, M.; Ho, M.; Yang, J. Y.; Appel, A. M.; DuBois, M. R.; Raugei, S.; Shaw, W. J.; DuBois, D. L.; Bullock, R. M. *J. Am. Chem. Soc.* **2012**, *134* (47), 19409.

(84) Moore, G. F.; Sharp, I. D. *J. Phys. Chem. Lett.* **2013**, *4* (4), 568.

(85) Favier, I.; Duñach, E. *Tetrahedron Lett.* **2004**, *45* (17), 3393.

(86) Gray, H. B. *Nat. Chem.* **2009**, *1*, 7.

(87) Lewis, N. S.; Nocera, D. G. *Proc. Natl. Acad. Sci.* **2006**, *103* (43), 15729.

(88) Costentin, C.; Robert, M.; Savéant, J.-M. *Acc. Chem. Res.* **2015**, *48*, 2996.

(89) Gratzel, M. *Acc. Chem. Res.* **2000**, *33* (5), 269.

(90) Gratzel, M. *Nature* **2001**, *414*, 338.

(91) Machan, C. W.; Sampson, M. D.; Chabolla, S. A.; Dang, T.; Kubiak, C. P. *Organometallics* **2014**, *33* (18), 4550.

(92) Marinescu, S. C.; Winkler, J. R.; Gray, H. B. *Proc. Natl. Acad. Sci. U. S. A.* **2012**, *109* (38), 15127.

(93) Valdez, C. N.; Dempsey, J. L.; Brunschwig, B. S.; Winkler, J. R.; Gray, H. B. *Proc. Natl. Acad. Sci. U. S. A.* **2012**, *109* (39), 15589.

(94) Hu, X.; Brunschwig, B. S.; Peters, J. C. *J. Am. Chem. Soc.* **2007**, *129* (29), 8988.

(95) Wiese, S.; Kilgore, U. J.; Dubois, D. L.; Bullock, R. M. *ACS Catal.* **2012**, *2*, 720.

(96) Reichardt, C.; Welton, T. *Solvents and Solvent Effects in Organic Chemistry*; Wiley-VCH Verlag GmbH: Weinheim, Germany, 2002.

(97) Coetzee, J. F. *Pure Appl. Chem.* **1986**, *58* (8), 1091.

(98) Haav, K.; Saame, J.; Kütt, A.; Leito, I. *European J. Org. Chem.* **2012**, *2012* (11), 2167.

(99) Kütt, A.; Rodima, T.; Saame, J.; Raamat, E.; Mäemets, V.; Kaljurand, I.; Koppel, I. a; Garlyauskayte, R. Y.; Yagupolskii, Y. L.; Yagupolskii, L. M.; Bernhardt, E.; Willner, H.; Leito, I. *J. Org. Chem.* **2011**, *76* (2), 391.

(100) Kütt, A.; Leito, I.; Kaljurand, I.; Sooväli, L.; Vlasov, V. M.; Yagupolskii, L. M.; Koppel, I. a. *J. Org. Chem.* **2006**, *71* (7), 2829.

(101) Klamt, A.; Eckert, F.; Leito, I. V. O.; Kaljurand, I.; Ku, A.; Diedenhofen, M. *J. Comput. Chem.* **2008**, *30*, 799.

(102) Fraze, K.; Wilson, A. D.; Appel, A. M.; Rakowski DuBois, M.; DuBois, D. L. *Organometallics* **2007**, *26* (16), 3918.

(103) Ho, M.; Raugei, S.; Rousseau, R.; Dupuis, M.; Bullock, R. M. *J. Chem. Theory Comput.* **2013**, *9*, 93505.

(104) Wiedner, E. S.; Brown, H. J. S.; Helm, M. L. *J. Am. Chem. Soc.* **2016**, *138*, 604.

(105) Kaljurand, I.; Kütt, A.; Sooväli, L.; Rodima, T.; Mäemets, V.; Leito, I.; Koppel, I. a. *J. Org. Chem.* **2005**, *70* (3), 1019.

(106) Rountree, E. S.; Dempsey, J. L. *Inorg. Chem.* **2016**, *55* (10), 5079.

(107) Kolthoff, I. M.; Chantooni, M. K.; Bhowmik, S. *Anal. Chem.* **1967**, *39*, 1627.

(108) Izutsu, K. *Acid-Base Dissociation Constants in Dipolar Aprotic Solvents; IUPAC Chemical Data Series*; Blackwell Science: Oxford, UK, 1990.

(109) Chantooni, M. K.; Kolthoff, I. M. *J. Am. Chem. Soc.* **1970**, *92* (8), 2236.

(110) Brown, H. J. S.; Wiese, S.; Roberts, J. a. S.; Bullock, R. M.; Helm, M. L. *ACS Catal.* **2015**, *5* (4), 2116.

(111) Appel, A. M.; Pool, D. H.; O'Hagan, M.; Shaw, W. J.; Yang, J. Y.; Rakowski DuBois, M.; DuBois, D. L.; Bullock, R. M. *ACS Catal.* **2011**, *1* (7), 777.

(112) Roberts, J. A. S.; Bullock, R. M. *Inorg. Chem.* **2013**, *52* (7), 3823.

(113) Felton, G. a N.; Glass, R. S.; Lichtenberger, D. L.; Evans, D. H. *Inorg. Chem.* **2006**, *45* (23), 9181.

(114) Milne, J. B. In *The Chemistry of Nonaqueous Solvents*; Lagowski, J. J., Ed.; Acedemic Press: New York, New York, 1978; pp 1–52.

(115) Di Tommaso, D. *CrystEngComm* **2013**, *15* (33), 6564.

(116) Wiedner, E. S.; Helm, M. L. *Organometallics* **2014**, *33*, 4617.

(117) Haddad, A. Z.; Kumar, D.; Sampson, K. O.; Matzner, A. M.; Mashuta, M. S.; Grapperhaus, C. A. *J. Am. Chem. Soc.* **2015**, *137*, 9238.

(118) Cavell, A. C.; Hartley, C. L.; Liu, D.; Tribble, C. S.; McNamara, W. R. *Inorg. Chem.* **2015**, *54* (7), 3325.

(119) Kal, S.; Filatov, A. S.; Dinolfo, P. H. *Inorg. Chem.* **2014**, *53*, 7137.

(120) Hartley, C. L.; DiRisio, R. J.; Chang, T. Y.; Zhang, W.; McNamara, W. R. *Polyhedron* **2015**.

(121) Connor, G. P.; Mayer, K. J.; Tribble, C. S.; McNamara, W. R. *Inorg. Chem.* **2014**, *53* (11), 5408.

(122) Wise, C. F.; Liu, D.; Mayer, K. J.; Crossland, P. M.; Hartley, C. L.; McNamara, W. R. *Dalt. Trans.* **2015**, *44* (32), 14265.

(123) Anslyn, E. V.; Dougherty, D. A. In *Modern Physical Organic Chemistry*; University Science Books: Sausilto, 2006.

(124) Salnikov, G. E.; Genaev, A. M.; Vasiliev, V. G.; Shubin, V. G. *Org. Biomol. Chem.* **2012**, *10* (11), 2282.

(125) Bonin, J.; Costentin, C.; Robert, M.; Savéant, J.-M.; Tard, C. *Acc. Chem. Res.* **2012**, *45* (3), 372.

(126) Fourmond, V.; Jacques, P.-A.; Fontecave, M.; Artero, V. *Inorg. Chem.* **2010**, *49* (22), 10338.

(127) Magoński, J.; Rajzer, B. *J. Chem. Soc. Perkin Trans. 2* **2000**, No. 6, 1181.

(128) Appel, A. M.; Helm, M. L. *ACS Catal.* **2014**, *4* (2), 630.

(129) Jackson, M. N.; Surendranath, Y. *J. Am. Chem. Soc.* **2016**, *138*, 3228.

(130) Kaupmees, K.; Kaljurand, I.; Leito, I. *J. Phys. Chem. A* **2010**, No. 114, 11788.

(131) Wang, M.; Chen, L.; Sun, L. *Energy Environ. Sci.* **2012**, *5* (5), 6763.

(132) Donovan, E. S.; Felton, G. a. N. *J. Organomet. Chem.* **2012**, *711*, 25.

(133) Alligrant, T. M.; Alvarez, J. C. *J. Phys. Chem. C* **2011**, *115* (21), 10797.

(134) Denisov, G. S.; Mikheev, V. A.; Sokornova, T. V; Shraiber, V. M. *Sov. J. Chem. Phys.* **1986**, *3* (8), 1739.

(135) Sandhya, K. S.; Suresh, C. H. *Organometallics* **2011**, *30*, 3888.

(136) Rossin, A.; Gonsalvi, L.; Phillips, A. D.; Maresca, O.; Lledos, A.; Peruzzini, M. *Organometallics* **2007**, *26*, 3289.

(137) Fulmer, G. R.; Miller, A. J. M.; Sherden, N. H.; Gottlieb, H. E.; Nudelman, A.; Stoltz, B. M.; Bercaw, J. E.; Goldberg, K. I. *Organometallics* **2010**, *29* (9), 2176.

(138) Thoi, V. S.; Sun, Y.; Long, J. R.; Chang, C. J. *Chem. Soc. Rev.* **2013**, *42* (6), 2388.

(139) Connolly, P.; Espenson, J. H. *Inorg. Chem.* **1986**, *25* (6), 2684.

(140) Szajna-Fuller, E.; Bakac, A. *Eur. J. Inorg. Chem.* **2010**, 2488.

(141) Hu, X.; Cossairt, B. M.; Brunschwig, B. S.; Lewis, N. S.; Peters, J. C. *Chem. Commun.* **2005**, 4723.

(142) Razavet, M.; Artero, V.; Fontecave, M. *Inorg. Chem.* **2005**, *44* (13), 4786.

(143) Baffert, C.; Artero, V.; Fontecave, M. *Inorg. Chem.* **2007**, *46* (5), 1817.

(144) Laga, S.; Blakemore, J.; Henling, L. *Inorg. Chem.* **2014**, No. Iii, 4.

(145) Andreiadis, E. S.; Jacques, P.-A.; Tran, P. D.; Leyris, A.; Chavarot-Kerlidou, M.; Jousselme, B.; Matheron, M.; Pécaut, J.; Palacin, S.; Fontecave, M.; Artero, V. *Nat. Chem.* **2013**, *5* (1), 48.

(146) Muresan, N. M.; Willkomm, J.; Mersch, D.; Vaynzof, Y.; Reisner, E. *Angew. Chemie Int. Ed.* **2012**, n/a.

(147) McCrory, C. C. L.; Uyeda, C.; Peters, J. C. *J. Am. Chem. Soc.* **2012**, *134* (6), 3164.

(148) Fihri, A.; Artero, V.; Razavet, M.; Baffert, C.; Leibl, W.; Fontecave, M. *Angew. Chem. Int. Ed. Engl.* **2008**, *47* (3), 564.

(149) Fihri, A.; Artero, V.; Pereira, A.; Fontecave, M. *Dalt. Trans.* **2008**, No. 41, 5567.

(150) Du, P.; Knowles, K.; Eisenberg, R. *J. Am. Chem. Soc.* **2008**, 11.

(151) Wang, M.; Na, Y.; Gorlov, M.; Sun, L. *Dalt. Trans.* **2009**, No. 33, 6458.

(152) Probst, B.; Kolano, C.; Hamm, P.; Alberto, R. *Inorg. Chem.* **2009**, *48* (5), 1836.

(153) Li, C.; Wang, M.; Pan, J.; Zhang, P.; Zhang, R.; Sun, L. *J. Organomet. Chem.* **2009**, *694* (17), 2814.

(154) Lazarides, T.; Mccormick, T.; Du, P.; Luo, G.; Lindley, B.; Eisenberg, R. *J. Am. Chem. Soc.* **2009**, *9* (pH 7), 9192.

(155) Du, P.; Schneider, J.; Luo, G.; Brennessel, W. W.; Eisenberg, R. *Inorg. Chem.* **2009**, *48* (11), 4952.

(156) Artero, V.; Chavarot-Kerlidou, M.; Fontecave, M. *Angew. Chemie Int. Ed.* **2011**.

(157) Krawicz, A.; Cedeno, D.; Moore, G. F. *Phys. Chem. Chem. Phys.* **2014**, *16* (30), 15818.

(158) Han, Z.; Eisenberg, R. *Acc. Chem. Res.* **2014**, *47* (8), 2537.

(159) McCormick, T. M.; Calitree, B. D.; Orchard, A.; Kraut, N. D.; Bright, F. V.; Detty, M. R.; Eisenberg, R. *J. Am. Chem. Soc.* **2010**, *132* (44), 15480.

(160) Krawicz, A.; Yang, J.; Anzenberg, E.; Yano, J.; Sharp, I. D.; Moore, G. F. *J. Am. Chem. Soc.* **2013**, *135* (32), 11861.

(161) Hawecker, J.; Lehn, J. m.; Ziessel, R. *Nouv. J. Chemie* **1983**, *7* (5), 271.

(162) Veldkamp, B. S.; Han, W.-S.; Dyar, S. M.; Eaton, S. W.; Ratner, M. A.; Wasielewski, M. R. *Energy Environ. Sci.* **2013**, *6* (6), 1917.

(163) Li, L.; Duan, L.; Wen, F.; Li, C.; Wang, M.; Hagfeldt, A.; Sun, L. *Chem. Commun.* **2012**, *48* (7), 988.

(164) Lakadamyali, F.; Reynal, A.; Kato, M.; Durrant, J. R.; Reisner, E. *Chem. - A Eur. J.* **2012**, *18* (48), 15464.

(165) Wen, F.; Yang, J.; Zong, X.; Ma, B.; Wang, D.; Li, C. *J. Catal.* **2011**, *281* (2), 318.

(166) Zhang, P.; Wang, M.; Li, C.; Li, X.; Dong, J.; Sun, L. *Chem. Commun.* **2010**, *46* (46), 8806.

(167) Solis, B. H.; Hammes-Schiffer, S. *Inorg. Chem.* **2011**, *50*, 11252.

(168) Dempsey, J. L.; Winkler, J. R.; Gray, H. B. *J. Am. Chem. Soc.* **2010**, *132* (47), 16774.

(169) Dempsey, J. L.; Winkler, J. R.; Gray, H. B. *J. Am. Chem. Soc.* **2010**, *132* (3), 1060.

(170) Muckerman, J. T.; Fujita, E. *Chem. Commun.* **2011**, *47* (46), 12456.

(171) Lacy, D. C.; Roberts, G. M.; Peters, J. C. *J. Am. Chem. Soc.* **2015**, *137* (14), 4860.

(172) Estes, D. P.; Grills, D. C.; Norton, J. R. **2014**, *4*, 4.

(173) Li, G.; Han, A.; Pulling, M. E.; Estes, D. P.; Norton, J. R. *J. Am. Chem. Soc.* **2012**, 20.

(174) Li, G.; Estes, D. P.; Norton, J. R.; Ruccolo, S.; Sattler, A.; Sattler, W. **2014**.

(175) Costentin, C.; Passard, G.; Savéant, J.-M. *J. Am. Chem. Soc.* **2015**, 150310160623005.

(176) Costentin, C.; Dridi, H.; Savéant, J.-M. *J. Am. Chem. Soc.* **2014**, *136* (39), 13727.

(177) Appel, A. M.; Lee, S.; Franz, J. A.; DuBois, D. L.; Rakowski DuBois, M.; Twamley, B. *Organometallics* **2009**, *28* (3), 749.

(178) Martin, D. J.; McCarthy, B. D.; Rountree, E. S.; Dempsey, J. L. *Unpubl. Work.*

(179) Costentin, C.; Drouet, S.; Robert, M.; Saveant, J.-M. *Science (80-.).* **2012**, *338* (6103), 90.

(180) Bhugun, I.; Lexa, D.; Saveant, J. *J. Am. Chem. Soc.* **1996**, *118* (0), 3982.

(181) Forshey, P. a.; Kuwana, T. *Inorg. Chem.* **1983**, *22* (5), 699.

(182) Andrieux, C. P.; Blocman, C.; Dumas-Bouchiat, J. M.; Saveant, J. M. *J. Am. Chem. Soc.* **1979**, *101* (13), 3431.

(183) Andrieux, C. P.; Blocman, C.; Dumas-Bouchiat, J. M.; M'Halla, F.; Savéant, J. M. *J. Electroanal. Chem. Interfacial Electrochem.* **1980**, *113* (1), 19.

(184) Nadjo, L.; Savéant, J. M.; Su, K. B. *J. Electroanal. Chem. Interfacial Electrochem.* **1985**, *196* (1), 23.

(185) Shi, C.; Anson, F. *Inorg. Chem.* **1990**, No. 8, 4298.

(186) Bakac, A.; Espenson, J. H. *J. Am. Chem. Soc.* **1984**, *106* (29), 5197.

(187) Crank, J. In *The Mathematics of Diffusion*; Oxford University Press: Bristol, England, 1975; pp 137–159.

(188) Liu, J.; Pope, G. A.; Seperhrnoori, K. *Appl. Math. Model.* **1995**, *19*, 162.

(189) Mishra, A.; Bäuerle, P. *Angew. Chemie Int. Ed.* **2012**, *51* (9), 2020.

(190) Dempsey, J. L.; Winkler, J. R.; Gray, H. B. *Chem. Rev.* **2010**, *110* (12), 7024.

(191) Huynh, M. H. V.; Meyer, T. J. *Chem. Rev.* **2007**, *107* (11), 5004.

(192) Hammes-Schiffer, S. *Acc. Chem. Res.* **2009**, *42* (12), 1881.

(193) Clough, A. J.; Yoo, J. W.; Mecklenburg, M. H.; Marinescu, S. C. *J. Am. Chem. Soc.* **2015**, *137* (1), 118.

(194) McCarthy, B. D.; Dempsey, J. L. *Inorg. Chem.* **2017**, *56* (3), 1225.

(195) Small, Y. A.; DuBois, D. L.; Fujita, E.; Muckerman, J. T. *Energy Environ. Sci.* **2011**, *4* (8), 3008.

(196) Esswein, A. J.; Nocera, D. G. *Chem. Rev.* **2007**, *107* (10), 4022.

(197) McNamara, W. R.; Han, Z.; Alperin, P. J.; Brennessel, W. W.; Holland, P. L.; Eisenberg, R. *J. Am. Chem. Soc.* **2011**, *133* (39), 15368.

(198) Costentin, C.; Drouet, S.; Passard, G.; Robert, M.; Saveant, J.-M. *J. Am. Chem. Soc.* **2013**.

(199) Brunner, E. *J. Chem. Eng. Data* **1985**, *30* (3), 269.

(200) Anxolabéhère-Mallart, E.; Costentin, C.; Fournier, M.; Robert, M. *J. Phys. Chem. C* **2014**, *118* (25), 13377.

(201) Dempsey, J. L.; Winkler, J. R.; Gray, H. B. In *Comprehensive Inorganic Chemistry II*; Reedijk, J., Poeppelmeier, K., Eds.; Elsevier: Oxford, 2013; Vol. 8, pp 553–565.

(202) Du, P.; Eisenberg, R. *Energy Environ. Sci.* **2012**, *5* (3), 6012.

(203) Duan, L.; Bozoglian, F.; Mandal, S.; Stewart, B.; Privalov, T.; Llobet, A.; Sun, L. *Nat. Chem.* **2012**, *4* (5), 418.

(204) Thoi, V. S.; Karunadasa, H. I.; Surendranath, Y.; Long, J. R.; Chang, C. J. *Energy Environ. Sci.* **2012**, *5* (7), 7762.

(205) Artero, V.; Fontecave, M. *Chem. Soc. Rev.* **2013**, *42* (6), 2338.

(206) Dempsey, J. L.; Winkler, J. R.; Gray, H. B. *J. Am. Chem. Soc.* **2010**, *132* (47), 16774.

(207) Costentin, C.; Passard, G.; Robert, M.; Savéant, J.-M. *J. Am. Chem. Soc.* **2014**, *136* (33), 11821.

(208) Britz, D. *Digital Simulation in Electrochemistry*, Third Edit.; Springer: Heidelberg, 2005.

(209) Ener, M. E.; Lee, Y.-T.; Winkler, J. R.; Gray, H. B.; Cheruzel, L. *Proc. Natl. Acad. Sci. U. S. A.* **2010**, *107* (44), 18783.

(210) Brdicka, R.; Wiesner, K. *Collect. Czechoslov. Chem. Communs.* **1947**, *12*, 39.

(211) Anslyn, E. V.; Dougherty, D. A. In *Modern Physical Organic Chemistry*; University Science Books: Sausalito, 2006; pp 355–420.

(212) Felton, G. a N.; Vannucci, A. K.; Chen, J.; Lockett, L. T.; Okumura, N.; Petro, B. J.; Zakai, U. I.; Evans, D. H.; Glass, R. S.; Lichtenberger, D. L. *J. Am. Chem. Soc.* **2007**, *129* (41), 12521.

(213) Costentin, C.; Dridi, H.; Savéant, J. *J. Am. Chem. Soc.* **2014**, *136*, 13727.

(214) Blackmond, D. G. *Angew. Chem. Int. Ed. Engl.* **2005**, *44* (28), 4302.